MULTISCALE MODELING OF SODIUM-ION BATTERY MATERIALS

BY

RATSHILUMELA STEVE DIMA

(15017654)

Thesis

PRESENTED IN FULFILMENT OF THE REQUIREMENTS FOR THE DOCTOR OF PHILOSOPHY (Ph.D.) DEGREE

IN

PHYSICS

FACULTY OF SCIENCE, ENGINEERING, AND AGRICULTURE

AT THE

UNIVERSITY OF VENDA

PROMOTER: Prof R.R MAPHANGA (CSIR)

Co-PROMOTER: Prof E.N MALUTA (UNIVEN)

YEAR: 2024

Declaration

I, Ratshilumela Steve Dima, declare that the thesis which is hereby submitted for the qualification of Doctor of Philosophy in Physics at the University of Venda is my own independent work and has not been submitted for any degree at any other university or institution. The thesis does not contain other people's writing, unless specifically acknowledged and referenced accordingly.

Signed (Student):  Date: 2024

Signed (Supervisor): _____ Date: 2024

Signed (Co-Supervisor): _____ Date: 2024

Abstract

In recent years, there has been a growing interest in alternative energy storage technologies as a result of the diminishing reserves of fossil fuels. The development of these technologies requires a careful evaluation of factors such as energy storage and conversion, implementation costs, and environmental impact. Rechargeable batteries are expected to become crucial energy storage devices and promote a more sustainable energy ecosystem. Battery technology has the potential to become cost competitive, especially for portable applications, and exhibits exceptional efficiency, exceeding 90% in electrical efficiency. Sodium ion batteries are considered to be cost-effective and economically feasible alternatives. This work used multiscale computer modelling techniques to understand, control, and improve the intrinsic properties of Na_xMnPO_4, an electrode material that undergoes Na intercalation and de-intercalation processes. This work aims to promote a more sustainable energy ecosystem.

Firstly, we examine the structural and electrochemical performance of Na_xMnPO_4 using the first-principle density functional theory method. Comparison of the exchange correlation functionals PBE, PBEsol, and PBE+U was conducted, and the results showed that the PBE+U replicated the structural parameters and the energy band gap values well and was used to further analyse the electrochemical performance of the de-intercalated systems. The effect of Na atom de-intercalation on the structural, electronic, mechanical, and thermodynamic properties of both maricite and olivine polymorphs of $NaMnPO_4$ has been investigated by first-principle calculations. The calculated values for the formation energy were found to be negative for all $NaMnPO_4$ systems, hence the solid solution is predicted for states of de-intercalation. The analysis of the electronic density of states indicated that, during the Na removal stages, the material exhibited a rise in its metallic properties between the first and third stages. On the contrary, in the fourth stage, the material displayed semiconductor behaviour, characterised by a band gap of 0.194 eV. A voltage range of 3.997 to 3.848 V was observed, and the computed formation energy values of the de-intercalated systems were determined to be negative, indicating the anticipated presence of a solid in the material.

Secondly, the *ab initio* molecular dynamics method was used to simulate the dynamic properties of Na_xMnPO_4 materials at different temperatures. The results showed an increasing mean-square displacement gradient as the number of de-intercalated Na atoms increased. The Na-ion diffusion coefficients for olivine and maricite $NaMnPO_4$ were calculated at 100 K and 300 K. Both polymorphs had low diffusion rates at 100 K but increased at 300 K, suggesting faster ion movement. These findings are crucial for understanding the behavior of Na_xMnPO_4 materials and their potential applications, as diffusion rates can affect processes such as charge / discharge rates in batteries and ion transport in solid-state electrolytes. Controlling temperature and understanding its influence on diffusion coefficients can optimize the performance of Na_xMnPO_4 materials.

Lastly, the cluster expansion (CE) method was introduced as a multiscale pipelining method, establishing a connection between first-principles calculation and large-scale atomistic simulations, as well as Monte Carlo simulation. CE was used to examine the phase stabilities of Na concentrations in relation to vacancies. The stability of the predicted structures on the isotopically optimized volume binary diagram was assessed by calculating their mechanical, electronic, and dynamic properties. Structures that underwent isotropic volume optimisation yielded a cross-validation score of 1.1 meV. This score suggests that the cluster expansion is of good quality, as it falls below the threshold of 5 meV per active position. Based on the analysis of the electronic structure, it is observed that both parent structures ($MnPO_4$ and $NaMnPO_4$) exhibit semiconducting behaviour, while the remaining structures (Na_1MnPO_4, $Na_{0.825}MnPO_4$, $Na_{0.75}MnPO_4$, $Na_{0.625}MnPO_4$, and $Na_{0.25}MnPO_4$) have semi-metallic characteristics. The mechanical stability of $NaMnPO_4$ was shown by the estimated elastic constants, since the stability conditions were met for all intercalated systems, except for the parent structure $MnPO_4$. Based on the Pugh criterion pertaining to the properties of ductility and brittleness, the structures of Na_1MnPO_4, $Na_{0.825}MnPO_4$, $Na_{0.75}MnPO_4$, $Na_{0.625}MnPO_4$, and $Na_{0.25}MnPO_4$ exhibit ductile characteristics, while the structures of $Na_{0.5}MnPO_4$ and $MnPO_4$ display brittleness. In addition, MD simulations were performed, revealing that the mean square displacement slope is influenced by the concentration of sodium ions, whereas the diffusion coefficients of sodium ions are influenced by the temperature. These findings suggest that the addition of sodium ions improves the ductility of $Na_{1-x}MnPO_4$ structures. The higher

concentration of sodium ions leads to increased ductility, as evidenced by the ductile characteristics observed in Na_1MnPO_4 and $Na_{0.825}MnPO_4$. However, as the concentration of sodium ions decreases, the structures become more brittle, as seen in $Na_{0.5}MnPO_4$ and $MnPO_4$. Furthermore, the MD simulations indicate that the movement of sodium ions within the structures is influenced by both the concentration of sodium ions and the temperature, highlighting the complex relationship between the composition and mechanical properties in these materials.

Dedications

I would like to dedicate this dissertation to my family: my late Father (Muhangwi Frank Dima), my amazing mother (Mbambadzeni Constance Dima), my two sisters (Adziambei Dima and Mukhethwa Dima), my two sons (Vhugala Oritonda Dima and Vhutali Thendo Dima) and the Dima Family for their moral support throughout my studies. Above all, I would love to dedicate this to the Almighty God for daily support and protection.

Acknowledgements

I would like to take this opportunity to thank my supervisor, Professor R.R. Maphanga, and co-supervisor, Professor N.E. Maluta, for the fantastic support, patience, encouragement, and constructive discussions that led to its conclusion.

I also appreciate the friendship and support of my friend during my Ph.D. studies. I also mention the help I received from my colleagues at the CSIR design and optimisation group. I also express my gratitude to the Physics Department for allowing me to continue with my PhD studies. I would like to thank CSIR-YREF for their financial assistance.

I express my gratitude to my mother, Mrs. Constance Dima, for her assistance throughout my Ph.D. studies. I would like to thank Almighty God for the wonderful gift of life, strength, wisdom, and perseverance. Finally, to my lovely boys, I love both of you and thank you for your patience and support, dad has finally returned home.

List of Figures

Figure 1: depicts (a) a simplified conceptual framework representing the interplay of renewable energy generation, the electrical grid, commercial secondary batteries, and hybrid/electric vehicle transportation, (b) shows a comparative analysis between sodium (Na) and lithium (Li), and (c) gives us a chronological account of the historical progression of battery development over the course of the last two centuries [3]. 2
Figure 2: working principle of both the LIB AND SIB cells [13]. 4
Figure 3: Schematic representation of simulations at various levels [9]. 8
Figure 4: Classification of Na–M–O layered materials with sheets of edge-sharing MO_6 octahedra and phase transition processes induced by sodium extraction [19]. 14
Figure 5: Crystal structure of (a) maricite $NaFePO_4$ and (b) olivine $NaFePO_4$ [33]. . 19
Figure 6: Calculated formation energies per formula unit for the most stable Na_xFePO_4 structures, including (a) $FePO_4$, (b) $Na_{2/3}FePO_4$, (c) $Na_{5/6}FePO_4$, and (d) $NaFePO_4$, as a function of the Na content [36]. 21
Figure 7: The first charging/discharging curves for $NaMnPO_4$ and $LiMnPO_4$ electrodes, showing charge and discharge capacity of $NaMnPO_4$ (black and red symbols) vs the number of cycles [38]. 22
Figure 8: Comparison of a wavefunction in the Coulomb potential of the nucleus (blue) to the one in the pseudopotential (red). The real and pseudo wave functions and potentials match above a certain cut-off radius r_c [58]. 38
Figure 9: The reciprocal lattices (dots) and corresponding first Brillouin zones of (a) square lattice and (b) hexagonal lattice [61]. 40
Figure 10: A diagram of the genetic algorithm [97] 64
Figure 11: Schematic crystallographic structures of (a) olivine and (b) maricite $NaMnPO_4$. 77
Figure 12: Spin-polarised band structure and DOS near Fermi level for $NaMnPO_4$ (a) PBE; (b) PBEsol and (c) GGA+U. The Fermi level is set to 0 eV and is shown by the dashed lines. In the DOS curve, the positive and negative values refer to the DOS of the spin-up and spin-down states. 79
Figure 13: Spin-polarised band structure and DOS near the Fermi level for olivine $NaMnPO_4$ (a) PBE; (b) PBEsol and (c) GGA+U. The Fermi level is set to 0 eV and is shown by the dashed lines. In the DOS curve, the positive and negative values refer to the DOS of the spin-up and spin-down states. 80

Figure 14: Crystallographic structures of maricite (a) $Na_{0.75}MnPO_4$, (b) $Na_{0.5}MnPO_4$, (c) $Na_{0.25}MnPO_4$, (d) $MnPO_4$ during Na extraction after relaxation. 84
Figure 15**:** Relaxed crystallographic structures of olivine (a) $Na_{0.75}MnPO_4$, (b) $Na_{0.5}MnPO_4$, (c) $Na_{0.25}MnPO_4$, (d) $MnPO_4$ during Na extraction. 85
Figure 16: De-intercalation potentials (V) for Na_xMnPO_4 (x=1, 0.75, 0.5, 0.25, 0) (a) maricite and (b) olivine. 89
Figure 17: Spin-polarised DOS near Fermi level of maricite Na_xMnPO_4 (x=1, 0.75, 0.5, 0.25, 0). The Fermi level is set to 0 eV and is shown by the dashed lines. In the DOS curve, the positive and negative values refer to the DOS of the spin-up and spin-down states..... 91
Figure 18: Spin-polarised DOS near Fermi level of olivine Na_xMnPO_4 (x = 1, 0.75, 0.5, 0.25, 0). The Fermi level is set to 0 eV and is shown by the dashed lines. In the DOS curve, the positive and negative values refer to the DOS of the spin-up and spin-down states, respectively. 93
Figure 19: Temperature-specific heat at constant volume (C_v) of Na_xMnPO_4 (x= 1, 0.75, 0.5, 0.25, 0). 101
Figure 20: The free energy versus temperature for Na_xMnPO_4 (x = 1, 0.75, 0.5, 0.25, 0). 101
Figure 21: Entropy vs. temperature for Na_xMnPO_4 (x = 1, 0.75, 0.5, 0.25, 0)..... 102
Figure 22: 5x5x5 supercells of (a) Na_1MnPO_4, (b) $Na_{0.75}MnPO_4$, (c) $Na_{0.5}MnPO_4$, (d) $Na_{0.25}MnPO_4$ structures used in the MD calculations, (where blue is the sodium atom, red is the oxygen atom, light green is the manganese atom and salmon is the phosphate atom). 110
Figure 23: The 5x5x5 supercells of (a) Na_1MnPO_4, (b) $Na_{0.75}MnPO_4$, (c) $Na_{0.5}MnPO_4$, (d) $Na_{0.25}MnPO_4$ structures after MD calculations at 100 K. 111
Figure 24: The radial distribution function of (a) Na_1MnPO_4, (b) $Na_{0.75}MnPO_4$, (c) $Na_{0.5}MnPO_4$, (d) $Na_{0.25}MnPO_4$ structures at 100 K. 112
Figure 25: The 5x5x5 supercells of (a) Na_1MnPO_4, (b) $Na_{0.75}MnPO_4$, (c) $Na_{0.5}MnPO_4$, (d) $Na_{0.25}MnPO_4$ structures after MD calculations at 300K. 114
Figure 26: The radial distribution function of (a) Na_1MnPO_4, (b) $Na_{0.75}MnPO_4$, (c) $Na_{0.5}MnPO_4$, (d) $Na_{0.25}MnPO_4$ structures at 300 K. 115
Figure 27**:** Mean squared displacement plots for Na_xMnPO_4 (X=0.25,0.5,0.75 and 1) for 5 ns at (a) 100 K and (b) 300 K. 117

Figure 28: Schematic shoeing VASP stages in cluster expansion. 123
Figure 29: Fully optimised ground state of $NaMnPO_4$ with a cross-validation score of 1.1 meV. The green block represents the DFT input, the red line is the DFT ground state line, and the grey and green crosses represent the anticipated structures from CE. 125
Figure 30: Projected densities of states of CE predicted $MnPO_4$ and Na_1MnPO_4. . 127
Figure 31: Spin-polarised DOS near Fermi level of olivine Na_xMnPO_4 (x = 0.25, 0.5, 0.625, 0.75, and 0.825) structures. The Fermi level is set to 0 eV and is shown by the dashed lines. 129
Figure 32: Temperature vs specific heat at constant volume (Cv) of Na_xMnPO_4 (x = 1, 0.825, 0.75, 0.625, 0.5, 0.25, 0). 134
Figure 33: Temperature vs. Free Energy of Na_xMnPO_4 (x = 1, 0.825, 0.75, 0.625, 0.5, 0.25, 0). 134
Figure 34: Temperature vs Entropy of Na_xMnPO_4 (x = 1,0.825, 0.75, 0.625, 0.5, 0.25, 0). 135
Figure 35: MSD vs time along the [100], [010], and [001] directions for a 5 ns simulation for $Na_{0.25}MnPO_4$ at 100 K. 138
Figure 36: MSD against time along the [100], [010], and [001] directions for a 5 ns simulation for $Na_{0.5}MnPO_4$ at 100 K. 139
Figure 37: Mean square displacement against time along the [010], [100], and [001] directions for 5 ns simulation for $Na_{0.75}MnPO_4$ at 100 K. 139
Figure 38: Mean square displacement versus time along the [100], [010], and [001] directions for 5 ns simulation for $Na_{0.25}MnPO_4$ at 300 K. 141
Figure 39: Mean square displacement against time along the [100], [010], and [001] directions for 5 ns simulation for $Na_{0.5}MnPO_4$ at 300 K. 141
Figure 40: MSD vs time along the [010], [100], and [001] directions for 10 ns simulation for $Na_{0.75}MnPO_4$ at 300 K. 142
Figure 41: MSD vs. time for $Na_{0.25}MnPO_4$ at 500 K in the [100], [010], and [001] directions for a simulation of 5 ns. 144
Figure 42: Mean square displacement versus time for $Na_{0.5}MnPO_4$ at 500 K in the [100], [010], and [001] directions for a simulation of 5 ns. 144
Figure 43: MSD against time for $Na_{0.75}MnPO_4$ at 500 K in the [100], [010], and [001] directions for a simulation of 5 ns. 145
Figure 44: The temperature schedule schematic. 149

Figure 45: The temperature profiles of the 10×10×10 Monte Carlo simulation cells of $Na_{0.25}MnPO_4$. 150
Figure 46: The temperature profiles of 10×10×10 Monte Carlo simulation cells of $Na_{0.5}MnPO_4$. 151
Figure 47: Temperature profiles of the 10×10×10 Monte Carlo simulation cells of $Na_{0.75}MnPO_4$. 152

List of Tables

Table 1: Calculated lattice parameters of maricite and olivine $NaMnOP_4$ and previously reported experimental results. 78
Table 2: Calculated lattice parameters of de-intercalated Na_xMnOP_4 polymorphs and their deviations from the initial structure. 86
Table 3: Elastic constants (C_{ij}) for the Na_xMnPO_4 maricite polymorph (x = 1, 0.75, 0.5, 0.25, 0). 95
Table 4: Elastic constants (C_{ij}) for the Na_xMnPO_4 olivine polymorph (x = 1, 0.75, 0.5, 0.25, 0). 95
Table 5: Bulk (B), Shear (G), and Young (E) moduli, Pugh ratio (B/G) for Na_xMnPO_4 olivine polymorphs (x = 1, 0.75, 0.5, 0.25, 0)..... 96
Table 6: Anisotropy in the shear elastic factor (A_i with i = 1,2,3), and anisotropy in the the compressibility and shear moduli (A_B and A_G in %). 97
Table 7: Calculated volumetric density ρ (in kg/m3), longitudinal vl transverse vt, and average sound velocities vt in m/s, and Debye temperature θD in Kelvin. 99
Table 8: Buckingham and three-body interatomic potentials for olivine Na_xMnPO_4. 107
Table 9: Olivine Na_xMnPO_4 lattice constants computed with DFT, ab initio MD, and LAMMPS-Buckingham potentials at 300 K..... 108
Table 10: The calculated Na^+ ion diffusion coefficients result for Na_xMnPO_4 (x = 0.25,0.5,0.75 and 1) for 5 ns at (a) 100 K and (b) 300 K. 119
Table 11: Phases determined to be the most stable based on the isotopically optimised convex hull diagram. 126
Table 12: The unique C_{ij} (GPa) for the triclinic Na_xMnPO_4 structures. 131
Table 13: Calculated elastic properties for Na_xMnPO_4 (x = 1, 0.825, 0.75, 0.625, 0.5, 0.25, 0) CE predicted structures. 132
Table 14: Calculated volumetric density ρ (in kg/m^3), longitudinal vl transverse vt, and average sound velocities vm in m/s, and Debye temperature θD in Kelvin. 133
Table 15**:** The calculated Na^+ ion diffusion coefficients for Na_xMnPO_4 (x=0.25,0.5 and 0.75) for 5 ns at 100 K, 300 K, and 500 K. 145

List of Abbreviations

Abbreviation	Full name
LIB	Lithium-ion battery
SIB	Sodium-ion battery
KIB	Potassium-ion battery
a.u.	Arbitrary unit
TMOs	Transition metal oxide compounds
PBA	Prussian blue analogous
MSM	Multiscale modelling
MD	molecular dynamics
kMC	kinetic Monte Carlo
FEM	Fiinite element method
cm	Centimeter
PVDF	Polyvinylidene fluoride
CV	Cyclic voltammetry
HEV	Hybrid electric vehicle
HRTEM	High-resolution transmission electron microscopy
(h k l)	Miller indices
M	Metal element
mm	Millimeter
nm	Nanometer
Li^+	Lithium ions
Na^+	Potassium ion
K^+	Sodium ion
Mn	Manganese
O	Oxygen
P	Phosphorus
DFT	Density functional theory
U	Hubbard correction term
LDA	Local density approximation
PBE	Perdew-Burke-Ernzerhof
PWP	Plane-wave pseudopotential
VASP	Vienna Ab-Initio Simulation Package

LAMMPS	Large-scale Atomic/Molecular Massively Parallel Simulator
UNCLE	Universal Cluster-Expansion
GGA	Generalised gradient approximation
CE	Cluster expansion
D	Diffusion coefficient
t	Diffusion time
DOS	Density of States
B	bulk modulus
G	shear modulus
E	Young's modulus
ν	Poisson's ratio
A	shear anisotropy factor
C_{ij}	elastic constants
Θ_D	Debye temperature
K	Boltzmann’s constant
MSD	Mean square diffusion
RDF	Radial distribution functions
BBGKY	Bogo Liubov–Born–Green–Kirkwood–Yvon
GA	Genetic algorithm
MCMC	Markov Chain Monte Carlo

Table of Contents

Declaration i

Abstract ii

Dedications v

Acknowledgements vi

List of Figures vii

List of Tables xi

List of Abbreviations xii

Table of Contents xiv

Chapter 1. Introduction 1

1.1. General Introduction 1

1.2. Multiscale and Multiphysics Modelling 7

1.3. Aim and Objectives 9

1.4. Significance of the Study 10

1.5. Problem Statement 10

1.6. Hypothesis 11

1.7. Motivation 11

Chapter 2. Literature Review 13

2.1. Cathode Materials for Sodium-ion Batteries 13

2.2. Layered Transition Metal Oxides 13

2.3. Polyanions 16

2.3.1. $NaMPO_4$ (M = Fe, Mn) Phosphate Materials 18

2.3.2. Olivine and Maricite 19

Chapter 3. Theoretical Methodologies 25

3.1. Density Functional Theory 25

3.1.1. Approximations 30

3.1.2. Plane-Wave Pseudopotential Method 33

3.1.3. Pseudopotential Method 36

3.1.4. Brillouin Zone 39

3.1.5. Theoretical Background for Calculated Properties 42

3.2. Classical Molecular Dynamics 46
3.2.1. Integration Algorithms 49
3.2.2. Energy Minimisation 50
3.2.3. Ensembles 50

3.3. Atomistic Interatomic Potential 53
3.3.1. Empirical Potential Model 53
3.3.2. Long Range Interactions 53
3.3.3. Short Range Interactions 55
3.3.4. Calculated Properties 56

3.3. Cluster Expansion 58
3.3.1. Universal Cluster Expansion 59
3.3.2. Effective Cluster Interactions 60
3.3.3. Inversion and Least Square Fitting 61
3.3.4. Truncating Structures and Clusters 62
3.3.5. Genetic Algorithm 63
3.3.6. Interactive Optimisation 65
3.3.7. Miscible Constituents 65
3.3.8. Miscibility Gap 66

3.4. Kinetic Monte Carlo 66
3.4.1. Sampling Through Markov Chains 69

3.5. Computer Codes 70
3.5.1. VASP 70
3.5.2. LAMMPS 70
3.5.3. MedeA UNCLE 71

Chapter 4. Radom De-Intercalation of Maricite and Olivine Polymorphs of $NaMnPO_4$ Using Density Functional Theory 74

4.1. Introduction 74

4.2. Computational Details 75

4.3. Maricite and Olivine $NaMnPO_4$ 76
4.3.1. Structural Properties 76
4.3.2. Electronic Properties 78

4.4. Sodium De-intercalated Maricite and Olivine $NaMnPO_4$ 82

4.4.1. Structural Properties 82
4.4.2. Formation Energy and Voltage 87
4.4.3. Electronic Properties 90
4.4.4. Mechanical Properties 94
4.5. Summary 102
Chapter 5. Atomistic Simulations of Na De-intercalated Olivine Na_xMnPO_4 105
5.1. Introduction 105
5.2. Development of Interatomic Potentials 106
5.2.5. Atomistic Potentials Model Validation 108
5.3. Computational Details 108
5.4. Sodium De-intercalated Olivine Na_xMnPO_4 109
5.4.1. Radial Distribution Functions 109
5.4.2. Diffusion of Na^+ in Na_xMnPO_4 116
5.5. Summary 120
Chapter 6. Structure Predictions Using Cluster Expansion 121
6.1. Introduction 121
6.2. Computational Details 122
6.3. Predicted Structures 124
6.4. Electronic Properties 126
6.4.1. Density of States for $MnPO_4$ and $NaMnPO_4$ Structures 126
6.4.2. Density of States for Intercalated Na_xMnPO_4 (x = 0.25, 0.5, 0.625, 0.75, and 0.825) Predicted Structures 129
6.5. Mechanical Properties 131
6.5.1. Elastic Properties 131
6.5.2. Thermodynamic Properties 132
6.6. Summary 135
Chapter 7. Molecular Dynamics Simulations of CE Predicted Structures 137
7.1. Introduction 137
7.2. Mean Square Displacements at 100 K 137
7.3. MD Mean Square Displacements at 300 K 140
7.4. Mean Square Displacements at 500 K 143

7.5. Na-ion Diffusion Coefficients 145
7.6. Summary 147
Chapter 8. Monte Carlo Simulations of Predicted Structures 148
8.1. Introduction 148
8.2. Computational Details 149
8.3. Phase Stability 150
8.4. Summary 152
Chapter 9. Conclusion and Future Prospects 153
9.1. Conclusions 153
9.2. Multiscale Modelling Framework 156
9.3. Future Prospects 159
Reference 160
Appendix A 174
Papers Presented at Local and International Conferences 174
Publications Papers 174

Chapter 1. Introduction

1.1. General Introduction

The global population is currently experiencing a significant development dilemma due to its continuous growth, with projections indicating that it will reach 9.6 billion by 2050 [1]. Along with the increasing population, the world's energy consumption is increasing rapidly from year to year. In 1998, energy consumption was reported to be 12.7 TW and is expected to be approximately 26.4 to 32.9 TW in 2050 [1]. Furthermore, it is predicted to increase to between 46.3 and 58.7 TW by 2100 [1]. The annual increase in global energy consumption resulting from population growth will generate a higher demand for finite resources such as coal, petroleum, and natural gas, ultimately leading to resource depletion. The global community is currently grappling with a significant energy crisis that is exerting a profound influence on the economic progress of nations around the world [1]. This predicament is particularly pronounced in South Africa, as seen by the ongoing occurrence of loadshedding. Therefore, it is crucial to prioritise the development of alternative and renewable energy sources that are both environmentally sustainable and cost-effective.

South Africa is classified as a developing nation, with its economy mainly reliant on energy-intensive industries such as manufacturing and mining. Although it has very low electricity costs, South Africa's energy utilisation has not demonstrated notable efficiency [2]. The country has only one electricity provider, a state entity called Eskom. And Eskom has admitted that electricity supply will be very limited for the next five years, and this is due to the drastic deterioration of power stations and the depletion of coal [2]. Most recently, Eskom announced that permanent loadshedding is expected for the next two years [2]. To address this limitation posed by Eskom, it is imperative to prioritise the utilisation of renewable energy sources and the implementation of reliable and ecologically sustainable energy storage technologies. Therefore, the development of novel materials for energy storage devices is imperative, characterised by enhanced qualities. In addition, it is imperative to include elements of material abundance, eco-efficient synthetic processes, and life-cycle analysis while developing novel energy storage systems. Currently, there are several technologies that aim to address these challenges. However, it is important to note that significant

obstacles of both a basic and a technological nature still need to be addressed in each case. The diagram in Figure 1 represents the interconnection between renewable energy generation and the movement of stocks. It also shows the historical advancement of battery technology spanning two centuries and the energy sources required for various electronic devices, including electric cars, which significantly impact our daily routines.

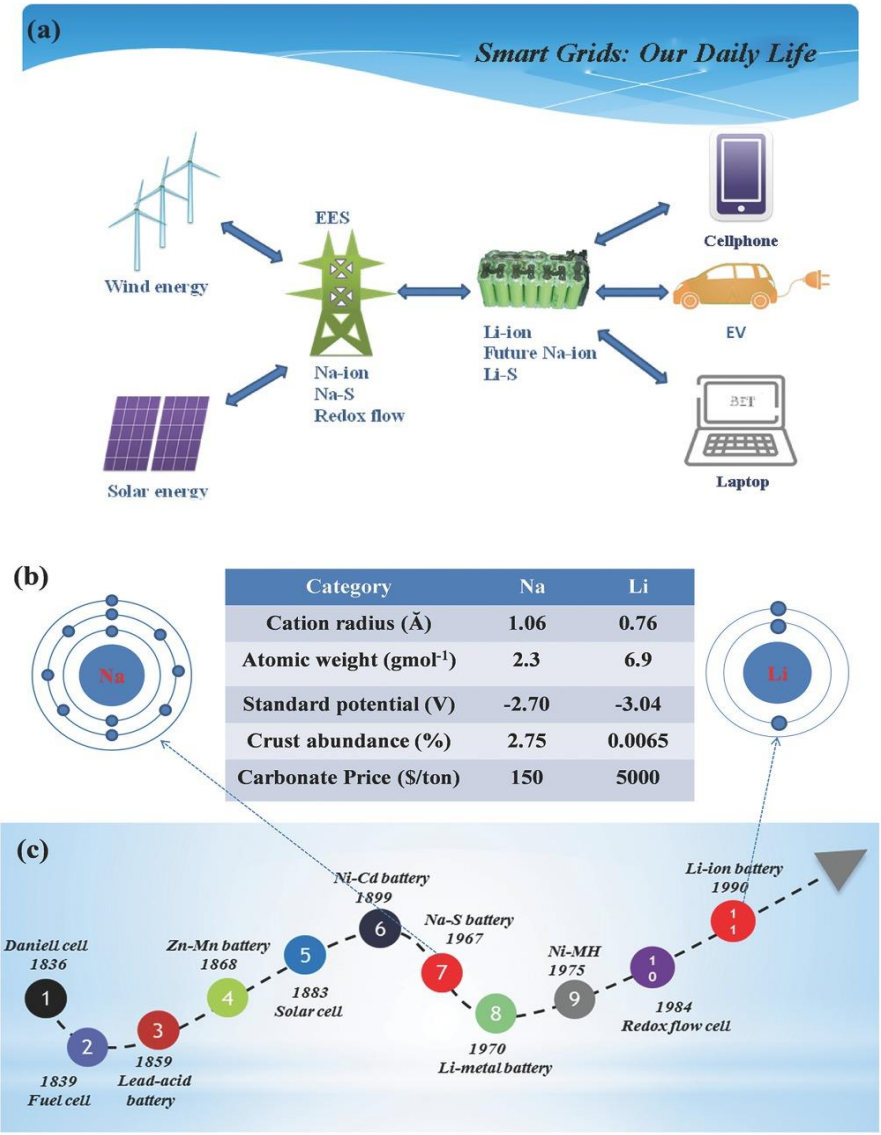

Figure 1: depicts (a) a simplified conceptual framework representing the interplay of renewable energy generation, the electrical grid, commercial secondary batteries, and hybrid/electric vehicle transportation, (b) shows a comparative analysis between sodium (Na) and lithium (Li), and (c) gives us a chronological account of the historical progression of battery development over the course of the last two centuries [3].

Currently, the dominant technology in the field of energy storage is the lithium-ion battery (LIB). This particular form of rechargeable battery operates by facilitating the movement of lithium ions from the negative electrode to the positive electrode during the discharge process and, conversely, during the charging process [4]. LIBs use an intercalated lithium compound as one of their electrode materials, compared to metallic lithium, which is used in a non-rechargeable lithium battery. The present configurations of LIB systems have undergone significant advancements in meeting the requirements of portable electronic devices, including laptops, cameras, mobile phones, smart watches, and similar devices. The utilisation of these LIB systems has positioned them as one of the most widely adopted technologies over the past two decades. However, the integration of this technology into extensive applications characterised by high power demands, such as electronic vehicles (EV), hybrid electronic vehicles (HEV), plug-in hybrid electric vehicles (PHEV), smart grids and aerospace applications, continues to present a significant difficulty, primarily due to their limited power density [5]. In addition, it is important to consider performance requirements such as energy/power density, cycling life, and safety concerns, particularly in high-power applications. These demands for electrical energy can potentially contribute to the depletion of lithium reserves.

The attraction of SIBs as a viable substitute for lithium-ion batteries stems from their characteristics and the potential exhaustion of lithium resources. The introduction of the commercialised LIB by Sony in 1991 has significantly contributed to the integration of portable electronics into daily routines. However, the growing demand for lithium metal has raised concerns about the availability of lithium due to its limited occurrence in the Earth's crust [6-8]. The availability of lithium resources is restricted to specific regions, namely North and South America, China, Australia, Portugal, and Zimbabwe. The escalating costs associated with mining and the dependence on foreign imports require the exploration of alternate battery chemistries. The growing interest in SIBs can be attributed to several factors. First, sodium exhibits a behaviour similar to that of lithium, making it a viable alternative for energy storage applications. Moreover, sodium is abundant in nature, which further enhances its attractiveness as a viable contender for battery technology. In addition, the relatively low cost of sodium contributes to the economic feasibility of SIB [7, 9, 10]. Additionally, using aluminium as a current collector is made possible by the use of Na-based anodes, preventing the

creation of a binary alloy with Na. This attribute leads to a more noticeable decrease in costs.

The battery components and the electrochemical storage method of SIBs and LIBs have a fundamental similarity, with the exception of their respective ion transporters. Regarding cathode materials, the intercalation chemistry of sodium exhibits notable similarities to that of lithium, allowing the utilisation of analogous compounds for both systems [8, 11-13]. The battery consists of two electrodes, namely an anode and a cathode, which are separated by a porous separator. The anode and cathode are in contact with a conductive electrolyte, creating a functional unit for energy storage. The voltage in the cell is generated by the potential difference that exists between the two electrodes. Figure 2 illustrates the fundamental structure and operational principle of an LIB and SIB. In the process of charging and discharging, the migration of sodium ions between the cathode and anode is facilitated by a specific redox reaction that transpires between the constituent materials [13].

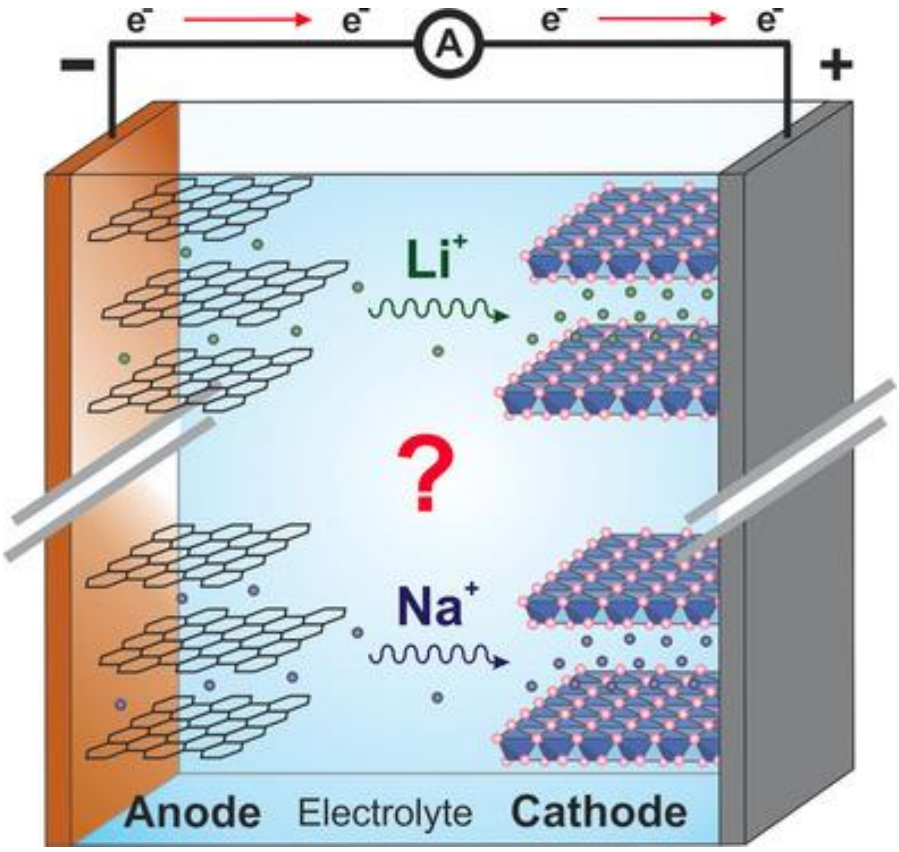

Figure 2: working principle of both the LIB AND SIB cells [13].

Despite sharing a similar working concept, there is an existing discernible distinction between SIB and LIB systems. As seen in Figure 1(b), it can be observed that Na^+ ions, characterised by an ionic radius of 1.02 Å, exhibit a larger size ionic radii compared to Li^+ ions, which possess an ionic radius of 0.76 Å. This disparity in size between the two ions has significant implications for various aspects, such as phase stability, transport properties, and the development of interphases [14]. Sodium exhibits a higher atomic mass than Li, with values of 23 g mol^1 and 6.9 g mol^1, respectively. Furthermore, Na possesses a higher standard electrode potential in comparison. Therefore, SIBs will exhibit consistent limitations in relation to energy density. Nevertheless, the mass of cyclable Li or Na is only a minor portion of the overall weight of the components. The capacity, on the other hand, is predominantly influenced by the properties of the host structures that function as electrodes. Therefore, in theory, the move from LIBs to SIBs should not result in any changes in energy density [13]. Moreover, it is noteworthy that aluminium exhibits an alloying reaction with lithium at potentials below 0.1 V versus the Li / Li^+ reference electrode. This observation suggests that aluminium can be effectively employed as a current collector for anodes in sodium-based cells. Henceforth, aluminium emerges as a financially viable substitute for copper in the capacity of an anode current collector for SIBs.

Concerted efforts on a global scale have yielded diverse configurations of cathode materials for SIBs, including layered transition metal oxide (LTMO), polyanionic compounds and Prussian blue analogous (PBA). These materials exhibit inherent inefficiencies, including suboptimal conductivity, sluggish kinetics, and significant volume fluctuations during intercalation-de-intercalation cycling. These factors predominantly impede the present commercialisation of SIBs. Consequently, numerous mitigation strategies, including structural modulation, surface modification, and elemental doping, have been employed to address these challenges; nevertheless, the search for the optimal cathode material persists.

Rechargeable batteries have evolved primarily through trial-and-error experimental methods since their inception. Volta created the first non-rechargeable battery to store electricity in 1800, long before Thomson discovered the electron in 1896 [15]. Due to the inherent novelty and immense potential for advancement in modern rechargeable

batteries, typically referred to as batteries, their rapid market penetration has occurred without necessitating an exhaustive understanding of their underlying operational principles. In stark comparison, in the present era, wherein substantial reductions in cost and enhancements in performance are imperative, the circumstances are swiftly undergoing transformation, necessitating the formulation of physical theories to provide guidance and rationalisation for design choices, which is undeniably indispensable.

A theory can be defined as a hypothesis or a collection of ideas with the purpose of explaining something, in particular, on the basis of general principles that are independent of the phenomenon described [16, 17]. The fundamental objective of physical theories is to provide a comprehensive framework that illustrates the observed outcomes of experimental investigations. In the field of batteries, the prevailing discourse revolves around the exposition of theoretical frameworks, often expressed through mathematical models consisting of interconnected mathematical equations. To attain a deeper comprehension of prevailing configurations and to anticipate the characteristics and efficacy of novel configurations, it is prudent to employ mathematical models, hereafter referred to as models, as they are the most apt selection for this purpose. The advantage lies in the inherent economy of modelling as opposed to protracted experimental inquiries, thereby enabling modelling to propel innovation and engender technological advancements, ultimately curtailing the temporal span required for the introduction of novel designs into the market. In the domain of battery research, mathematical models serve as invaluable tools for the exploration and utilisation of novel materials and their intricate combinations.

The predominant focus in the field of battery materials development has been on employing conventional modelling techniques, primarily centred around a single scale. In the context of examining the macro-scale dynamics of a system within an engineering framework, the influence of the underlying micro-scale phenomena are accounted for through the utilisation of constitutive relationships. If one’s focus lies on the intricate microscopic mechanism of a process, it is postulated that there exists a lack of noteworthy occurrences at the macroscopic scales. This implies that the process in question exhibits homogeneity when observed on larger scales.

In comparison with SIBs as a case in point, within the context of the electrochemical discharge reaction mechanism, the Na ion, acting as an intercalating entity, undergoes migration from the negative electrode to the positive electrode. This migration induces a reduction in the oxidation state of the transitional metal ion present in the positive electrode, thereby facilitating the generation of a valuable electric current. In this context, it is observed that the properties of most materials undergo alterations in response to variations in the concentrations of Na intercalating species, which occur at different states of charge. The inherent complexity associated with comprehending and manipulating these dynamic charges poses a formidable challenge in the pursuit of optimising the electrochemical performance of a cell through conventional modelling techniques. Thus, it is imperative to adopt a more expansive modelling framework that incorporates mathematical representations of phenomena occurring on various spatial scales [17]. This modelling strategy, known as multiscale modelling, will be used in this study to simulate the characteristics of SIB materials and their functionality at various length and timescales.

1.2. Multiscale and Multiphysics Modelling

The concept of multiscale simulation refers to model systems that can be separated into various simulation models linked through a handshake bridge, based on their unique scales, which are often spatial or temporal. Multiscale simulations are becoming more commonly used to represent systems in which the effects of small-scale, tightly connected events are more loosely connected to the larger-scale evolution of the system through building. Multiscale modelling (MSM) methods strive to significantly minimise the reliance on empirical assumptions compared to standard modelling methods. This is due to their explicit depiction of mechanisms at scales that are overlooked in conventional modelling approaches.

Multiscale models exhibit a hierarchical arrangement, in which the solution variables within a lower hierarchy domain possess a more refined spatial resolution compared to those resolved within a higher hierarchy domain. Therefore, the physical and chemical quantities pertaining to the realm of physics at smaller length scales are assessed using a more refined spatial resolution in order to discern the influence of the corresponding geometric features at the microscopic level. The computation of

larger-scale quantities is accomplished by employing a less refined spatial resolution, thereby amalgamating the intricate geometric attributes of smaller scales.

Figure 3 shows a schematic illustration of various materials modelling techniques employed in the formulation of scaling rules based on spatial and temporal variables. At the subatomic scale, the field of quantum mechanics, called ‘ab initio’, employs computational methods to construct potential energy functions, with the aim of improving the efficacy of microscopic models. As the length or time scale increases, the characterisation of material behaviour transitions from molecular dynamics (MD) and kinetic Monte Carlo (kMC) simulations to micro- or mesoscopic models, and ultimately to continuum mechanics approaches, such as the finite element method (FEM).

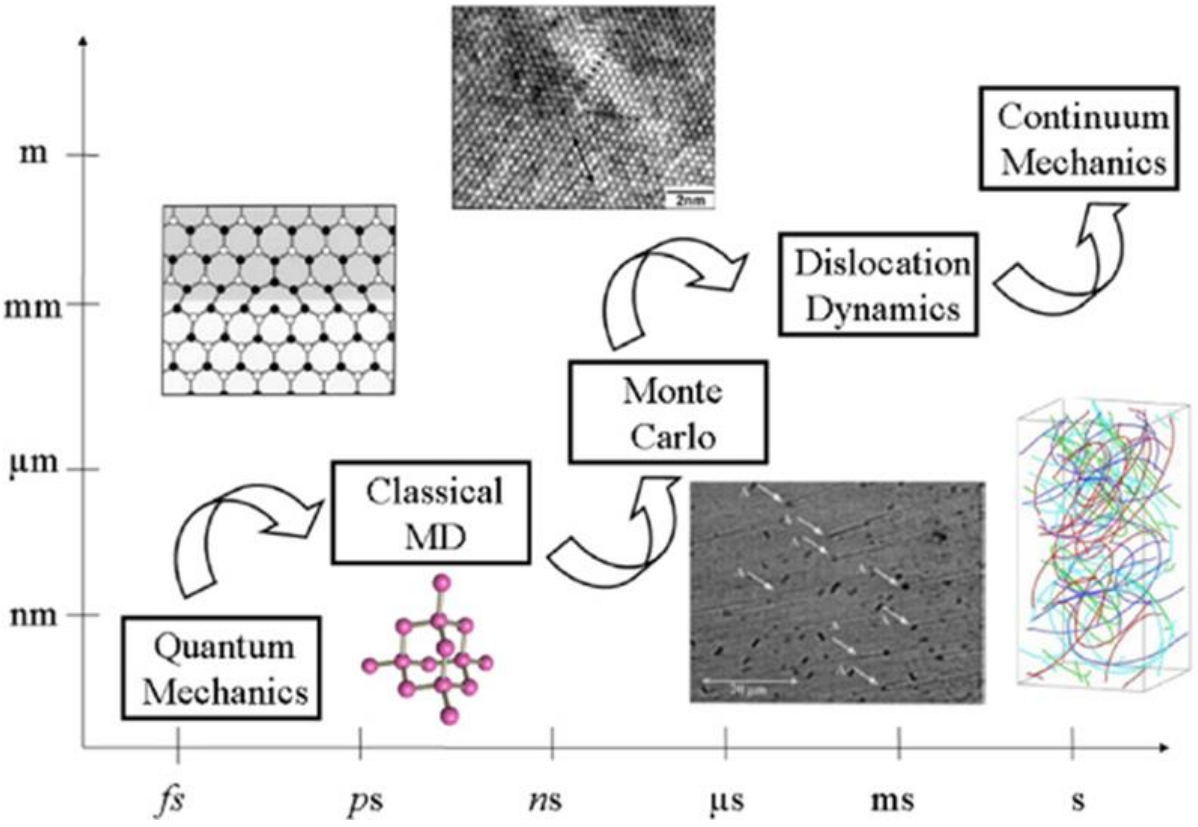

Figure 3: Schematic representation of simulations at various levels [9].

In this study, multiscale computational modelling investigations will be carried out to understand, control and improve the intrinsic properties of the well-known high energy density Na intercalated electrode material Na_xMnPO_4 (x = 1,2, 3...). In particular, the battery performance properties of Na_xMnPO_4 will be carried out on various length and time scales, with the goal of bridging the gaps between the various scales at the lower level.

1.3. Aim and Objectives

The aim of this study work is to formulate a resilient and dependable methodology for modelling materials at various scales, ranging from the nanoscale to the macroscale. This approach will be employed to enhance the design and optimize the performance of SIBs. The performance properties of Na_xMnPO_4 encompass alterations in its structure, the mobility of ions, and the molecular shape of materials during potential phase transitions. The specific objectives will be to:

- Develop electronic structure models to investigate the de-intercalation of Na ion, through the calculation of structural, electronic and mechanical properties, using three different functionals implemented in the first-principle method.
- Interatomic potentials/forcefields models that are suitable for describing the structural and thermodynamic characteristics of Na_xMnPO_4 will be fitted and tested.
- Carry out MD simulations, in combination with interatomic potentials generated from empirical data, calculate the radial distribution functions (RDF) and diffusion coefficient for Na_xMnPO_4 de-intercalated systems at various temperatures.
- Predict new stable phases of $NaMnPO_4$ using the combination of density functional theory (DFT) and CE methods.
- Investigate the new predicted stable structures, through the calculation of structural, electronic and mechanical properties, using first-principle method.
- Use MD simulations, in combination with interatomic potentials generated from empirical data, calculate the RDF and diffusion coefficient for the new predicted stable structures at various temperatures.
- Use CE as a bridging length scales method in combining first-principle method with Monte Carlo to investigate the phase stability of materials at various temperatures.

1.4. Significance of the Study

The key to promoting innovation in terms of materials, components and/or SIB operation procedures is the creation of adequate knowledge about the link between multiscale modelling methodologies. Understanding the intercalating species mobility within SIB systems is also essential for performance optimisation because, by moving from the negative electrode to the positive electrode, it makes it easier to charge and discharge the SIB system. For the creation of high capacity and high charging rates, it is crucial to have knowledge about the investigations into understanding, controlling, and improving the intrinsic features of known and unknown high-energy-density Na intercalation electrode materials. This study employs multiscale methods to provide insights into SIB materials properties, as well as to predict new structures using cluster expansion method.

1.5. Problem Statement

Although SIBs exhibit promising potential as a viable alternative to LIBs, it is important to note that they generally demonstrate inferior electrochemical activity in comparison to their LIB counterparts. This phenomenon can be elucidated by the presence of two intrinsic limitations associated with sodium as an electrode material,

(i) Na exhibits a comparatively reduced ionisation potential in relation to Li, resulting in diminished operational voltages and subsequently decreased energy densities when compared to LIBs.
(ii) Na^+ exhibits greater mass and size in comparison to Li^+, resulting in reduced diffusion rates within a solid electrode-electrolyte interface during the cycling of SIBs. This phenomenon is often accompanied by a more pronounced expansion of the electrode's volume and lower energy densities when compared to LIBs.

The presence of these inherent shortcomings requires the utilisation of distinct crystalline materials that possess an open framework structure or three-dimensional arrangements, featuring expansive insertion channels to effectively facilitate the intercalation and de-intercalation of the comparatively larger Na. In conjunction with these shortcomings, the advancement of rechargeable batteries is predominantly propelled by empirical methodologies reliant on trial-and-error experimentation.

Mathematical models have demonstrated their efficacy in attaining a heightened level of fundamental comprehension pertaining to extant substances, as well as in prognosticating the attributes and efficacy of said substances. The majority of materials modelling endeavours pertaining to the advancement of battery materials primarily rely on conventional methodologies of modelling, which centre around the execution of simulations at a singular scale. The study aimed to develop an integrated multiscale modelling approach while improving the performance properties of SIB.

1.6. Hypothesis

Applying multiscale modelling methods to investigate Na_xMnPO_4 will give more understanding, control, and improvement on the intrinsic properties of high-energy density Na intercalated electrode material, by reducing empirical assumptions that are done in traditional methods of modelling.

1.7. Motivation

The acceleration of global energy consumption has been attributed to rapid industrial development, a growing population, and increased energy demand. Given the current pace of consumption, it is unavoidable that global energy depletion will occur. The worldwide community has shown significant interest in the use of renewable energy sources as a means to mitigate the potential consequences of energy depletion and to prevent potential disasters. To optimise the use of renewable energy, it is imperative to advance energy storage and conversion systems that exhibit superior performance, affordability, and environmental sustainability. The widespread implementation of renewable energy sources requires the use of advanced technologies derived from groundbreaking scientific discoveries in the fields of materials science, physics, chemistry, and engineering.

Rechargeable lithium batteries have gained widespread global recognition and are extensively utilized in numerous portable electronic devices. Despite extensive efforts, it has been shown that increasing the size or capacity of initial generation batteries for the purpose of storing renewable energy or facilitating transportation has proven to be a challenging task. The primary issue pertains to the positive electrodes that incorporate Li, which are characterised by high costs, toxicity, and safety concerns, particularly in the context of larger battery systems. To tackle the challenges

associated with energy storage, we investigated the inherent characteristics of SIB material that encompass structural alterations, ion mobility, and morphology, while considering potential phase transitions at higher temperatures.

Chapter 2. Literature Review

2.1. Cathode Materials for Sodium-ion Batteries

The operating voltage of SIBs is controlled by the electrochemical potential differences between the cathode and anode materials. The cathode material exerts a substantial influence on the energy density and cycle life of SIBs. Polyanionic compounds, TMOs, and PBAs are currently cathode materials being actively researched for SIBs. Ideal cathode materials should exhibit electrochemical characteristics such as high specific energy, adequate ion diffusivity, and excellent structural stability at low temperatures. In addition, there is significant interest in developing cathode materials that can operate at high rates without degradation. This will be crucial for the widespread adoption of SIBs in various applications such as electric vehicles and grid-scale energy storage. In this chapter, we present a brief literature on layered oxides and phosphates cathode materials for SIBs relevant to this study.

2.2. Layered Transition Metal Oxides

The transition metal oxide with the generic chemical formula Na-based layered Na_xMO_2 (M = transition metal) has a characteristic structure made up of layers of MO_6 and NaO_6 octahedra that are alternately stacked and share edges. According to the Delmas notation [18], these layered materials can be classified as O3 and P2, depending on the octahedral and prismatic coordination environments of the Na^+ ion, respectively. The notation provides a useful way to categorise the layered transition-metal oxide on the basis of the octahedral and prismatic coordination environments of the Na^+ ion. Here, the numbers “2” or “3” indicate how many layers of a particular type of transition metal there are. Figure 4 shows a schematic illustration of such layered crystals.

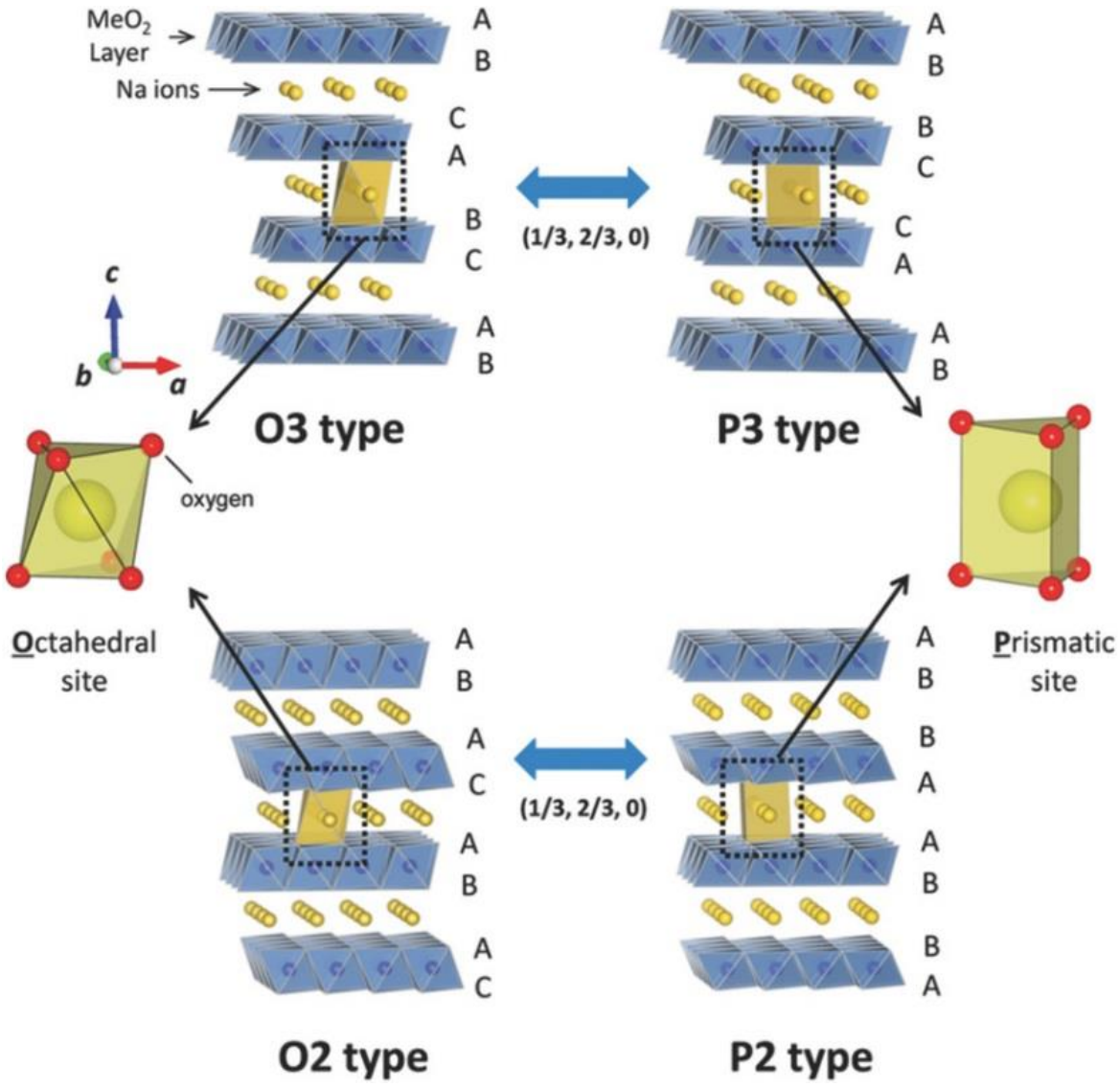

Figure 4: Classification of Na–M–O layered materials with sheets of edge-sharing MO_6 octahedra and phase transition processes induced by sodium extraction [19].

Compared to other layered compounds, P2-type oxides are more desired due to their high capacity and low hygroscopicity. Another advantage of P2-type compounds is their higher ionic conductivity [20]. The typical P2-type $Na_{2/3}MnO_2$ compound has a high initial capacity and low material cost, but the Jahn-Teller distortion caused by the presence of Mn^{3+} in the structure must be addressed to ensure long-term cycling stability.

To address the drawback on the movement of the Mn^{3+}-O_6 in octahedra, the introduction of electro-inactive elements (Mg [21] and Zn [22]) and electroactive elements (Fe [23], Co [24], Ni [25], and Cu [26]) has been considered as a potential

solution to mitigate Jahn-Teller distortion. This helps to lessen the anisotropic movement of Mn^{3+} along the z-axis in Mn^{3+}-O_6 in P2-$Na_{2/3}[Mn_{1-x}M_x]O_2$ by reducing the concentration of Jahn-Teller Mn^{3+} ions in the structure. The aforementioned substitutions also suppress the continuous phase transition seen in P2- $Na_{2/3}[Mn_{1-x}M_x]O_2$, illustrated by the smoother charge and discharge curves in all cases compared to P2-$Na_{2/3}MnO_2$.

Ma *et al.* [14] reported the electrochemical characteristics of P2 monoclinic $NaMnO_2$, which was created through a solid-state process. The findings showed that during potential-statical intermittent charge and discharge, respectively, approximately 0.85 Na can be de-intercalated from $NaMnO_2$, and 0.8 Na can be intercalated again. Galvanostatical cycling between 2.0 V and 3.8 V resulted in a discharge capacity of 185 mAh/g in the first cycle at a C/10 rate and a residual capacity of 132 mAh/g after 20 cycles [14].

The features of a layered $NaMn_xO_x$ material (specifically $NaMn_3O_5$) have been reported by Guo *et al.* [15] as a promising cathode material for SIBs. Their structural analysis indicated the presence of a conventional birnessite structure, characterised by the arrangement of synthetic nanosheets in a layered stacking pattern. Electrochemical experiments demonstrated a significantly high discharge capacity of 219 $mAhg^{-1}$ within the voltage range of 1.5–4.7 V compared to the reference electrode Na/Na^+. The average recorded potential was 2.75 V compared to sodium metal-layered $NaMn_3O_5$. This material exhibited a substantial energy density of 602 Whkg-1, as well as favourable rate capability [15].

In O3-type structures, the sites that undergo initial stabilisation for sodium ions are characterised by edge-shared octahedral configurations. When Na^+ are extracted, in part, from the O3 phase, the prismatic positions experience a stabilisation in their energy levels. This can be accomplished by translating the MO_2 layers while maintaining the integrity of the chemical bonds of the structures. By modifying the oxygen arrangement within the structural framework, it is possible to generate P3-type materials. In Na cells, the transition from the P3/O3-type phase to the P2-type phase is not feasible under existing conditions. This transition can be accomplished solely through the process of reforming and breaking of M-O bonds in an environment characterised by high temperatures. In the sodium intercalation process, it is observed

that the O3 phase undergoes a consistent transformation into the P3 phase. In the realm of materials, it is generally observed that O3-type materials exhibit a higher abundance of Na compared to P2-type materials. Optimal battery capacity performances are correlated with O3-based systems exhibiting elevated sodium stoichiometry [27].

Zhang *et al.* [28] used first-principle calculations to successfully evaluate the electrochemical performance of monoclinic O3 $NaMnO_2$ for SIBs. These calculations were carried out under typical circumstances with a temperature of 0 K. The findings revealed that $NaMnO_2$ has a voltage window of 3.54 to 2.52 V and a predicted reversible capacity of 136 $mAhg^{-1}$. Furthermore, the study discovered that during Na extraction, the metallicity of monoclinic $NaMnO_2$ gradually increases and that the Na migration energy barrier is 0.18 eV, ensuring optimum conductivity and reversible capacity. The monoclinic $NaMnO_2$ reversible capacity cannot be increased due to the Jahn-Teller distortion effects, but it is still a good cathode material for SIB [28]. Their computational results agree excellently with the experimental findings [29].

The composition and structural variety of the layered transition metal oxides made them potential candidates for SIB cathode materials. Large-scale applications were hampered by their complicated phase transitions during cycling. When the synergistic impact of materials with hybrid P and O phases is utilised, it is thought that layered TMOs with high capacity and extended cycle life at low temperatures may be created. [30].

2.3. Polyanions

Polyanion-type electrodes fall into the category of materials that falls under the classification of compounds. These compounds consist of a sequence of anion units in the form of tetrahedra, denoted $(XO_4)^{n}$- or their derivatives $(X_mO_{3m+1})^{n-}$, where X represents elements such as S, P, Si, As, Mo, or W. These anion units are characterised by the presence of strong covalent bonds within MO_x polyhedra, where M denotes a transition metal [30]. The stabilisation of active redox potentials of transition metals and the facilitation of fast-ion conduction in an open framework are commonly observed in most compounds of the polyanion type. This is achieved through incorporation of $(XO_4)^{n-}$, which is selected as the working alkali ion during discharge. The addition or removal of alkali-metal atoms can be facilitated more

effectively through the use of a specific framework composed of 2D van der Waals bonding or 3D frameworks [31]. The presence of strong X-O bonding in compounds of polyanion type can induce ionic characteristics in the M-O bonding. This weaker ionic bonding in M-O leads to an increased separation between the antibonding orbitals compared to that of the Na/Na^+ redox pair, hence yielding a higher redox potential. The phenomenon described as the "inductive effect" is commonly observed in polyanion electrode materials [31]. Additionally, the presence of robust X-O covalent bonds significantly enhances the stability of oxygen inside the lattice structure. This increased stability contributes to the improved safety of these materials, making them very suitable for use in secondary rechargeable batteries.

Various forms of polyanion electrode materials can be identified, for example, phosphates, pyrophosphates, and fluorine transition metal salts (e.g., $NaM(XO_4)F$, where M represents Fe, Co, V, or Mn, and X represents P or S). Additionally, transition metal sulphates (e.g., $Na_xM_y(SO_4)_z$, where M represents Fe, Mn, Co, or Ni) and transition metal silicates (e.g., Na_2MSiO_4, where M represents Fe, Mn, or Co) are also included in this category. In relation to this research, the discourse is centred on sodium phosphates substances, drawing inspiration from the study conducted by Padhi *et al.* [31]. In their investigation, they examined the reversible extraction of lithium from $LiFePO_4$ (triphylite) and the subsequent insertion of lithium into $FePO_4$ at a voltage of 3.5 V compared to lithium at a current density of 0.05 mA/cm^2. The results of the study indicate that triphylite exhibits potential as a viable option for the cathode material in a low-power, rechargeable lithium battery. This material possesses desirable attributes such as cost-effectiveness, nontoxicity, and environmental friendliness. Electrochemical extraction was constrained to a maximum of 0.6 Li/formula unit. Despite this limitation, the specific capacity achieved ranged from 100 to 110 mAh/g. A comprehensive chemical extraction process was performed to obtain lithium, resulting in the formation of a novel phase of $FePO_4$. This phase was found to be isostructural to the heterosite, specifically $Fe_{0.65}Mn_{0.35}PO_4$ [31].

Phosphate framework materials have garnered significant interest in recent years due to their exceptional electrochemical properties and adaptable structure [32]. Consequently, they are considered highly promising sodium storage electrodes based on the following factors:

(i) Phosphate frameworks exhibit notable structural stability due to the presence of stable P-O frameworks, thereby ensuring the prolonged cycling and safety of SIBs. The thermal properties of phosphate materials are directly correlated with the stability of the phosphate-metal bonds, which significantly diminishes the probability of oxygen liberation from the structure.

(ii) The three-dimensional framework exhibits numerous spacious interstices, resulting in reduced volumetric expansion and minimized phase transition during the insertion and extraction of sodium ions. This characteristic contributes to the enhancement of structural stability.

(iii) Phosphate or other substituent groups demonstrate an inductive influence on the redox pair, resulting in elevated redox potential values compared to Na/Na^{+}. Nevertheless, the substantial dimensions and inherent isolating characteristics of the PO_4^{3-} groups result in a limited capacity and diminished electron conductivity. In this particular context, the implementation of intricate architectures comprising a matrix with exceptional conductivity is a viable strategy for enhancing the overall performance of phosphate materials.

Phosphate framework materials come in a wide range, with their structure and electrochemical performance being adaptable and customisable. Most electrochemical reactions are attributed to phase-transition processes, while a few are associated with solid solution, surface, or interface charging mechanisms [32]. In this section, we discuss previous studies on sodium-based single-phosphate materials, focusing only on maricite and olivine polymorphs of phosphate materials.

2.3.1. $NaMPO_4$ (M = Fe, Mn) Phosphate Materials

Possible SIB cathode materials include the phosphate family with the chemical formula $NaMPO_4$ (M = transition metal). Among them, $NaFePO_4$ was one of the first phosphate compounds investigated [33]. Maricite and olivine are the two different phases of $NaFePO_4$. They both crystallise into the orthorhombic Pnma space group; however, their unit cell characteristics are different. Both of these polymorphs have their structures made from FeO_6 octahedra and PO_4 tetrahedra. In the maricite phase, the surrounding FeO_6 units are joined with PO_4 to share the corners, and then the edges are shared with one another. There are no cationic channels that allow sodium ions to flow (see Figure 5(a)). In contrast, the corner-shared FeO_6 units in the olivine phase

are coupled with PO_4 molecules. On the b-axis, there is unmistakable evidence of a one-dimensional Na^+ diffusion channel within the crystal framework, as shown in Figure 5(b). The maricite phase has traditionally been regarded as an electrochemically inactive electrode for SIBs because it does not include any potential Na^+ ion diffusion channels. However, it does not violate the laws of thermodynamics because it can be manufactured at high temperatures [33].

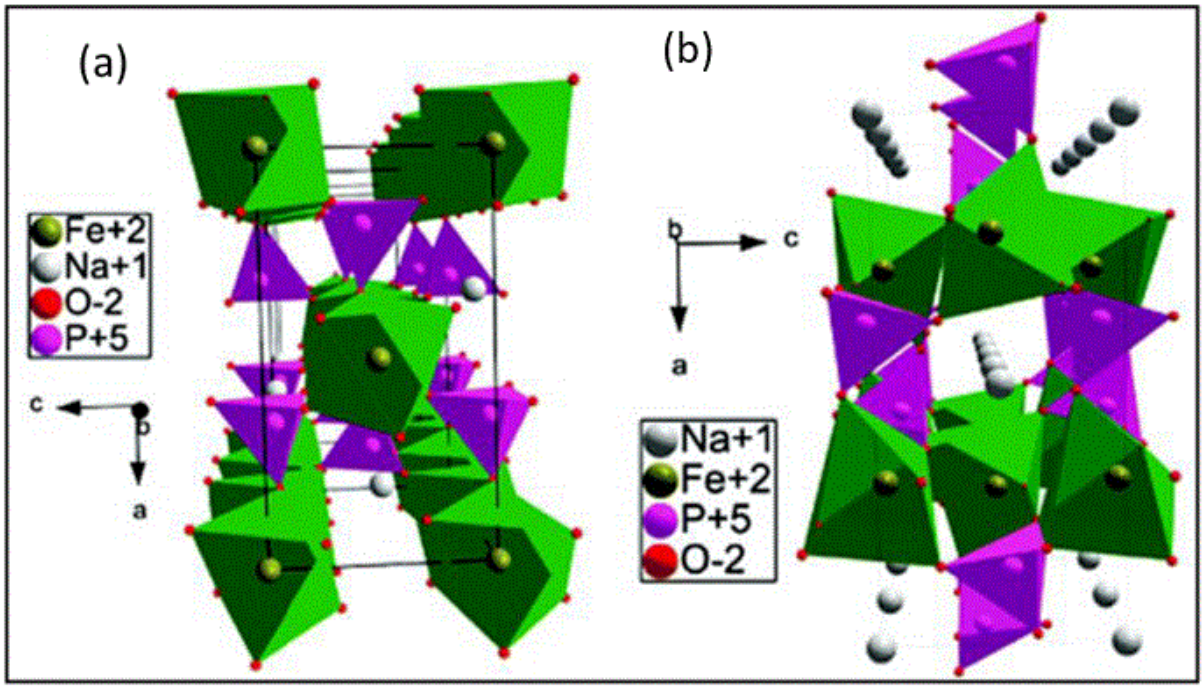

Figure 5: Crystal structure of (a) maricite $NaFePO_4$ and (b) olivine $NaFePO_4$ [33].

2.3.2. Olivine and Maricite

2.3.2.1. Structure and Energetics

Although the olivine structure is considered more energetically favourable than the maricite structure in the case of $LiFePO_4$, certain computational studies suggest that both structures possess comparable energies in $NaMPO_4$. For example, Oh *et al.* [34] reported on the convection of an electrochemical process in $LiFePO_4$ to $NaFePO_4$ and showed that the material can serve as a cathode in a sodium ion battery, exhibiting exceptional performance in relation to cycle life and rate capacity. The electrochemical process of converting olivine $LiFePO_4$ to $FePO_4$ was carried out under controlled conditions to ensure complete de-lithiation of $LiFePO_4$ and its complete replacement with $FePO_4$ for sodium intercalation [34].

The considerable disparity in power density between the $LiFePO_4$ and $NaFePO_4$, olivine polymorphs, together with their ion and electron transport properties, was investigated by Nakayama *et al.* [35] using first-principles density functional theory. There was a lack of significant disparity observed in the electronic migration energies between the bulk forms of $LiFePO_4$ and $NaFePO_4$. On the contrary, the migration energy of the sodium ion in $NaFePO_4$ is 0.05 eV greater than that of the lithium ion in $LiFePO_4$. This disparity in migration energy could perhaps explain the sluggish kinetics observed on the $NaFePO_4$ electrode. Additional research has been conducted to explore the phase stability and migration of alkaline ions in $(Li/Na)FePO_4$ and $FePO_4$.

The Na insertion / de-insertion behaviour of olivine $NaFePO_4$ has been investigated by Casas-Cabanas *et al.* [35]. The intermediate $Na_{2/3}FePO_4$ phase was observed to occur during both the charging and the discharging processes. The intermediate phase was subsequently characterised by means of Na/ vacancies ordering. The process of Na insertion and de-insertion is governed by distinct mechanisms, which can be attributed to the significant volumetric disparity between $FePO_4$ and $NaFePO_4$. This difference in unit volume amounts to 17.58%.

Saracibar *et al.* [36] reported the discovery of a $Na_{5/6}FePO_4$ intermediate phase $Na_{5/6}FePO_4$ using DFT calculations and high-resolution synchrotron X-ray diffraction (HRXRD). The use of DFT calculations led to the identification of two intermediate structures that regulate phase stability at x = 2/3 and x = 5/6, as shown in Figure 6. Unit cells are displayed as black rectangles. The plane (110) is indicated by the dashed red line in (b). Fe^{2+} ions blue, Fe^{3+} ions are purple, while sodium atoms yellow. The $[PO4]^{3-}$ groups are depicted by a light grey polyhedral. For the sake of clarity, the O atoms at the corners of each polyhedron are not displayed.

Compared to the widely used $LiFePO_4$ isostructural cathode in LIBs, the aforementioned $NaFePO_4$ exhibited a contrasting behaviour. The ground states of $Na_{2/3}FePO_4$ and $Na_{5/6}FePO_4$ exhibited a diagonal alignment of vacancies within the *ab* plane (110), which is coupled to an alignment of Fe^{2+}/Fe^{3+}. HRXRD data obtained for Na_xFePO_4 materials with $2/3 < x < 1$ indicated the presence of shared superstructure reflections up to x = 5/6 among the compositions examined. The voltage profile obtained by computation indicated a voltage disparity of 0.16 V between

$NaFePO_4$ and $Na_{2/3}FePO_4$, which is consistent with the observed voltage discontinuity during electrochemical insertion according to experimental findings [36].

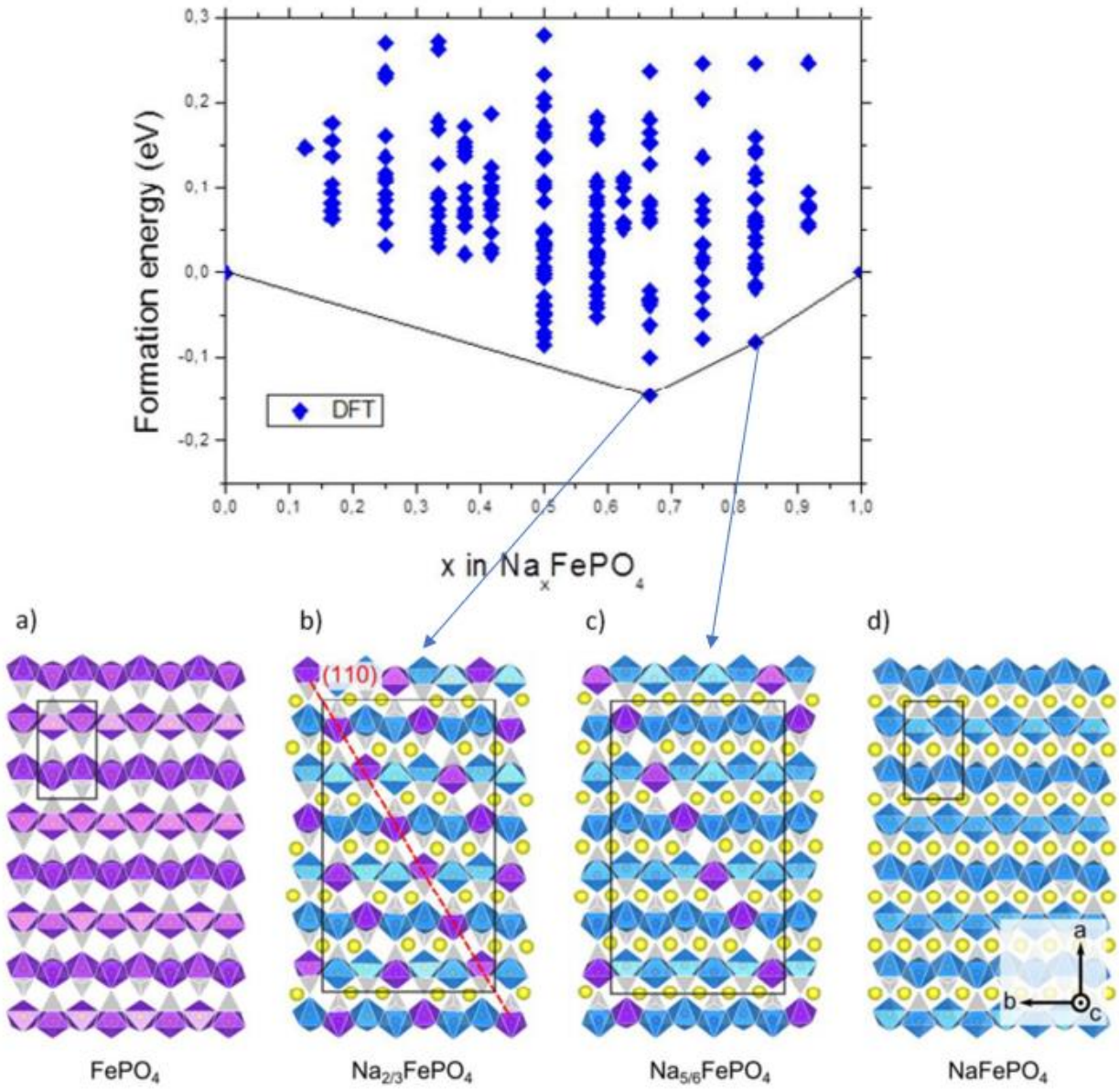

Figure 6: Calculated formation energies per formula unit for the most stable Na_xFePO_4 structures, including (a) $FePO_4$, (b) $Na_{2/3}FePO_4$, (c) $Na_{5/6}FePO_4$, and (d) $NaFePO_4$, as a function of the Na content [36].

Prior research on cathodes composed of $NaMPO_4$ (where M represents a transition-metal) phosphates has predominantly focused on $NaFePO_4$, with limited attention given to other variants such as $NaMnPO_4$. Koleva *et al.* [37] investigated the synthesis of olivine and maricite $NaMnPO_4$ without defects using precursors by thermal

decomposition of a freeze-dried phosphate formate precursor. The resulting product was $NaMPO_4$ with maricite structure, which was obtained at a temperature of 400 °C [37].

Reversible intercalation of Na and Li in carbon-coated olivine-$NaMnPO_4$ was initially documented by Boyadzhieva *et al*. [38]. The study investigated the process of reversible intercalation / de-intercalation cycling by employing ex situ X-ray powder diffraction, transmission electron microscopy (TEM), high-angle annular dark field scanning transmission electron microscopy (STEM) analysis, infrared spectroscopy, and electron paramagnetic resonance spectroscopy (EPR). The initial and subsequent discharge capacities of Li and Na at a rate of C/50 were approximately 125 mAh/g and 85 mAh/g, respectively. Figure 7 shows the stability of the capacity during cycling.

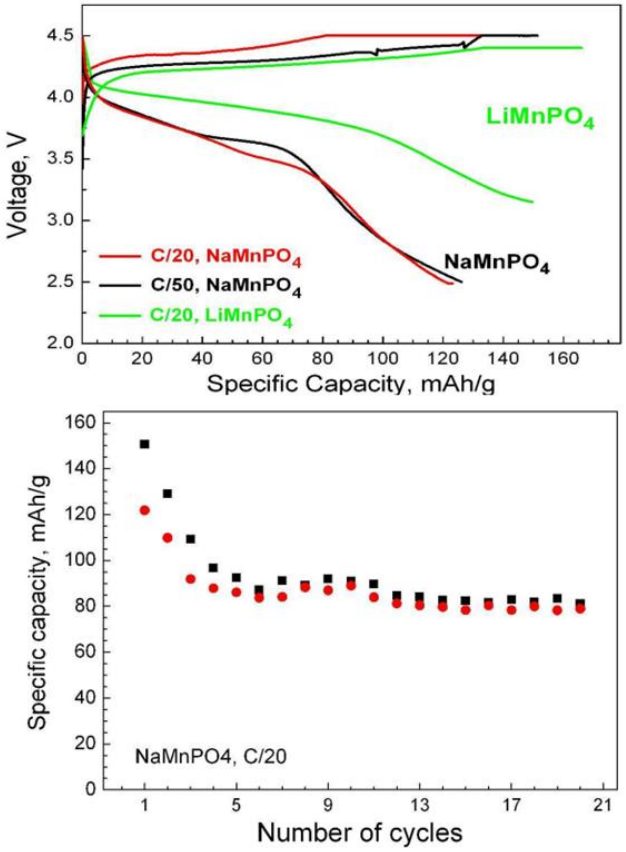

Figure 7: The first charging/discharging curves for $NaMnPO_4$ and $LiMnPO_4$ electrodes, showing charge and discharge capacity of $NaMnPO_4$ (black and red symbols) vs the number of cycles [38].

Venkatachalam *et al.* [39] conducted a study on maricite $NaMnPO_4$, focusing on the impact of the length on the polyol process to enhance its electrochemical activity. The findings demonstrated that the elongation of the diol chain through the use of ethylene glycol, diethylene glycol and poly(ethylene glycol) (400 and 6000) facilitates the production of a homogenous substance via a solitary process. The molecular structural dynamics of maricite $NaMnPO_4$ was investigated, which revealed intramolecular charge transfer and validated the electrostatic activity of the system. Additionally, the substance has been utilised as a cathode material in sodium ion batteries. The findings indicate an initial discharge capacity of 102 mAh/g, and the performance was monitored for 182 cycles at a rate of 0.1C [39].

2.3.2.2. Transport Properties

Comprehending the fact that diffusion of Na^+ in Na_xMPO_4 holds fundamental significance in the context of its potential application as a cathode substance in Na-ion batteries, transport properties are briefly discussed in this subsection. Although DFT investigations have yielded significant findings on various properties of $NaMPO_4$ materials, their scope is restricted to brief time frames along predetermined migration routes. To investigate extended temporal ranges unencumbered by migration path limitations, less complex classical interatomic potentials are required.

In their study, Chowdary *et al.* [40] investigated the diffusion process of sodium ions in an olivine $NaMnPO_4$crystal structure. The study used first-principle GGA+U calculations to analyse this phenomenon and obtained a final energy per atom of -7.03 eV [40]. The diffusion energy for Na was found to be 0.65 eV and determined to undergo diffusion along the crystallographic direction [010]. The Mn crystal structure has significant interlayer and intralayer distances, measuring 3.156 Å and 6.312 Å, respectively. These distances provide viable pathways for efficient diffusion of sodium ions along the [010] direction.

Bonilla *et al.* [41] used the generalised shadow hybrid Monte Carlo method of randomised shell mass of randomised shell mass (RSM-GSHMC) in conjunction with a force field developed specifically to describe Na_xFePO_4 over the entire range of sodium compositions in order to investigate Na^+ diffusion in this material. The study proposed a new mechanism by which Na^+/Fe^{2+} antistites defects stops Na^+ transport

in the main diffusion direction [010] while activating diffusion in the [001] channels. A similar mechanism for Li^+ was reported in $LiFePO_4$ [100], indicating that olivine structures generally undergo a transition from one-dimensional to two-dimensional diffusion triggered by the formation of antisite defects. The study of sodium intercalation at the molecular level is complicated by the addition of structural complexity resulting from the formation of stable Na^+ arrangements. The matter is of great significance, especially in the context of investigating dynamic attributes such as Na^+ mobility through simulations. This requires the utilisation of extensive supercells and prolonged simulation durations to accommodate potential sodium orderings. The computational cost associated with first-principles methods, such as DFT, renders their utilisation impractical in light of these stipulations.

The utilisation of multiscale modelling methods is often necessary to accurately represent the materials and processes involved in a modern battery cell, because of the intricate nature of the materials used and the operational principles. Consequently, multiscale modelling approaches are commonly used to effectively model materials and processes. In this study, we will employ the use of MSM methodologies, specifically, we will utilise cluster expansion as a method to bridge the length scales between first-principle computations and Monte Carlo simulations. The suggested approach involves a sequence of calculations, namely; (i) conducting initial electronic structure calculations to determine electronic, structural, and mechanical properties, as well as deriving and validating atomic potentials using ab initio MD, (ii) performing local cluster expansion calculations to investigate partially disordered states in various configurations, and (iii) employing kinetic Monte Carlo simulations and atomistic MD to numerically estimate diffusion coefficients by simulating the stochastic migration of ions within a host structure.

Chapter 3. Theoretical Methodologies

The most common strategy for materials modelling is based on the notion of "divide and conquer." This approach involves utilising techniques that are appropriate for particular dimensions and durations to study and understand the complexities of material phenomena that only occur within those dimensions. As a result, many methodological streams have emerged, which can be broadly categorised as ab initio density functional theory, molecular dynamics, and statistical approaches that use kinetic Monte Carlo algorithms. This chapter presents a brief overview of the theoretical foundations behind the approaches employed in this research, namely density functional theory, molecular dynamics, cluster expansion, and kinetic Monte Carlo.

3.1. Density Functional Theory

Density functional theory, commonly referred to as DFT, is a method of quantum mechanics that is used to analyse the energies of many-body systems in their ground states [42, 43]. Currently, DFT is the preeminent method for achieving the highest precision in the computation of the electronic structures of the material. The approach in question is a highly prevalent and versatile methodology that is extensively used in the domains of condensed matter physics, computational physics, and computational chemistry [44]. Because of this theoretical framework, it has become feasible to calculate the charge density of tangible materials, yielding very precise outcomes. The initial theorem proposed by Hohenberg and Kohn [45] demonstrates that the fundamental characteristics of the ground states of the many-body system can be exclusively determined through an electron density that exhibits a dependence on three spatial variables. The Hohenberg-Kohn theorem can be extended to the time-independent domain to construct the framework of time-dependent density functional theory (TDDFT), which facilitates the characterisation of excited states. The second Hohenberg-Kohn theorem establishes the energy functional for a given system and provides a demonstration that the energy functional is minimised by the proper ground-state electron density. In the context of Kohn-Sham Density Functional Theory (DFT), the complex issue of dealing with the interactions between electrons in stationary potentials is simplified into a more manageable problem where electrons are

considered to be noninteracting and move through an effective potential. The system's total energy is mathematically represented as:

$$E = E[\rho(r)] \quad (1)$$

Thus, the value *E* represent the total energy and while ρ is the density. Mattson *et al.* and Slater have provided a comprehensive description of the process for building a valid DFT computation [42, 43, 46]. The electron density and total energy are contingent upon the specific type and spatial configuration of the atomic nuclei. Therefore, the relation in equation (1) can be written as:

$$E = E[\rho(r), \{ R_{\propto} \}] \quad (2)$$

The set $\{ R_{\propto} \}$ represents the positions of all atoms, α, in the system being studied. Equation 2 plays a pivotal role in comprehending the atomic-level electrical, structural, and dynamic characteristics of matter. Additionally, it has the capability to predict the stable configuration of solids, surface reconstruction phenomena, and the equilibrium molecular geometry of adsorbates on surfaces. The majority of concerns in DFT are predicated upon the Born-Oppenheimer approximation, a fundamental assumption that posits the electron motions to be exponentially faster than the motions of the atomic nuclei. This implies that the electronic configuration is calculated for a predetermined atomic configuration, after which the atoms are displaced utilising classical mechanics [47].

The total energy equation (1) under the framework of DFT is decomposed into three distinct components: the kinetic energy *(T_0)*, Coulomb energy (*U*) which accounts for classical electrostatic interactions between all charged particles in the system, and exchange-correlation energy E_{XC}, which encompasses all many-body interactions. The equation is expressed as:

$$E = T_O + U + E_{XC} \quad (3)$$

The term denoted as *U* in the context refers to the Coulomb energy, which can be considered as the most direct and uncomplicated expression. The nature of the system can be described as classical, characterised by the presence of electrostatic energy arising from the Coulombic interaction between electrons and nuclei, as well as the repulsive forces between all electronic charges and nuclei. This can be expressed mathematically as:

$$\mathrm{U} = \mathrm{U_{en}} + \mathrm{U_{ee}} + \mathrm{U_{nn}} \quad (4)$$

with

$$U_{en} = -e^2 \sum_{\propto} Z_{\propto} \int \frac{\rho}{|\, r - R_{\propto}\,|}\, dr \tag{5}$$

$$U_{ee} = e^2 \iint \frac{\rho(r)\rho(r')}{|\, r - r'\,|}\, dr dr' \tag{6}$$

$$U_{nn} = e^2 \sum_{\propto\propto'} \iint \frac{Z_{\propto} Z_{\propto'}}{|\, R_{\propto} - R_{\propto'}|} \tag{7}$$

In the given context, e represents the fundamental charge associated with a proton, while Z_{α} denotes the atomic number of the atom denoted as a. Summations encompass the entirety of atomic entities, while integrations span the entirety of spatial dimensions. Once the distribution of electron density and the atomic numbers and positions of all atoms are determined, the evaluation of expressions (5) to (6) can be accomplished employing the methodologies of classical electrostatics.

The first term in equation (3) denoted as T_0, which represents the kinetic energy, possesses a more nuanced nature. In the framework of DFT, the actual electrons constituting a given system are substituted by effective electrons that possess identical charge, mass, and density distribution. In the realm of electron dynamics, it is pertinent to recognise that effective electrons exhibit behaviour akin to that of independent entities traversing through an effective potential. Conversely, the motion of a “real” electron is intrinsically intertwined with the collective movements of its electron counterparts. T_0 can be defined as the aggregate of the kinetic energies possessed by all effective electrons, each of which is in motion as an independent entity. Frequently, individuals do not explicitly delineate the differentiation between electrons in their true form and those that exhibit effective behaviour.

In the context of quantum mechanics, if we consider each effective electron to be described by a single particle wave function, denoted as ψ_i, then the total kinetic energy of all the effective electrons in the system can be expressed as:

$$T_0 = \sum n_i \int \psi_i^* (r) \left[\frac{\hbar^2}{2m} \nabla^2 \right] \psi_i(r) dr \tag{8}$$

The expression (8) can be understood as the summation of the expectation values of the kinetic energies of individual particles. Here, n_i represents the quantity of electrons occupying the state i. In the context of T_0, it is important to note that the construction inherently precludes the inclusion of dynamical correlations among the electrons.

The third term in equation (3), denoted as the exchange-correlation energy, E_{XC}, encompasses all remaining intricate electronic contributions to the overall energy. The Hohenberg-Kohn-Sham theorem, a fundamental principle in density functional theory, establishes that the total energy reaches its minimum value for the ground-state density. Furthermore, it asserts that the total energy remains stationary when subjected to first-order variations in the density, i.e.

$$\frac{\partial E[\rho]}{2\rho} | \rho = \rho_0 = 0 \tag{9}$$

In connection with the kinetic energy, we have added one-particle wave functions $\psi_i(r)$, which give rise to the electron density:

$$\rho(r) = \sum_i n_i |\psi_i(r)|^2 \tag{10}$$

The variable n_i represents the occupation number of the eigenstate i, which is denoted by the one-particle wave function ψ_i. The quantity $\rho(r)$ in equation (10) is the precise density of the many-electron system determined by its creation.

The target of the subsequent phase entails the formulation of equations that can be effectively employed for density functional computations in practical applications. The variational condition (9) can be employed to deduce the criteria for the wave functions of one particle that give rise to the density of the ground state. To achieve that goal, equation (10) is substituted into expression (9), and the total energy is then varied with regard to each wave function. The following equations are produced by this process:

$$\left[-\frac{\hbar^2}{2m} \nabla^2 V_{ion}(r) + V_{eff}(r) \right] \psi_i(r) = \varepsilon_i \psi_i(r), \tag{11}$$

With

$$V_{eff}(r) = V_H(r) + V_{XC}(r) \tag{12}$$

The equations denoted (11) and (12) are commonly referred to as the Kohn-Sham equations in academic literature. The electron density associated with these wave functions represents the density of electrons in their lowest energy state, known as the ground state, which is characterised by the minimum total energy.

In order to incorporate the third term (E_{xc}), the ensemble of waves that minimise the Kohn-Sham energy functional can be determined by solving the self-consistent equation:

$$\left[-\frac{\hbar^2}{2m}\nabla^2 V_{ion}(r) + V_H(r) + V_{XC}(r)\right]\psi_i(r) = \varepsilon_i\psi_i(r), \tag{13}$$

In the given context, ψ_i represents the wave function corresponding to the electronic state i, ε_i denotes the Kohn-Sham eigenvalue, and E_{XC} represents the exchange-correlation functional, which encompasses various intricate electronic factors contributing to the overall energy. The variable V_{ion} represents the cumulative potential energy between electrons and ions in a static system, while V_H denotes the Hartree potential of the electron, as expressed by the equation:

$$V_H(r) = e^2 \int \frac{\rho\,(r')}{|r - r'|} d^3r' \tag{14}$$

The exchange-correlation potential V_{XC} , is given formally by the functional derivative:

$$V_{XC}(r) = \frac{\delta E_{XC}[\rho(r)]}{\delta\rho(r)} \tag{15}$$

$\rho(r)$, is the electron density given by:

$$\rho\,(r) = 2\sum_i |\psi_i r|^2 \tag{16}$$

Therefore, the Kohn-Sham total-energy functional is written as:

$$E = 2\sum_{occ} \varepsilon_i + \cup_{ion-ion} - \frac{e^2}{2}\iint \frac{\rho(r)\rho(r')}{r-r'} + E_{XC}[\rho(r])$$
$$- \int \rho(r)\, V_{XC} dr \qquad (17)$$

To formally analyse the Kohn-Sham, it is necessary to estimate the exchange-correlation energy E_{XC}. This can be achieved by employing an approximation method, which will be discussed in the subsequent subsections.

3.1.1. Approximations

3.1.1.1. Local Density Approximation

The local density approximation (LDA) is recognised as a straightforward approach to characterising the exchange-correlation energy of an electron system. It is extensively employed in total-energy pseudopotential calculations. The expression provided accurately represents the sum rule for the exchange correlation hole. The LDA model operates under the assumption that the exchange-correlation energy is solely influenced by the electron density in the immediate vicinity of each individual volume element and denoted as dr. Using the approximation, the exchange correlation energy at a specific location r, pertaining to a density $\rho(r)$, can be equated to the exchange correlation energy per electron within a uniform gas possessing a density equivalent to that of the electron gas, as indicated by [48-52]:

$$\mathrm{E_{xc}^{LDA}} = \int \rho(\mathrm{r})\, \in_{\mathrm{xc}} (\rho)\, \mathrm{dr} \qquad (18)$$

The symbol $\in_{xc} (\rho)$ represents the exchange-correlation energy per particle in the context of a uniform electron gas with a density denoted as n. The incorporation of density functionals into spin-polarised systems is a very straightforward process for the exchange component, as the precise scaling with respect to spin is already established. However, when it comes to correlation, additional approximations must be utilised. In the context of DFT, a spin-polarised system utilises two spin-densities, denoted asρ_α and ρ_β, where the total density is represented by $\rho = \rho_\alpha + \rho_\beta$. The local spin density approximation (LSDA) is given by the following.

$$\mathrm{E_{xc}^{LSDA}} = \int \mathrm{dr}\rho(\mathrm{r}) \in_{\mathrm{xc}} (\rho_\alpha, \rho_\beta) \qquad (19)$$

Although LDA has achieved notable success, it is not without limits. LDA demonstrates favourable performance in systems characterised by gradual variations in density, effectively reproducing chemical trends. However, LDA exhibits two consistent trends: first, weak bonds are observed to be shorter than expected, and second, the computed binding energies tend to be higher than expected [49-52]. This led to a requirement for additional functionals following LDA, which will be outlined in the following subsection.

3.1.1.2. Generalised Gradient Approximation

In an inhomogeneous system, the exchange and correlation effects beyond the LDA are nonlocal in nature because they depend on the electrons in the region. This phenomenon is commonly known as gradient correction. The components inside the exchange-correlation expression are contingent upon the gradient of the electron density, rather than solely relying on the value at individual spatial points. The introduction of the generalised gradient approximation (GGA) was initially achieved by Perdew and Wang [52, 53]. The GGA functionals, while remaining localised, incorporate the density gradient at the corresponding coordinate as the newly introduced variable. The GGA exchange energy is given by [48]:

$$\mathrm{E}_{\mathrm{x}}^{\mathrm{GGA}}\,\mathrm{c}(\,\rho) = \int \mathrm{dr}\rho(\mathrm{r})\,\epsilon_{\mathrm{xc}}\,[\rho(\,\mathrm{r})\,,\|\nabla\,\rho(\,\mathrm{r})\| \tag{20}$$

The symbol ϵ_{XC} represents the exchange correlation energy, while $E[\rho]$ denotes the gradient term. Generalised gradient approximations have been observed to enhance several energy-related properties, including total energies, atomisation energies, energy barriers, and structural energy differences. Furthermore, it is worth noting that the local spin density approximation can have the effect of both expanding and softening bonds. This phenomenon can lead to corrections or even overcorrections in certain cases. Physics problems are the ones that most frequently employ the GGA functional.

3.1.1.3. Hybrid Functionals

Hybrid functionals are a type of approximations to the exchange-correlation energy functional that arise within the context of Density Functional Theory (DFT). These functionals integrate a portion of the precise exchange calculated from Hartree-Fock theory with the supplementary component of the exchange-correlation energy

acquired from other sources. Hybrid functionals exhibit the ability to obtain a more accurate estimation of the exchange-correlation energy functional, regardless of whether it is produced from ab initio or empirical methods. The exchange energy functional, which is expressed in terms of the Kohn-Sham orbitals rather than the density, is commonly known as an implicit density functional. It can be defined as follows:

$$E_X^{HF} = -\frac{1}{2}\sum_{i,j}\iint \psi_i^*(\boldsymbol{r}_1)\,\psi_i^*(\boldsymbol{r}_2)\frac{1}{\boldsymbol{r}_{12}}\psi_j(\boldsymbol{r}_1)\psi_i(\boldsymbol{r}_2)d\boldsymbol{r}_1 d\boldsymbol{r}_2 \qquad (21)$$

In most cases, the exact Hartree-Fock exchange functional and any number of explicit exchange and correlation density functionals are combined to produce a hybrid exchange–correlation functional. This type of functional is often built as a linear combination. The weights of each individual functional are typically determined by fitting the functional's predictions to experimental or accurately calculated thermochemical data. However, in the case of "adiabatic connection functionals," the weights can be predetermined.

3.1.1.4. DTF+U

Anisimov and Gunnarsson [54] developed the DFT+U approach in order to address problems in (semi) local DFT with the description of localised states. These problems provide a significant challenge when dealing with strongly correlated materials [54] such as the one considered in this study. Within the framework of the DFT enhanced with the Hubbard U term (DFT+U), the energy functional of DFT is expanded by incorporating an on-site potential equivalent to the Hubbard scheme,

$$E_{DFT+U}[\varrho(\boldsymbol{r})] = E_{DFT}[\varrho(\boldsymbol{r})] + E_{Hub}^1\left[\rho_{mm'}^{I\sigma}\right] - E_{DC}^I\left[\{\rho_{mm'}^{I\sigma}\}\right] \qquad (22)$$

The energy term E_{DFT} represents the total energy of the electron system calculated using DFT. Meanwhile, E_{Hub}^1 corresponds to the energy corresponding to the Hubbard interaction of the localised correlated orbitals of atom I. Lastly, E_{DC}^I denotes the approximated DFT interaction energy of the orbitals, which needs to be subtracted to prevent duplication of the interaction contribution from the corrected orbitals. In order to minimise the notation, we shall focus on systems featuring simply one atomic site exhibiting correlation, thereby omitting the superscript I.

Similar to other materials with high correlations, DFT+U can be used for open-shell orbitals, such as d and f orbitals, found in transition metal elements. These localised orbitals are present in elongated s-p states. Electrons form a complex many-electron issue when localised orbitals, which have high correlations with each other and a slight interaction with the extended states, are not removed. When applying the Hubbard model, the focus is on identifying the key degrees of freedom that contribute to the correlation between the localized orbital electrons. This involves considering the renormalized or screened Coulomb interaction (U) between the electrons. In other words, the localised states (d- and f-states) that make up the band gap's localised orbitals are too close to the Fermi energy. From that perspective, the U value should be utilised to move these states away from the Fermi level, such as that offered by the GGA+U theory, which adds to the Hamiltonian a term that increases the total energy, preventing the unwanted delocalisation of the d- or f-electrons when two d- or f-electrons are located on the same cation. It is important to note that, unlike fitting many other features, using excessively high values of U may over-localise the states and result in an unphysical flattening of the suitable bands, which will worsen the fit. Due to the electronic interaction error, a rise in the U value can also lead to an overestimation of the lattice constants and an incorrect assessment of the ground-state energy.

3.1.2. Plane-Wave Pseudopotential Method

The utilisation of the plane-wave pseudopotential (PWP) method has emerged as a robust and reliable approach to investigating the characteristics of a wide range of materials. The utilisation of plane-wave pseudopotential as a methodology for structural investigations, which relies on a quantum-mechanical approach to analyse the electronic subsystems, is primarily driven by the significance placed on the total energy and its associated features. A key aspect of the PWP method involves the simplification of the DFT problem by the exclusive consideration of valence electrons. The exclusion of core electrons is based on the idea that their charge density remains unaffected by variations in the chemical environment. This approximation is well understood and gives several computational advantages such that [55, 56]:

- The pseudopotential has significantly lower strength within the core region compared to the genuine Coulomb potential of the nucleus, and it lacks a singularity at the nucleus's position.
- The resulting pseudo-wave functions are smooth and nodeless in the core region.
- There are fewer electronic states in solid-state calculations.
- Both pseudopotentials and pseudo-wave functions can be efficiently represented using a plane wave basis set.

The plane wave pseudopotential method is applicable to large systems that are subjected to 3D periodic boundary conditions.

3.1.2.1. Plane-Wave Basis

Thus far, no discussion has been presented regarding the appropriate approach to address the challenges of managing the unlimited population of interacting electrons that are in motion within the static field generated by an endless number of ions. There are two primary challenges that need to be addressed. First, it is necessary to compute the wave function for every electron, which entails dealing with an unlimited number of electrons. Furthermore, this wave function must encompass the entirety of the solid's spatial domain. Secondly, the base set utilised to define the wave function will also be infinite in nature. The utilisation of Bloch's theorem relies on the inherent periodic nature of a crystal lattice, enabling the reduction of the vast number of one-electron wave functions that need to be computed. This reduction simplifies the determination of the number of electrons present within the crystal's unit cell, or half that number if the assumption is made that the electronic orbitals are doubly occupied, accounting for spin degeneracy. The wave function is written as the product of a cell periodic part and a wavelike part [57]:

$$\Psi_{ki}(r) = exp[ik.r]f_i(r) \quad (23)$$

The first term is the wavelike part, which will be discussed below. The second term is the periodic part of the wave function. This can be expressed by expanding it into a finite number of planewaves whose wave vectors are reciprocal lattice vectors of the crystal, given by:

$$f_i(r) = \sum_G G_{i,G} exp[iG.r] \quad (24)$$

where G represents reciprocal lattice vectors given by $G.I = 2\pi m$ for I, where I is a lattice of the crystal and m is an integer. Thus, each electronic wave function can be written as a sum of plane waves such that:

$$\Psi_{ki}(r) = \sum_{G}^{\Sigma} G_{i,k+G}[i(k+G).r] \tag{25}$$

where $G_{i,k+G}$, the coefficients for the plane are waves that need to be solved and depend entirely on the specific kinetic energy, $\left(\frac{h^2}{2m}\right)|k+G|^2$.

The convergence of the expansion is affected by the selection of the kinetic energy cut-off point, since plane waves with lower kinetic energy generally play a more significant role compared to those with higher kinetic energy. The implementation of a plane wave energy cut-off results in the reduction of the basis set to a finite size. The imposition of a kinetic energy cutoff may introduce a discrepancy in the overall energy of the system. However, it is theoretically feasible to minimise this discrepancy by expanding the basis set size and permitting a higher energy cutoff. The determination of the cut-off value utilised in practical applications is dependent on the specific system being examined. The plane waves are used as a basis set for the electronic wave functions, and substitution of equation (24) into equation (25), which leads to:

$$\left\{\frac{\hbar^2}{2m}\nabla^2 + V(r)\right\}\varphi_i(r) = c_i\varphi_i(r) \tag{26}$$

The integration over r gives the following secular equation:

$$\sum_{G'}\left[\frac{h^2}{2m}|k+G|^2\delta_{GG'} + V_{ion}(G-G') + V_H(G-G')\right]C_{i,k+G'} = \varepsilon_i C_{i,k+G} \tag{27}$$

It should be noticed that the kinetic energy, the initial component, is diagonal, whereas the different potential contributions are represented by their Fourier transforms. This may be written in terms of the Hamiltonian matrix elements $H_{k+G,k+G'}$ as:

$$\sum_{G'} H_{k+G,K+G'}C_{i,k+G'} = \varepsilon_i C_{i,k+G'}. \tag{28}$$

The solutions of the Kohn-Sham equation are obtained by diagonalising the Hamiltonian matrix elements $H_{k+G,k+G'}$. The size of these matrix elements is determined by the choice of energy cut-off $\left(\frac{h^2}{2m}\right)|k+G|^2$, and will be large for systems that contain both valence and core electrons.

Bloch's theorem proposes that electronic wave functions can be expressed as a sum of discrete plane waves. However, when it comes to expanding electronic wave functions, a plane-wave basis set is generally ill-suited. This is because a significant number of plane waves are required to accurately represent the tightly bound core orbitals and capture the rapid oscillations exhibited by the wave functions of valence electrons in the core region. Performing all-electron computations necessitates the utilisation of an exceedingly extensive plane-wave basis set, while the computation of electronic wave functions demands a substantial allocation of computational time. This problem can be overcome by using the pseudopotential approximation [55, 58].

3.1.3. Pseudopotential Method

In the field of physics, pseudopotential or effective potential is employed as an approximation to provide a simpler depiction of intricate systems. Applications of this technique encompass the resolution of issues of atomic physics and neutron scattering. The pseudopotential approximation was initially proposed by Hans Hellmann in 1933 [59]. In essence, the concept of pseudopotential aims to substitute the intricate influences arising from the movement of non-valence electrons within an atom's nucleus with an effective potential, commonly referred to as pseudopotential. This substitution is intended to modify the effective potential term in the Schrödinger equation, thereby replacing the conventional Coulombic potential term associated with core electrons. Figure 8 illustrates the ionic potential $\left(\frac{Z}{r}\right)$, the valence wave function (ψ_v), the corresponding pseudopotential $\left(V_{pseudo}\right)$, and pseudo-wave function $\left(\psi_{pseudo}\right)$ respectively [58]. The pseudopotential is a manufactured potential that serves as an effective replacement for the atomic all-electron potential (full potential). Its purpose is to eliminate core states and characterise the behaviour of valence electrons using pseudo-wave functions that exhibit a reduced number of nodes. This enables the pseudo-wave functions to be characterised using a significantly reduced number of Fourier modes, hence rendering plane-wave basis sets feasible for utilisation. Typically, this methodology focusses solely on the chemically active valence electrons, specifically considering them, while treating the core electrons as 'frozen'. The core electrons are regarded as non-polarisable ion cores, assumed to be hard and combined with the nuclei. The incorporation of the chemical environment into the pseudopotential can be achieved through self-consistent updates, therefore

relaxing the frozen-core approximation. However, this practice is hardly used. The first-principles pseudopotentials are obtained by deriving them from an atomic reference state. This derivation process ensures that the pseudo- and all-electron valence eigenstates possess identical energies and amplitudes, resulting in the same density outside a selected core cutoff radius. Pseudopotentials possessing a greater cut-off radius are commonly seen as being softer, exhibiting quicker convergence. However, it is important to note that these pseudopotentials are concurrently less transferrable, resulting in reduced accuracy when reproducing realistic features in diverse settings. Undoubtedly, the pseudopotential approximation is the predominant technique employed in electronic structure theory for the treatment of heavy atoms, necessitating the inclusion of relativistic effects. Pseudopotential calculations exhibit lower accuracy compared to all-electron calculations; yet they frequently yield results that closely approximate those obtained by the latter method, while requiring significantly reduced computational resources.

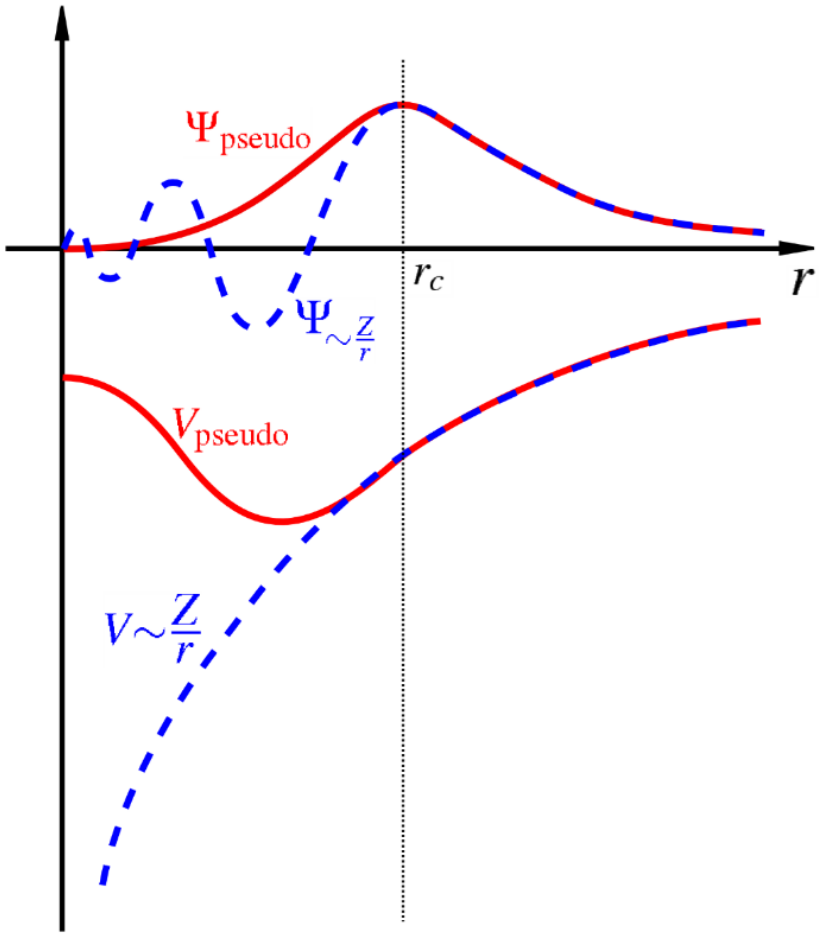

Figure 8: Comparison of a wavefunction in the Coulomb potential of the nucleus (blue) to the one in the pseudopotential (red). The real and pseudo wave functions and potentials match above a certain cut-off radius r_c [58].

The pseudopotential approximation offers the advantage of enabling the expansion of the electronic wave function through a reduced set of plane wave basis states. Consequently, this leads to a diminished computational time requirement for achieving energy convergence. The pseudopotential takes the analytical form:

$$V_{NL} = \sum_{lm} |lm\rangle V_l \langle lm|, \tag{29}$$

where $|lm\rangle$ is the spherical harmonics and V_l is the pseudopotential for the angular momentum l. Most of the pseudopotential currently used in the electronic structure is generated from all electron-atomic calculations.

A local pseudopotential is defined as a pseudopotential that employs a uniform potential for all the angular momentum components of the wave function. The

pseudopotential, which is specific to the local region, is a mathematical function that is solely based on the variation of the potential with respect to distance. The norm-conserving pseudopotential (NCP) proposed by Kleinmann and Bylander (1969) serves as an illustration of a nonlocal pseudopotential, wherein distinct potentials are employed for each angular momentum component of the wave function. In recent times, the ultra-soft pseudopotential (USP) formulated by Vanderbilt [60] has been incorporated into plane wave calculations. Within this particular design, it is conceivable for the pseudo-wave functions to exhibit a high degree of softness within the core region. Atoms encompass a broad spectrum, which incorporates transition metals.

3.1.4. Brillouin Zone

The initial Brillouin zone (BZ), named after Léon Brillouin, is a primitive cell that is distinctly defined in reciprocal space and is commonly utilised in the fields of mathematics and solid-state physics. Analogously to the partitioning of the Bravais lattice into Wigner-Seitz cells in physical space, the reciprocal lattice is subdivided into Brillouin zones. The planes delimiting the cell are determined by points on the reciprocal lattice. The significance of the Brillouin zone arises from its role in the depiction of waves in a periodic medium as described by Bloch's theorem. This theorem establishes that the solutions can be fully delineated by their conduct within a solitary BZ.

The initial BZ is also defined as the set of points within the reciprocal space that exhibit a closer proximity to the origin of the reciprocal lattice in comparison to all other reciprocal lattice points. This definition is derived from the Wigner-Seitz cell. An alternative characterisation pertains to the collection of points in the k-space that are accessible from the origin while avoiding any intersection with a Bragg plane. This can be expressed as the Voronoi tessellation that covers the origin of the reciprocal lattice.

The K vectors that exceed the initial Brillouin zone (red) do not convey any additional information compared to their equivalents (black) within the first Brillouin zone. The wavenumber k located at the edge of the BZ represents the spatial Nyquist frequency of waves propagating within the lattice. This is due to the fact that it corresponds to a half-wavelength equivalent to the interatomic lattice spacing denoted as in Figure 9.

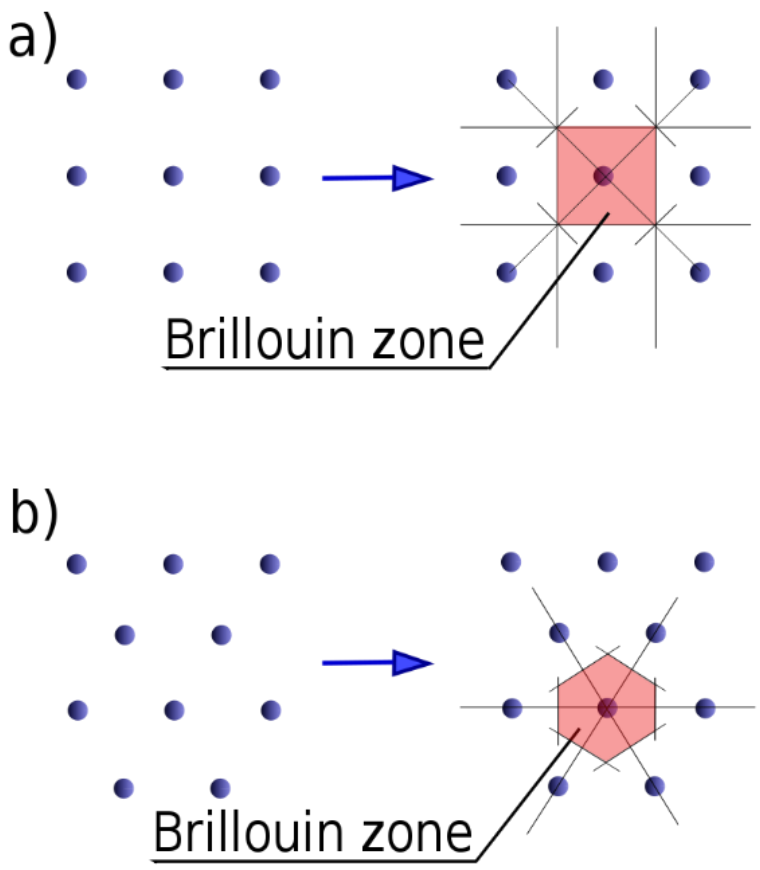

Figure 9: The reciprocal lattices (dots) and corresponding first Brillouin zones of (a) square lattice and (b) hexagonal lattice [61].

The illustration in Figure 9 depicts the BZ in purple and the irreducible BZ in red, pertaining to a hexagonal lattice. In addition, there exist subsequent Brillouin zones beyond the first, such as the second and third zones, which correspond to a series of non-overlapping regions of identical volume located at progressively greater distances from the origin. However, these zones are less commonly utilised. Consequently, the initial Brillouin zone is frequently referred to as the Brillouin zone, without any further elaboration. In general, the n^{th} Brillouin zone encompasses a collection of points that are accessible from the origin by precisely traversing $n-1$ unique Bragg planes. The notion of an irreducible Brillouin zone pertains to the initial BZ that has been diminished by the complete set of symmetries present in the point group of the lattice or crystal.

3.1.4.1. k-Points Sampling

The electronic states in a bulk solid are restricted to a specific set of k-points, which are specified by the boundary conditions imposed on the system. The density of

permissible k-points exhibits a direct proportionality with the volume of the solid. Simultaneously, with its departure from one surface, a particle joins the crystal at the opposing surface. The presence of an unlimited number of electrons in the solid is explained by the existence of an endless number of k-points. However, it is important to note that at each k-point, only a finite number of electronic states are occupied. The number of k-points increases when the spacing is decreased. In reciprocal mode, the k-points are given by:

$$\vec{k} = x_1\overrightarrow{b_1} + x_2\overrightarrow{b_2} + x_3\vec{b}_3 \tag{30}$$

where $\vec{b}_{1\ldots3}$ the three reciprocal basis are vectors, and ... is the supplied values. In the Cartesian input format, the k-points are given by:

$$\vec{k} = \frac{2\pi}{a}(x_1, x_2, x_3) \tag{31}$$

The unit cell of a face-centred cubic lattice is spanned by the following basis vectors:

$$A = \begin{pmatrix} 0 & \frac{a}{2} & \frac{a}{2} \\ \frac{a}{2} & 0 & \frac{a}{2} \\ \frac{a}{2} & \frac{a}{2} & 0 \end{pmatrix} \tag{32}$$

And the reciprocal lattice is defined as the matrix:

$$2\pi B = \begin{pmatrix} -1 & -1 & 1 \\ 1 & -1 & 1 \\ 1 & 1 & -1 \end{pmatrix} \tag{33}$$

Accurately determining the appropriate number of k-points to utilise in PWP calculations is crucial to achieving both expeditious convergence and precise total energy outcomes. The highest possible accuracy is achieved from the number of k-points which were used by Hohenberg and Kohn, Kohn, as well as Sham [62]. In this study, the Monkhohorst-Pack method was used to determine an optimal set of special k-points for use, as referenced in [45, 63].

3.1.4.2. Energy Cut-off

In order to establish the suitable kinetic energy cutoff for the material, single-point energy calculations were executed for various kinetic energy cutoffs at the default number of k-points for each system using GGA (PBE, PBEsol, and PBE+U) and LDA. The study used ultrasoft pseudopotentials as opposed to norm-conserving potentials [64], due to their reduced computational demands. The determination of the number

of plane waves necessary for a calculation is contingent upon the energy cut-off parameter in PWP computations, rendering it a crucial factor. The different energy cut-offs that were used in this study are presented in respective chapters, as outlined in the methodology sections.

3.1.5. Theoretical Background for Calculated Properties

3.1.5.1. Heats of Formation

Heat of formation, also known as standard heat of formation or enthalpy of formation or standard enthalpy of formation, is the amount of heat absorbed or evolved when one mole of a compound is produced from its component elements in their normal physical condition (gas, liquid, or solid). Typically, it is assumed that the compound is created at 25 ° C (273.15 K) and 1 atmosphere of pressure, in which case the heat of formation can be called the standard heat of formation. Zero is arbitrarily attributed to the heat of production of an element. Using Hess's law of heat summation, it is possible to determine the heat absorbed or evolved in any chemical process by adding the known temperatures of formation or combustion for each phase of the reaction. The heat of formation of compounds and associated entropies serve as the foundation for comprehending and creating phase diagrams. Knowledge of these quantities provides the possibility of determining which of the observed phases may be produced by modifying the method of production. The formation heat can be estimated using the analytical expression:

$$\Delta H_f = E_c - \sum_i x_i E_i \tag{34}$$

where E_c is the calculated total energy of the compound, E_i is the calculated total energy of element i in the compound. In this study, heats of formation are calculated from ab initio calculations to predict the stability trend of Na de-intercalated systems, using the equation:

$$\Delta H_f = \frac{1}{6}[E - (E_{Na} + E_M + E_P + 4E_O)] \tag{35}$$

where N is the total number of atoms in the unit cell, E is the total energy of the compound, $NaMnPO_4$ and E_{Na}, E_{Mn}, E_P and E_O are the individual total energies of Na, Mn, P and O, respectively.

3.1.5.2. Density of States

The density of states (DOS) is a fundamental concept in solid-state physics and condensed matter physics, which characterises the number of modes within a given frequency range. The definition of the density of states is given by the expression:

$$DE = \frac{N(E)}{V}, \tag{36}$$

where $N(E)\delta E$ is the number of states in the system of volume V, whose energies lie in the range from E to $E + \delta E$. The DOS of a system represents the number of accessible states per energy interval at each energy level. Unlike isolated systems, such as atoms or molecules in the gas phase, the density distributions are continuous rather than discrete. With a given energy level, a high DOS indicates that there are several states accessible for occupancy. A DOS of zero indicates that no states may exist at the given energy level. In general, a DOS is the mean of the system's occupied space and time domains. Local differences, often caused by distortions in the underlying system, are frequently referred to as local density of states (LDOS). Due to the presence of local potential, the LDOS might be non-zero even though the DOS of an undisturbed system is zero.

The density of states plays an essential role in the kinetic theory of the solid. The number of occupied states per unit volume at a given energy is the product of the density of states and the probability distribution function for a system in thermal equilibrium. Using two prevalent distribution functions, demonstrate how to apply a distribution function to the state density. This value is commonly used to explore various physical characteristics [65, 66].

3.1.5.3. Elastic Constants

Elastic characteristics are related to fundamental solid-state features that include the equation of state, interatomic potentials, lattice constants, and phonon spectra. They include critical information about the material's strength against an externally imposed strain and serve as stability criteria in the research of structural mechanical stability alterations [67, 68]. Elastic constants of a material, in general, describe its response to the external applied strain required to maintain a given deformation and provide useful information about the material's strength, as characterised by the bulk modulus (B), shear modulus (G), Young's modulus (E), Poisson's ratio (v), and shear anisotropy

factor (A). Born [69] pioneered the computation of elastic constants. The Born stability criterion is a set of conditions on the elastic constants (C_{ij}) that are connected to the second-order shift in a crystal's internal energy during formation. However, it was later discovered that the Born stability ranges are sensitive to the choice of coordinates. The elastic constants calculated using a Taylor expansion are derived from equation (37) [70].

$$U(v,\varepsilon) = U(V_0,0) + V_0\left[\sum_i \tau_i\varepsilon_i\delta_i + {}^1/_2\sum_{ij} C_{ij}\varepsilon_i\delta_i\varepsilon_j\delta_j\right], \tag{37}$$

where $U(V_0,0)$ represents the energy of the unstrained system energy, V_0 is the equilibrium volume, τ_i is the element in the stress tensor, and δ_i is a factor of Voigt index. For cubic, tetragonal, orthorhombic and monoclinic crystals, there are three (C_{11}, C_{12}, C_{44}), six (C_{11}, C_{12}, C_{13}, C_{33}, C_{44}, C_{66}), nine (C_{11}, C_{22}, C_{33}, C_{12}, C_{13}, C_{23}, C_{44}, C_{55}, C_{66}) and thirteen (C_{11}, C_{22}, C_{33}, C_{12}, C_{13}, C_{23}, C_{44}, C_{55}, C_{66}, C_{15}, C_{25}, C_{35}, C_{46}) independent elastic constants, respectively. Relevant to this study, for orthorhombic system elastic constants, C_{11}, C_{22} and C_{33} indicate the degree of directional resistance to linear compressions of *a*, *b,* and *c*, respectively. While C_{44}, C_{55}, and C_{66} measure shear resistance to the (100), (010) and (001) planes, respectively. The Born mechanical stability criteria for orthorhombic systems are as follows:

$$\begin{aligned}&(C_{11}-C_{12})>0,(C_{11}+C_{33}-2C_{13}>0,\\&(2C_{11}+C_{33}+2C_{12}+4C_{13})>0,\\&C_{11}>0,C_{33}>0,C_{44}>0,C_{66}>0\end{aligned} \tag{38}$$

The vast majority of observed crystals exhibit a unique characteristic known as elastic anisotropy. A comprehensive understanding of this anisotropic behaviour holds significant implications not only in the fields of engineering science and crystal physics but also in various other scientific disciplines. The shear anisotropic factors can be determined by quantifying the level of anisotropy in the interatomic bonding across different planes. The shear anisotropic factors serve as a quantitative indicator of the extent of anisotropy in the interatomic bonding across distinct crystallographic planes. The shear anisotropic factor for the directions (100) and [011] and [010] is calculated as:

$$A_1 = \frac{4C_{44}}{C_{11}+C_{33}-2C_{13}} \tag{39}$$

For the {(010), (001)} shear planes between the ([011] and [010], [110], [001] respectively) directions are:

$$A_3 = \frac{4C_{66}}{C_{11} + C_{22} - 2C_{12}} \quad (40)$$

$$A_2 = \frac{4C_{55}}{C_{22} + C_{33} - 2C_{23}} \quad (41)$$

From the calculated elastic constants, the macroscopic mechanical parameters, namely bulk, shear, and Young's modulus, are obtained using the Voigt-Reuss-Hill approach [71],

$$B_V = \frac{1}{9}(C_{11} + C_{22} + C_{33}) + \frac{2}{9}(C_{12} + C_{13} + C_{23}), and\ B_R = [(S_{11} + S_{22} + S_{33}) + 2(S_{12} + S_{13} + S_{23})^{-1}], \quad (42)$$

$$G_V = \frac{1}{15}(C_{11} + C_{22} + C_{33} - C_{12} - C_{13} - C_{23}) + \frac{1}{5}(C_{44} + C_{55} + C_{66}), \quad (43)$$

$$G_R = 15[4(S_{11} + S_{22} + S_{33}) - 4(S_{12} + S_{13} + S_{23}) + 3(S_{44} + S_{55} + S_{66})]^{-1}, \quad (44)$$

$$B_H = \frac{1}{2}(B_R + B_V), \quad (45)$$

$$G_H = \frac{1}{2}(G_R + G_V), \quad (46)$$

$$E_H = \frac{9B_H G_H}{G_H + 3B_H}, \quad (47)$$

where B, G and E are the bulk, shear and Young's moduli respectively, while V, R and H are the Voigt, Reuss and Hill bounds, respectively, and S_{ij} is the inverse matrix of the elastic constant's matrix C_{ij}, which is given by Ravindran *et al.* [72].

3.1.5.4. Debye Temperature and Thermodynamics

The Debye temperature Θ_D is the temperature of a crystal's highest normal mode of vibration, and it correlates the elastic properties with the thermodynamic properties such as phonons, thermal expansion, thermal conductivity, specific heat, and lattice enthalpy. In this work, the Debye temperature Θ_D of Na_xMnPO_4 compounds have been calculated from the averaged elastic-wave velocity using the equation:

$$\theta_D = \frac{h}{k_B}\left(\frac{3}{4\pi}\right)^{1/3} v_m \quad (48)$$

where h and k_B are Planck's and Boltzmann's constants, respectively, and V_a is the atomic volume. The average sound velocity in polycrystalline systems, v_m, are evaluated by the expression:

$$v_m = \left[\frac{1}{3}\left(\frac{2}{v_t^3} + \frac{1}{v_l^3}\right)\right]^{-1/3} \quad (49)$$

where v_t and v_l are the mean longitudinal and transverse sound velocities, which can be related by the shear and bulk moduli from Navier's equations:

$$v_t = \left(\frac{3B+4G}{3\rho}\right)^{1/2} and\ v_t = \left(\frac{G}{\rho}\right)^{1/2}. \quad (50)$$

3.2. Classical Molecular Dynamics

Molecular dynamics simulation is a computational methodology employed for the investigation of atomic motions within a specified system, encompassing solid materials, solid solutions, liquids, and gases. Its purpose is to gain insight and make predictions about the structural, dynamic, kinetic, and equilibrium properties under specific conditions such as compositions, temperatures, and pressures [73]. MD is a highly effective technique used for the investigation of the structural properties of many states of matter, including solids, liquids, and gases. The utilisation of electronic computers, including supercomputers, is a contemporary approach to this procedure. MD simulations have several similarities to actual experimental procedures in several aspects. When conducting a genuine experiment, the procedure often involves the following steps. A sample of the substance under investigation is prepared in advance. The sample is connected to a measuring device, such as a thermometer, manometer, or viscometer, to measure the property of interest during a specific time period. If the measurements we obtain are affected by statistical noise, which is a common occurrence, increasing the duration of the averaging process improves the accuracy of our measurement.

In the context of MD simulation, the identical approach is adhered to. Initially, a sample is prepared by carefully selecting a model system with N particles. Subsequently, the governing equations of motion, as formulated by Newton, are solved for this system. This computational process is continued until the system's parameters reach a state

of temporal stability, indicating that the system has achieved equilibrium. Following the process of equilibration, the subsequent step involves conducting the actual measurement. Indeed, there exist several common errors that can occur during the execution of a computer experiment, which bear resemblance to errors encountered in traditional experiments. These errors include inadequate sample preparation, insufficient measurement duration, occurrence of irreversible changes in the system during the experiment, and discrepancies between intended and actual measurements [74]. MD is a computer simulation technique that involves the integration of equations of motion to track the temporal evolution of a system comprising interacting atoms. MD simulations are a valuable tool for examining intricate atomistic systems.

The utilisation of MD technology enables the simulation of the kinetic and thermal characteristics of atoms within solid materials. By conducting simulations at various temperatures and analysing the temporal displacements of the ions, it is possible to make predictions regarding diffusion coefficients. The MD technique encompasses the computational solution of Newton's laws of motion for a given time interval, applied to every constituent particle inside a given system. One notable distinction from the energy minimisation method examined in the preceding section is that MD simulation incorporates the influence of temperature by imparting kinetic energy to the atoms within the simulation cell. Consequently, this approach enables the tracking of the atoms and molecules over time, thereby providing insight into their trajectory. In contrast to energy minimisation calculations, it is possible for atoms and molecules to overcome energy barriers and reach a global minimum. However, this phenomenon is limited to small energy barriers, typically on the scale of a few times the thermal energy (k_BT), due to the constrained "real time", available in MD simulations. In molecular dynamics simulation, the particles are initially assigned random velocities, such that the system starts with the required temperature and that the simulation cell has no translational momentum, i.e.:

$$\sum_{i=1}^{N} m_i . v_i^2 = 3Nk_BT \tag{51}$$

and

$$\sum_{i=1}^{N} m_i . v_i^2 = 0 \tag{52}$$

where N is the number of particles, k_B is the Boltzmann constant, T is the temperature, m_i is the mass of ion i_i, and v_i its velocity. The second step of a molecular dynamic's simulation is to calculate the force acting on each particle. Once the forces, F_i, are obtained the accelerations, a_i, can be calculated and the velocities, v_i, and positions F_i, are updated, for an infinitely small-time step, according to

$$a_i(t) = \frac{F_i(t)}{m_i} \tag{53}$$

$$v_i(t + \delta t) = v_i(t) + a_i(t).\delta t \tag{54}$$

$$r_i(t + \delta t) = r_i(t) + v_i(t).\delta t \tag{55}$$

The equations of motion formulated by Newton are applicable mainly within the confines of an infinitesimally small-time interval. In practical applications, computer codes commonly employ integration techniques, such as the Verlet algorithm [75], to effectively solve Newton's laws of motion. The selection of the time step, denoted as δt, in these equations holds significant importance. If the time step, denoted as δt, is very big, it will result in molecular vibrations occurring inside that time interval, leading to significant inaccuracies. However, if the time interval, denoted as δt, is excessively tiny, the particles will require an extended duration to traverse a substantial distance. Furthermore, it is imperative to take into account an additional consideration when selecting the temporal aspect. Following each iteration, many dynamic parameters of the system are computed, including but not limited to potential energy, temperature, and pressure. Subsequently, the aforementioned procedure is iterated numerous times, often on the order of thousands or millions, in order to attain the desired duration of the simulation. During the initial stages of the simulation, the velocities of the particles are adjusted proportionally to achieve the target temperature. The current time interval is commonly referred to as the equilibrium period, during which the system is allowed to reach a state of equilibrium under specific temperature and pressure conditions prior to data collection. Subsequently, the simulation is executed

for an extended duration, without adjusting the velocities of the particles, in order to obtain stabilised averages of the desired attributes and minimise the impact of statistical fluctuations. In molecular dynamics, the Newtonian second law for the time evolution of a system is expressed as cited by Komaduri *et al*. [76, 77]:

$$\frac{m_i d^2 r_i}{dt^2} = f_{i,}\ (i = 1, \dots\dots, N) \tag{56}$$

where N is the total number of atoms, m_i is the mass of the i^{th} atom with position vector $\mathbf{r}_i$, $f_i = -\nabla_i V(r_1, r_2, \dots\dots, r_N)$ is the force acting on the i^{th} atom due to interaction with other atoms in the system, and $V(r_1, r_2, \dots\dots, r_N)$ is the interaction potential. The initial positions and velocities of the atoms, together with the interaction potential define the whole set of thermodynamic, elastic, and mechanical properties of the material. The set of 3N second-order differential equations, as given in equation (56), is often solved by recasting it as a set of 6 N first-order Hamiltonian equations of motion, thus:

$$\frac{dp_i}{dt} = f_i = -\nabla_i(r_1, r_2, , \dots, r_N), \qquad \frac{dr_i}{dt} = \frac{P_i}{m_i} \tag{57}$$

where p_i is momenta. Integration of equation (56) results in the system's overall trajectory given the initial locations and momenta of the system. One may determine the spatial and temporal distributions of energy, temperature, and pressure, as well as keep track of the system's structural and phase changes, by knowing the trajectories of all the atoms.

3.2.1. Integration Algorithms

An integration algorithm is employed to systematically solve the equations of motion by utilising a finite difference algorithm. The algorithm employed in this study is the Verlet algorithm [75] and is briefly discussed herein. The locations, velocities, and accelerations are determined using a Taylor expansion of the positions with respect to time t:

$$\begin{aligned} r(t+\delta t) &= r(t) + v(t).\delta t + \frac{1}{2}a(t)\delta t^2 + \frac{1}{6}b(t)\delta t^3 + \cdots \\ v(t+\delta t) &= v(t) + a(t).\delta t + \frac{1}{2}b(t)\delta t^2 + \cdots \\ a(t+\delta t) &= a(t) + b(t).\delta t + \cdots \\ b(t+\delta t) &= b(t) + \cdots \end{aligned} \tag{58}$$

In this context, the variables are defined as follows: r represents the position of the particle, v denotes its velocity, a signifies its acceleration, and b refers to the third

time derivative of r. The position of a particle, denoted as a, can be determined using equation (58) both before and after a time step, denoted as δt, by calculating the position of the particle relative to the position function $r(t)$.

$$r(t+\delta t) = r(t) + v(t).\delta t + \frac{1}{2}a(t)\delta t^2 + \frac{1}{6}b(t)\delta t^3 + \boldsymbol{\vartheta}(\delta t^4) \tag{59}$$

$$r(t-\delta t) = r(t) - v(t).\delta t + \frac{1}{2}a(t)\delta t^2 - \frac{1}{6}b(t)\delta t^3 + \boldsymbol{\vartheta}(\delta t^4) \tag{60}$$

where $\delta(t\delta^4)$cd is the order of accuracy. By adding (59) and (60) gives

$$r(t+\delta t) + r(t-\delta t) = 2r(t) + a(t)\delta t^2 + \boldsymbol{\vartheta}(\delta t^4) \tag{61}$$

It has been observed that the Verlet method (61) exhibits time-reversibility, meaning that the positions at time $t + \delta t$ and $t - \delta t$ can be interchanged.

3.2.2. Energy Minimisation

The energy minimisation process yields different configurations of the system that correspond to the minima of the energy function. Therefore, the process of energy minimisation entails the utilisation of numerical techniques to locate the lowest point on the potential energy landscape, starting from an initial configuration characterised by higher energy. In certain instances, the insights derived from the principle of energy minimisation can yield sufficient predictive power to accurately determine the properties of the given system. If the identification of all minimum configurations on the energy surface is feasible, then it becomes possible to employ statistical mechanical formulae in order to deduce a partition function from which various thermodynamic properties can be computed. However, this phenomenon can only be observed in the context of minuscule molecular conglomerates within the gaseous milieu. The process of energy minimisation is typically undertaken in order to ascertain the existence of a conformer that exhibits stability. This phenomenon is alternatively referred to as the optimisation of geometric configurations.

3.2.3. Ensembles

MD, as previously described in section 3.2, is a technique for modelling the kinetic and thermodynamic characteristics of molecular systems using Newton's laws of motion. Typically, the Verlet algorithm is used in MD to perform the numerical integration of

the equation of movements [78, 79]. If all forces appearing in Newton's equation of motions are related to the potential energy of the system, then the total energy of the system is conserved and given by the following:

$$E = E_K + E_P \tag{62}$$

There are different types of ensembles employed in MD simulations, and they are discussed briefly in the next subsections.

3.2.3.1. Microcanonical Ensemble

The system is shielded from variations in the number of molecules *(N)*, the volume *(V),* and the energy *(E)* during the microcanonical ensemble, also known as the NVE ensemble. It is the same as an adiabatic process, which means there is no heat transfer. The total amount of energy is maintained throughout a microcanonical trajectory of molecular dynamics, which can be conceptualised as an exchange of potential and kinetic energy. The following pair of first-order differential equations can be written in Newton's notation for a system of *N* particles with coordinates *X* and velocities *V* [80]:

$$F(X) = -\nabla U(X) = MV\,(t) \tag{63}$$

$$V(t) = X\,(t) \tag{64}$$

where the potential energy function *U(X)* of the system is a function of the particle coordinates *X*.

3.2.3.2. Canonical Ensemble

In the field of statistical mechanics, a canonical ensemble, also known as an *NVT*, is used to isolate a system from variations in moles *(N)*, volume *(V)*, and temperature *(T)*. It is a statistical ensemble that is used to represent the possible states of a mechanical system that is in thermal equilibrium with a heat bath. The system is in thermal equilibrium with a heat bath when it is said to be in thermal equilibrium. The system is considered to be closed in the sense that it can exchange energy with a heat bath. As a result, the total energy that a system possesses can vary depending on which of its possible states it is in. In all its states, the system maintains the same composition, volume, and shape, regardless of the state it is in [80]. In layman's terms, the canonical ensemble allots a probability, denoted by the following exponential, to each individual microstate:

$$P = e^{\frac{A-E}{kT}}, \tag{65}$$

where *P* is probability, *A* is free energy (Helmholtz free energy), *E* is the total energy of the microstate, *K* is Boltzmann's constant and *T* is the temperature of the system.

3.2.3.3. Grand Canonical Ensemble

The isothermal-isobaric ensemble is a statistical mechanical ensemble that keeps the temperature, T, and pressure, P, applied at the same level throughout the experiment. The NPT ensemble, also known as the isothermal-isobaric ensemble, is characterised by the maintenance of a constant number of particles, temperature, and pressure during the entirety of the experimental procedure. It is worth noting that the probability distribution function for the grand canonical (μVT) ensemble must also include N as one of its variables. This is because the number of particles that are in thermal equilibrium can, in principle, be any non-negative integer. This is due to the fact that the relationship of particles existing in a state of thermal equilibrium can theoretically assume any nonnegative integer value. The NPT ensemble is a valuable tool for assessing the equation of state of model systems with incomputable virial expansion for pressure. It is also applicable in measuring the equation of state of systems in proximity to first-order phase transitions.

Following the same approach as in the NPT ensemble, the equilibrium distribution of the grand canonical (μVT) ensemble can be obtained using the relation:

$$\rho(\{q_i\}\{p_i\}N) = \frac{1}{Z} e^{-\beta(H\{q_i\}\{p_i\}-\mu N)} \tag{66}$$

where

$$Z = \sum_{N=0}^{\infty} \int \prod_{i=3}^{3N} dq_i dp_i \, e^{-\beta(H\{q_i\}\{p_i\}-\mu N)} \tag{67}$$

$$= \sum_{N=0}^{\infty} e^{\beta\mu N} Z(N,V,T) \tag{68}$$

The parameter, ρ is grand canonical distribution and Z (N, V, T) is the normalisation factor in the canonical ensemble for N particles.

3.3. Atomistic Interatomic Potential

3.3.1. Empirical Potential Model

Theoretical models known as empirical/atomistic potential models elucidate the energy fluctuations of molecules or solids based on their atomic coordinates [81]. The dependability of the computations is contingent upon the calibres and precision of the potential model.

The used atomistic simulation techniques in this work are based on the Born model of solids [82]. The present model suggests that the energy and its derivatives can be delineated as the aggregate of all interatomic interactions within the system, thereby engendering the overall interaction and resultant net force exerted on each atom by its counterparts [83]. Furthermore, the atoms of a system are represented as point-charge particles that interact via long-range electrostatic forces and short-range interactions. Hence, the interaction energy between two ions is obtained by:

$$\phi_{ij} = \frac{1}{4\pi \in_0} \frac{q_i q_j}{r_{ij}} \Phi(r_{ij}) \tag{69}$$

The initial term in the expression denotes the Coulombic interactions that occur over a considerable distance. The symbol $\in_0$ represents the permittivity of vacuum, while q_i and q_j denote the charges of the respective ions. The variable r_{ij} represents the interatomic distance. The term $\Phi(r_{ij})$ pertains to the interactions between ions that occur at a short range. These interactions encompass the repulsion that arises from the electron charge clouds and the attractive forces that stem from van der Waals.

3.3.2. Long Range Interactions

The long-range nature of electrostatic interactions between charged particles implies that a given particle i will engage in interactions with all other particles j present within the simulation box. Additionally, these interactions will extend to the periodic images of the particles, including those of i. Hence, the interaction energy's Coulombic component, denoted by ϕ_i, can be expressed as:

$$\phi_i = \frac{1}{2}\left(\frac{1}{4\pi \in_0}\right) \sum_{n} \sum_{i=1}^{N} \sum_{j=1}^{N} \frac{q_i q_j}{|r_{ij} + nL|} \tag{70}$$

The equation for the electrostatic potential energy between two particles i and j is given by the expression where q_i and q_j denote the respective charges of the particles,

r_{ij} represents the interatomic distance, $\in_0$ corresponds to the permittivity of free space, and L denotes the simulation cell vectors that reflect the periodicity of the simulation box. The summation with respect to n represents the aggregation of all periodic images, where n is the ordered triplet of integers that characterises the periodic images of the simulation cell. The presence of a prime symbol in the first summation denotes the exclusion of cases where $i = j$, specifically when $n = 0$ is equal to zero. In this instance there is a slow convergence of the sum in attributable to the presence of the $1/r$ term. Thus, it is necessary to employ a more efficient and dependable method of summation, such as Ewald summation.

The Ewald summation method, as described in reference [84], is a highly effective approach for the computation of electrostatic interactions within three-dimensional periodic systems. It is particularly efficient in its ability to summate the interactions between an ion and its infinite periodic counterparts. The approach employed in this study involves the partitioning of the Coulombic potential into three distinct components, namely a reciprocal space term denoted as ϕ_1, a real space term represented as ϕ_2, and a self-interaction term designated as ϕ_3. It follows that the overall Coulombic potential can be expressed as the sum of these three constituent terms:

$$\phi = \phi_1 + \phi_2 + \phi_3 \tag{71}$$

The Ewald method assumes that each particle with a charge of q_i is encompassed by a charge distribution that is spherically symmetric and of opposite sign. This distribution is designed to cancel out the q_i charge and is typically modeled as a Gaussian distribution. Specifically, the distribution is represented by the equation:

$$\rho_i(r) = -q_i \left(\frac{\alpha}{\pi}\right)^{3/2} exp(-\alpha r^2) \tag{72}$$

The distribution's width is determined by the arbitrary parameter α, while r denotes the position with respect to the distribution's center. Hence, solely the portion of q_i that remains unscreened is accountable for generating the electrostatic potential attributed to particle i. As the distance increases, the afore-mentioned fraction exhibits swift convergence towards zero, indicating that the interactions that are screened possess a limited range. Consequently, the electrostatic interactions among these screened charges can be computed through direct summation in actual space.

3.3.3. Short Range Interactions

The interactions that occur at short-range exhibit diverse components. At short distances, the electron charge clouds exhibit a significant degree of interaction, resulting in mutual repulsion. Moreover, at such distances, the dipole-dipole interactions, arising from the fluctuating dipoles on each ion, will give rise to attractive van der Waals forces. Moreover, in the context of covalent systems, the model can incorporate the short-range interactions among three or more ions to account for the directional nature of bonding. This study outlines the characterisation of short-range attractive and repulsive interactions through the utilisation of parameterised potential functions. Empirical derivation of potential parameters can be accomplished through fitting to experimental data, including crystallographic positions, elastic or dielectric properties, and infrared frequencies. Alternatively, fitting to more precise simulations, such as electronic calculations, can also be employed.

3.3.3.1. Buckingham Potential

The Buckingham-Coulomb potential incorporates the Coulomb interaction alongside the Pauli repulsion and van der Waals interaction, thereby ensuring accurate and dependable outcomes in modelling ionic interactions [85]. The Buckingham potential is characterised by the substitution of the repulsive term with an exponential term, resulting in the following expression for the potential:

$$U(r_{ij}) = A_{ij} \times exp\left({}^{-r_{ij}}/_{\rho_{ij}}\right) - \frac{C_{ij}}{{r^6}_{ij}} \tag{73}$$

where A_{ij} and ρ_{ij} are parameters that represent the ion size and hardness, respectively. The initial term is commonly referred to as the Born-Mayer potential, while the inclusion of the attraction term led to the development of the Buckingham potential. Frequently, in the context of cation-anion interactions, the attractive component is commonly disregarded due to its negligible impact on the short-range potential. Alternatively, this interaction is often incorporated into the A and ρ parameters.

3.3.3.2. Three-Body Potential

The bond-bending factor is an additional element of the interactions between covalent species that is taken into account to assess the energy expenditure associated with

deviations from the equilibrium value. Therefore, this potential function characterises the orientation of the bonds and exhibits a simple harmonic structure:

$$U(\theta_{ijk}) = \frac{1}{2} k_{ijk} (\theta_{ijk} - \theta_0)^2 \tag{74}$$

where k_{ijk} is the three-body force constant and θ_0 is equilibrium angle.

3.3.4. Calculated Properties

3.3.4.1. Strain and Stress

The stress-strain relationship in MD simulations is typically derived from tensile models. In every instance of applied deformation, the nominal strain of the entire MD model in the loading direction can be calculated by normalising the change in nominal length with respect to the initial length. The concept of stress in the field of thermodynamics is characterised by the partial derivative of the internal energy with regard to the strain per unit volume.

In MD, the total energy is the summation of the energy of individual atoms, E^{α}, and is expressed as:

$$E^{\alpha} = T^{\alpha} + U^{\alpha} = \frac{1}{2} M^{\alpha} (V^{\alpha})^2 + \Phi^{\alpha}(r), \tag{75}$$

where T^{α} is the kinetic energy, U^{α} the potential energy, M^{α} the mass, V^{α} the magnitude of its velocity and $\Phi^{\alpha}(r)$ the potential energy at the atom location r. Thus, the stress components for a given atom are written as:

$$\sigma_{ij}^{\alpha} = \frac{1}{V^{\alpha}} \left(M^{\alpha} v_i^{\alpha} v_j^{\alpha} + \sum_{\beta} F_i^{\alpha\beta} r_j^{\alpha\beta} \right), \tag{76}$$

where V^{α} is the atomic volume of the atom α, v_i^{α} and v_j^{α} are components of velocity. $F_i^{\alpha\beta}$ are the components of force between atoms α and β from the derivative of the potential energy, and $r_j^{\alpha\beta}$ are the components of the distance between atoms α and β. The nominal stress is determined by calculating the mean value of the atomic stresses across the entire volume of the model. Thus, the nominal stress components of each model are expressed by:

$$\sigma_{ij}^{\alpha} = \frac{1}{V^{\alpha}} \sum_{\alpha} \left(M^{\alpha} v_i^{\alpha} v_j^{\alpha} + \sum_{\beta} F_i^{\alpha\beta} r_j^{\alpha\beta} \right)' \tag{77}$$

where V is the volume of the MD model and $V = \sum_{\alpha} V^{\alpha}$.

3.3.4.2. Diffusion Coefficients

The mean square diffusion (MSD) of ions is used to calculate the diffusion coefficient from equilibrium molecular dynamics (EMD) simulations. The self-diffusion coefficient is given by the Einstein relation:

$$D_s = \lim_{t\to\infty} \frac{1}{6Nt} \sum_{i=1}^{N} \langle \left(\Delta \boldsymbol{r}_i(t)\right)^2 \rangle \tag{78}$$

where D_s is self-diffusion coefficient, $\Delta r_i(t)$ is s displacement of the i^{th} of N ions over a period, t, and $\langle \ldots \rangle$ indicates an ensemble average. The collective diffusion coefficient D_c (or ion center of mass diffusion coefficient) is given by:

$$D_c = \lim_{t\to\infty} \frac{1}{6Nt} \langle \left(\sum_{i=1}^{N} \boldsymbol{r}_i(t) - \sum_{i=1}^{N} \boldsymbol{r}_i(0) \right)^2 \rangle \tag{79}$$

where $\boldsymbol{r}_i(t)$ is the position of the i^{th} ion at time t. If the ions exhibit non-independent movement, there is a discrepancy between the self- and collective diffusion coefficients. The conductivity obtained through the implementation of an electric potential in experimental settings is indicative of the combined diffusion coefficient. Conversely, the self-diffusion coefficient can be determined through nuclear magnetic resonance experiments. It is worth noting that the statistical error associated with the calculation of the self-diffusion coefficient is lower than that of the collective diffusion coefficient. Therefore, if the two coefficients are anticipated to have comparable values, it is preferable to focus on the self-diffusion coefficient.

3.3.4.3. Radial Distribution Functions

The probability of locating a particle at a distance r from a designated particle is defined by the RDF, which is represented mathematically as $g(r)$ in equations [86-89]. The magnitude of the RDF is contingent upon the nature of the substance, thus exhibiting significant variations across solids, gases, and liquids. The term "bulk density" (ρ) is commonly used to denote the average density of a liquid at a given location [86]. The density of a liquid remains constant for a specific liquid. The local density, denoted as $\rho(r)$, is defined as the density of a liquid at a specific distance r from another molecule. This quantity is influenced by the structural characteristics of the liquid. The radial distribution function can be evaluated as follows:

$$g(r) = \frac{dn_r}{dV_r * \rho} \approx \frac{dn_r}{4\pi r^2 dr * \rho} \tag{80}$$

where dn_r is a function that determines how many particles there are inside a shell with thickness dr, whereby $dV_r \approx 4\pi r^2 dr$ is the volume of the spherical shell (with the approximation being true for tiny shell thicknesses). The local density and the bulk density are connected by the correlation function, $g(r)$. This formula can be used to determine the local density:

$$\rho(r) = \rho^{bulk} g(r) \tag{81}$$

Solid materials exhibit a characteristic crystalline arrangement, wherein constituent molecules exhibit periodic fluctuations in proximity to their respective lattice sites. Due to the highly specific structure over a significant distance, the occurrence of defects in solids is infrequent. The RDF of a solid exhibit's discrete peaks at values of σ, √2σ, √3σ. The broadened shape of each peak is attributed to the vibrational motion of particles around their respective lattice sites. The likelihood of locating a particle within the inter-peak regions is negligible, owing to the regular and optimal packing of molecules to occupy space. Each peak in the data corresponds to a coordination shell of the solid, wherein the first coordination shell comprises the nearest neighbors, the second coordination shell comprises the second nearest neighbors, and so forth.

3.3. Cluster Expansion

The Cluster Expansion method is a computational method used to characterise the energy or a similar scalar parameter of a system. It involves analysing the occupancy variables for each lattice position to determine the system's energy. On a lattice of this nature, the arrangement of atoms, encompassing the dispersion of atomic species (including vacancies), is subject to variation, and the energies associated with the ensuing arrangements may be promptly predicted [90, 91]. CE can also be defined as a type of mathematical model that can be considered as a generalisation of Ising models [91]. These expansions are designed to incorporate interactions between several particles, often known as many-body interactions. The CE methods are commonly employed in the disciplines of materials science, physical chemistry, and condensed matter physics to investigate materials that display substitutional disorder. This disorder refers to the situation in which certain crystalline sites can be inhabited by multiple types of atoms. In 1973, Van Baal [92] conducted groundbreaking research on the computation of phase diagrams that depict the order and disorder of a face-centred cubic (FCC) binary alloy. This was achieved through the use of the CE

formalism. Subsequently, CE has been effectively employed to investigate numerous crystalline materials that possess bulk characteristics, meaning that they exhibit periodicity in three dimensions.

In recent times, there have been significant advancements in the field of nanostructured materials, which have consequently led to the utilisation of CE in low-dimensional systems [93-96]. The understanding of structure-property correlations for surfaces and nanostructured materials is currently limited due to the constraints imposed by experimental approaches and the high computing expenses associated with investigating materials with low symmetry. Nevertheless, the ongoing rise in computational power have considerably diminished the expense associated with producing CE. As a result, it has become viable in recent times to employ CE for investigating low-dimensional systems at length scales that are relevant to experimental observations.

3.3.1. Universal Cluster Expansion

The CE approach is a method employed in the field of quantum mechanics to effectively address the issue of the BBGKY hierarchy problem. The BBGKY hierarchy, also known as the Bogoliubov–Born–Green–Kirkwood–Yvon hierarchy, encompasses a series of equations that describes the behaviour of a system consisting of numerous particles that interact with one another. The CE approach is specifically aimed at addressing this problem when solving for the quantum dynamics of interacting systems. The CE, also known as the high-temperature expansion or hopping expansion, refers to a power series expansion of the partition function in statistical mechanics. This expansion is centered around a model that consists of a combination of non-interacting 0-dimensional field theories within a statistical field theory framework.

The concept of CE was first introduced in the study conducted by Mayer and Montroll [97]. In contrast to the conventional perturbation expansion method, CE exhibits convergence within certain non-trivial regions even when the interaction is of minor magnitude. The cluster expansion refers to a mathematical technique used to expand the partition function of a statistical field theory. This expansion is expressed as a power series and is centered around a model consisting of a collection of non-interacting 0-dimensional field theories. Contemporary DFT methodologies have the

capability to accurately determine material properties, exhibiting varying degrees of precision contingent upon the quality of the approximations employed to account for exchange and correlation effects. However, the applicability of the standard DFT is limited to unit cells containing only a few hundred atoms. In order to represent a material with diverse atomic concentrations and crystal structures, a substantial quantity of significantly large supercells would be required if one were to approach the problem using an abrupt force. Hence, the procedure would be considered lethal. One potential approach to address this constraint is proposed by the CE [98] in conjunction with Monte Carlo simulations.

3.3.2. Effective Cluster Interactions

An optimised cluster expansion could produce a collection of efficient cluster interactions, which can then be employed in extensive Monte Carlo simulations for the examination of temperature-dependent order-disorder phenomena and phase segregation processes. In a fundamental lattice, multiple atoms, such as those of type A and B, are arranged to establish structure $\vec{\sigma}$, a periodic arrangement of A and B atoms. This configuration is described by the pseudo spin operator $\vec{\sigma}_q = \pm 1$, which has the value +1 if atom *A* is located on site q or -1 if that atom is *B*.

Energy $E(\vec{\sigma})$, associated with structure $\vec{\sigma}$ can be described by an expansion of cluster interaction and their respective interaction energies, J using the expression:

$$E(\vec{\sigma}) = J_0 + J_1 \sum_i \vec{\sigma} + \sum_{i>1} J_{ij}\sigma_i\sigma_j + \sum_{i>1>k} J_{ijk}\sigma_i\sigma_j\,\sigma_k + \cdots \qquad (82)$$

In this equation, the first term J_0, describes a constant, configuration independent contribution. The second term is concentration-dependent and is a sum over all N sites of structure $\vec{\sigma}$ with onsite energy J_i times the pseudo spin operator σ_i at each site i. Further terms describe the cluster interactions between multiple sites, for example, two-body interactions J_{ij} or three-body interaction J_{ijk}. They contain spin products $\sigma_i\sigma_j$ ... overall $\vec{f}$ vertices of a cluster times its effective cluster interaction energy J_{ij} summed up over all the possible ways that the cluster can be placed on the lattice of structure $\vec{\sigma}$.

In other words, the energy $E(\vec{\sigma})$ of structure $\vec{\sigma}$ is broken down into clusters with their associated effective interaction energies. The core issue of cluster expansion is to identify a universal set of interactions, J best-suited to describe a given model.

To accomplish this, it is useful to reformulate the (82) into the more compact form given by:

$$E(\vec{\sigma}) = \sum_{C_\varepsilon \dot{C}} J_C \prod_C (\vec{\sigma}) \tag{83}$$

The cluster expansion equation sums up the product of cluster', C's interaction energy, J_C with its correlation function:

$$\prod_C (\vec{\sigma}) = N^{-1} \sum_{i=1}^{N} \sum_{k \epsilon C} \prod_{v \epsilon f} \sigma_v \tag{84}$$

The expression represents the summation of all potential configurations in which a cluster C, consisting of $\vec{f}$ vertices, can be positioned on the N sites of the structure. The correlation function involves the summation of the spin product $\sigma_1 \ldots \sigma_f$ across all $\vec{f}$ vertices inside the cluster. In the current analysis, only clusters that exhibit distinct symmetry are taken into account. Additionally, clusters that are part of an expansion can be gathered using the vector $\vec{C} = \{C_1, \ldots, C_1\}$.

3.3.3. Inversion and Least Square Fitting

A training set of structures is required in order to locate the solution for the cluster expansion, which is to identify appropriate and effective cluster interactions. This training set includes m structures $\{\vec{\sigma}_1, \ldots, \vec{\sigma}_m\}$ with the corresponding energies $\vec{E} = (E_1, \ldots, E_m)^T$. Together with the cluster vector $\vec{C} = (C_1, \ldots, C_1)^T$, containing all n inequivalent clusters, and the corresponding effective cluster interactions $\vec{J} = (J, \ldots, J_n)^T$ the $m \times n$ correlation matrix is defined.

$$\overline{\prod} = \begin{pmatrix} \prod_{C_1}(\vec{\sigma}_1) & \cdots & \prod_{C_n}(\vec{\sigma}_1) \\ \vdots & \ddots & \vdots \\ \prod_{C_1}(\vec{\sigma}_1) & \cdots & \prod_{C_n}(\vec{\sigma}_m) \end{pmatrix} \tag{85}$$

The cluster expansion problem can be expressed using this correlation matrix as follows:

$$\bar{E} = \bar{\Pi}\vec{J} \tag{86}$$

Inversion is a simple method for defining the values of the effective cluster interactions $\vec{J}$.

$$\vec{J} = \bar{\Pi}^{-1}\vec{E} \tag{87}$$

Nevertheless, this methodology presents significant limitations. It is imperative that the quantity of clusters n is equivalent to the quantity of structures m present in the training set. Thus, this approach is devoid of any superfluous elements. In order to assess the energy of a novel configuration, it is necessary to incorporate an additional cluster into the existing cluster expansion. The feasibility of conducting an efficient ground-state search or a Monte Carlo simulation is hindered by this. An additional concern pertains to the uncertain nature of energy values associated with the training set structures, which are often subject to noise. Fitting the effective cluster interactions to noise through inversion may result in a perfect fit, but it does not accurately represent the underlying physics. A more optimal method for determining the efficacious cluster interactions involves employing a least-squares fitting technique on an expanded training set comprising m structures, where $m > n$:

$$\left(\vec{E} - \bar{\Pi}\vec{J}\right)^{T}\left(\vec{E} - \bar{\Pi}\vec{J}\right) \rightarrow min \tag{88}$$

3.3.4. Truncating Structures and Clusters

The first step in the cluster expansion involves the establishment of a defined pool of individuals. While the input structures impose limits on the number of distinct figures that can be symmetrically generated, it is possible for the list to contain an excess of figures beyond what is necessary for constructing a precise cluster expansion. The methodology involves selecting a specific "cut-off radius" and including all numerical values that are smaller than the chosen cut-off. In accordance with the general trend, wherein the significance of figures tends to diminish with an increase in the number of vertices, smaller cut-offs are designated for figures with a higher number of vertices, as noted in reference [97].

One crucial responsibility of a convergent computational experiment is to ensure the training set and its corresponding effective interaction energies are unbiased and free from any potential biases. In order to avoid any misinterpretation of the entire system due to an incorrect input selection, cluster expansion employs the selected figure set to appropriately match the energy of alternative structures. Novel structures can be devised and, if their energetic state is lower than that of the current ground state line, they can be subjected to DFT recalculations, resulting in a fresh collection of input structures. Subsequently, a fresh collection of numerical values is adjusted, and the process is reiterated. The utilisation of an iterative methodology confers the benefit of attaining a dependable ground state boundary alongside a set of figures that furnish precise outcomes. The fundamental concept involves the examination of structures and clusters that provide the most accurate representation of the limited set of energies available. The expansion incorporates compact many-body clusters, including but not limited to three-body and four-body clusters.

3.3.5. Genetic Algorithm

The utilisation of a genetic algorithm (GA) for the CE through a minimisation technique was initially introduced by Hart *et al.* [99]. This technique employs a binary string to denote the figure list. In instances where a figure is employed, it is assigned a value of 1, while in its absence, the value is 0. Furthermore, the depiction of interaction energies in this representation is in the form of a binary string. The amalgamation of two binary strings, encompassing the numerical values employed and the intermolecular forces between them, forms the hereditary "DNA" of a given solution, and the CVS furnishes an evaluation of the solution's feasibility. In comparison to alternative solutions, the present one exhibits a higher coefficient of variation of the sample, suggesting that it is comparatively less appropriate than its counterparts.

A population consisting of n_{pop} distinct solutions is generated, and the fitness of each solution is evaluated. A subset of the population consisting of the most physically capable individuals, where the number of individuals selected is denoted by n_{fit} ($0 < n_{fit} < n_{pop}$), are chosen to progress to the subsequent iteration process. The non-promising and non-fitting solutions are substituted by the offspring of the most viable parent solutions that have survived. Their ‘DNA’ is created by two different processes as sketched in Figure 10. Thus:

(i) In crossover, the ‘DNA’ of the ‘offspring’ is created by mixing the ‘DNA’ of two randomly selected ‘parent’ solution. Thereby the ‘DNA’ of one ‘parent’ solution is used up to the crossover point. After that point, the ‘DNA’ of the second ‘parent’ is used.

(ii) In mutation, a random binary bit of the ‘DNA’ string is flipped from one state to the other, i.e. $1 \dot{\Leftarrow} 0$ or $0 \dot{\Rightarrow} 1$.

Note, that one may replace all surviving ‘parent’ solutions with the ‘children’, as long as only the fittest ‘parent’ solutions are used to create them.

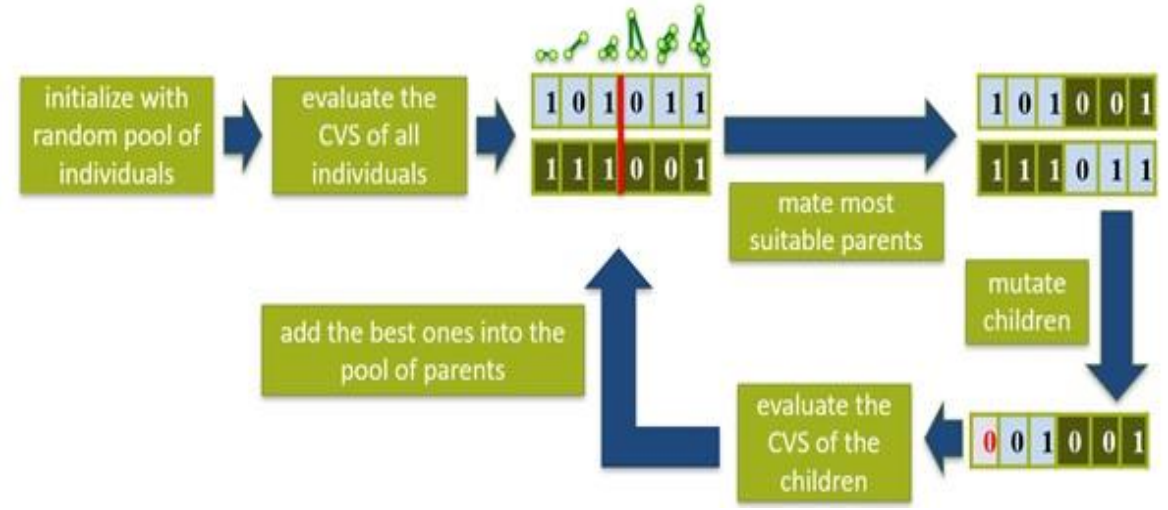

Figure 10: A diagram of the genetic algorithm [97]

An instance of crossover is proided. A "child" solution is produced by utilising two "parent" solutions that are distinguished by the colors red and green. The illustration depicts a mutation. A single bit within the binary sequence undergoes a spontaneous transition to its complementary state. Consequently, the evaluation of the fitness of the newly generated "population" can be reassessed, and the entire process is reiterated until a solution with a sufficiently low coefficient of variation of the sample is attained. This algorithm is guaranteed to identify the minimum value. However, it is currently ambiguous whether a local or global minimum has been ascertained. Consequently, it is recommended to conduct multiple independent cross-validation experiments and select the solution with the lowest coefficient of variation of the errors (CVS) as the ultimate solution. UNCLE code (to be presented later under the section on computer codes) has the capability to automate this process by executing multiple runs consecutively and retaining solely the optimal solution upon completion.

3.3.6. Interactive Optimisation

The method for selecting structures for the training set varies depending on whether the model exhibits a miscibility gap or consists of miscible constituents. In order to differentiate between the aforementioned models, the heats of formation $\Delta H_f(\vec{\sigma})$ are computed for all structures present in the training set. The term is characterised by:

$$\Delta H_f(\vec{\sigma}) = \frac{E_{DFT}(\vec{\sigma}) - \sum n_i(\vec{\sigma}) E^i_{DFT}}{\sum n_i(\vec{\sigma})} \tag{89}$$

wherein $E_{DFT}(\vec{\sigma})$ describes the DFT total energy of structure $\vec{\sigma}$, $n_i(\vec{\sigma})$, is the number of atoms of atomic species i contained in $\vec{\sigma}$, and E^i_{DFT} denotes the DFT total energy of the pure phase of atomic species i. The sums go over all type of atoms contained in structure $\vec{\sigma}$.

Models with miscible constituents have structures with negative $\Delta H_f(\vec{\sigma})$ (thermodynamically stable, ordered structures) while models with a positive $\Delta H_f(\vec{\sigma})$, where none of the ordered structures is thermodynamically stable and phase separation occurs, have a miscibility gap. Models including miscible constituents exhibit structures characterised by a negative $\Delta H_f(\vec{\sigma})$, indicating thermodynamic stability and the presence of ordered arrangements. Conversely, models with a positive $\Delta H_f(\vec{\sigma})$ lack thermodynamically stable ordered structures, leading to phase separation and the formation of a miscibility gap.

The iterative approach in UNCLE code originates with the inclusion of a certain number of independent and identically distributed structures, as determined by the user-defined parameter "Number of structures to initialise the first iteration" in the setup panel, into the training set. By default, the model's type is automatically determined after the initial iteration, prompting the method to transition to the appropriate mode of miscibility.

3.3.7. Miscible Constituents

In the case where a model consists of elements that are miscible, it is crucial to prioritise structures with energies that closely approximate the ground states. Specifically, structures with the lowest $\Delta H_f(\vec{\sigma})$ at a given concentration are of utmost significance. Consequently, the accuracy of the cluster expansion is expected to be highest for these particular structures. In order to achieve this objective, the structures

that have been predicted by the cluster expansion to possess more favourability (as indicated by a smaller $\Delta H_f(\vec{\sigma})$)) and have not yet been included in the training set are incorporated into the training set. The process is repeated iteratively until the cluster expansion no longer predicts any new structures that are more favourable than the ones currently included in the training set. At this stage, the cluster expansion has reached convergence, and among the various structures examined, those that exhibit thermodynamic stability have been discerned.

3.3.8. Miscibility Gap

In the event that the model undergoes phase separation, it can be observed that there are no stable ordered structures that exist beyond the two pure phases. Furthermore, it can be noted that all structures hold equal significance to the cluster expansion. Consequently, it is imperative that the process of selecting structures to be included in the training set is optimised to enhance the overall quality of the cluster expansion, regardless of their respective formation energies $\Delta H_f(\vec{\sigma})$.

The utilisation of the stochastic nature of the genetic algorithm is employed to evaluate the accuracy of the predicted energies of the structures through the cluster expansion method. Several cluster expansions are executed utilising an indistinguishable set of training data. The energies of all considered structures are then predicted by these multiple J's and a standard deviation of the predicted energies is evaluated. The structures exhibiting the greatest standard deviation are those that are characterised by the poorest cluster expansion description. Consequently, these items are incorporated in a step-by-step manner into the training dataset.

In this study, CE was used to predict stable $NaMnPO_4$ structures, from which the most stable structures with concentration Na_xMnPO_4 (x = 0.25, 0.5, 0.625, 0.75, and 0.825) were further investigated by calculating same properties discussed in the previous subsection 3.1.5.

3.4. Kinetic Monte Carlo

In section 3.2, we covered how the MD method may be used to simulate a classical many-particle system. This involves solving the equations of motion for all the particles in the system, allowing computation of statistical means of both stationary and

changing physical magnitudes. The Monte Carlo (MC) method is an alternative approach for modelling classical many-particle systems. It involves creating artificial dynamics based on random numbers. The utilisation of artificial dynamics in the MC approach hinders its applicability in identifying dynamical physical qualities in the majority of circumstances. However, it remains highly favoured for the analysis of static properties.

When applied to systems at thermodynamic equilibrium, Monte Carlo methods consider only positions, not velocities, as outlined by Ungerer [100]. The contribution of velocities to the partition function is determined analytically. Compared with equilibrium molecular dynamics, Monte Carlo methods allow building statistical ensembles at thermodynamic equilibrium. As they do not follow the evolution of a system with time, they do not address the dynamic properties of matter, such as diffusion, viscosity or thermal conductivity. In compensation, they may address important changes in the configuration space, such as the withdrawal or insertion of molecules in the system, which would be difficult to address with molecular dynamics. They are therefore the privileged way to simulate for example, sorption with the grand canonical ensemble or fluid phase equilibrium with the Gibbs ensemble.

Suppose that the probability of finding a system in state σ at time *t* is $P(\sigma, t)$ and that the rate of transitions per unit time from σ' to $W(\sigma, \sigma')$ is the equation of motion for *P* is the master equation given by:

$$\frac{\partial P}{\partial t} = \sum_{\sigma'} P(\sigma', t) W(\sigma', \sigma) - \sum_{\sigma} P(\sigma, t) W(\sigma, \sigma'). \tag{90}$$

kMC methods define the computational strategies utilised for solving the master equation. These algorithms operate by accepting or rejecting transitions based on probabilities that ensure the accurate development of a non-equilibrium system. The approach introduces an additional layer of abstraction beyond that of the molecular dynamic's method. The consideration of stochastic transition rates for slower events allows for the analysis of the impact of fast dynamical events. The transition rates are commonly expressed as the multiplication of an attempt rate and the likelihood of success each try. This probability is typically modelled as an exponential function that incorporates the energy barrier associated with the process. Every event *i* is assigned a rate r_i given by:

$$r_i = v_i \, exp(-E_i/k_B T), \tag{91}$$

The variable v_i represents a frequency pre-factor, which is commonly on the scale of a vibrational frequency (1013 s^{-1}) for surface processes. The symbol E_i represents the free energy barrier associated with the operation, whereas T denotes the absolute temperature. While the specific mechanism responsible for kinetic processes remains unknown, kMC simulations offer a practical solution by circumventing the need for explicit calculations of atomic trajectories. As a result, these simulations can be conducted over extended durations, ranging from seconds to hours or even days, depending on the specific requirements. The variable v_i in equation (91) essentially denotes the temporal scale of the most rapid process. In the molecular dynamics approach, this quantity is directly calculated, whereas in the kMC method, the exponential factor extends this timeframe to encompass the actual transitions. The kMC method presents significant advantages compared to the MD method. These advantages pertain to both the temporal span of the simulation and the number of atoms included within it. This is due to the fact that a substantial portion of the computational effort required in MD is allocated to the evolution of the system during infrequent occurrences.

The development of a model for a kMC simulation frequently finds value in utilising a corresponding classical or quantum MD simulation. This approach improves in the identification of significant physical processes and facilitates the estimation of pre-factors and kinetic barriers. The transition rates are specific to the processes under investigation and must be determined through direct computation, first-principles calculation, MD simulation, or inferred from experimental data. The capability to conduct comprehensive simulations within experimental timelines enables the examination of different parameterisations and the validation of kinetic models. Simulations of this nature are key components within many multiscale modelling methodologies.

A kMC simulation proceeds by tabulating all of the rates r_i and then advancing the system by a single configuration change chosen from all possible events. In the '*n*-fold way' algorithm [101], this is achieved by first computing the total rate $R = \sum_i r_i$. A number $\xi 1 \in (0,1)$ is then selected randomly, the integer *n* is identified such that:

$$\sum_{i=1}^{n-1} \frac{r_i}{R} < \xi \leq \sum_{i=1}^{n} \frac{r_i}{R} \tag{92}$$

and the system is updated by the execution of t. The system clock is subsequently increased by selecting a second random number $\xi_2 \in (0,1)$. As a result, the simulation time is advanced from t to $t + \Delta t$, where:

$$\Delta t = -\frac{ln\,\xi_2}{R}. \tag{93}$$

3.4.1. Sampling Through Markov Chains

A Markov chain is a stochastic process that undergoes transitions between a series of states according to certain probabilistic rules. The key property of a Markov chain is that the probability of transitioning to any particular state depends solely on the current state and time elapsed, regardless of how the system arrived at its current state. Sampling through Markov Chains refers to a broad category of computational techniques used to generate samples from a target probability distribution using Markov chain dynamics. The Markov chain is constructed such that its stationary distribution matches the desired target distribution. Two popular methods for sampling through Markov chains are Markov Chain Monte Carlo (MCMC) and Metropolis-Hasting's algorithm.

A sequence $X_1, X_2, \ldots$ of random items from a set is considered a Markov chain if the distribution of X_{n+1}, given $X_1, \ldots\ldots, X_n$, is dependent solely on X_n. The collection of values that the X_i can assume is referred to as the state space of the Markov chain. The transition probabilities of a Markov chain are considered stable if the conditional distribution of X_{n+1} given X_n remains constant regardless of the value of n. This is the primary type of Markov chain that is of interest in MCMC methods. The joint distribution of a Markov chain is determined by two factors: the initial distribution, which is the marginal distribution of X_1, and the transition probability distribution, which is the conditional distribution of X_{n+1} given X_n. It is worth noting that the transition probability distribution remains constant regardless of the value of n, thanks to the assumption of stationary transition probabilities. Individuals who are exposed to Markov chains in a standard stochastic processes course typically encounter instances where the state space is limited to a finite or countable set. If the state space is finite, denoted as $\{X_1, \ldots\ldots, X_n$, then the initial distribution can be represented by a vector $\lambda = (\lambda_1, .., \lambda_n)$,

where $Pr(X_1 = X_2) = \lambda_i$ for $i = 1,\ldots,n$. Similarly, the transition probabilities can be represented by a matrix P with elements p_{ij}, defined as $Pr(X_{n+1} = X_i|X_n = X_i|) = P_{ij}$ for $i = 1,\ldots,n$ and $j = 1,\ldots,n$. When the state space is countably unlimited, we can conceptualise an unbounded vector and matrix. However, the majority of Markov chains that are relevant in MCMC have a state space that is not countable. Consequently, it is not possible to conceptualise the initial distribution as a vector or the transition probability distribution as a matrix. It is necessary to regard them as an absolute probability distribution and a dependent probability distribution. The first one should be seen as an absolute probability distribution, whereas the second one should be seen as a probability distribution that is dependent on certain conditions.

3.5. Computer Codes

The different computer codes that were employed for different methods are briefly summarized in the next subsections.

3.5.1. VASP

The Vienna ab initio simulation package, also known as VASP, is a first-principle computational programme that is used to model materials on an atomic scale [102]. VASP provides an approximation to the solution to the many-body Schrodinger equation, and it does so within density functional theory, by solving the Kohn-Sham equations [44], or within the HF approximation, by solving the Roothaan equations [102]. Calculations involving the electronic structure and quantum-mechanical molecular dynamics are within the scope of VASP capability. The projector augmented wave method can describe the interaction that takes place between ions and electrons.

3.5.2. LAMMPS

The Large-scale Atomic/Molecular Massively Parallel Simulator (LAMMPS) is a molecular dynamics software [103] LAMMPS performs molecular dynamics simulations by integrating Newton's equations of motion for a group of interacting particles. A single particle may be an atom, molecule, or electron, a coarse-grained cluster of atoms, or a mesoscopic or macroscopic material clump. The code has various interatomic potentials implemented therein. The majority of the interaction potential models contained in LAMMPS are short ranged; with fewer long-range models included. LAMMPS makes use of neighbour lists to monitor surrounding

particles. The lists are tuned for systems with short-distance repulsive particles, so that the local particle density never becomes excessively high. LAMMPS is capable of calculating properties such as the cohesive energy density, thermal conductivity, viscosity, diffusion, and surface tension.

3.5.3. MedeA UNCLE

The MedeA Universal Cluster-Expansion (UNCLE) computing package [104], was used to perform all the CE calculations in this study. The code can forecast the ground states of systems with up to three elements and can conduct a full CE fit using a genetic approach. This approach was used to predict all new structures through intercalation. Monte Carlo simulations implemented in UNCLE code are used to derive results for temperatures T= 0, taking into account configurational entropies.

3.5.3.1. Canonical Ensemble

In the context of Monte Carlo simulations, the canonical ensemble is a specific ensemble used to simulate a system at constant temperature, volume, and number of particles. The canonical ensemble is essential for studying the statistical mechanics of systems that exchange energy with a heat bath, allowing the system to explore different configurations consistent with a fixed temperature. In a canonical ensemble, the conserved quantity is the concentration of each atom type within the simulation box. During each iteration, the positions of two atoms are randomly swapped. By doing this, the energy of the composition inside the box is altered, and the rate of transition can be expressed as:

$$P^{*}_{\sigma\sigma'} = \begin{cases} 1 & if \ \in < \ e^{-\left(E(\sigma')-E(\sigma)\right)/kT} \\ 0 & if \ \in > \ e^{-\left(E(\sigma')-E(\sigma)\right)/kT} \end{cases}$$

The random trajectory in phase space is iterated until a certain number of steps is reached or the variation in the system's energy falls below a predetermined numerical threshold.

3.5.3.2. Grand Canonical Ensemble

The grand canonical ensemble is a statistical ensemble defined by the system's volume V, temperature T, and chemical potential μ. The chemical potential is the energy required to add a single particle to the system without any heat exchange, and

its precise description will be provided later. The statistical ensemble is well-suited for analysing a physical system where particles and energy can go through the system's walls. In the grand canonical ensemble, both the number of particles and the energy of the system are allowed to fluctuate. This makes it particularly useful for studying systems in contact with both a heat reservoir and a particle reservoir, where particles can enter or leave the system and energy can be exchanged. The grand canonical ensemble provides a framework to calculate the probabilities of different particle and energy configurations, allowing for a deeper understanding of the system's behaviour.

In the grand canonical ensemble, the system is regarded as the focal crystal connected to an atom reservoir capable of migrating into the system. The Boltzmann distribution of the old and new systems is computed and compared to determine whether the transition occurs. The number of atoms in the simulation box must remain constant, necessitating the removal of one atom when another is introduced. The chemical potential μ governs the movement of atoms entering and exiting the box by thermodynamics. Increasing the chemical potential of a specific atom type in the system will reduce the number of atoms of that type. The rationale for this is that when an atom (e.g. atom A) is extracted from the system and another atom (e.g. B) is introduced, the chemical potential undergoes a change denoted as $\Delta\mu = \mu A - \mu B$, where μ_i represents the chemical potentials of the respective atomic species. The transition rate for changing a configuration σ into σ' is then defined as:

$$P^*_{\sigma\sigma'} = \begin{cases} 1 & if \ \in < \ e^{-(\Delta E - \Delta\mu)/kT} \\ 0 & if \ \in > \ e^{-(\Delta E - \Delta\mu)/kT} \end{cases}$$

If the decrease in energy of the system resulting from the atom exchange is greater than the change in chemical potential, the step will be authorised. Otherwise, it will be compared to the random number using the same method as explained above. Using the Ising model of the cluster expansion makes it straightforward to modify an atom type at a defined point. The atom is selected at random, and by altering its spin variable, the atom's kind is visibly modified. The subsequent stage is the computation of the energy of the simulation box utilising the ECIs, hence enabling the calculation of the energy difference, denoted as ΔE. The chemical potentials of the atom types denoted as $\Delta\mu$, are crucial initial parameters. Additionally, the Boltzmann factors are also defined.

The current study employed grand canonical simulations to investigate binary systems, with a specific limitation on the number of steps performed. In these simulations, the behaviour of the cluster expansion predicted systems was observed under varying conditions and interactions. The limitation on the number of steps ensured that the simulation remained computationally feasible while still capturing important dynamics. By utilising grand canonical simulations, the study aimed to understand the equilibrium properties and phase transitions of these predicted systems within the given constraints.

Chapter 4. Radom De-Intercalation of Maricite and Olivine Polymorphs of $NaMnPO_4$ Using Density Functional Theory

4.1. Introduction

Environmental issues such as air pollution and greenhouse gas emissions have led to significant efforts to build environmentally friendly energy storage technologies. Because of their high energy/power density, Li-ion batteries are widely used as energy storage systems for portable personal electronic devices such as cameras, cellphones, laptops, etc. [104] and has recently been used in electric vehicles and energy storage in the grid [3]. However, LIBs have a high production cost due to the limited Li reserves available in the Earth's crust, raising concerns about whether LIBs alone can meet the growing demand for large-scale energy storage. Considering the abundant Na supplies in the Earth's crust and their reaction mechanism resembling that of LIBs, Na-ion batteries are seen as promising alternatives to LIBs, offering improved safety, power, and energy density [28, 105, 106]. $NaMPO_4$ (M = transition metal) has become a focus of several studies on sodium-ion battery cathode materials, and this was prompted by the success of $LiMnPO_4$.

Maricite and olivine are two polymorphs of minerals based on phosphate. A minor distinction between these two polymorphs is that in maricite sodium ions occupy *4c* Wyckof sites while transition metals occupy *4a* Wyckof sites, whereas in olivine the reverse is true. The maricite phase appears to be inert electrochemically, while the olivine phase is reactive [107]. According to previous publications, various experimental investigations have been conducted on $NaMnPO_4$ [28]. Although some reports have been made, the formation of this material into a well-defined crystal structure and fabrication of it by making it electrochemically active remains a monumental effort. To gain a better understanding of the electrochemical activity of maricite and the structural stability of olivine $NaMPO_4$, previous studies used atomistic simulation methods to investigate the structural, electrochemical, and ionic transport properties of these systems [28, 38, 108, 109].

First-principles calculations based on density functional theory have become a powerful technique even in the field of sodium-ion and lithium-ion batteries research. It is capable not only of illustrating the electronic structure, but also of predicting the

electrochemical properties of electrode materials [109]. For example, the redox potential can be estimated with an error of 0.2 V without the use of experimental parameters [110]. Zhang *et al.* [28] reported the use of first-principles calculations to investigate the electrochemical performance of monoclinic $NaMnO_2$ for sodium ion batteries. They obtain a voltage window of 3.54–2.52 V and a theoretical reversible capacity of 136 mAh/g from their calculations. Additionally, the study also reported that the metallicity of monoclinic $NaMnO_2$ increases gradually during Na extraction [28].

Searching for suitable electrode materials that match the long-cycling stability criterion, that can store and distribute large amounts of energy quickly, is a vital step in the implementation of large-scale SIB applications. Given their similar intercalation chemistries, a variety of phases that allow Li ion (de)-intercalation as a Na + host have been studied, including layered metal oxides Na_xMO_2 [111-113] and polyanionic compounds [34, 114]. However, by employing traditional Na equivalents, performance equal to the high-rate capability and cycling stability reported for LIB electrodes is difficult to attain [9]. The most significant explanation is that Na^+ has a substantially larger radius size (r = 0.102 nm) than Li^+ (r = 0.076 nm), resulting in slower ion mobility and larger volume changes in its host structure [19]. Na^+ movement is slow in layered oxides generated by cubic closed-packed oxide arrays, and Na ion de-intercalation induces difficult phase transitions, resulting in rapid electrode deterioration [113].

In this chapter, the structural, thermodynamic, electrical, and mechanical properties of maricite and olivine $NaMnPO_4$ structures were investigated using density functional theory. To establish their stability and competency as possible cathode materials, deintercalated (Na^+ de-intercalated) systems were simulated. And to simulate the stability trend at 0 K, the formation energies, electronic densities of states, elastic constants, and thermodynamic properties were calculated. To understand their battery performance, voltage profiles were determined.

4.2. Computational Details

All calculations were performed using VASP software [115-118] based on density functional theory (DFT). Two different functionals were used to examine the $NaMnPO_4$ system, ie, PBE and PBEsol, PBE is a GGA functional widely used in DFT. While PBEsol is a revised version of the PBE functional, specifically designed to improve the

accuracy of calculations for solid-state systems by better describing equilibrium properties like lattice constants and bulk moduli. A spin-polarised generalised gradient approximation was used to solve the Kohn-Sham equations with the PBE and PBEsol exchange-correlation functional. The valence states of the Na (3s), Mn (3d, 4s), O (2s, 2p) and P(3p) orbitals are considered. Furthermore, considering the strong onsite Coulomb repulsion among Mn 3d electrons, the Hubbard correction term U (i.e., GGA + U) was also employed. The effective U value of 5.0 eV for Mn was used in this work, which is selected based on previous work [119] and verified by our test calculations. As the ground state energies of the compound obtained from different spin configurations are very close, the results presented herein are based on the ferromagnetic configuration. The Monkhorst-Pack scheme with 5 × 5 × 7 k point mesh was used. The cut-off energy for the expansion of the plane wave function was 560 eV. The atomic positions and the lattice parameters were considered and fully relaxed when the final force on all the ions is less than 0.01 eV/Å. A similar process was followed when investigating de-intercalated maricite and olivine $Na_{1-x}MnPO_4$ (x = 0,25, 0.5, 0.75 and 1).

4.3. Maricite and Olivine $NaMnPO_4$

4.3.1. Structural Properties

Compared to $LiMnPO_4$, $NaMnPO_4$ has two structural variants, namely, maricite-type and olivine-type [106, 120]. Both structures have the same phosphate group framework as the space group Pnma. The distinction is due to the preferred occupancy of two octahedral sites by Na^+ and Mn^{2+} ions in the olivine structure, as shown in Figure 13 (a), while in the maricite-type structure, the opposite is true (see Figure 13 (b)). Na+ containing octahedral sites share edges and create zigzag chains along the b axis in the olivine structure [120]. The calculated lattice parameters are in good agreement with the experimental values, indicating that the calculation methods and models are reasonable, and the calculated results should be authentic. Therefore, the lattice parameters a, b, and c are consistent with the results of the literature [121], [16], where the stability of the maricite and olivine structure of $NaMnPO_4$ was evaluated using experimental methods and this can be seen in Table 1.

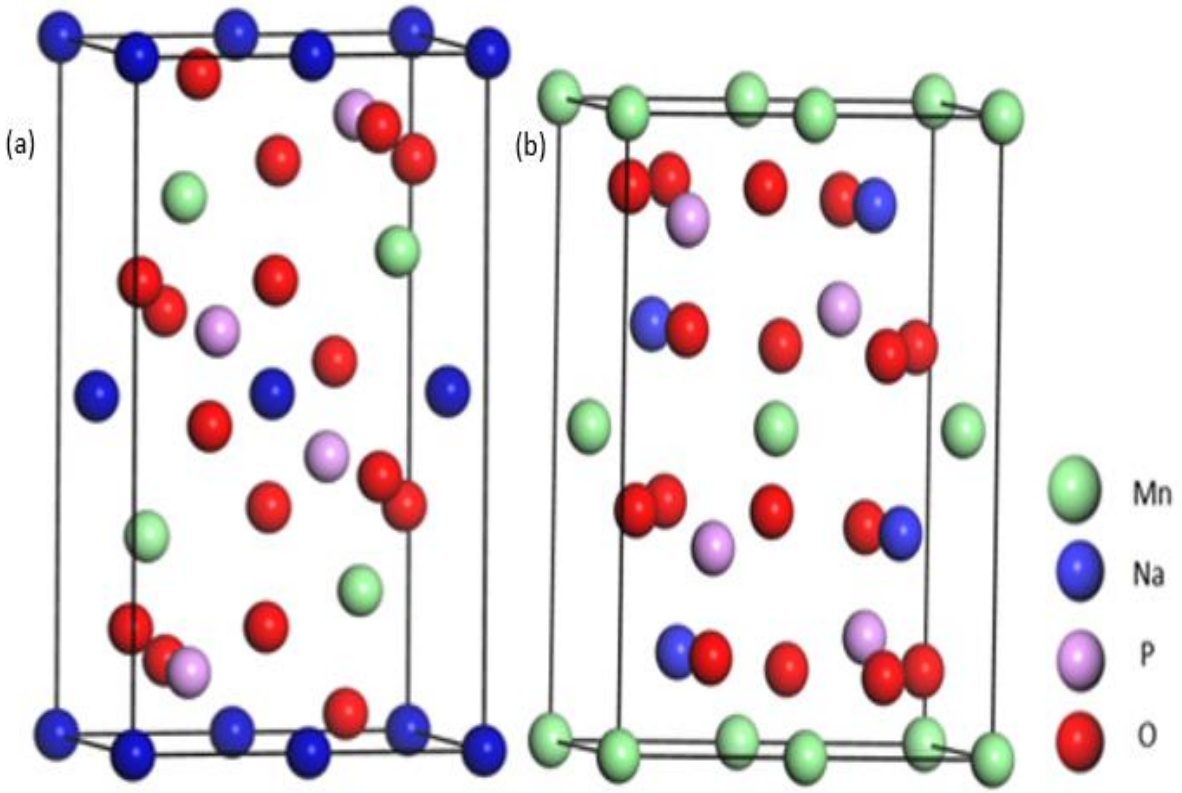

Figure 11: Schematic crystallographic structures of (a) olivine and (b) maricite $NaMnPO_4$.

The comparison of lattice parameters from the relaxation structure using different functionals and previously experimental results are listed in Table 1. The use of different functionals was conducted to determine which is more accurate. The calculated lattice parameters, a, b, and c are within 2% of the deviation from the experimental results, and the volume deviation was found to be within 5% of the deviation from the reported results. The differences between the calculated and experimental values are found to be small, indicating that the theoretical method applied is moderate. When the three different functionals were compared, PBEsol underestimated all the lattice parameters, while PBE and PBE+U overestimated the lattice parameter a. Even though the lattice parameter a is overestimated by PBE+U, the results gave a total volume that is closest to the experimental value. Hence, all the subsequent results of the de-intercalation process presented in this work are based on the GGA PBE+U hybrid functional.

Table 1: Calculated lattice parameters of maricite and olivine $NaMnOP_4$ and previously reported experimental results.

Materials	Method	a (Å)	a (Å) dev (%)	b (Å)	b (Å) dev (%)	c (Å)	c (Å) dev (%)	Volume ($Å^3$)	V ($Å^3$) dev (%)
Maricite $NaMnPO_4$	PBEsol	9.004	0.924	6.904	0	5.043	1.369	308.276	0.949
	PBE	9.093	0.055	6.864	0.579	5.091	0.430	317.796	3.936
	PBE+U	9.107	0.209	6.878	0.377	5.101	0.235	319.507	0.415
	Exp [122]	9.088	-	6.904	-	5.113	-	320.84	-
Olivine $NaMnPO_4$	PBEsol	9.904	5.927	5.955	5.790	4.894	1.825	288.645	12.99
	PBE	10.090	4.160	6.055	4.208	4.946	0.782	302.192	8.907
	PBE+U	10.693	1.567	6.421	1.582	5.053	1.364	346.995	4.599
	Exp [37]	10.528	-	6.321	-	4.985		331.74	-

4.3.2. Electronic Properties

For both maricite and olivine, the electronic structure of $NaMnPO_4$ is investigated using the spin-polarised density of states as shown in Figures 12 and 14, respectively, comparing the three functionals. The DOS of a system describes the number of states per energy interval of each level available. The DOS indicates how densely packed the quantum states are in a system. For maricite, the electronic structure shown in Figure 14 shows that $NaMnPO_4$ is a semiconductor with band gaps of 1.510 eV, 1.297 eV and 3.321 eV for PBE, PBEsol, and PBE+U, respectively. The band gaps of PBE and PBEsol are found to be very small compared to the literature value of 3.062 eV [123], while the value of PBE + U is found to be consistent with the experimental results, with 8 % deviation. The Mn-3d and O-2p orbitals are the major compositions for both the valence and conduction bands. Hybridisation between Mn-3d and O-2p orbitals is clearly observed for PBE+U, indicating that the Mn-3d and O-2p orbitals play a crucial role in charge transfer. There is a small contribution of P-3p in both the valence and conduction bands, but the contribution is observed far from the Fermi level. For isolated Na atoms, the electronic states of Na-2p orbitals are not found near the Fermi level, which shows the high ionisation of Na atoms. Moreover, the PBE and PBEsol functionals show three Mn-3d spin-down splitting peaks at 1.8 eV, 2.2 eV, and

2.9 eV. PBE+U is showing one peak at 5.1 eV. GGA + U also shows O-2p much closer to the Fermi energy than PBE and PBEsol. From the review of the literature, we could not find any theoretical calculation of the electronic properties of maricite $NaMnPO_4$.

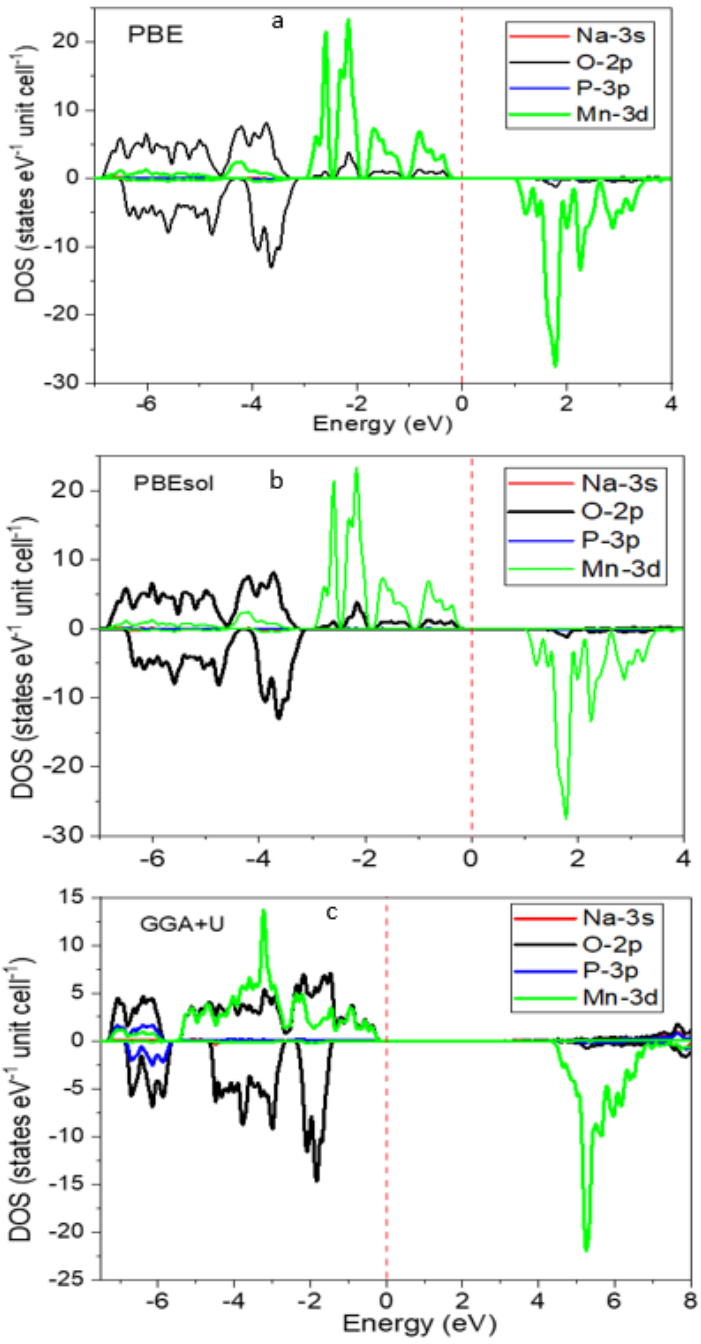

Figure 12: Spin-polarised band structure and DOS near Fermi level for $NaMnPO_4$ (a) PBE; (b) PBEsol and (c) GGA+U. The Fermi level is set to 0 eV and is shown by the dashed lines. In the DOS curve, the positive and negative values refer to the DOS of the spin-up and spin-down states.

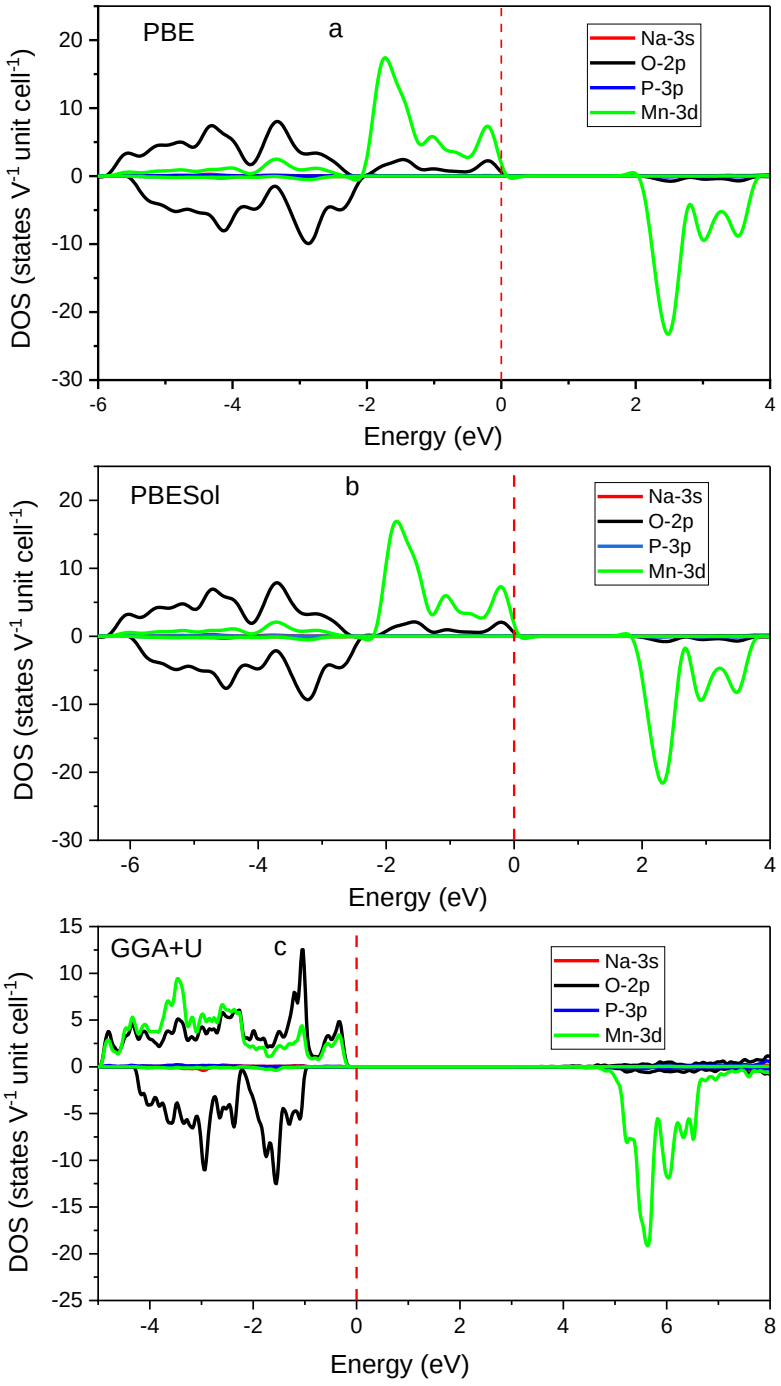

Figure 13: Spin-polarised band structure and DOS near the Fermi level for olivine $NaMnPO_4$ (a) PBE; (b) PBEsol and (c) GGA+U. The Fermi level is set to 0 eV and is shown by the dashed lines. In the DOS curve, the positive and negative values refer to the DOS of the spin-up and spin-down states.

For olivine, the electronic structure shown in Figure 13 shows that $NaMnPO_4$ is a semiconductor with band gaps of 2.166 eV, 1.939 eV and 3.363 eV for PBE, PBEsol and PBE+U, respectively. The band gaps of PBE and PBEsol are found to be very low

compared to the literature value of 3.062 eV [123], while the value of PBE + U is found to be consistent with the experimental results, with 8 % deviation. The Mn-3d and O-2p orbitals are the major compositions for both the valence and conduction bands. DOS hybridisation between Mn-3d and O-2p orbitals is evident in PBE+U, complementing findings made in maricite. This observation illustrates the significant involvement of the Mn-3d and O-2p orbitals in facilitating charge transfer. The presence of P-3p is detected in both the valence and conduction bands, although in a small capacity, and its contribution is mostly recognised at a considerable distance from the Fermi level. The electronic states of the Na-2p orbitals in isolated sodium atoms are not observed to be close to the Fermi level, indicating a significant degree of ionisation in sodium atoms. Additionally, it is seen that the PBE and PBEsol functionals exhibit three distinct peaks in the spin-down splitting of the Mn-3d orbitals, located at energy values of 2.2 eV, 2.8 eV, and 3.7 eV. The PBE+U method exhibits two distinct peaks at energy levels of 5.8 eV and 6.0 eV. The GGA+U method exhibits a significantly higher contribution of O-2p orbitals in close proximity to the Fermi energy compared to the PBE and PBEsol approaches [118].

4.4. Sodium De-intercalated Maricite and Olivine $NaMnPO_4$

Compared to lithium oxide-based systems, lithium transition-metal phosphates of olivine type, such as $LiFePO_4$, are often characterised by improved cycle and thermal stability as cathode materials [124-126]. Furthermore, the volumetric mismatch between olivine structured $LiFePO_4$ and de-lithiated $FePO_4$ is 6.9%, but Na analogues have a mismatch of 17.58% [127]. Such a large volume shift has a negative impact on structural stability during cycling. In this context, it is critical to look for new Na host materials that promote viable Na^+ (de)-intercalation while requiring low-volume change. Another major source of concern is the cost of electrode materials designed for SIBs. Even though Na ions are inexpensive charge carriers, many reported cathode materials still rely on redox centres that are scarce and/or need hazardous transition metal components such as cobalt [111, 128], nickel [128], vanadium [129], and chromium [113]. As a result, the benefits of SIBs in terms of cost and sustainability are greatly diminished. It is critical for large-scale applications to create electrode materials based on Earth-abundant transition metals, preferably Fe and Mn being the most prevalent transition metal in the Earth's crust. Recently, $NaMnPO_4$ has attracted the attention of numerous researchers as a cathode matrix for SIBs, inspired by the $LiMnPO_4$ structure. Compared to $LiMnPO_4$, $NaMnPO_4$ has two structural variants: maricite-type and olivine-type [120, 130]. Previous research studies reported that maricite is the most thermodynamically stable phase compared to olivine. The maricite phase is found to be 0.016 eV/formula unit more stable than olivine [131, 132]. However, because of the edge-sharing MnO_6 octahedrons that share edges and the lack of cationic channels for Na diffusion, this material is unlikely to be used in the construction of sodium ion batteries.

In this section, systematic first-principles calculations were carried out to investigate structural, electronic, mechanical, and electrochemical properties of de-intercalated maricite and olivine $NaMnPO_4$, focusing on energetics such as the sodium ions that are removed from the systems.

4.4.1. Structural Properties

Next, we investigate the Na extraction, which is the de-intercalation processes, in the $NaMnPO_4$, this process is used to simulate the charging process. For this process, we only considered the calculated results obtained from the use of GGA+U as indicated

previously that this functional reproduced experimental structural parameter well. The use of GGA+U is also supported by the work reported by Chakrabarti *et al.* [133] Li de-intercalation voltage for transition metal composites is better estimated with the DFT GGA + U method corrected. This is due to the fact that in transition metal composites, there exists a strong Coulomb repulsion between spin-up and spin-down electrons in the localised d orbital of transition metal atoms that is not considered by standard DFT (GGA method)-based calculations. This discrepancy causes a self-interaction error in the calculation, which underestimates the band gap and Li de-intercalation voltage. This was also the case in this work, where we noted that the band gap is underestimated using PBE and PBEsol. In the GGA + U method, Hubbard U considers this intra-site strong Coulomb repulsion while other states are simulated in the plain GGA scheme as implemented in the original DFT. In this way, both the localised and delocalised orbitals are described by the same theory. Shown in Figures 14 and 15 are the models showing the de-intercalation process of Na ions and their calculated structural parameters are listed in Table 2 together with their deviation from the initial maricite structure. During every extraction stage, the Na atom is removed from the original binding site, and the changed structure relaxes.

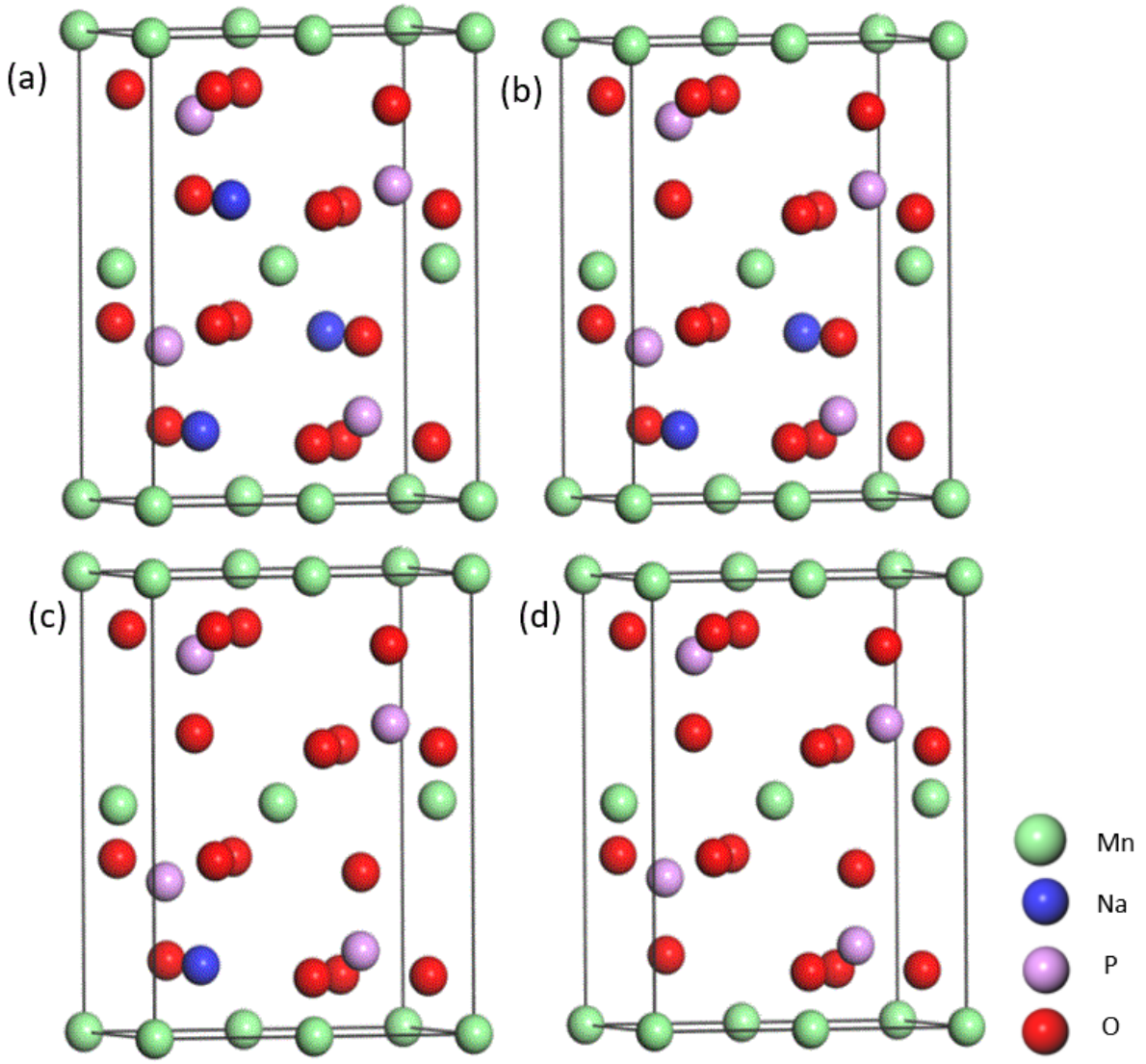

Figure 14: Crystallographic structures of maricite (a) $Na_{0.75}MnPO_4$, (b) $Na_{0.5}MnPO_4$, (c) $Na_{0.25}MnPO_4$, (d) $MnPO_4$ during Na extraction after relaxation.

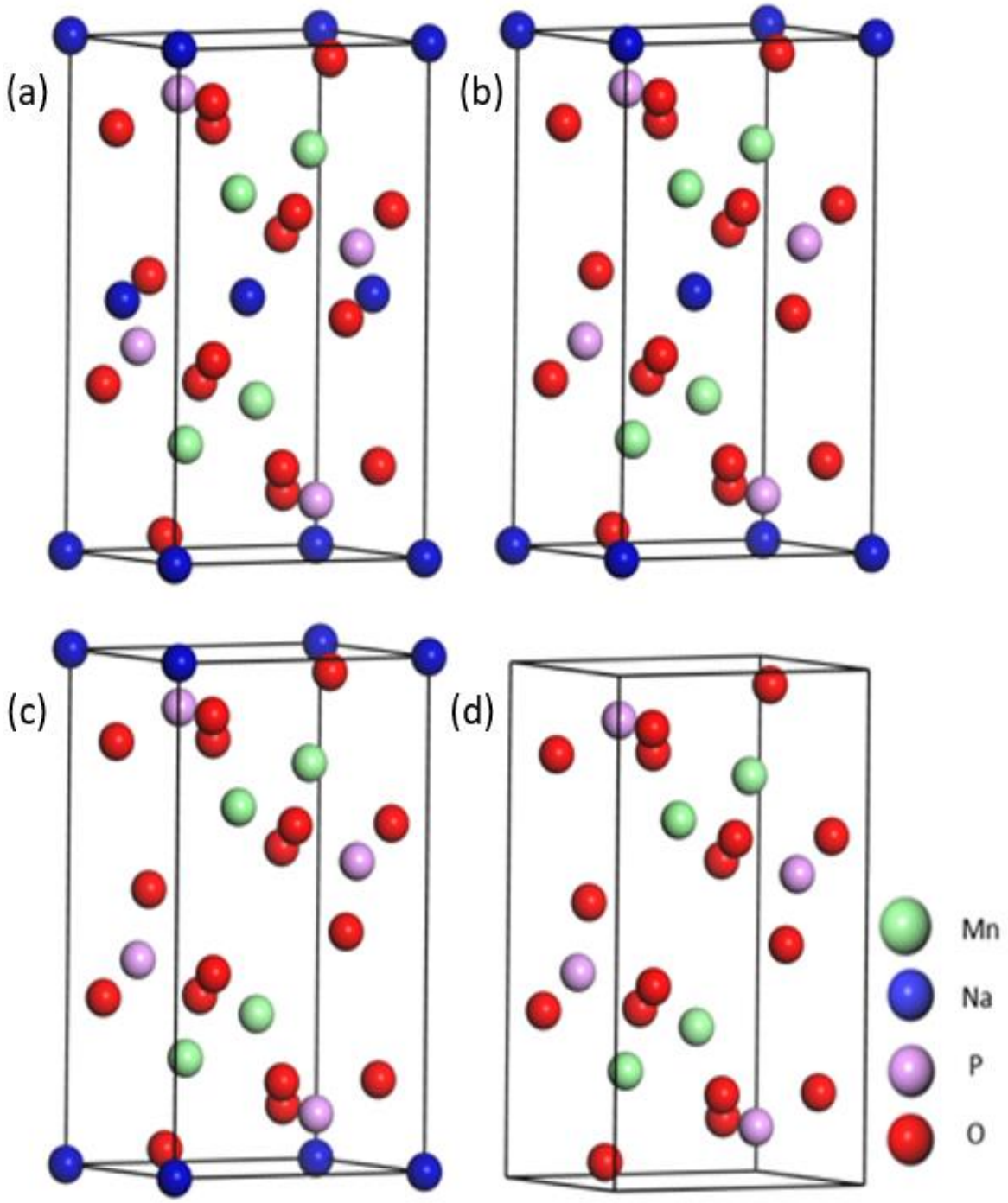

Figure 15**:** Relaxed crystallographic structures of olivine (a) $Na_{0.75}MnPO_4$, (b) $Na_{0.5}MnPO_4$, (c) $Na_{0.25}MnPO_4$, (d) $MnPO_4$ during Na extraction.

Table 2: Calculated lattice parameters of de-intercalated Na_xMnOP_4 polymorphs and their deviations from the initial structure.

Phase		a (Å)	b (Å)	c (Å)	V (Å^3)	V deviation (%)	a deviation (%)	b deviation (%)	c deviation (%)
Maricite	Na_1MnOP_4	9.107	6.878	5.101	319.507	—	—	—	—
	$Na_{0.75}MnO_4$	9.056	6.985	5.121	323.913	10.137	0.560	1.556	0.392
	$Na_{0.5}MnO_4$	8.924	6.935	5.043	312.080	9.766	2.009	0.829	1.137
	$Na_{0.25}MnO_4$	8.753	6.834	4.950	296.144	9.268	3.887	0.640	2.960
	$MnPO_4$	8.632	6.666	4.817	277.168	8.674	5.216	3.082	5.568
Olivine	Na_1MnO_4	10.693	6.421	5.053	346.995	—	—	—	—
	$Na_{0.7}MnO_4$	10.537	6.325	5.066	337.644	2.7	1.5	1.5	0.3
	$Na_{0.5}MnO_4$	10.350	6.231	5.062	326.453	3.3	1.8	1.5	0.1
	$Na_{0.25}MnO_4$	10.082	6.166	5.028	312.509	4.3	2.6	1.0	0.7
	$MnPO_4$	9.874	5.057	4.918	294.152	5.9	2.1	1.8	2.2

The lattice parameters and changes in cell volume of the olivine and maricite Na_xMnPO_4 systems during Na extraction are listed in Table 2. During the Na extraction process of Na_xMnPO_4 (x = 1, 0.75, 05, 0.25, 0), the lattice parameter and the changes in cell volume are less than 7% and 5% for maricite and olivine, respectively, indicating that structural stability is well maintained throughout the various stages. During the first extraction, it was noted that the lattice parameter along the b direction increased from 6.878 Å to 6.985 Å, causing the change in the structural volume from 319.507 Å^3 to 323.913 Å^3 for maricite. Apart from the volume deviations, the largest lattice parameter was obtained for the fully Na extracted $MnPO_4$ along the c direction. Furthermore, after the extraction of the fourth Na atom (x = 0), where the olivine structure is fully de-intercalated, the cell volume changed by 5.9%, which was found to be higher than the other concentrations. It is worth noting that this volume change is not large enough to cause irreversible destruction of the structure. The results for a fully de-intercalated structure are found to have a lower deviation percentage than those previously reported by Fang *et al.* [127]. The study reported on the high-performance olivine $NaFePO_4$ microsphere cathode synthesised by the aqueous electrochemical displacement method, with the volumetric mismatch between olivine

structured $LiFePO_4$ and de-lithiated $FePO_4$ being 6.9%, while Na analogues were found to have a larger mismatch of 17.58% [10].

4.4.2. Formation Energy and Voltage

To understand the formation of solid solutions of Na removal from Na_xMnPO_4, the formation energy per unit of formula was calculated using the expression:

$$FE = E(Na_xMnPO_4) - x * E(NaMnPO_4) - (1-x)E(MnPO_4) \quad (94)$$

$E(Na_xMnPO_4)$ is the energy of the partially de-intercalated material, whereas $E(NaMnPO_4)$ and $E(MnPO_4)$ are the energies of the pristine and totally de-intercalated structures, respectively. To understand the formation of solid solutions of Na removal in Na_xMnPO_4, the formation energy per unit of formula was calculated using the expression in equation (88). The calculated formation energy of de-intercalated states is negative for all the systems, with values -53.445 eV, -40.131 eV, -26.867 eV, and -13.577 eV for maricite $Na_{0.75}MnPO_4$, $Na_{0.5}MnPO_4$, $Na_{0.25}MnPO_4$ and $MnPO_{,4}$ respectively. Thus, the findings predict a solid solution upon de-intercalation. For olivine, the formation energies for different systems are calculated to be -60.12 eV, -45.291, -30.153 and 0 for Na_1MnPO_4, $Na_{0.75}MnPO_4$, $Na_{0.5}MnPO_4$, $Na_{0.25}MnPO_4$ and $MnPO_4$, respectively. We observe that the formation energy of the intercalation stages is negative for all materials, with the exception of the last stage where x = 0. The negative value of the formation energies symbolises the prediction of a solid solution possessed by these materials.

The energy change of the individual Na atom at every de-intercalation stage of the $NaMnPO_4$ structure is calculated using analytical expression:

$$\Delta E = E\left(Na_{x-y}MnPO_4\right) + yE(Na) - E(Na_xMnPO_4) \quad (95)$$

where ΔE is the change in energy of the process that $y(Na)$ atoms are extracted between the $NaMnPO_4$ layers, $E(Na_{x-y}MnPO_4)$, $E(Na)$ and $E(Na_xMnPO_4)$ are the energy of $(Na_{x-y}MnPO_4)$, Na metal and Na_xMnPO_4 respectively.

Accordingly, the cathode voltage is calculated as follows:

$$U = {}^{\Delta E}/_{ye} \quad (96)$$

The cathode voltage is U, the absolute value of the electron charge is e, and the number of Na atoms extracted is y.

The average cathode voltage of both maricite and olivine at each de-intercalation stage was calculated using equations (75) and (76), plotted in Figure 16. The voltage value ranges from 5.132 V to 4.655 V for maricite, which implies that the voltage window is suitable for use as SIB cathodes. The calculated voltage window was found to be higher than that reported in the literature ranging from 4.5 V to 2.5 V [134]. For olivine, the voltage or potential required to remove Na ions from Na_xMnPO_4 ranged between 3.997 and 3.848 V. Furthermore, the $Na_xMn_2O_4$ potentials are consistent with previously calculated data for the Mn-based isostructural olivine $LiMnPO_4$ [135]. These findings suggest that maricite and olivine can be effectively used as cathodes in SIBs because of their suitable voltage windows. Furthermore, the similarity in potentials between $Na_xMn_2O_4$ and other Mn-based isostructures further supports their potential as cathode materials.

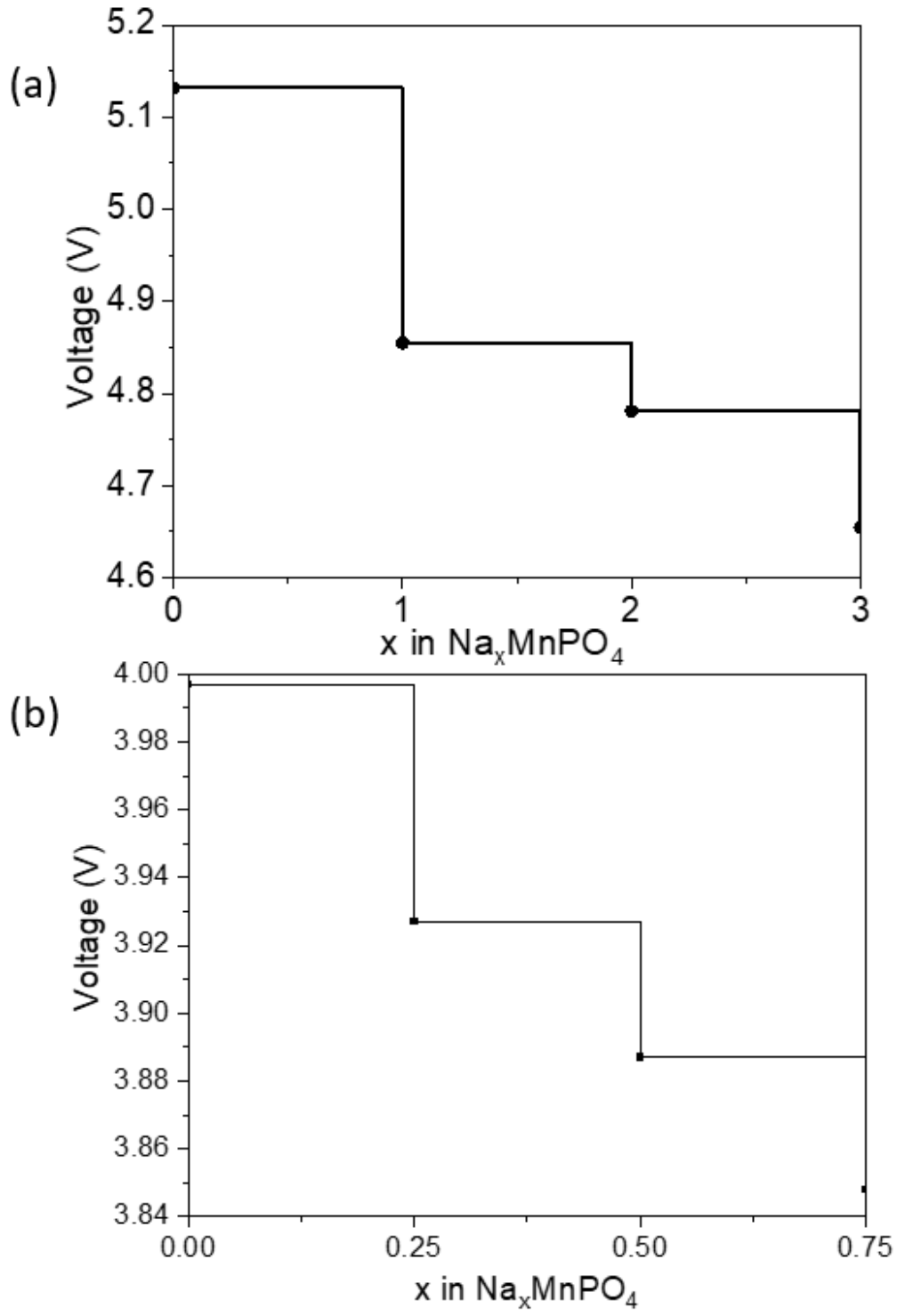

Figure 16: De-intercalation potentials (V) for Na_xMnPO_4 (x=1, 0.75, 0.5, 0.25, 0) (a) maricite and (b) olivine.

4.4.3. Electronic Properties

Figure 17 shows the spin-polarised partial density of the states of the Mn 3d, O 2p, and P 3p states for the maricite system. The calculated electronic structures suggest that Na_1MnPO_4 is a magnetic insulator with a gap of 3.321 eV. The large band gap demonstrates the poor electronic conductivity existing in $NaMnPO_4$, which can be resolved by carbon coating and low temperature synthesis routes. For concentration x = 3, 2, 1 and 0 in Figure 17, it is observed that there are small multiple noticeable peaks near the Fermi level in the PDOS plots. This shows the increased metallicity of the material during the de-intercalation process. In all stages of de-intercalation, the valence band is dominated by O-2p states near the Fermi level and the conduction band is dominated by Mn-3d states near the Fermi level. Moreover, there is a notable shift towards the Fermi energy of the Mn-3d spin-down peaks in the conduction band; this shifting is also accompanied by the splitting of the same peak during the $Na_{0.5}$ and $Na_{0.25}$ de-intercalation stages. During all de-intercalation stages, it can be noted that O-2p is up- and down-spin polarised, as observed in the figure.

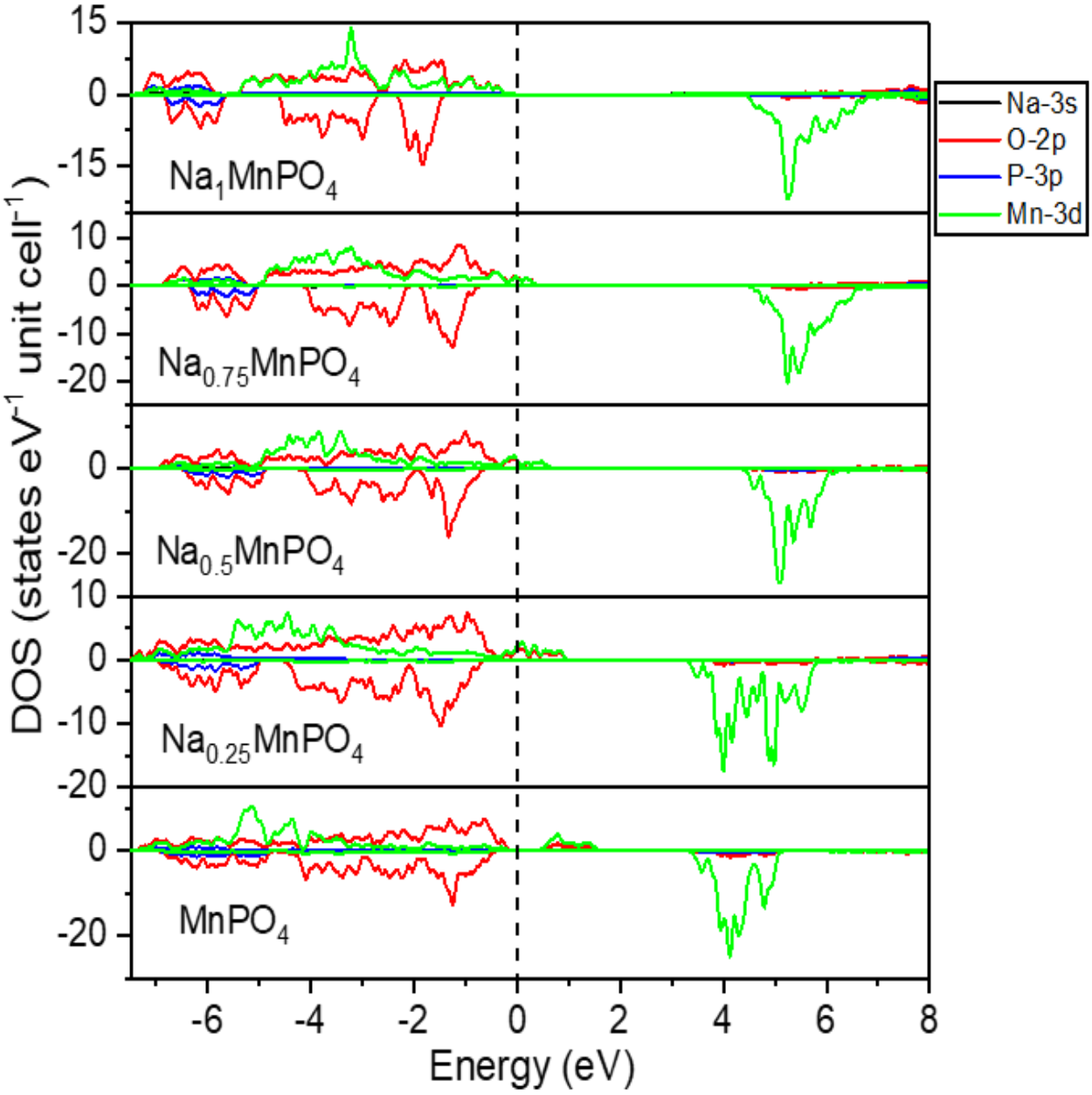

Figure 17: Spin-polarised DOS near Fermi level of maricite Na_xMnPO_4 (x=1, 0.75, 0.5, 0.25, 0). The Fermi level is set to 0 eV and is shown by the dashed lines. In the DOS curve, the positive and negative values refer to the DOS of the spin-up and spin-down states.

We calculated the densities of states of magnetic olivine Na_xMPO_4 systems in the magnetic spin-polarised state to elucidate their electronic conductivity. The total and orbital projected partial DOSs are separated, generating a band gap near the Fermi level as shown in Figure 18. To understand the electronic conductivity of materials, concepts of Fermi level and band gaps are required. The Fermi energy is employed

as the energy scale's zero, and the energy band gaps for both spin-up and spin-down states were observed. The states near the Fermi level are mostly Mn 3d and O 2p, with just minor contributions from the Na and P states. Due to the smaller band gap, it can be concluded that the spin-up states are primarily insulators (in good accordance with theoretical data [135]), while the spin-down states are semiconductors. The partial DOS of de-intercalated olivine Na_xMPO_4 structures are presented in Figure 18. For the initial structure Na_1MnPO_4 the DOS are separated, forming a band gap near the Fermi level. The system was found to be a magnetic insulator with a direct band gap of 3.363 eV. The valence band (spin-up) maximum is located near (0.00 0.00 0.00), at -0.203 eV with respect to the Fermi level. The conduction band (spin-up) minimum is located near (0.00 0.00 0.00), at 3.161 eV with respect to the Fermi level. The centre of the gap is located at 1.479 eV with respect to the Fermi level.

During extraction, the Fermi level is located on the Mn 3d and O 2p bands, except for the $MnPO_4$ system, suggesting that some valence band states jump the Fermi level barrier to the conduction band. The energy band gap value and the location of the Fermi level suggest that $Na_{0.75}MnPO_4$ is semi-metallic, resulting in good electrical conductivity in Na-ion batteries. This metallicity increases as the number of Na atoms extracted increases. However, interestingly, a fully de-intercalated $MnPO_4$ system was found to be a magnetic semiconductor with a direct band gap of 0.194 eV. The maximum valence band (spin-up) is located near (0.00 0.00 0.00), at -0.100 eV with respect to the Fermi level, whereas the conduction band (spin-up) minimum is located near (0.00 0.00 0.00), at 0.094 eV with respect to the Fermi level. The centre of the gap is located at -0.003 eV with respect to the Fermi level. The Fermi energy is used as the zero of the energy scales (Spin-down). It was found that Mn 3d had moved from ~5.1 eV to ~3.7 eV. Generally, it was noted that the partial density of states reveals that the Mn 3d states contribute significantly to both the conduction band and the valence band, whereas the O 2p states contribute more to the valence band. Also, there are minimal contributions from the Na and P states.

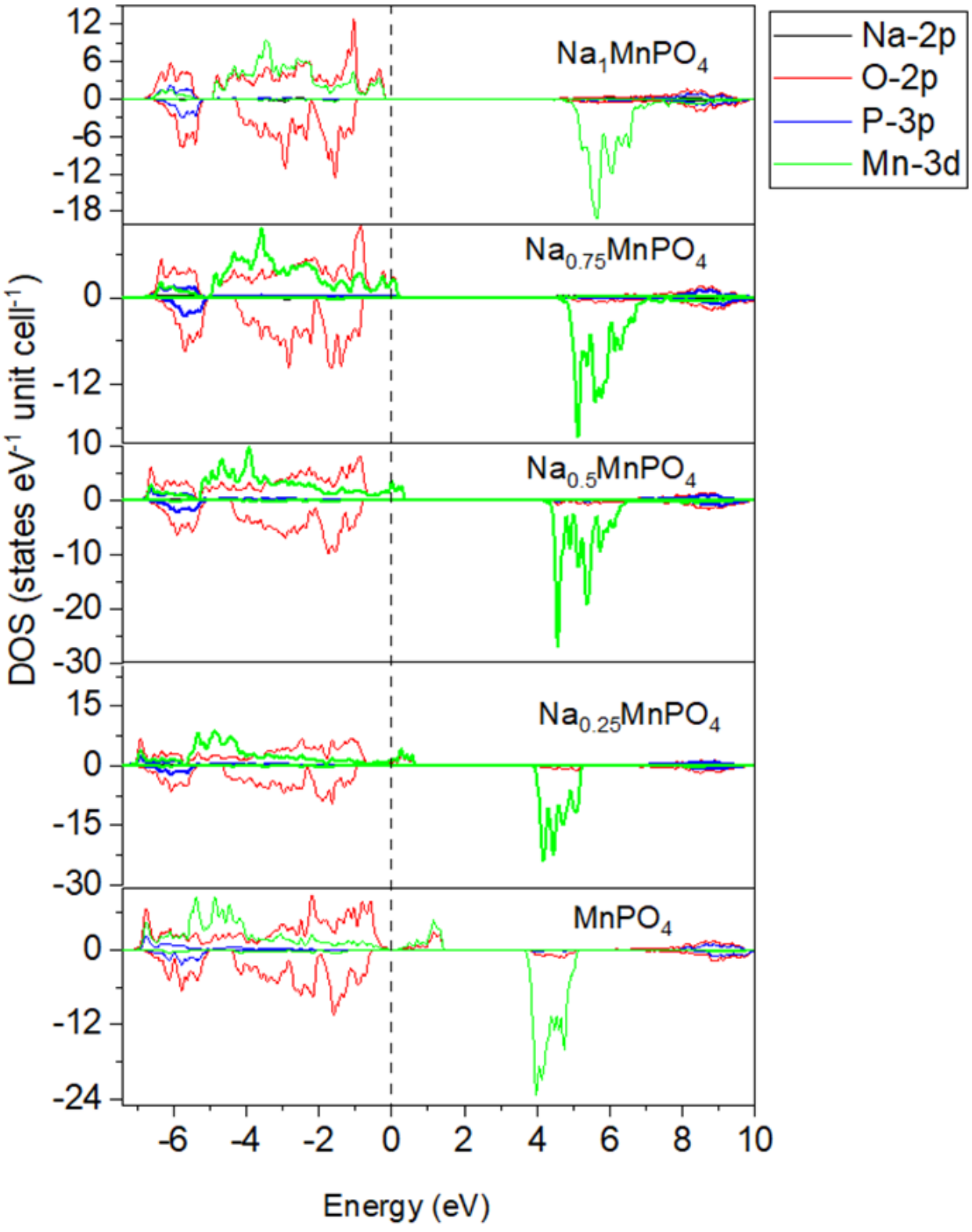

Figure 18: Spin-polarised DOS near Fermi level of olivine Na_xMnPO_4 (x = 1, 0.75, 0.5, 0.25, 0). The Fermi level is set to 0 eV and is shown by the dashed lines. In the DOS curve, the positive and negative values refer to the DOS of the spin-up and spin-down states, respectively.

4.4.4. Mechanical Properties

4.4.4.1. Elasticity

Elastic characteristics are related to fundamental solid-state features that include the equation of state, interatomic potentials, lattice constants, and phonon spectra. They include critical information about the strength of the material against externally imposed strain and serve as stability criteria in the research of structural mechanical stability alterations [67, 68]. Elastic constants of a material, in general, describe its response to the external applied strain required to maintain a given deformation and provide useful information about the material's strength, as characterised by the bulk modulus (B), shear modulus (G), Young's modulus (E), Poisson's ratio (v), and shear anisotropy factor (A). Born [69] pioneered the computation of elastic constants. The Born stability criteria are a set of conditions on the elastic constants (C_{ij}) that are connected to the second-order shift in a crystal's internal energy during formation.

However, it was later discovered that the Born stability ranges are sensitive to the choice of coordinates. Elastic constants for maricite and olivine were calculated using a Taylor expansion [70] and are presented in Tables 3 and 4, respectively. The Born mechanical stability criteria for orthorhombic systems were discussed in Chapter 3. All stability requirements are satisfied, indicating the mechanical stability of Na_1MPO_4 compounds in the maricite structure. During the extraction stages, the initial Na extraction stage did not meet all Born's mechanical stability criteria, as $C_{44} > 0$ was not achieved due to C_{44} = -0.37 GPa. However, for the second Na extraction to de-intercalate completely, all Born mechanical stability criteria had to be met. Table 3 shows the elastic constants (C_{ij}) of the olivine $NaMPO_4$ structures. We noted that all the stability criteria were met, indicating that the olivine $NaMPO_4$ compounds are mechanically stable. Unlike in the maricite phase during the extraction phases, in the first to third Na extraction phases, Born mechanical stability criteria were met. But for the fully de-intercalated structure, the $C_{44} > 0$ criteria were not achieved, since C_{44} = -39.20 GPa. This is the first study to report the elastic constant on both maricite and olivine Na_xMnPO_4 systems when Na was removed.

Table 3: Elastic constants (C_{ij}) for the Na_xMnPO_4 maricite polymorph (x = 1, 0.75, 0.5, 0.25, 0).

C_{ij}	Na_1MnPO_4	$Na_{0.75}MnPO_4$	$Na_{0.5}MnPO_4$	$Na_{0.25}MnPO_4$	$MnPO_4$
C_{11}	159.34	154.39	-	180.80	188.02
C_{12}	45.26	44.99	-	45.67	47.45
C_{13}	69.20	64.28	-	69.49	66.65
C_{22}	143.6	133.45	-	136.95	113.57
C_{23}	46.25	40.66		34.32	36.86
C_{33}	155.76	136.89	-	128.69	151.75
C_{44}	42.23	-0.37	-	28.27	51.57
C_{55}	51.01	58.54	-	58.04	51.27
C_{66}	38.0	31.84	-	35.26	66.28

Table 4: Elastic constants (C_{ij}) for the Na_xMnPO_4 olivine polymorph (x = 1, 0.75, 0.5, 0.25, 0).

C_{ij}	Na_1MnPO_4	$Na_{0.75}MnPO_4$	$Na_{0.5}MnPO_4$	$Na_{0.25}MnPO_4$	$MnPO_4$
C_{11}	124.46	116.46	119.25	116.19	201.63
C_{12}	61.43	50.10	35.94	17.73	55.84
C_{13}	58.55	48.93	43.67	36.24	72.41
C_{22}	125.29	127.87	140.41	171.12	153.41
C_{23}	51.49	33.59	21.92	9.29	38.30
C_{33}	148.46	131.67	114.56	94.66	139.66
C_{44}	42.28	32.12	25.48	24.25	-39.20
C_{55}	49.01	47.22	46.74	45.05	56.59
C_{66}	46.71	38.99	36.35	33.95	11.88

Furthermore, the values we calculated for C_{11}, C_{22}, and C_{33} are significantly higher than the values we calculated for C_{44}, C_{55}, and C_{66} in the maricite phase. This suggests that the materials have high directional resistance to linear compressions against uniaxial pressures, but a lower resistance to shear deformations. The elastic characteristics of the maricite $NaMnPO_4$ polymorph were calculated to be higher than those reported here for the olivine phase by Lethole *et al.* [135]. Furthermore, our calculated olivine C_{11}, C_{22} and C_{33} are much larger than C_{44}, C_{55}, and C_{66}, implying

that, like maricite, the olivine phase also has strong directional resistance to linear compressions against uniaxial pressures, but limited resistance to shear deformations.

From the calculated elastic constants, the macroscopic mechanical parameters, namely bulk, shear, and Young's modulus, are obtained using the Voigt-Reuss-Hill approach [71]. The resultant bulk, shear and Young's moduli are listed in Table 5. Bulk and Young's moduli determine the hardness and stiffness of the material, respectively, while the shear modulus determines the resistance to deformation under shear stress. The bulk modulus also measures the resistance to volume change under pressure [72]. The positive bulk, shear, and Young's moduli of Na_xMnPO_4 structures are relatively large, which suggests that these structures are hard, have a great resistance to volume change, deformation, and stiffness, respectively, this is with an exception the shear, and Young's moduli of Maricite $Na_{0.75}MnPO_4$ which are significantly lower than the others.

Table 5: Bulk (B), Shear (G), and Young (E) moduli, Pugh ratio (B/G) for Na_xMnPO_4 olivine polymorphs (x = 1, 0.75, 0.5, 0.25, 0).

Phase	**Structure**	**B**	**G**	**E**	**B/G**	ν
Olivine	Na_1MnPO_4	81.48	42.36	108.3	1.924	0.2785
	$Na_{0.75}MnPO_4$	69.97	38.78	98.19	1.805	0.2661
	$Na_{0.5}MnPO_4$	63.08	38.34	95.63	1.655	0.2473
	$Na_{0.25}MnPO_4$	53.76	37.25	90.74	1.443	0.2185
	$MnPO_4$	89.81	35.73	94.05	2.514	0.1384
Maricite	Na_1MnPO_4	86.21	45.67	116.44	1.89	0.28
	$Na_{0.75}MnPO_4$	80.01	11.04	25.73	7.2	0.43
	$Na_{0.5}MnPO_4$	-	-	-	-	-
	$Na_{0.25}MnPO_4$	80.42	38.94	100.46	2.07	0.29
	$MnPO_4$	72.28	51.03	123	1.42	0.21

Furthermore, we note that B is greater than G, suggesting that the shear modulus is the parameter that limits the amount of mechanical stability that Na_xMnPO_4 structures can exhibit [33]. In addition, the Pugh ductility and brittleness criterion was determined through the testing process. Pugh proposed the bulk-to-shear modulus (B/G) ratio for polycrystalline phases. Pugh did so under the assumption that the shear modulus

represents the resistance to plastic deformation, while the bulk modulus represents the resistance to fracture. The B/G ratio is inversely proportional to ductility; therefore, a low B/G value is associated with brittleness, and a high B/G value is associated with ductility. The value of 1.75 is the critical number that determines whether a material is ductile or brittle. For maricite, B/ G was found to be greater than 1.75 for Na_1MnPO_4, $Na_{0.75}MnPO_4$, and $Na_{0.25}MnPO_4$ which makes them ductile. This means that these materials can bend without deformation, resulting in fewer cracks while using the battery [34]. While $MnPO_4$, on the other hand, is brittle due to the fact that the predicted B / G ratio is less than 1. 75. For the olivine phase, the structures of the Na_1MnPO_4, $Na_{0.75}MnPO_4$, and $MnPO_4$ structures are ductile, as B / G is found to be greater than 1.75, while $Na_{0.5}MnPO_4$ and $Na_{0.25}MnPO_4$ are both brittle.

4.4.4.2. Anisotropy

An accurate description of the anisotropic behaviour shows that almost all known crystals, in terms of their elastic properties, exhibit significant consequences for the fields of engineering science and crystal physics, as well as for a variety of other research areas. It is feasible to calculate the shear anisotropic factors by first determining the degree of anisotropy in the bonding between atoms in various planes. This will allow the anisotropic shear factors to be determined. The shear anisotropic factors offer a degree measurement of anisotropy in the bonding that occurs between atoms in different planes of the material. The shear anisotropic factor for the [100] and [110], [010] directions is calculated as:

$$A_1 = \frac{4C_{44}}{C_{11} + C_{33} - 2C_{13}} \tag{97}$$

For the shear planes (010), (001) between the directions ([011] and [010], [110], [001] and [010], [110], [001], respectively) directions are:

$$A_2 = \frac{4C_{55}}{C_{22} + C_{33} - 2C_{23}} \tag{98}$$

$$A_3 = \frac{4C_{66}}{C_{11} + C_{22} - 2C_{12}} \tag{99}$$

Table 6: Anisotropy in the shear elastic factor (A_i with i = 1,2,3), and anisotropy in the the compressibility and shear moduli (A_B and A_G in %).

	Structure	A_1	A_2	A_3	A_B	A_G
Maricite	Na_1MnPO_4	0.956	0.986	1.250	0.545	0.975
	$Na_{0.75}MnPO_4$	0.010	1.239	0.644	0.619	210.869
	$Na_{0.5}MnPO_4$	-	-	-	-	-
	$Na_{0.25}MnPO_4$	0.657	1.178	0.623	2.980	13.277
	$MnPO_4$	0.999	1.073	1.283	16.104	8.123
Olivine	Na_1MnPO_4	1.085	1.145	1.409	1.4	1.2
	$Na_{0.75}MnPO_4$	0.855	0.989	1.065	1.9	1.3
	$Na_{0.5}MnPO_4$	0.696	0.886	0.844	4.1	3.7
	$Na_{0.25}MnPO_4$	0.701	0.937	0.632	10.9	9.8
	$MnPO_4$	0.798	1.046	0.226	8.9	7.6

The shear anisotropic factors of maricite and olivine, as determined through our theoretical analysis, are presented in Table 6. Factors A_1, A_2, and A_3 must all be one for an isotropic crystal, while any number less than or greater than unity indicates the degree of elastic anisotropy of the crystal. For the maricite phase, the values of A_1 (0.956), A_2 (0.986), and A_3 (1.250) for Na_1MnPO_4 diverge from unity, suggesting an isotropic characteristic. During the de-intercalation stages, $Na_{0.25}MnPO_4$ and $MnPO_4$ displayed slight deviations from the unity, whereas A_1 and A_3 for $Na_{0.75}MnPO_4$ showed the greatest deviation from the unity, with A_1 having a 0.01 value. While for olivine, the values of A_1 (1.085), A_2 (1.145), and A_3 (1.409) for Na_1MnPO_4 diverge from unity by 8.50%, 14.50%, and 40.09%, suggesting an isotropic characteristic. During the de-intercalation stages, all the materials displayed slight deviations from the unity, whereas A_1 and A_3 for $MnPO_4$ showed the greatest deviation from the unity, with A_1 having a negative value. A new term for noncubic systems, percent elastic anisotropy, was developed by Chung and Buessem [136]. It is a measure of the amount of elastic anisotropy held by the crystal under discussion. The percentage anisotropy in compressibility and shear moduli is described by the equations $A_B = B_V - B_R / B_V + B_R$ and $A_G = G_V - G_R / G_V + G_R$, respectively, for compressibility and shear moduli. $B_R = B_V$ is related with isotropic elastic constants, but a value of 100 % is associated with the maximum amount of anisotropy that may be achieved.

It can be noted that Na de-intercalations from maricite phase generally increase A_B and A_G values except for $Na_{0.75}MnPO_4$, suggesting an enhancement in isotropy and

reduction of micro cracks and dislocations during the charge/discharge process. The percentage of shear modulus anisotropy A_G is less than the percentage of bulk modulus anisotropy A_B, in all de-intercalation stages, except for $MnPO_4$. On the other hand, it was observed that Na de-intercalations from olivine generally increase A_B and A_G values except for $MnPO_4$, suggesting an enhancement in isotropy and reduction of micro cracks and dislocations during the charge/discharge process. The percentage of shear modulus anisotropy A_G is less than the percentage of bulk modulus anisotropy A_B, in all de-intercalation stages.

4.4.4.3. Thermodynamic Properties

4.4.4.3.1. Debye Temperature

We calculate the Debye temperature (Θ_Θ) from the average sound velocity (V_m) using the equation (48)-(50) presented in chapter 3. Volumetric density, sound velocities, and Debye temperature as a function of Na removal are presented in Table 7. Derived from the calculated elastic constants, the calculated Debye temperature $\boldsymbol{\theta_D}$ for maricite Na_1MnPO_4 was found to be 528.3 K.

Table 7: Calculated volumetric density ρ (in kg/m3), longitudinal ν_l transverse ν_t, and average sound velocities ν_t in m/s, and Debye temperature θ_D in Kelvin.

	Structure	$\boldsymbol{\rho}$	$\boldsymbol{\nu_t}$	$\boldsymbol{\nu_l}$	$\boldsymbol{\nu_m}$	$\boldsymbol{\theta_D}$
Maricite	Na_1MnPO_4	3498	3626	6132	4046	528.3
	$Na_{0.75}MnPO_4$	3432	1790	5242	2035	265.2
	$Na_{0.5}MnPO_4$	-	-	-	-	-
	$Na_{0.25}MnPO_4$	3498	3326	6132	3711	486.0
	$MnPO_4$	3498	3811	6320	4214	550.9
Olivine	Na_1MnPO_4	3309	3576	6454	3984	512.7
	$Na_{0.75}MnPO_4$	3288	3435	6084	3821	490.0
	$Na_{0.5}MnPO_4$	3284	3417	5897	3792	485.0
	$Na_{0.25}MnPO_4$	3308	3357	5593	3713	476.2
	$MnPO_4$	3385	3379	5216	3707	497.8

Unfortunately, we were unable to uncover any experimental or theoretical data with which to compare our computed results. As seen in Table 7, Na de-intercalation

resulted in a monotonic drop in all sound velocities as well as the $\boldsymbol{\theta_D}$ for $Na_{0.75}MnPO_4$ and $Na_{0.25}MnPO_4$ systems. Considering that the $\boldsymbol{\theta_D}$ in a solid may be used to define its covalent strength, the drop in $\boldsymbol{\theta_D}$ as a result of Na de-intercalated that the covalent strength of $NaMnPO_4$ decreases with each de-intercalation step. Although the thermal conductivity of the material increases with increasing $\boldsymbol{\theta_D}$ in general, our results indicated a modest drop in $\boldsymbol{\theta_D}$, indicating that the thermal conductivity of the material was maintained after the Na de-intercalation. It is noteworthy that the volumetric density, sound velocities, and Debye temperature increase during the fourth step of Na de-intercalation, with a Debye temperature calculated to be 550.9 K increases.

Taking into account the calculated elastic constants, the calculated Debye temperature $\boldsymbol{\theta_D}$ for olivine Na_1MnPO_4 was found to be 512.7 K. Unfortunately, we were unable to uncover any experimental or theoretical data with which to compare our computed results. As seen in Table 7, Na de-intercalation resulted in a monotonic drop in all sound velocities as well as the $\boldsymbol{\theta_D}$ for all the systems. Considering that the $\boldsymbol{\theta_D}$ in a solid may be used to define its covalent strength, the drop in $\boldsymbol{\theta_D}$ as a results of Na de-intercalation indicated that the covalent strength of $NaMnPO_4$ decreases with each de-intercalation step. Although the thermal conductivity of the material increases with increasing $\boldsymbol{\Theta_D}$ in general, our results indicated a modest drop in $\boldsymbol{\Theta_D}$, indicating that the thermal conductivity of the material was maintained after Na de-intercalation. It should be noted that the volumetric density, sound velocities, and Debye temperature increase during the fourth step of Na de-intercalation, with a Debye temperature calculated at 497.8 K4.

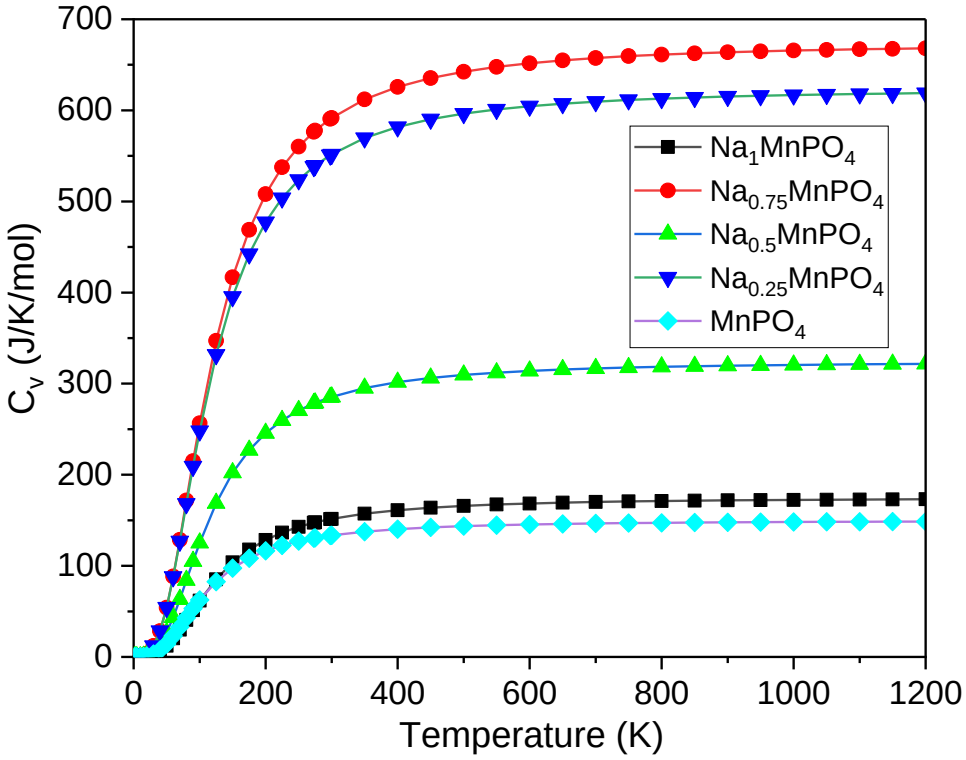

Figure 19: Temperature-specific heat at constant volume (C_v) of Na_xMnPO_4 (x= 1, 0.75, 0.5, 0.25, 0).

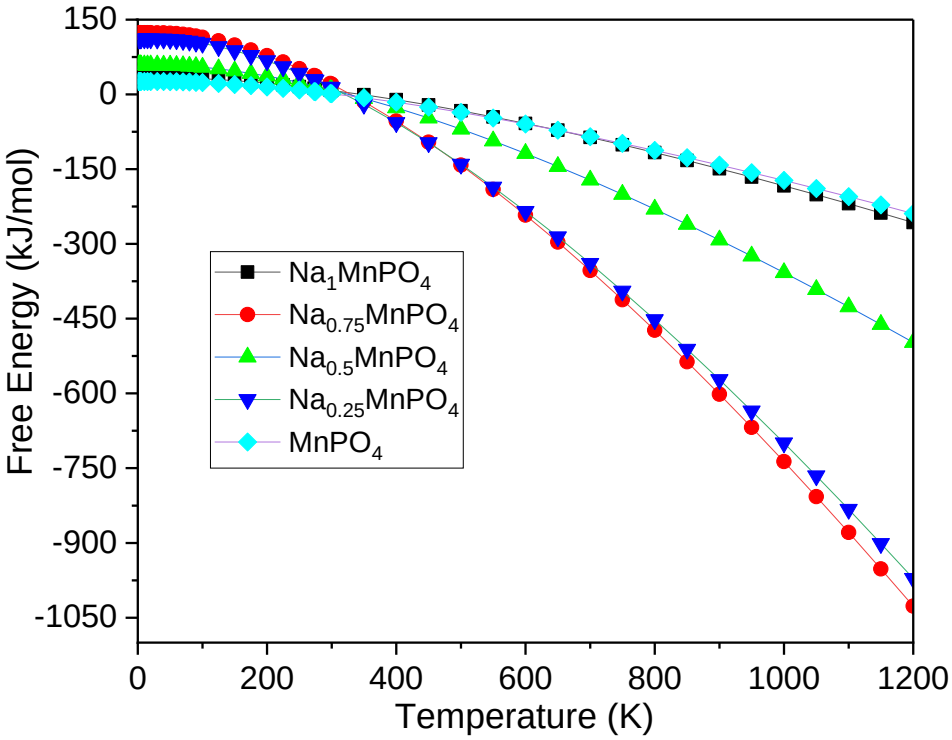

Figure 20: The free energy versus temperature for Na_xMnPO_4 (x = 1, 0.75, 0.5, 0.25, 0).

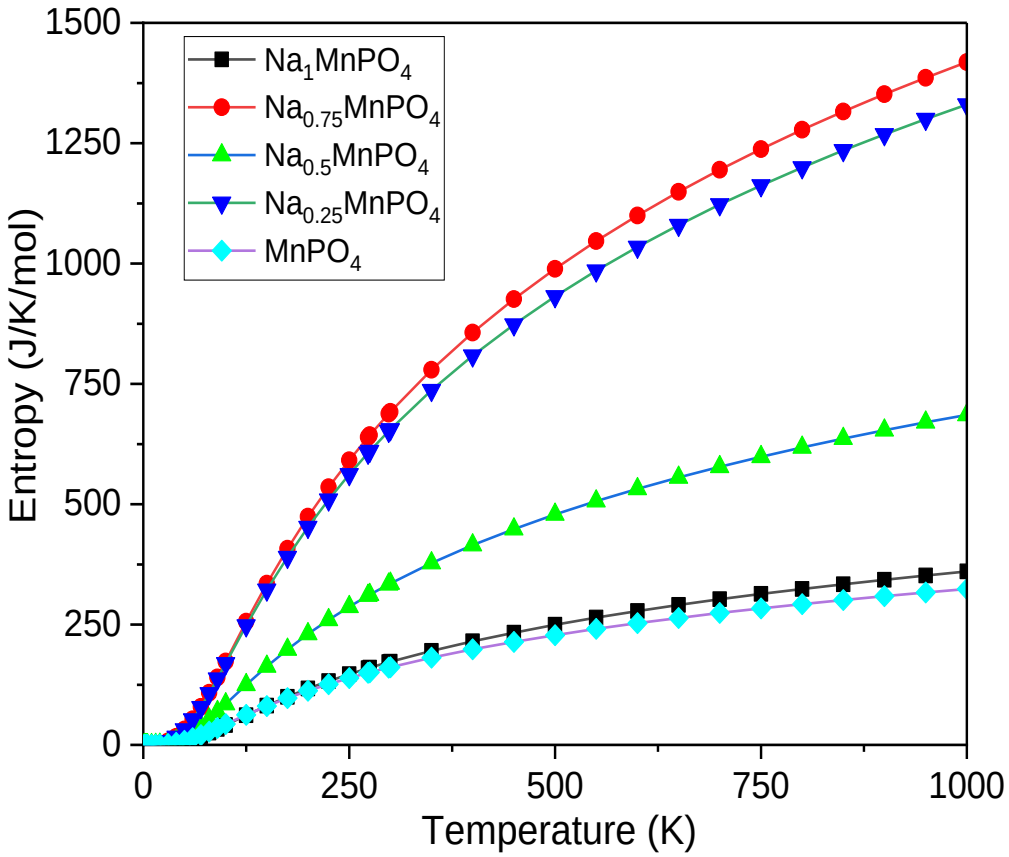

Figure 21: Entropy vs. temperature for Na_xMnPO_4 (x = 1, 0.75, 0.5, 0.25, 0).

The VASP programme was used to investigate essential thermodynamic parameters such as specific heat in Cv, Helmholtz free energy, and entropy calculated at pressure and temperatures (0–1200 K). From Figures 19 to 21, the influence of temperature on Cv, free energy, and entropy has been calculated and shown to be significant. At low temperatures, the Cv rate of increase is rapid for all intercalation phases, regardless of the intercalation stage. During high-temperature de-intercalation, the value of Cv of all de-intercalation stages approaches the classical asymptotic limit, also known as the Dulong–Petit limit. At low temperatures, the fluctuation of free energy versus temperature, as well as the variation of Cv versus temperature, shows that the increase in free energy is significant for all de-intercalation stages

4.5. Summary

We examined the structural and electrochemical performance of Na_xMnPO_4 based on the first-principles method. The comparison of the PBE, PBEsol, and PBE+U functionals showed that the PBE+U reproduced structural parameters and energy

band gap values that are consistent with those of the literature and were used to further analyse the electrochemical performance of the de-intercalated systems. Subsequently, the effect of Na atom de-intercalation on the structural, electronic, mechanical, and thermodynamic properties of both maricite and olivine $NaMnPO_4$ has been investigated by first-principle calculations.

Maricite: During the maricite discharge process Na_xMnPO_4, the changes in structural parameters are less than 7 %, indicating that the structures remain intact. The voltage window for $NaMnPO_4$ was found to be between 5.132 V and 4.655 V. In addition, the results reveal that the metallicity of maricite $NaMnPO_4$ increases progressively during the Na extraction process. The calculated values for the formation energy were found to be negative for all $NaMnPO_4$ systems, hence the solid solution is predicted for states of de-intercalation. The calculated results are consistent with the experimental investigations. During the de-intercalation stages, the calculated elastic constants suggested mechanical instability since the stability criteria were not satisfied for all the de-intercalated structures. According to the Pugh criterion of ductility and brittleness, we note that the Na_1MnPO_4, $Na_{0.75}MnPO_4$, and $Na_{0.25}MnPO_4$ structures are ductile, whereas $MnPO_4$ was found to be brittle.

Olivine: During the Na de-intercalation stages of olivine Na_xMnPO_4, the lattice parameters and the volume showed a deviation of less than 6%, which is not enough to cause irreversible distraction to the system. The electronic DOS revealed that during the Na removal stages, between the 1st and the 3rd stages, the material showed an increase in metallicity, while during the 4th stage the material showed a semiconductor behaviour with a band gap of 0.194 eV. The voltage window of 3.997 to 3.848 V was obtained, and the calculated formation energy values were found to be negative, which symbolises the prediction of a solid possessed by the material. The calculated elastic constants suggested mechanical stability for $NaMnPO_4$ since the stability criteria were satisfied for all the de-intercalated systems except fully de-intercalated $MnPO_4$. According to the Pugh criterion of ductility and brittleness, we note that the Na_1MnPO_4, $Na_{0.75}MnPO_4$, and $MnPO_4$ structures are ductile, whereas $Na_{0.5}MnPO_4$ and $Na_{0.25}MnPO_4$ are both brittle. It was also noted that following the de-intercalation process, there was a noticeable and consistent decrease in the sound velocities and $\boldsymbol{\theta_D}$ values for all the systems. The covalent strength of $NaMnPO_4$ decreases with each stage of de-intercalation, as results of a decrease in $\boldsymbol{\theta_D}$. Although it is commonly

believed that the thermal conductivity of the material increases as $\boldsymbol{\theta_D}$ increases, our research revealed a slight decrease in $\boldsymbol{\theta_D}$. It shows that the material's thermal conductivity was not impacted by the removal of Na. In the fourth step of Na de-intercalation, it's crucial to note that there is an increase in volumetric density, sound velocities, and Debye temperature. Based on the thermodynamics calculations, it was observed that the rate of increase in C_v is significant for all de-intercalation phases, regardless of the stage, at low temperatures. At high temperatures, de-intercalation reaches its classical asymptotic limit. Meanwhile, the fluctuation of free energy and C_v with temperature suggests a notable rise in free energy at lower temperatures.

Chapter 5. Atomistic Simulations of Na De-intercalated Olivine Na_xMnPO_4

5.1. Introduction

The use of atomistic simulation techniques, as expounded in this section, involves the implementation of basic, empirically derived equations to depict interatomic interactions. First-principles techniques, which were previously discussed as electronic structure techniques, rely on the fundamental principles of quantum mechanics and, therefore, exhibit a higher degree of complexity when compared to other methods. The decision of which technique to use is frequently influenced by the desired information and the availability of computational time and resources, as perceived by theoreticians. Atomistic methodologies enable the simulation of a significant number of atoms reaching tens of thousands. Therefore, MD techniques well suited for modelling the relaxation phenomena surrounding defects, whose impact can have a considerable reach into the crystal lattice of a given system. The approach is well suited for generating precise statistical information from MD simulations, which necessitates extensive simulation times and large simulation cells.

In addition to the obvious gaps in mass and size between lithium and sodium cations, the chemical behaviour, specifically the electrochemical performance, of compounds with Li and Na intercalation can also vary significantly due to electronic structure effects. Atomistic modelling is a valuable method for bridging the current gap in our extensive understanding of electroactive materials based on lithium and their sodium counterparts. Basic research has shown that the process of intercalation of lithium and sodium in MPO_4 is noticeably distinct. The variations are commonly ascribed to the development of organised partly sodiated structures in $NaMPO_4$, in contrast to the single-phase characteristics of $LiFePO_4$. The presence of stable Na^+ configurations introduce structural complexity to the investigation of sodium intercalation at the molecular scale. When investigating dynamic features like the mobility of Na^+ using simulations, it is important to consider the issue of sodium orderings. This requires the use of large supercells and long simulation periods. The computing costs of using first-principles approaches, such as density functional theory, is too high to meet these needs.

Theoretical investigations conducted in the past have focused on calculating the one-dimensional diffusion that occurs along the Li or Na [010] channel [137]. Given that self-diffusion of Li or Na ions in iron phosphate ($FePO_4$) is a thermally driven phenomenon, the use of molecular dynamics simulations presents a more direct means to investigate viable diffusion pathways.

This chapter explores the temperature dependence of random Na de-intercalation stages through the use of classical MD. Starting from this chapter 5, our investigations are directed towards the olivine $NaMnPO_4$ polymorph because of the mechanical instability observed in the maricite polymorph, as discussed in the previous chapter.

5.2. Development of Interatomic Potentials

The derivation of interatomic potentials constitutes a fundamental aspect within the field of materials science and engineering. The process entails the formulation of mathematical models that elucidate the interplay among atomic entities within a given material. There exist two distinct methodologies for deriving force fields. One potential method involves modifying the parameters to align them with the observed experimental data. The efficacy of this methodology depends on the accessibility of a diverse array of empirical data. The second method involves the adjustment of the parameters in order to accurately replicate the data of the electronic structure ab initio. This adjustment is achieved by modifying the energy in relation to the atomic position. In contemporary times, the use of this approach has become increasingly prevalent due to progress in computer technologies and the availability of sophisticated ab initio software tools, such as VASP and CASTEP codes, for example. Historically, the initial approach was preferred because of the time-consuming nature of electronic structure calculations and the limited computational power available at that time, resulting in high computational costs, and that has changed with time. In this study, the second approach was employed to derive the interatomic potential model for $NaMnPO_4$. However, both methodologies employ a shared underlying principle, namely the development of a model capable of effectively replicating the existing data. Data may include various physical properties such as elastic constants, bulk moduli, dielectric constants, or phonon frequencies. When performing a fitting procedure, it is crucial to establish a metric that quantifies the precision of the obtained results, commonly referred to as the sum of squares F given by:

$$F = \sum_{i=1}^{N_{obs}} W\left(f_i^{obs} - f_i^{calc}\right)^2 \quad (100)$$

In this context, N_{obs} represents the total count of observables. The variables f_i^{obs} and f_i^{calc} denote the fitted and calculated values of the observable, respectively. Additionally, W_i represents the weighting factor assigned to the observable. There exist multiple criteria to determine the selection of an appropriate and rational weighting factor. In the context of fitting experimental data, it is advisable to assign a weighting factor that is inversely proportional to the uncertainty associated with the measured value. Moreover, in order to achieve uniformity among values irrespective of their units, it is necessary to assign a weighting factor that is inversely proportional to the square of the observable's magnitude. The fitting process entails minimisation of the objective function F by adjusting the potential parameters. Table 8 shows the interatomic potentials for olivine $NaMnPO_4$ obtained by fitting properties obtained in chapter 4 (namely, structural and elastic properties) through the short-range interactions implemented in Buckingham and three-body potential models. These derived interatomic potentials are used to perform all molecular dynamics simulations in this study.

Table 8: Buckingham and three-body interatomic potentials for olivine Na_xMnPO_4.

Buckingham potentials						
Pair	A (eV)	ρ(A)	C (eV·Å^6)	Y	K (eV·Å^{-})	Cut-off
Na^+ - O^{2-}	560	0.32	0.00	1	99999.0	20
Na^+ - O^{2-}	1497.83	0.28748	0	1	99999.0	20
Na^+ - F^-	8000	0.20	0	1	99999.0	20
Mn^{2+} - O^{2-}	1305.25	0.31	0.00	2.99	19.26	20
P^{5+} - O^{2-}	897.25	0.35	0.00	5	99999.0	20
O^{2-} - O^{2-}	22764.3	0.14	44.5	-2.96	65.00	20
O^{2-} - F^-	200	0.3	8.99955	-	-	200
F^- - F^-	1153	0.1365	0	-2.32	63.57	1153
Three body potential						
Bond	K (eV ·rad^{-2})		Θ_0 (°)		Cut-offs R_{ii}, R_{ik}, R_{jk}	
O^{2-} - P^{5+} - O^{2-}	1.322		109.47		1.8, 1.8, 3.2	

5.2.5. Atomistic Potentials Model Validation

We validate the precision and performance of the newly developed force field by comparing the computed structural parameters and the unit cell parameters with the results obtained from *ab initio* MD at 300 K, DFT at 0 K and experiments. After simulating 100 ps using NVT in LAMMPS at a constant pressure of 1 atom and a temperature of 300 K, we measured the unit cell parameters for Na_1MnPO_4 to evaluate the precision of the newly proposed force field. The simulation results are presented in Table 9 together with the DFT values and *ab initio* MD values that were also calculated using VASP. Additionally, the table contains the experimental data for further validation. The results showed that there were no significant differences between the unit cell parameters estimated using the fitted force fields. Furthermore, the calculated values are to a certain degree consistent with the experimental results than the values that were obtained through other experimentations, in particular DFT calculated and ab initio MD simulations.

Table 9: Olivine Na_xMnPO_4 lattice constants computed with DFT, *ab initio* MD, and LAMMPS-Buckingham potentials at 300 K.

	Lattice Param	**Exp [122]**	**DFT-This work**	***Ab intio* MD**	**LAMMPS-Potential Model**	**% errors**
$NaMnPO_4$	a (Å)	10.528	10.693	10.646	10.623	0.89
	b (Å)	6.321	6.421	6.408	6.393	1.13
	c (Å)	4.985	5.053	5.065	5.053	1.35
	V $Å^3$	331.740	346.995	345.512	343.180	3.39

5.3. Computational Details

In order to calculate structural and transport properties of Na de-intercalated systems, molecular dynamics simulations were performed using the LAMMPS simulation package employing the velocity Verlet algorithm for integrating Newton's equations of motion. The LAMMPS simulation process consists of six stages, namely, initialise, minimise, initialise velocities, ensemble NVT, ensemble NPT and diffusion calculations. The initialisation stage was created by generating 5x5x5 supercell bulk model and assigning the fitted interatomic forcefields. Then simulation was

equilibrated through an energy minimisation procedure using Verlet algorithm, followed by a grand canonical ensemble NVT (fixed number of particles, volume and temperature) simulation. The simulations were carried out with a time step of 1 fs in the NVT ensemble at 100 K to 500 K. The atom positions were stored every 100 ps. The temperature was controlled by the Nosé-Hoover chain thermostat with a time constant of 0.8 ps. The cut-off of the non-bonded interactions was set to 9 nm, with a standard dispersion correction for energy and pressure. The simulation was further equilibrated via NPT ensemble (fixed number of particles, pressure and temperature) simulation. Finally, the diffusion coefficient was calculated from the mean square displacement values obtained during the pressure P on the last configuration of the NPT stage.

5.4. Sodium De-intercalated Olivine Na_xMnPO_4

Interatomic potentials play a crucial role in atomistic molecular dynamics, as they dictate the forces experienced by individual atoms [138]. Atomistic molecular dynamics calculations serve as a highly effective simulation technique for the study of systems comprising a significant number of atoms. This method offers valuable information on the dynamic behaviour of atomic positions and velocities at different time intervals during simulation [139]. In this section, the derived interatomic potentials of $NaMnPO_4$ are used to examine the influence of temperature on sodium-de-intercalated structures using the classical molecular dynamics technique and the results are discussed in the next subsections.

5.4.1. Radial Distribution Functions

To demonstrate the phase transitions of the Na_xMnPO_4 structure, we constructed 5x5x5 supercells of Na_1MnPO_4, $Na_{0.75}MnPO_4$, $Na_{0.5}MnPO_4$, and $Na_{0.25}MnPO_4$ structures, as illustrated in Figure 22. A distinct pattern of progressively increasing vacancies was observed in Figures 22 (a)-(d) when the Na atoms were removed. The vacancies that arise as a result of de-intercalation can serve as a pathway for diffusion, allowing for the movement of ions within the crystal structure. This diffusion process is crucial for the phase transitions observed in the Na_xMnPO_4 system. As Na atoms are de-intercalated, the number of vacancies increases, leading to a higher degree of

freedom for ion movement and ultimately influencing the overall behaviour and properties of the material.

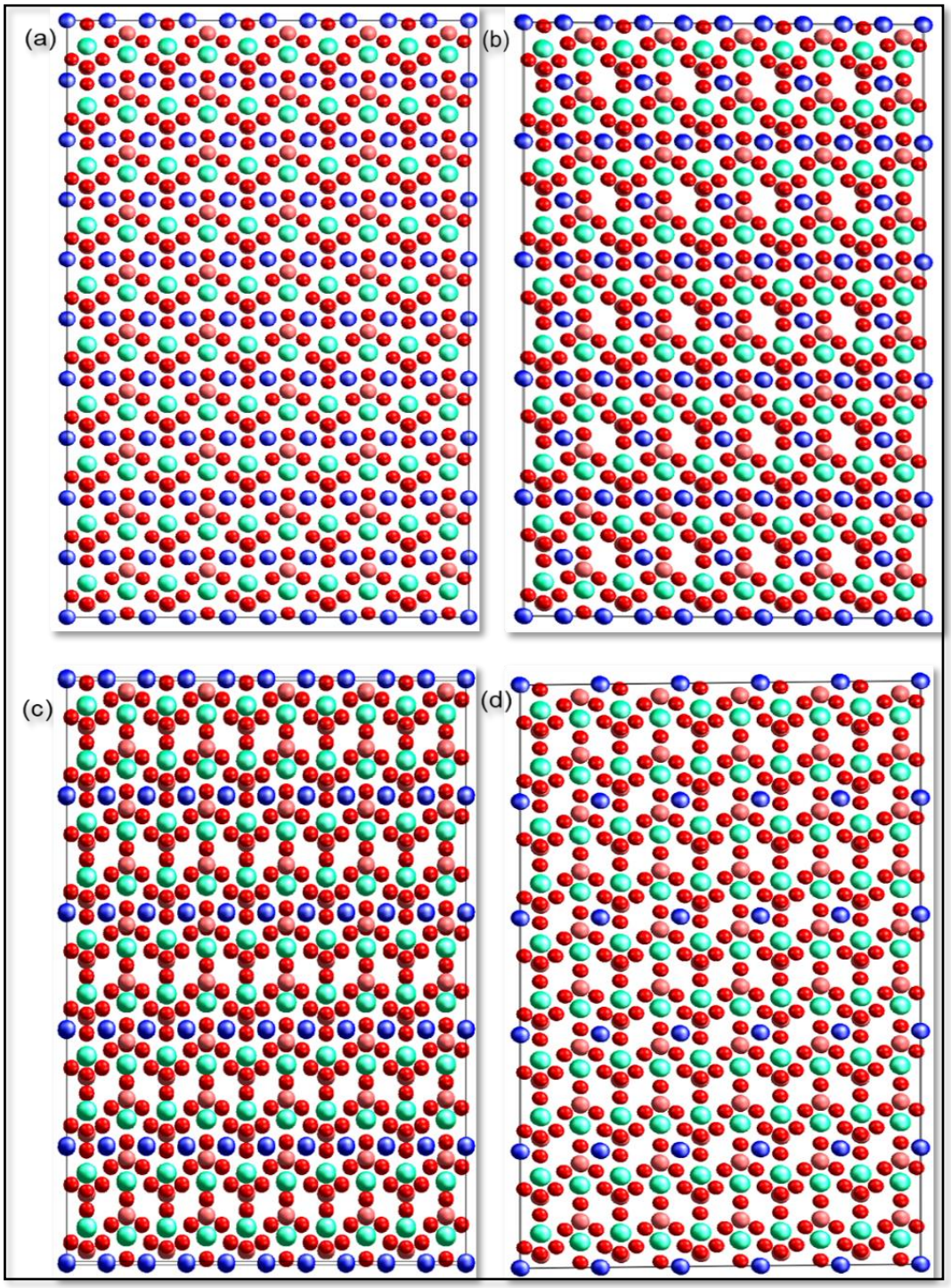

Figure 22: 5x5x5 supercells of (a) Na_1MnPO_4, (b) $Na_{0.75}MnPO_4$, (c) $Na_{0.5}MnPO_4$, (d) $Na_{0.25}MnPO_4$ structures used in the MD calculations, (where blue is the sodium atom, red is the oxygen atom, light green is the manganese atom and salmon is the phosphate atom).

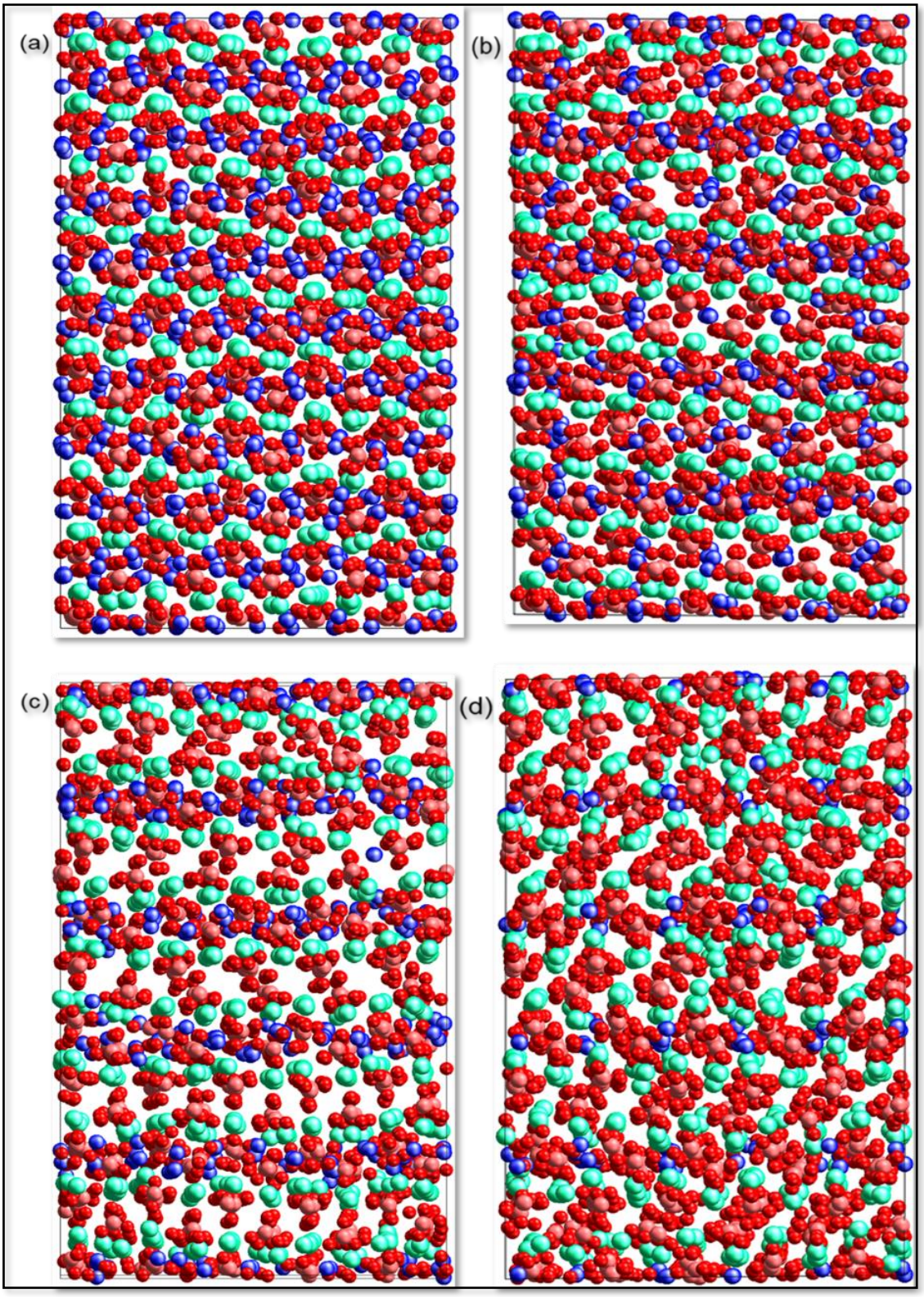

Figure 23: The 5x5x5 supercells of (a) Na_1MnPO_4, (b) $Na_{0.75}MnPO_4$, (c) $Na_{0.5}MnPO_4$, (d) $Na_{0.25}MnPO_4$ structures after MD calculations at 100 K.

Figure 23 illustrates the structures of Na_1MnPO_4, $Na_{0.75}MnPO_4$, $Na_{0.5}MnPO_4$, and $Na_{0.25}MnPO_4$ after being subjected to a temperature of 100 K. It can be seen that all Na_xMnPO_4 structures retain their orthorhombic shape at 0 K as the particles move around. However, at temperatures of 100 K, the atomic arrangement disappears, and this disappearance is more dominant in Figure 23 (d). This is due to the high number of vacancies, which allow enough space for atoms to move around.

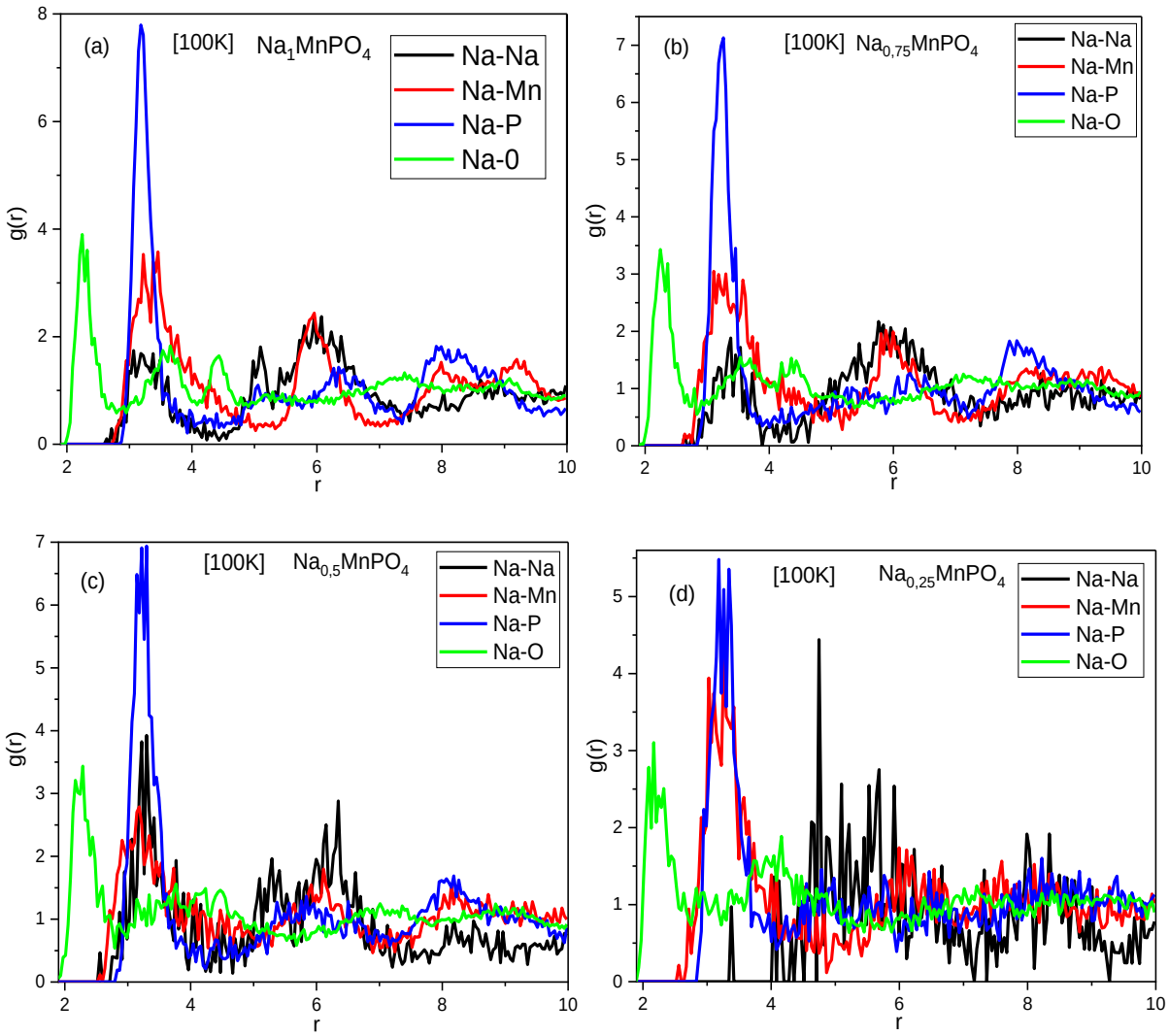

Figure 24: The radial distribution function of (a) Na_1MnPO_4, (b) $Na_{0.75}MnPO_4$, (c) $Na_{0.5}MnPO_4$, (d) $Na_{0.25}MnPO_4$ structures at 100 K.

Figure 24 shows the RDFs obtained from the fitted Buckingham interatomic potential for Na-Na, Na-Mn, Na-P and Na-O interactions within the crystal structures of Na_1MnPO_4, $Na_{0.75}MnPO_4$, $Na_{0.5}MnPO_4$, and $Na_{0.25}MnPO_4$ at a temperature of 100 K. In the context of the ionic bond present in Na_1MnPO_4, the most prominent peak is observed at a distance slightly greater than 2 Å, while two additional peaks are

noticeable within the range of 3 Å to 5 Å. As the number of de-intercalated Na atoms is increased, the initial peak exhibits a wider distribution, while the two peaks within the range of 3 Å and 5 Å progressively combine, resulting in the formation of a singular peak centred around 4 Å. A similar trend has been observed in the Na-Na, Na-P, and Na-Mn cases, wherein the number of peaks decreases as the number of Na atoms de-intercalated increases. The interatomic distance of Na-O, specifically measuring 2.246 Å, exhibits a notably low value that can be easily observed. Subsequently, the Na–Na and Na–P interactions were observed, exhibiting interatomic distances of 3.066 Å and 3.184 Å, respectively. However, the Na-Mn interaction exhibits the most significant separation distance, measuring 3.820 Å. In Figure 24 (d), which represents the $Na_{0.25}MnPO_4$ structure, the presence of reduced Na-Na interaction can be attributed to the absence of discernible peaks at this concentration. The position of the first peak for Na-O systematically shifts to a smaller distance as the Na atoms being de-intercalated increases, and it was also observed that this peak decreases in intensity and becomes broader (Figure 24 (b) to (d)).

In Figure 22, which represents the initial state of the compounds at 0 K, the atoms are tightly packed and arranged in a well-defined pattern. However, as the temperature increases to 300 K, as shown in Figure 25, the atoms begin to lose their ordered arrangement and become more disordered. This loss of structural disorder can be attributed to the increased temperature, which allows the atoms to move more freely and disrupt their original positions. As a result, the atoms gradually shift from their initial opposition, leading to a gradual disappearance of the atomic pattern arrangement during the de-intercalation stages. The observed trend of gradual disappearance of the pattern arrangement was found to be more evident at a temperature of 300 K (see Figure 25) compared to 100 K (see Figure 23).

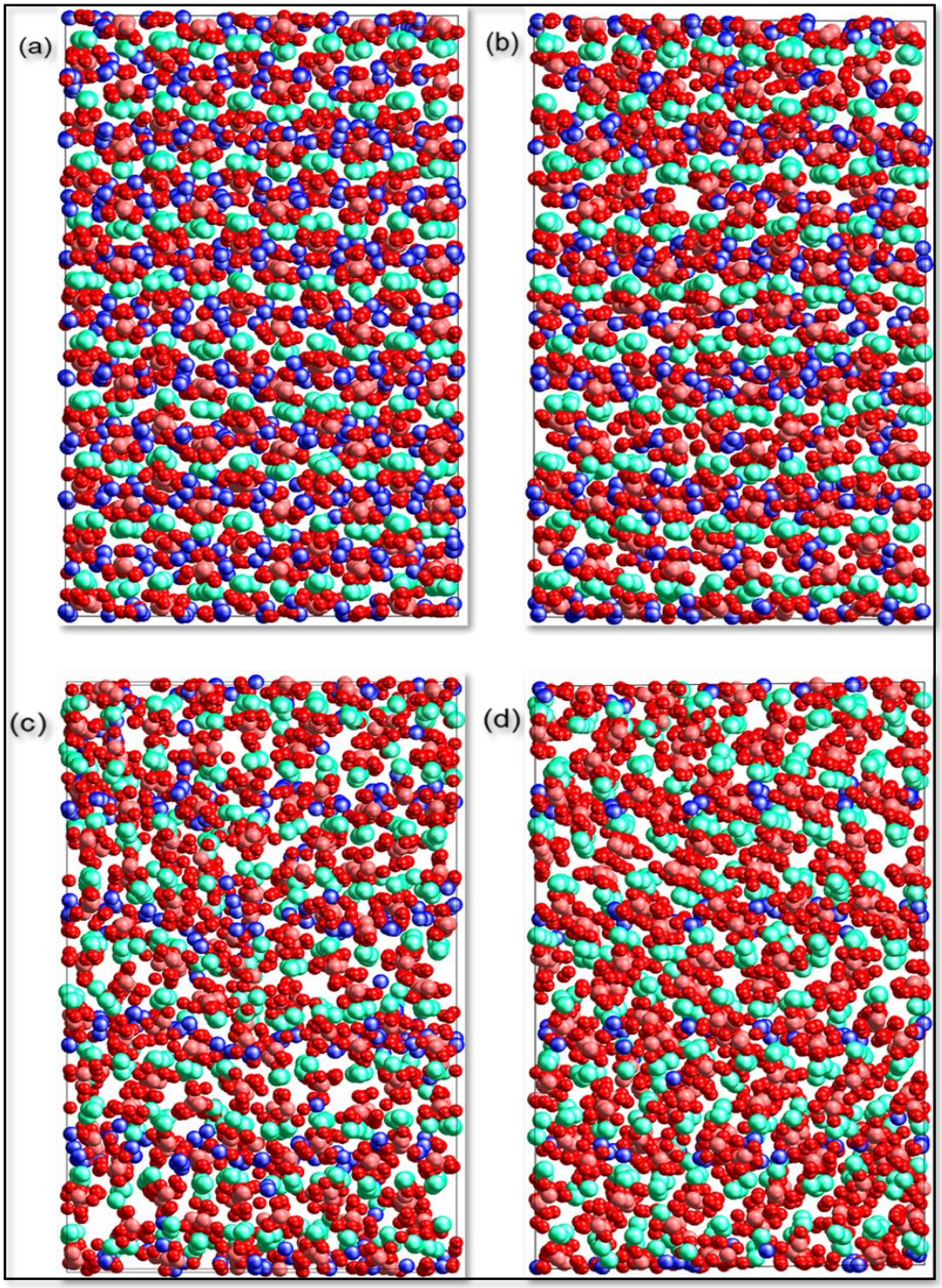

Figure 25: The 5x5x5 supercells of (a) Na_1MnPO_4, (b) $Na_{0.75}MnPO_4$, (c) $Na_{0.5}MnPO_4$, (d) $Na_{0.25}MnPO_4$ structures after MD calculations at 300K.

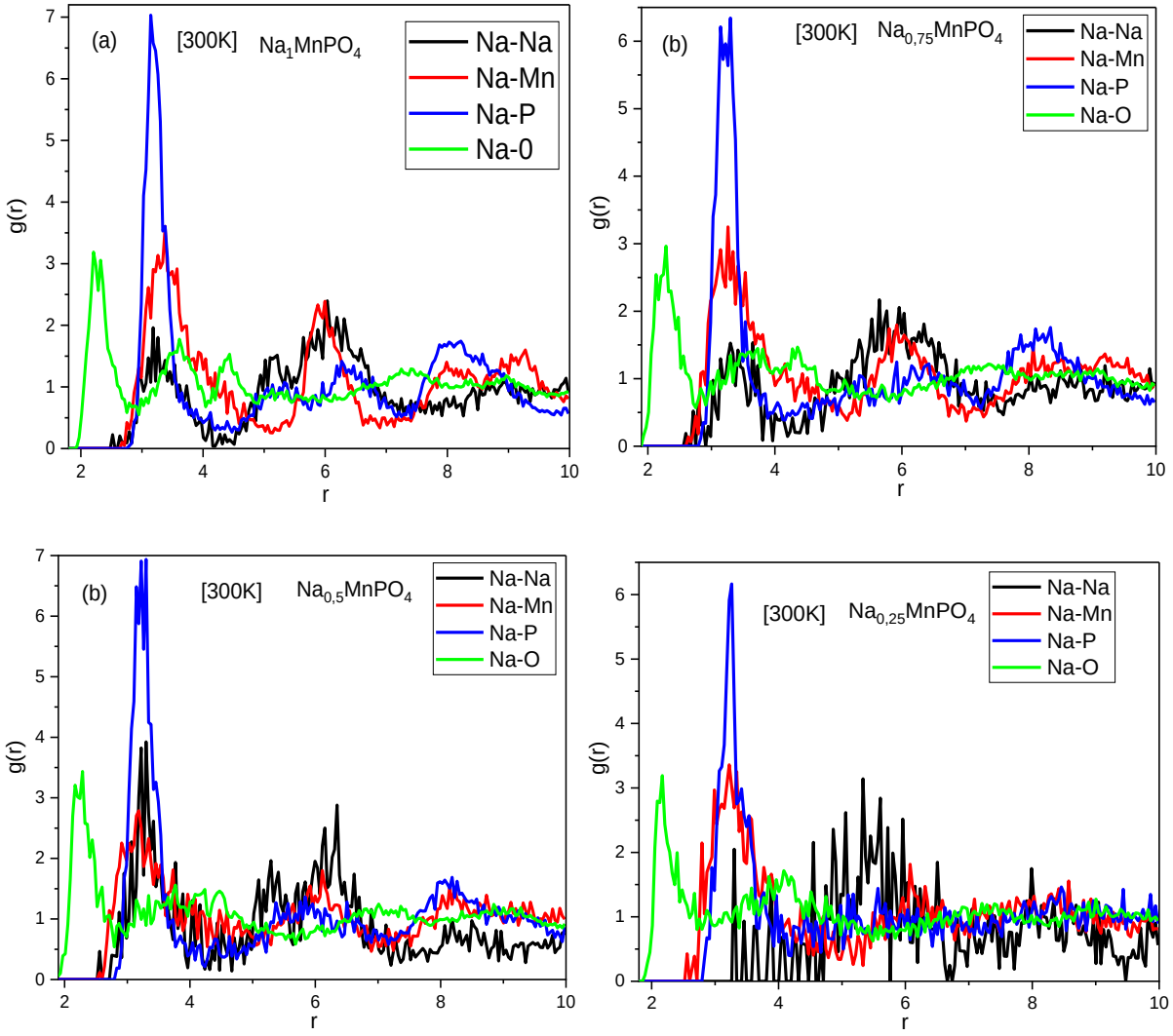

Figure 26: The radial distribution function of (a) Na_1MnPO_4, (b) $Na_{0.75}MnPO_4$, (c) $Na_{0.5}MnPO_4$, (d) $Na_{0.25}MnPO_4$ structures at 300 K.

Based on the analysis of the RDFs presented in Figure 26, it is observed that a decrease in the number of Na atoms is associated with broader peaks and a reduction in the overall number of peaks as observed at 100 K. Furthermore, the collective RDF in Figure 26 (a), which represents the results for Na_1MnPO_4, indicates that the second and third peaks exhibit distinct and clearly identifiable characteristics, in line with the number of Na atoms in the structure. However, a decrease in amplitude in the peaks is observed between Figure 26 (b) and (d) representing $Na_{0.75}MnPO_4$, $Na_{0.5}MnPO_4$ and $Na_{0.25}MnPO_4$, respectively. The Na-O interatomic distance, measured at 2.207 Å, demonstrates a significantly small value that is easily distinguishable, and it is also lower than the values obtained at 100K. Subsequently, the first peaks representing the interactions between Na-Na and Na-P were observed, displaying interatomic

distances of 3.184 Å and 3.145 Å, respectively. However, the interactions containing Na and Mn show the most notable separation distance, measuring 3.379 Å, which is lower compared to the measurement obtained at 100K. The absence of noticeable peaks at this specific concentration of $Na_{0.25}MnPO_4$ can be attributed to the presence of a reduced Na-Na interaction. The difference between 100 K and 300 K of RDFs shows that the temperature increase has a great effect on the interaction between atoms during the de-intercalation process.

5.4.2. Diffusion of Na^+ in Na_xMnPO_4

To fully understand the factors that affect the electrochemical characteristics of the Na_xMnPO_4 cathode material, it is imperative to understand Na transport properties at the atomic scale. Despite that transport characteristics play a crucial role in determining charge/discharge rates and high-power capabilities, basic understanding of the atomistic mechanism that determines the migration of Na ions within this phosphate cathode is characterised by a significant level of misconception. Furthermore, accurately determining these features using experimental methods can often pose challenges. In this study, we expand on our investigation on DFT presented in chapter 4 by employing a combination of energy minimisation and classical MD simulation methods to unravel transport properties of Na de-intercalated Na_xMnPO_4. Our objective is to investigate, for the first time, the mechanisms underlying Na ion diffusion in the Na_xMnPO_4 material.

MD calculations of the Na_xMnPO_4 de-intercalation process were performed using the LAMMPS code, as described in chapter 3. Calculations were carried out in a simulation box consisting of a 5x5x5 super cell Na_xMnPO_4 olivine structure, using periodic boundary conditions. As shown in Figure 22, the original Na_xMnPO_4 configurations had varying percentages of Na vacancies (and related Mn^{3+} species), which were randomly distributed. The simulations were conducted using both the NVT and NPT ensembles, with a time step of 100 fs. The simulations were run for a longer period of 5 ns at temperatures of 100 K and 300 K. Figures 27 (a) and (b) presented in this study show the mean squared displacements, denoted by $\langle|r(t)|^2\rangle$, for sodium de-intercalated stages of the olivine Na_xMnPO_4 structures at two different temperatures. Figure 27 (a) shows the MSDs at 100 K, while Figure 27 (b) illustrates the MSDs at 300 K.

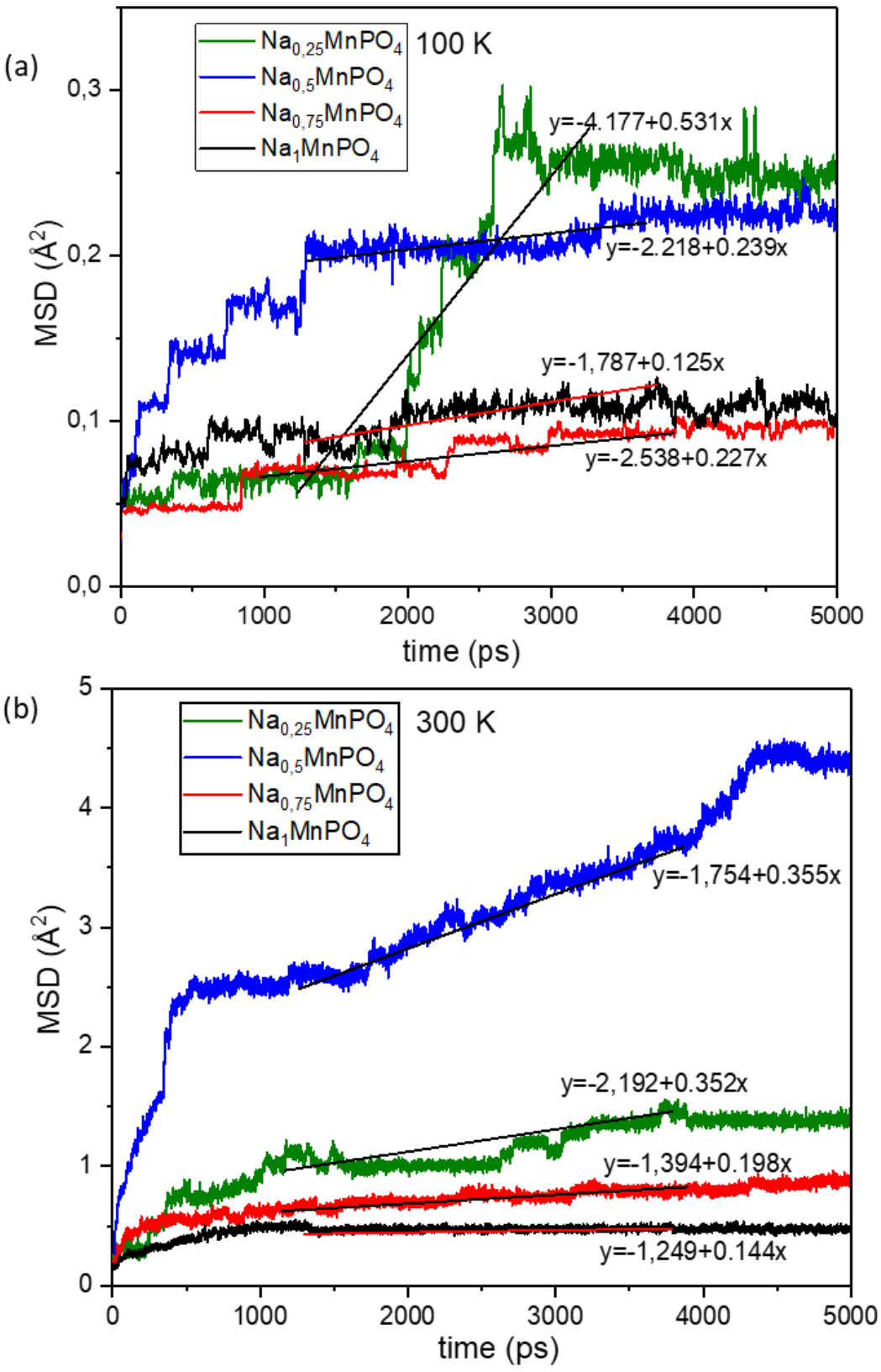

Figure 27: Mean squared displacement plots for Na_xMnPO_4 (X=0.25,0.5,0.75 and 1) for 5 ns at (a) 100 K and (b) 300 K.

From the MSD plots of Na^+ ions in olivine Na_xMnPO_4 at 100K in Figure 27 (a), it is evident that the gradient of MSD increases as the number of de-intercalated Na atoms increases. For $Na_{0.75}MnPO_4$ and Na_1MnPO_4 the MSD of the Na-ions tends to move forward to a constant value faster than $Na_{0.25}MnPO_4$ and $Na_{0.5}MnPO_4$ and confirms that there is less ion diffusion in these two compositions. Figure 27 (b) shows the MSD after 5 ns at 300 K. Similarly, the number of particles involved in the hopping is considerably greater compared to the amount observed at a temperature of 100 K (refer to Figure 27 (a)). However, the MSD observed in all stages of intercalation illustrated in Figure 27 (a) exhibits a very consistent linear trend, which acts as an indicator of the diffusion coefficient.

It should be noted that the slopes of the MSD curve at 300 K demonstrate much higher values compared to those at 100 K. This observation implies that elevated temperatures promote the transport of particles down smaller pathways that are perpendicular to the primary diffusion axis. The mentioned phenomenon was also observed in $LiFePO_4$ molecular dynamics simulations at a temperature of 500 K, with a frequency of 1 or 2 occurrences every 60 ps [140]. In this particular case, it is likely that the observed result is the result of volumetric expansion of the structure coupled with the thermally generated disorder. In fact, it has been established that the use of thermal treatment leads to the conversion of olivine $NaMnPO_4$ to the maricite phase, which is characterised by greater thermodynamic stability. Similar observations as in 100 K were for $Na_{0.75}MnPO_4$ and Na_1MnPO_4, the MSD of the Na ions tends to move toward a constant value faster than $Na_{0.25}MnPO_4$ and $Na_{0.5}MnPO_4$ and confirms that there is less ion diffusion in these compositions also at 300 K.

These findings at 100 and 300 K suggest that the diffusion of Na ions in $NaMnPO_4$ is influenced by the Na concentration. At lower Na concentrations ($Na_{0.25}MnPO_4$ and $Na_{0.5}MnPO_4$), the MSD of Na ions reaches a constant value more quickly, indicating faster and more efficient ion diffusion. On the other hand, at higher Na concentrations ($Na_{0.75}MnPO_4$ and Na_1MnPO_4), the MSD of the Na ions takes longer to stabilise, suggesting slower and less efficient ion diffusion in these compositions. In general, these findings highlight the importance of Na concentration in determining the ion diffusion behaviour in $NaMnPO_4$.

The Na-ion diffusion coefficients (D_{Na}) for de-intercalated olivine Na_xMnPO_4, calculated using equation (104), at 100 K and 300 K are listed in Table 10.

$$D = \left(\frac{1}{6t}\right) < [r(t)]^2 \quad (101)$$

Table 10: The calculated Na^+ ion diffusion coefficients result for Na_xMnPO_4 (x = 0.25,0.5,0.75 and 1) for 5 ns at (a) 100 K and (b) 300 K.

Structures	**Diffusion coefficients (D_{Na})**	
	100 K	300 K
Na_1MnPO_4	$1.842X10^{-10}$	$5.075X10^{-11}$
$Na_{0.75}MnPO_4$	$2.136X10^{-10}$	$1.020X10^{-9}$
$Na_{0.5}MnPO_4$	$1.418X10^{-9}$	$7.929X10^{-9}$
$Na_{0.25}MnPO_4$	$1.722X10^{-9}$	$2.945X10^{-9}$

The Na_xMnPO_4 materials exhibit diffusion coefficients within the range of 1.842×10^{-10} to 1.722×10^{-10} cm^2s^{-1} at a temperature of 100 K. These diffusion coefficients indicate that Na_xMnPO_4 materials have relatively low diffusion rates. This suggests that the movement of ions within the material is slow, which could impact its overall performance in certain applications. At a temperature of 300 K, observed values were determined to fall within the range of 5.075×10^{-11} and 7.929×10^{-9} cm^2s^{-1}. At this higher temperature, the diffusion coefficients of the Na_xMnPO_4 materials are still relatively low compared to other materials. However, it should be noted that the diffusion rates have increased compared to the values observed at 100 K. This suggests that the movement of ions within the material becomes slightly faster as the temperature increases. These findings are important to understand the behaviour of Na_xMnPO_4 materials and their potential applications, as diffusion rates can affect processes such as charge/discharge rates in batteries or ion transport in solid state electrolytes. It is important to note that the diffusion coefficients of Na_1MnPO_4 were found to be lower at 300 K compared to 100 K. However, the diffusion coefficients at 300 K for other materials were found to be higher than those at 100 K. This suggests that temperature plays a crucial role in the diffusion behaviour of Na_xMnPO_4 materials. At lower temperatures, the diffusion rates are slower, indicating a more controlled and efficient charge/discharge process in batteries. However, at higher temperatures, the diffusion rates increase, which can result in faster ion transport in solid-state

electrolytes. These findings pave the way for optimising the performance of Na_xMnPO_4 materials in various applications by controlling the temperature and understanding its influence on diffusion coefficients.

5.5. Summary

The study used the LAMMPS code to fit the interatomic potentials of $NaMnPO_4$ and calculated the RDFs, diffusion coefficients and MSD, at 100 K and 300 K. The results showed that the MSD gradient increases as the number of Na atoms de-intercalated increases. The observed MSD curve at a temperature of 300 K exhibits a significantly greater magnitude compared to that at 100 K. This discrepancy implies that higher temperature promotes the transport of particles along narrower pathways that are orientated perpendicular to the primary axis of diffusion. While the orthorhombic shape of the structure is maintained at a low temperature of 100 K, the situation changes significantly as the temperature increases to 300 K. At this elevated temperature, as shown in Figure 25, the atoms start losing their ordered arrangement, leading to a more disordered structure. This disorder arises from the increased thermal energy at 300 K, which allows atoms to move more freely and deviate from their original positions.

The study also revealed that the Na-Mn interaction exhibits the most significant separation distance, measuring 3.820 Å at 100 K. The absence of defined peaks at this specific concentration in $Na_{0.25}MnPO_4$ can be attributed to the presence of a reduced Na-Na interaction. The study also investigated the diffusion of Na^+ in Na_xMnPO_4, which is crucial to understanding the electrochemical characteristics of the Na_xMnPO_4 cathode material. Na ion diffusion coefficients for olivine $NaMnPO_4$ were calculated at 100 K and 300 K, showing that Na_xMnPO_4 materials have relatively low diffusion rates at 100 K. However, at 300 K, the diffusion rates increased, suggesting that the movement of ions within the material becomes slightly faster. The diffusion of Na ions in $NaMnPO_4$ is influenced by the concentration of Na, with lower concentrations resulting in faster and more efficient ion diffusion. Higher concentrations, such as $Na_{0.75}MnPO_4$ and Na_1MnPO_4, cause slower and less efficient ion diffusion. These findings are crucial for understanding the behaviour of Na_xMnPO_4 materials and their potential applications, as diffusion rates can affect processes such as charge / discharge rates in batteries and ion transport in solid-state electrolytes.

Controlling temperature and understanding its influence on diffusion coefficients can optimise the performance of Na_xMnPO_4 materials in various applications.

Chapter 6. Structure Predictions Using Cluster Expansion

6.1. Introduction

Cluster expansions are mathematical models that describe the behaviour of physical systems by taking into account the interactions between multiple particles. These models, which can be considered as generalisations of the Ising model, provide a framework for studying the effects of many-body interactions. In the domains of materials science, physical chemistry, and condensed matter physics, cluster expansions find extensive application in the investigation of materials that manifest substitutional disorder, wherein certain crystalline positions can accommodate multiple atomic species. In 1973, Van Baal [141] conducted groundbreaking research on the computation of phase diagrams that depict the interplay between order and disorder in a binary alloy with a face-centred cubic (FCC) structure. This was achieved by employing the cluster expansion formalism. Subsequently, cluster expansions have been used effectively to investigate an assortment of crystalline materials that exhibit bulk characteristics, which means that they possess periodicity in three spatial dimensions. The expression can be rewritten using the principles of mathematics as discussed in chapter 3.

During the discharge process (battery operation), Na^+ are introduced into the crystal lattice of $NaMnPO_4$. This is typically accompanied by reduction reactions, involving the reduction of $Mn4^+$ to lower oxidation states. Na^+ occupy vacant sites within the crystal lattice, leading to an intercalated state of $NaMnPO_4$. The insertion of Na^+ increases the overall unit cell volume. The sequence of phase transitions that occurs during the Na intercalation and deintercalation in $NaMnPO_4$ is still unclear due to their random nature. Therefore, a statistical model such as CE is necessary to accurately intercalate Na ions in the crystal structure of $NaMnPO_4$. This model would take into account the random nature of the phase transitions that occur during Na intercalation and

deintercalation. Understanding the sequence of these phase transitions allows for more accurate predictions and control over the insertion and extraction of Na ions. This, in turn, enhances the prediction of the high performance and stability of $NaMnPO_4$ as a cathode material for energy storage applications. In this chapter, we discuss the findings of $NaMnPO_4$ simulations obtained using cluster expansion method, in particular, to the findings on the evaluation of the stability of Na intercalation in the $NaMnPO_4$ olivine phase.

6.2. Computational Details

A flow chart implemented in UNCLE code was used to perform cluster expansion calculations using genetic algorithm approach. The flow chart starts by optimising the structures of the training set with respect to atom position, cell volume, and cell shape using VASP 5.4 with a GGA exchange correlation functional. The calculations started by considering $MnPO_4$ structure with multiple vacancies occupying the same sites as the Na ion, defining a cluster expansion in which an occupation value is smaller than 1, followed by defining a cluster expansion with vacancies.

The number of possible configurations scales with $N^{k,}$ whereby k defines the rank of the CE (i.e., how many elements are located on the active site) and N defines the number of sites considered by CE. The latter is a product of the number of active sites in the primitive unit cell times the number of unit cells up to which to perform the search. The configuration search was set to 4-unit cells. The high throughput stage was set for GGA calculations, containing two minimisations' stages to reduce base set errors and a static single-point energy stage to derive accurate energies. The accuracy was set to standard 500 steps with the plane-wave basis set cut-off at 500 eV and real space projection.

The two minimisations' stages to optimise both atom positions and cell parameters, and one static single-point energy calculation, as shown in Figure 28.

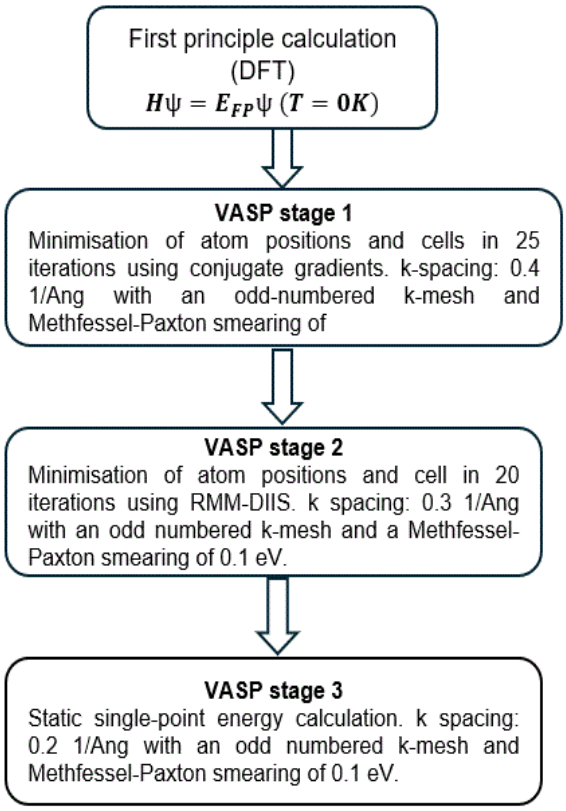

Figure 28: Schematic shoeing VASP stages in cluster expansion.

When investigating the configuration space, attention was paid to 4-unit cells. As mentioned, genetic algorithm was used to optimise the fitting of effective cluster interactions. The fitting scheme was designed to execute a maximum of 20 iterations, with a maximum of 10 structures added in each iteration. The scheme began with an initial training set of 10 structures. The iterative process persisted until the energies of all structures, as projected by the cluster expansion, surpassed the energy computed for the ground state structure at each concentration level that was sampled. It was determined that the constituents were not miscible and that all energies were higher compared to those of the pure element structures. A total of five different cluster expansion fits were performed, and subsequently the standard deviation of the energy predictions was assessed.

To calculate the electronic, mechanical and thermodynamic properties of the predicted structures, the structures were fully optimised using first principles calculations. These calculations were carried out within the framework of the projector augmented wave technique. The Perdew-Burke-Ernzerhof [36] generalised-gradient approximation (GGA) and GGA + U [37] were employed as the exchange-correlation functionals for

the majority of the calculations. The calculations were initiated with a high-spin ferromagnetic setup, ensuring spin polarisation throughout. Energy cut-off of 540 was found to be the optimal energy for all structures and k-pint spacing were varied among the structures as: 7x3x5 ($MnPO_4$), 7x7x5 ($Na_{0.25}MnPO_4$), 9x5x7 ($Na_{0.5}MnPO_4$), 7x7x5 ($Na_{0.65}MnPO_4$), 5x5x5 ($Na_{0.75}MnPO_4$), 3x5x5 ($Na_{0.85}MnPO_4$), and 7x3x5 (Na_1MnPO_4), The DOS computations were performed utilising the non-magnetic GGA and PBE functional at a temperature of 0 K.

6.3. Predicted Structures

To obtain the convex hull plot, in this case two minimisation stages were considered, and both stages were minimised by optimising the volume of the structure isotopically. Figure 29 illustrates the convex hull plot that was obtained after the isotropic optimisation of the volume of the structure. The results of the isotropic volume optimisation calculations indicate that the elements are miscible, suggesting that the phases formed near the ground states with the lowest ΔHf at a specific concentration are likely to be stable. The red line that is emphasised represents systems in the ground state of density functional theory, and the structures located on this red line predicted from the training set are considered to be thermodynamically stable and the selected structure are the ones predicted from the training set. The convex hull plot yielded a total of 62 newly discovered stable phase structures, of which only 7 were found to be stable. The stable structures derived from the binary diagram depicted in Figure 29 exhibits distinct structural properties such as space groups, lattice parameters, and formation energy. The isotropically optimised structures exhibit a cross-validation score of 1.1 meV, suggesting a favourable cluster expansion. This score is below the 5 meV threshold per active position, which represents the standard deviation of 95% of the structures and serves as a reliable indicator of a well-performing cluster expansion.

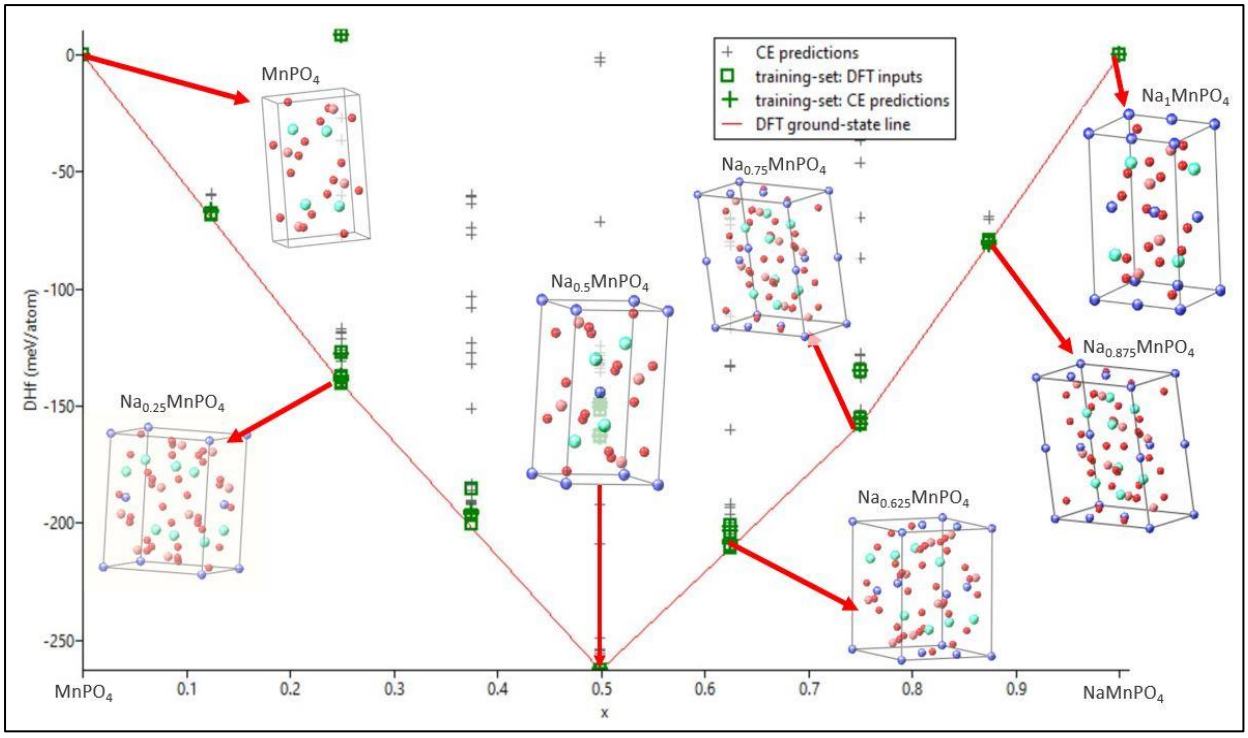

Figure 29: Fully optimised ground state of $NaMnPO_4$ with a cross-validation score of 1.1 meV. The green block represents the DFT input, the red line is the DFT ground state line, and the grey and green crosses represent the anticipated structures from CE.

The parent structures, $MnPO_4$ and $NaMnPO_4$, are randomly mixed to generate the stable phase structures. These parent structures are also expected to be stable according to the DFT ground state line. The predicted structures, namely $Na_{0.25}MnPO_4$, $Na_{0.-5}MnPO_4$, $Na_{0.625}MnPO_4$, $Na_{0.75}MnPO_4$, and $Na_{0.875}MnPO_4$, exhibit distinct lattice parameters characterised by non-equal values for the parameters a, b, and c. The convex hull plot, which was optimised isotropically, provided predictions for the compositions of the $NaMnPO_4$ materials as presented in Table 11. The data presented show that $Na_7Mn_8P_8O_{32}$ exhibits the lowest energy compared to the other structures, mainly attributed to its elevated Na content.

Table 11: Phases determined to be the most stable based on the isotopically optimised convex hull diagram.

Configuration	Unit cell			Volume (Å^3)	Space group	Energy of formation, E_f (kJ/mol)
	a (Å)	b (Å)	c (Å)			
$MnPO_4$	9.938	6.052	4.967	298.710	(Pnma)	-1126.260
$Na_{0.25}MnPO_4$	7.632	9.905	7.677	569.425	(P2_1/c)	-4771.090
$Na_{0.5}MnPO_4$	5.037	10.198	6.197	318.878	(P2_1/c)	-2512.770
$Na_{0.625}MnPO_4$	11.460	8.008	8.050	648.358	P-1	10290.100
$Na_{0.75}MnPO_4$	10.107	20.761	8.085	1319.655	Cc	-5258.680
$Na_{0.825}MnPO_4$	10.343	7.966	7.999	671.536	P-1	-10744.910
Na_1MnPO_4	10.573	6.415	5.042	340.020	Pnma	-1371.750

6.4. Electronic Properties

The PDOS is a valuable tool for examining the atomic states that contribute to the creation of chemical bonds. The strengths and positions of the PDOS bands provide valuable insights into the various electronic interactions taking place inside the system, including charge transfer, ionic interactions, and covalent interactions. Figures 30 and 31 illustrate the comprehensive DOS and PDOS for isotropic and completely optimised systems. This section examines the PDOS for Na intercalation structures obtained from a cluster expansion calculation.

6.4.1. Density of States for $MnPO_4$ and $NaMnPO_4$ Structures

Figure 30 depicts the projected density of states for Na_1MnPO_4 structure and fully de-intercalated $MnPO_4$. The formation of an intermediate band (IB) composed of O p and Mn d states in the deintercalated system significantly reduces the band gap, which is a key difference between the intercalated and deintercalated systems in terms of their electronic structures.

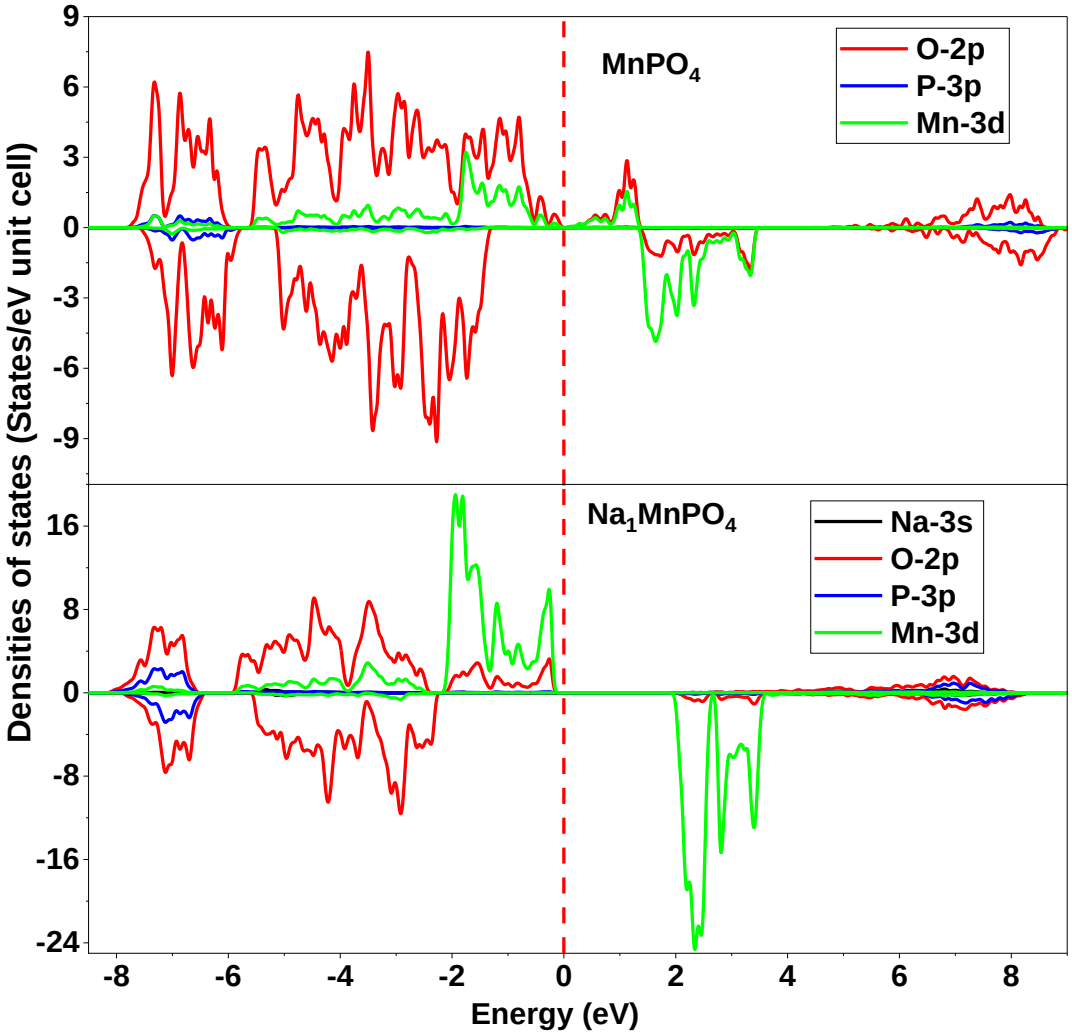

Figure 30: Projected densities of states of CE predicted $MnPO_4$ and Na_1MnPO_4.

The energy difference between the valence band and the conduction band, as illustrated in the DOS plot, for Na_1MnPO_4 is 2.4 eV, while for the de-intercalated system is 0.18 eV. The primary source of the spin-up VBM is attributed to the Mn d states, whereas the spin-down VBM is predominantly influenced by the O p states in the fully intercalated system. Figure 30 shows that the spin up VBM in the fully de-intercalated system exhibits Mn d states that are accompanied by significant O p states. Conversely, the spin down VBM in the same system is primarily composed of O p states, which is comparable to the fully intercalated phase. The spin-down states of Mn d electrons are responsible for the contributions to the conduction band edge in Na_1MnPO_4. The de-intercalated base's conduction band edge is primarily attributed to Mn up-spin d electrons, with a minor contribution from O p states. This stands in contrast to other factors being considered. The compound Na_1MnPO_4 exhibits a valence band edge that is mainly influenced by up-spin electrons of Mn. On the other

hand, the downspin electrons the downspin electrons are situated approximately 1 eV below the VBM. This suggests that the redox reaction is predominantly driven by the majority of spin electrons. The vacant states located at the Na_1MnPO_4 band edge of Na_1MnPO_4 exhibited considerable dispersion across a wide spectrum of energy levels. In the state of complete de-intercalation, the band edge unoccupied states are confined to a limited energy range of 0.7 to 1.6 eV in the spin-up states. Both Na_1MnPO_4 and $MnPO_4$ exhibit a valence band in which the spin-up states of the Mn and O atoms are situated within a comparable energy range, indicating the formation of a directional covalent bond between them. On the contrary, the relocation of the Mn d states to the conduction band in the minority spin state is attributed to magnetic polarisation. The p states of oxygen are distributed in the minority spin channel of the valence band because of their non-magnetic nature. The electronic states of P and O in the energy range of -4 to -5 eV for Na_1MnPO_4 and -4 to -6 eV for $MnPO_4$ exhibit energetic degeneracy, suggesting the potential for the formation of a covalent interaction between them. In addition, these states are inactive in terms of the chemical reaction, since they are located at a considerable depth in the valence band.

6.4.2. Density of States for Intercalated Na_xMnPO_4 (x = 0.25, 0.5, 0.625, 0.75, and 0.825) Predicted Structures

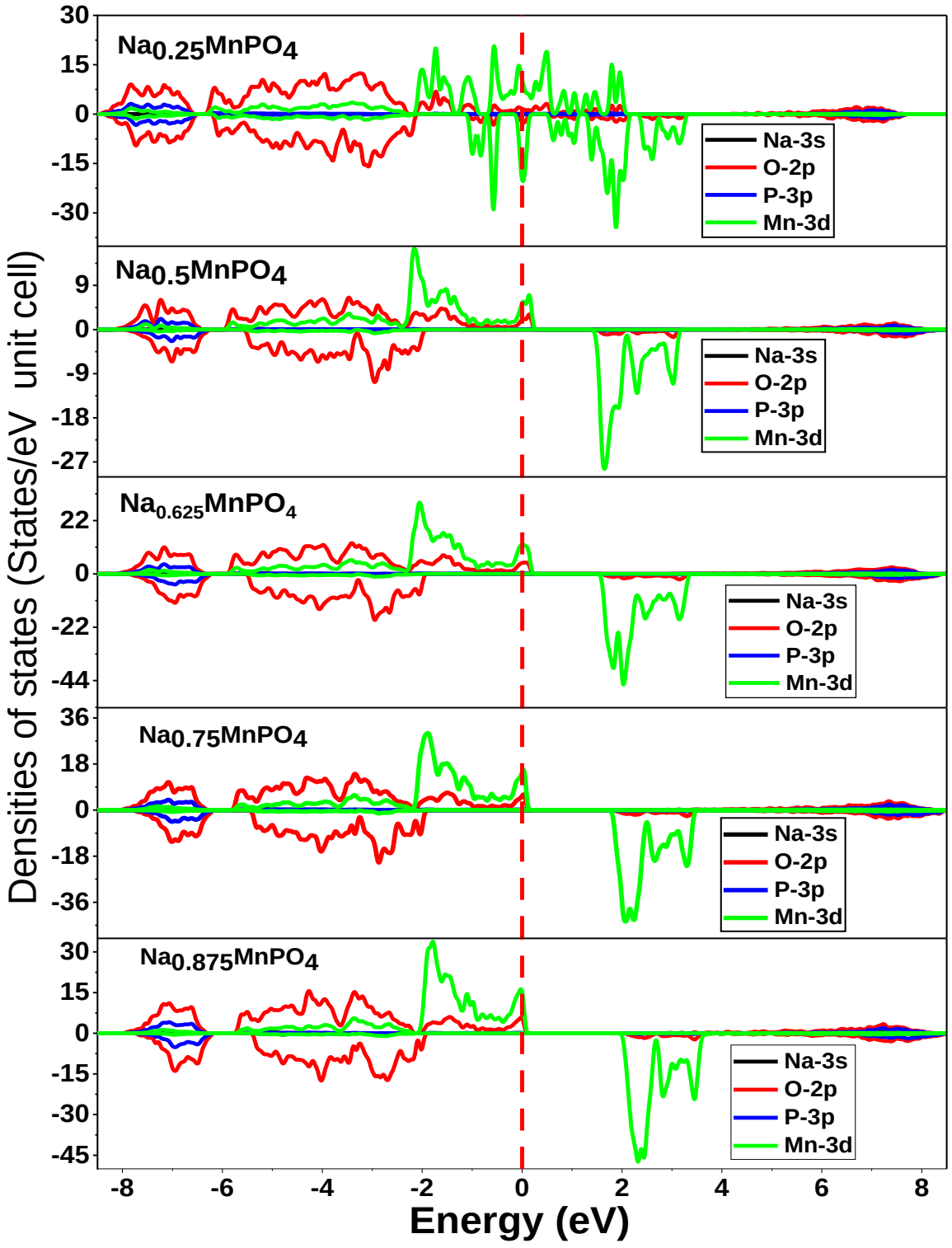

Figure 31: Spin-polarised DOS near Fermi level of olivine Na_xMnPO_4 (x = 0.25, 0.5, 0.625, 0.75, and 0.825) structures. The Fermi level is set to 0 eV and is shown by the dashed lines.

Figure 31 shows the DOS projected on atoms for the intermediate ground states of Na_xMnPO_4, with compositions x = 0.25, 0.5, 0.625, 0.75, and 0.825. These ground states were generated using the cluster expansion approach, as explained in the section 6.2 on computational details. From the parent structure Na_1MnPO_4, it was observed that DOS consists of spin-up electronic states of Mn d states and O p states between 0.2eV and 0.8 eV near the Fermi line, and spin-down Mn d states between 2 and 4 eV near the Fermi line in the CBM. Interestingly, compared to other de-intercalated structures, the DOS for the de-intercalated $Na_{0.825}MnPO_4$ reveals similar features to that of $MnPO_4$. This is evidenced by the presence of intermediate band states, which emerge from the spin-up electronic states of the Mn d states. Additionally, these IB states show a considerable contribution from O-p states. Additionally, Figure 31 shows the progression of de-intercalation from $Na_{0.75}MnPO_4$ to $Na_{0.25}MnPO_4$, highlighting the role of O in the IB states. Moreover, a drop in the Na concentration can be observed to lead to a systematic increase in the breadth of the IB. Furthermore, the energy levels of the Mn d and O p states are found to degenerate throughout the valence band. This observation suggests the existence of a covalent bonding between the Mn and O atoms. However, the Mn d states in the valence band exhibit concentrated characteristics within the energy range of -6 to -2 eV, whereas the O p states primarily occupy the higher energy region. Therefore, the bonding relationship between Mn and O exhibits a mixed ionocovalent character. Furthermore, the energetic degeneracy of the P-p and O-p-states is observed throughout the entire VB region for both spin channels. This degeneracy is particularly significant within the energy range of -6 to -6 eV.

6.5. Mechanical Properties

6.5.1. Elastic Properties

Precision determination of elasticity is crucial to gaining a comprehensive understanding of the mechanical stability and elastic characteristics of the predicted structures $MnPO_4$, $Na_{0.25}MnPO_4$, $Na_{0.5}MnPO_4$, $Na_{0.75}MnPO_4$, $Na_{0.625}MnPO_4$, $Na_{0.85}MnPO_4$, and Na_1MnPO_4. As usual, calculations were carried out at a temperature of absolute zero (0 K) in order to minimise any temperature-dependent variations in the C_{ij} values. The calculation of the elasticity tensor components, denoted C_{ij}, was performed using the first derivatives of the stresses obtained through density functional theory calculations, as opposed to utilising the second derivatives of the total energy with respect to strain. Therefore, this approach effectively circumvents the numerical challenges commonly encountered when evaluating the second derivatives of the overall energy with respect to strain, while also minimising the required number of DFT calculations. The sensitivity of C_{ij} to the k-point mesh necessitated conducting a set of convergence calculations for each structure. These calculations were performed to determine the appropriate k-point and cut-off energy values for each distinct C_{ij} in every material as outlined in section 6.2.

Table 12: The unique C_{ij} (GPa) for the triclinic Na_xMnPO_4 structures.

C_{ij}	Na_1MnPO_4	$Na_{0.85}MnPO_4$	$Na_{0.75}MnPO_4$	$Na_{0.625}MnPO_4$	$Na_{0.5}MnPO_4$	$Na_{0.25}MnPO_4$	$MnPO_4$
C_{11}	138.40	132.38	140.57	129.55	129.69	137.39	108.12
C_{12}	73.18	70.45	67.37	47.67	38.56	59.01	-8.79
C_{13}	65.25	68.70	45.69	51.38	47.41	74.15	15.67
C_{22}	127.39	125.23	144.49	144.45	156.22	166.78	226.60
C_{23}	54.82	58.80	61.16	29.42	18.41	60.90	-13.23
C_{33}	156.40	129.69	137.05	126.93	118.13	136.60	55.72
C_{44}	40.42	46.40	44.94	23.93	28.65	48.49	26.11
C_{55}	42.28	47.24	29.92	51.65	46.83	71.83	46.49
C_{66}	44.62	46.75	45.86	33.63	45.68	54.15	29.43

Independent elastic constants for the crystal structure are denoted as C_{11}, C_{22}, C_{33}, C_{12}, C_{13}, C_{23}, C_{44}, C_{55} and C_{66}.

Table 12 represents the calculated elastic constants $MnPO_4$, $Na_{0.25}MnPO_4$, $Na_{0.5}MnPO_4$, $Na_{0.625}MnPO_4$, $Na_{0.875}MnPO_4$, and Na_1MnPO_4 CE predicted structures. It has been established that for a structure to maintain mechanical stability, it is important that both B and C_{44} possess positive values. Therefore, the findings presented in Table 12 demonstrate that the predicted structures effectively meet the stability criteria of a crystal at a pressure of 0 GPa.

Table 13 presents the elastic properties calculated for Na_xMnPO_4 CE predicted structures. Based on the Pugh criterion, it is seen that Na_1MnPO_4, $Na_{0.825}MnPO_4$, $Na_{0.75}MnPO_4$, $Na_{0.625}MnPO_4$, and $Na_{0.25}MnPO_4$ crystal structures exhibit ductile behaviour, while the $Na_{0.5}MnPO_4$ and $MnPO_4$ structures demonstrate brittleness.

Table 13: Calculated elastic properties for Na_xMnPO_4 (x = 1, 0.825, 0.75, 0.625, 0.5, 0.25, 0) CE predicted structures.

Structures	B_H	G_H	E_H	B/G	ν
Na_1MnPO_4	89.60	40.19	104.89	2.206	0.303
$Na_{0.825}MnPO_4$	86.79	39.73	103.41	2.1844	0.3014
$Na_{0.75}MnPO_4$	85.22	40.02	103.80	2.1297	0.2970
$Na_{0.625}MnPO_4$	72.69	38.23	97.57	1.9012	0.276
$Na_{0.5}MnPO_4$	67.42	42.58	105.52	1.5833	0.2391
$Na_{0.25}MnPO_4$	90.88	48.64	123.80	1.8684	0.2729
$MnPO_4$	37.55	41.31	90.68	0.9090	0.0975

6.5.2. Thermodynamic Properties

6.5.2.1. Debye Temperature

Table 14 shows the calculated volumetric density, sound velocities, and Debye temperature as a function of Na removal. Derived from the calculated elastic constants, the calculated Debye temperature $\boldsymbol{\theta_D}$ for all structures were found to be ranging between 544.1 K and 484.6 K, with $Na_{0.625}MnPO_4$ having the lowest value and

$Na_{0.25}MnPO_4$ having the highest value. Unfortunately, we were unable to uncover any previous experimental or theoretical data with which to compare our computed results. But we compared the values obtained from the CE structures with the structures obtained from the random substitutions of maricite and olivine from chapter 4.

Table 14: Calculated volumetric density ρ (in kg/m^3), longitudinal ν_l transverse ν_t, and average sound velocities ν_m in m/s, and Debye temperature θ_D in Kelvin.

	ρ	ν_t	ν_l	ν_m	θ_D
Na_1MnPO_4	3358	3463	6536	3870	500
$Na_{0.825}MnPO_4$	3363	3440	6452	3843	496.6
$Na_{0.75}MnPO_4$	3365	3450	6420	3852	497.8
$Na_{0.625}MnPO_4$	3357	3362	6047	3745	484.6
$Na_{0.5}MnPO_4$	3362	3558	6076	3945	509.4
$Na_{0.25}MnPO_4$	3631	3762	6732	4188	544.1
$MnPO_4$	3333	3515	5263	3841	494.0

It was noted that the $\boldsymbol{\theta_D}$ values for the parent structures from CE are comparable with those obtained in substitutions of maricite and olivine with a small deviation. While $Na_{0.25}MnPO_4$ was found to be showing a high $\boldsymbol{\theta_D}$ value of 544.1 K compared to 486.0 K and 476.2 K for structures obtained from the random substitutions in maricite and olivine, respectively. As seen in Table 14, the Na intercalation through CE results show no monotonic drop in all sound velocities as well as the $\boldsymbol{\theta_D}$ for all the systems.
Additionally, DFT was used to inverstigate essential thermodynamic parameters such as specific heat at constant volume (Cv), free energy, and entropy calculated at 0 GPa pressure and 0–3000 K temperatures as depicted in Figure 32 to 34. The findings reveal that the influence of temperature on Cv, free energy, and entropy is significant for all the systems. At low temperatures, the rate of increase of Cv is rapid for all intercalation phases, regardless of the intercalation stage. During high temperature intercalation, the value of Cv of all stages of the intercalation approaches the classical asymptotic limit, also known as the Dulong–Petit limit. At low temperatures, the fluctuation of free energy versus temperature, as well as the variation of Cv versus temperature, shows that the increase in free energy is significant for all intercalation stages.

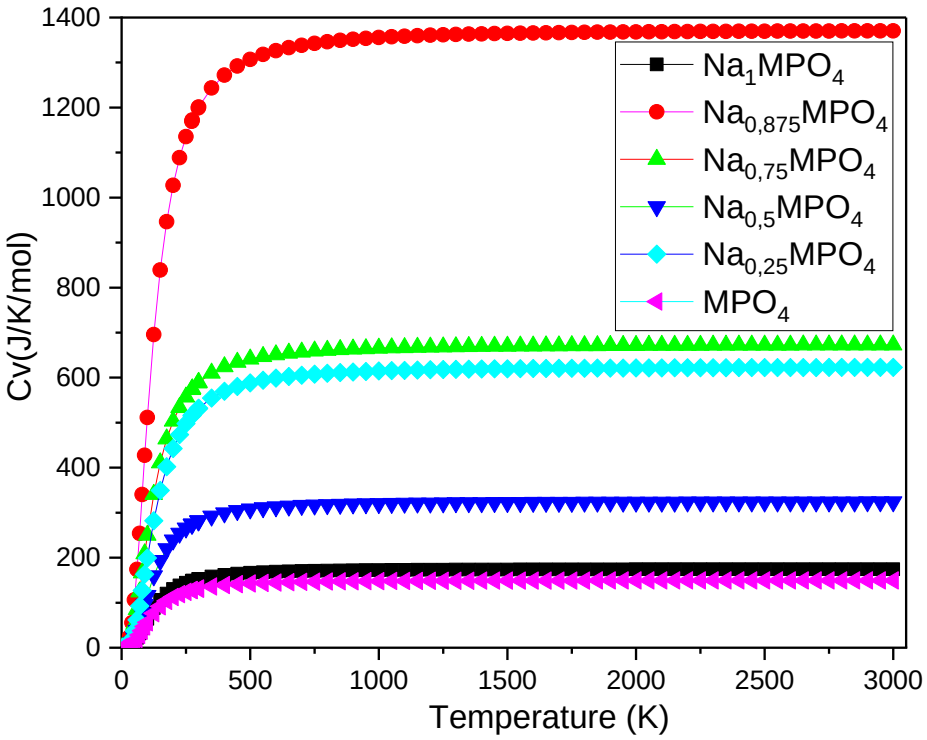

Figure 32: Temperature vs specific heat at constant volume (Cv) of Na_xMnPO_4 (x = 1, 0.825, 0.75, 0.625, 0.5, 0.25, 0).

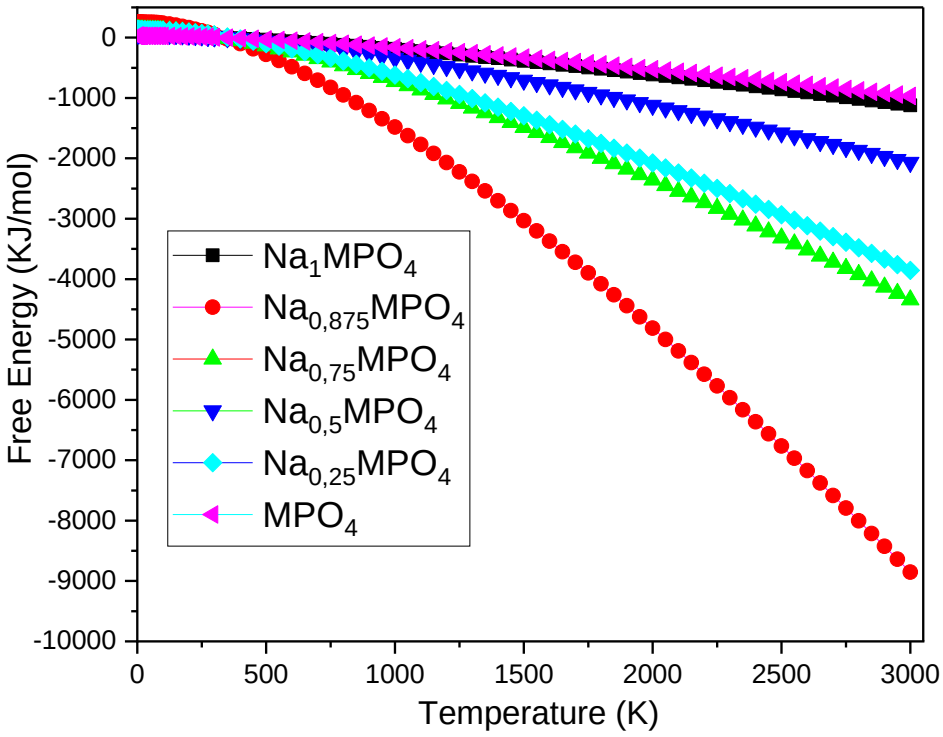

Figure 33: Temperature vs. Free Energy of Na_xMnPO_4 (x = 1, 0.825, 0.75, 0.625, 0.5, 0.25, 0).

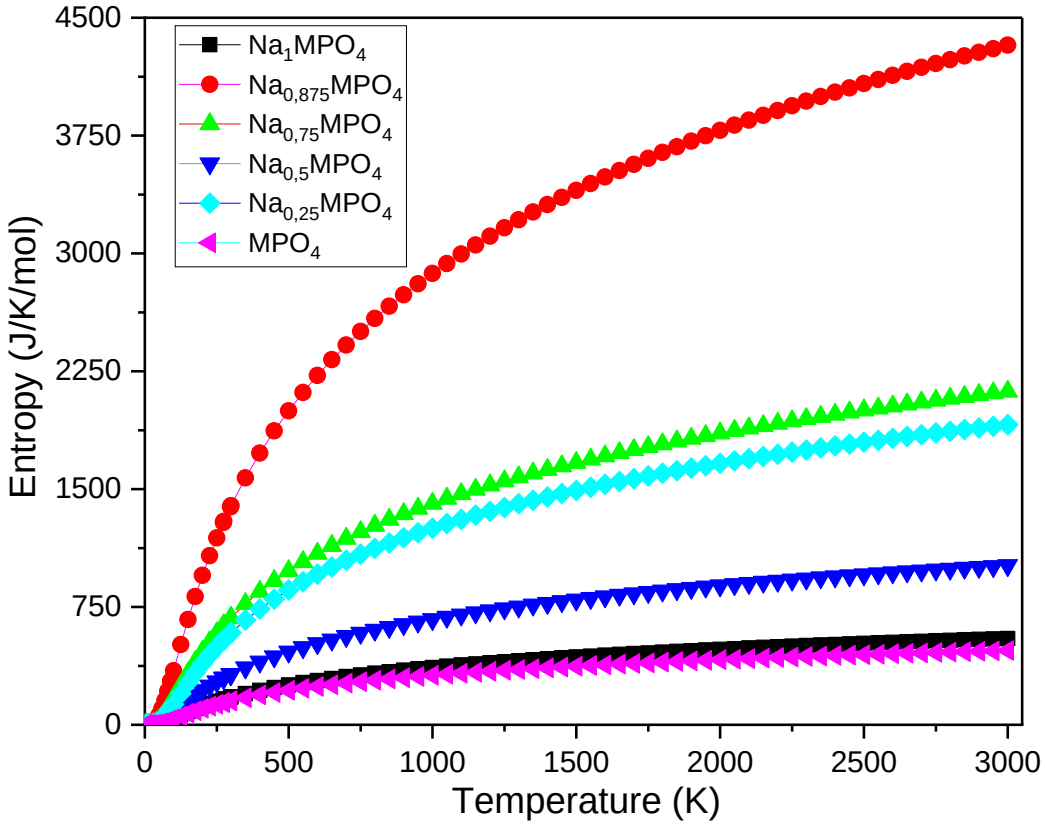

Figure 34: Temperature vs Entropy of Na_xMnPO_4 (x = 1,0.825, 0.75, 0.625, 0.5, 0.25, 0).

6.6. Summary

This chapter introduces the utilisation of cluster expansion as a multiscale pipelining method, establishing a connection between first-principles calculation and large-scale atomistic simulations as well as Monte Carlo simulation. In the present case, CE was employed to examine the phase stabilities of Na de-intercalation in $NaMnPO_4$. The phase diagram of the ground state exhibits a range of configurations characterised by varying concentrations and symmetries. The structures that underwent isotropic volume optimisation yielded a cross-validation score of 1.1 meV, suggesting that the cluster expansion is of good quality as it falls below the threshold of 5 meV per active position. The stability of the structures found on the isotropically optimised volume and fully optimised binary diagram was assessed by calculating their mechanical and electronic properties using DFT. On the basis of the analysis of the electronic

structure, it is observed that both of the parent structures exhibited semiconducting behaviour, while the remaining structures exhibited semi-metallic characteristics. The mechanical stability of $NaMnPO_4$ was shown by the estimated elastic constants, since the stability conditions were met for all intercalated systems, with the exception of the parent structure $MnPO_4$. Based on the Pugh criterion on ductility and brittleness properties, it was observed that the structures of Na_1MnPO_4, $Na_{0.825}MnPO_4$, $Na_{0.75}MnPO_4$, $Na_{0.625}MnPO_4$, and $Na_{0.25}MnPO_4$ exhibit ductile characteristics, while the structures of $Na_{0.5}MnPO_4$ and $MnPO_4$ display brittleness. These findings suggest that the addition of Na ions enhances the ductility of $Na_{1-x}MnPO_4$ structures. The higher concentration of Na ions leads to increased ductility, as evidenced by the ductile characteristics observed in Na_1MnPO_4 and $Na_{0.825}MnPO_4$.

Chapter 7. Molecular Dynamics Simulations of CE Predicted Structures

7.1. Introduction

Molecular dynamics approach provides significant information on the dynamic characteristics of atomic locations and velocities at various time intervals throughout the simulation as discussed in chapter 3 [139]. In this chapter, the performance of the developed interatomic potentials of olivine $NaMnPO_4$ presented in chapter 5 are evaluated by calculating transport properties of CE predicted structures, relevant to battery performance profile. Thus, the effect of temperature on Na diffusion characteristics is investigated using the energy minimisation technique. Similar computational details presented in section 5.3. of chapter 5 were followed.

7.2. Mean Square Displacements at 100 K

The mean square displacements of Na+ ions for the systems $Na_{0.25}MnPO_4$, $Na_{0.5}MnPO_4$, and $Na_{0.75}MnPO_4$ at a temperature of 100 K are depicted in Figures 34 to 36. Despite the significant electrostatic attraction between Na+ ions and their respective lattice sites in crystalline materials, the simulation that spanned a time period of 5 nanoseconds performed at 100 K temperature demonstrated the presence of Na^+ ion migration within all examined structures. The ballistic trajectory of Na^+ ions for extremely short durations (<1 ps) has been reported in the case of $Na_{0.25}MnPO_4$ and $Na_{0.75}MnPO_4$.

Nevertheless, over a significant duration of picoseconds, the MSDs of Na^+ ions exhibit a proportional increase with time, suggesting a change in the dynamics of Na^+ ions towards the diffusive regime. This finding illustrates that a simulation length of 5 ns is adequate for acquiring dependable observations regarding the long-range movements of Na^+ ions, while also preserving the confidentiality and integrity of the data. The ballistic trajectory observed for Na^+ ions in $Na_{0.25}MnPO_4$ and $Na_{0.75}MnPO_4$ indicates their rapid linear motion over a brief temporal interval. However, with the passage of time, the MSDs of Na^+ ions exhibit a linear growth pattern, suggesting that their motion becomes increasingly stochastic and diffusive. This discovery provides confirmation

that a simulation duration of 5 ns is sufficient to investigate the long-range dynamics of sodium ions.

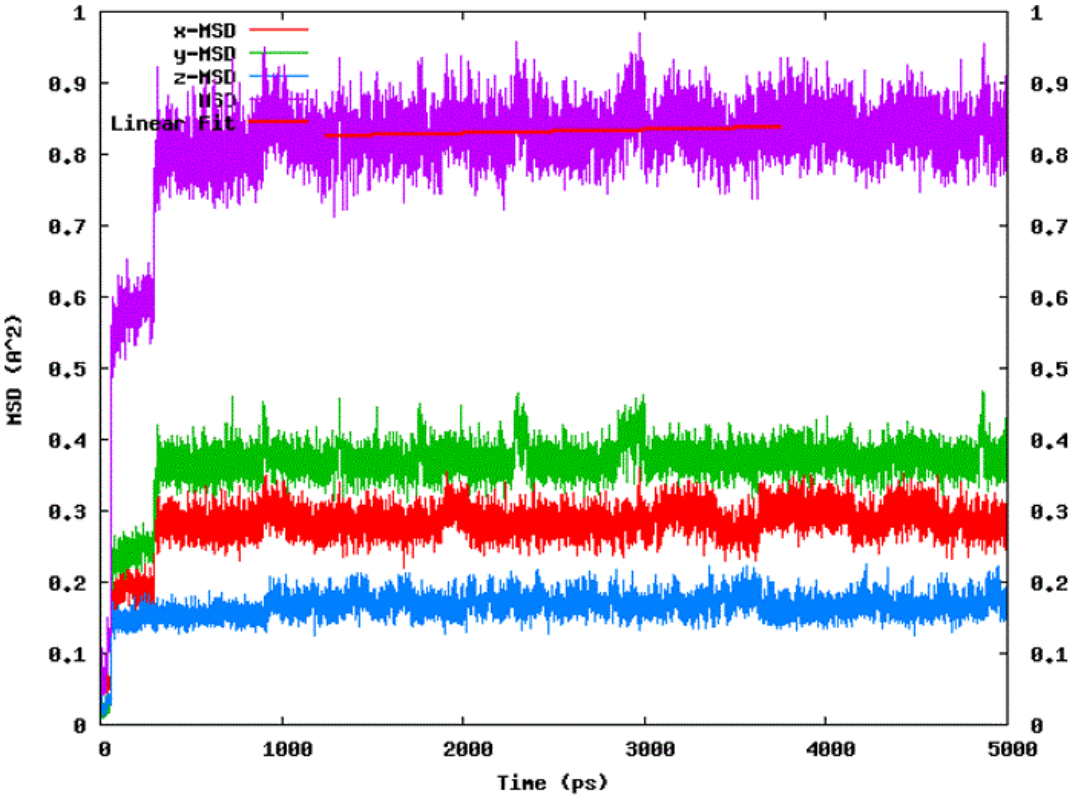

Figure 35: MSD vs time along the [100], [010], and [001] directions for a 5 ns simulation for $Na_{0.25}MnPO_4$ at 100 K.

From the MSD plots of Na^+ ions in olivine Na_xMnPO_4 at 100 K in Figures 35 to 37, it was observed that the calculated gradient of MSD for $Na_{0.25}MnPO_4$, $Na_{0.5}MnPO_4$, and $Na_{0.75}MnPO_4$ is 4.85×10^{-9}, 2.088×10^{-7}, and 7.16×10^{-9}, respectively. For $Na_{0.25}MnPO_4$, the MSD of the Na+ ions tend to move toward a constant value faster than $Na_{0.5}MnPO_4$ and $Na_{0.75}MnPO_4$, suggesting that there is less ion diffusion in this composition, which is consistent with findings for randomly substituted Na_xMnPO_4 structures.

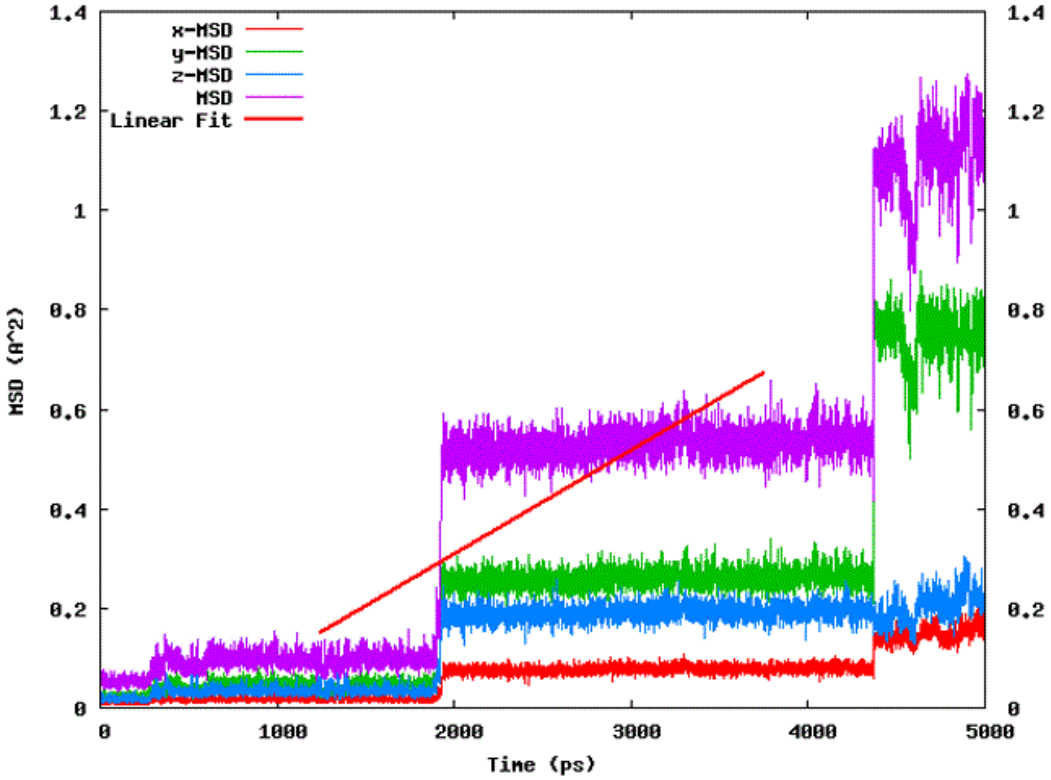

Figure 36: MSD against time along the [100], [010], and [001] directions for a 5 ns simulation for $Na_{0.5}MnPO_4$ at 100 K.

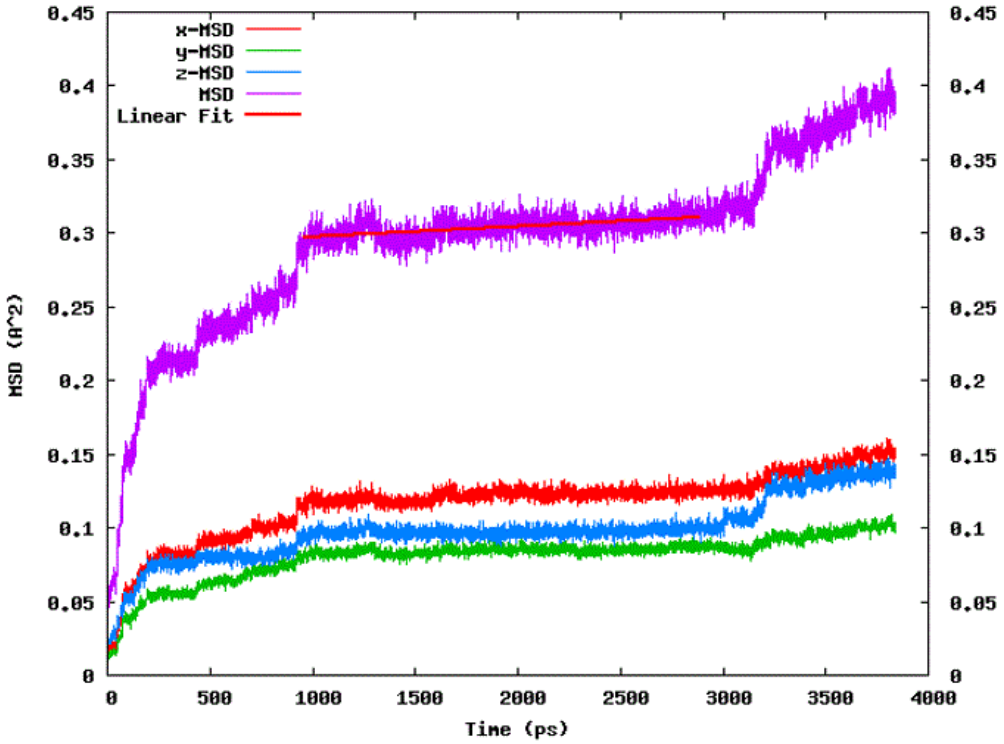

Figure 37: Mean square displacement against time along the [010], [100], and [001] directions for 5 ns simulation for $Na_{0.75}MnPO_4$ at 100 K.

Based on the findings obtained, it was observed that the MSD of $Na_{0.25}MnPO_4$ along the [001] direction, as shown in Figure 35, shows a consistently linear increase over time. This characteristic behaviour serves as an indicator of the diffusion coefficient. It should be noted that the slope of the MSD curve in the crystallographic direction [001] has a significantly reduced magnitude in $Na_{0.75}MnPO_4$ compared to other structural configurations. This suggests that the diffusion of sodium ions in $Na_{0.75}MnPO_4$ is slower and more restricted along the [001] direction, possibly due to the presence of structural arrangement or constraints. These findings are in line with the expectations based on the crystal structure of $Na_{0.75}MnPO_4$, which features tighter packing and a more ordered arrangement of atoms along the [001] direction. Therefore, the reduced magnitude of the slope in the MSD curve supports the hypothesis that the diffusion behaviour in $Na_{0.75}MnPO_4$ is influenced by the structural template along the [001] direction.

7.3. MD Mean Square Displacements at 300 K

The MSD plots of Na^+ ions in olivine Na_xMnPO_4 at a higher temperature are illustrated in Figures 39 to 40. The figures depict the MSD after a 5 ns duration at a temperature of 300 K. As expected, the number of particles engaged in the hopping is markedly greater at 300 K compared to the quantity seen at a temperature of 100 K, as depicted in Figure 38. The intercalation stages of $Na_{0.5}MnPO_4$ and $Na_{0.75}MnPO_4$, as depicted in Figures 39 and 40, respectively, exhibit a rather consistent and linear trend in terms of MSD, which serves as an indicator of the diffusion coefficient. However, after a substantial period of picoseconds, the MSDs of Na^+ ions demonstrate a direct correlation with time, indicating a shift in the behaviour of Na^+ ions towards the diffusive regime.

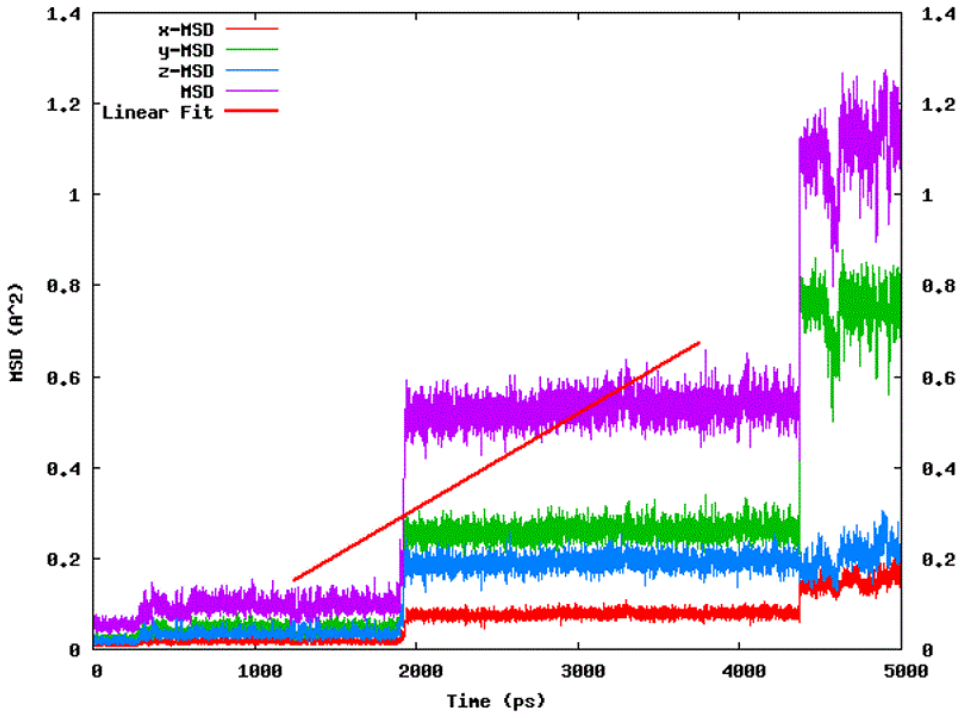

Figure 38: Mean square displacement versus time along the [100], [010], and [001] directions for 5 ns simulation for $Na_{0.25}MnPO_4$ at 300 K.

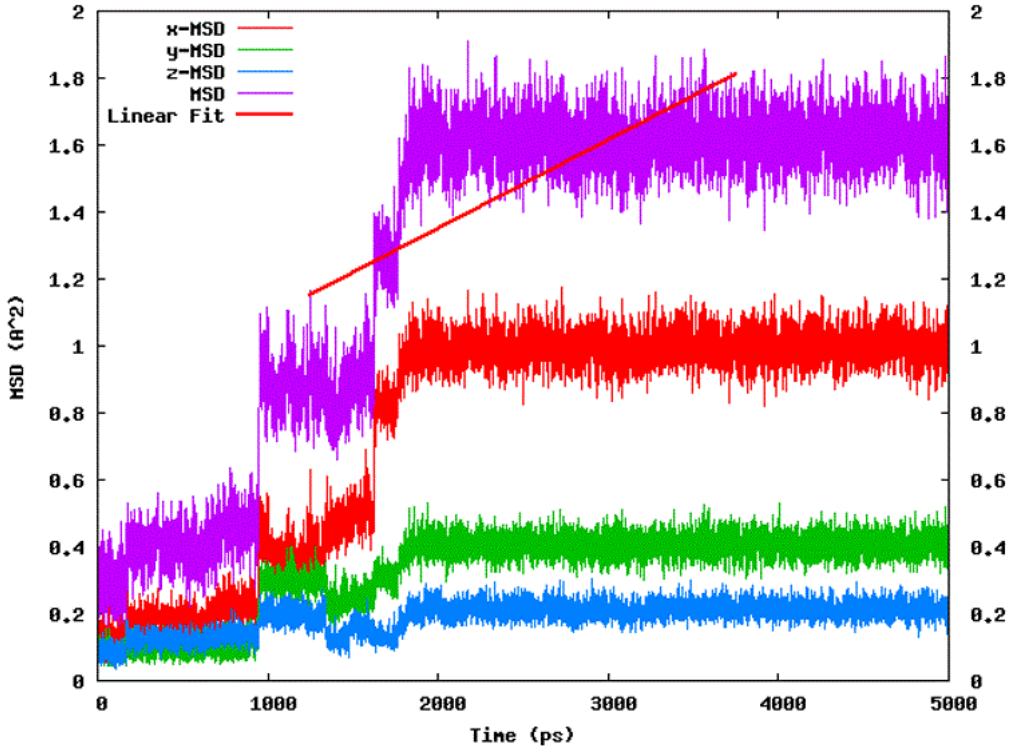

Figure 39: Mean square displacement against time along the [100], [010], and [001] directions for 5 ns simulation for $Na_{0.5}MnPO_4$ at 300 K.

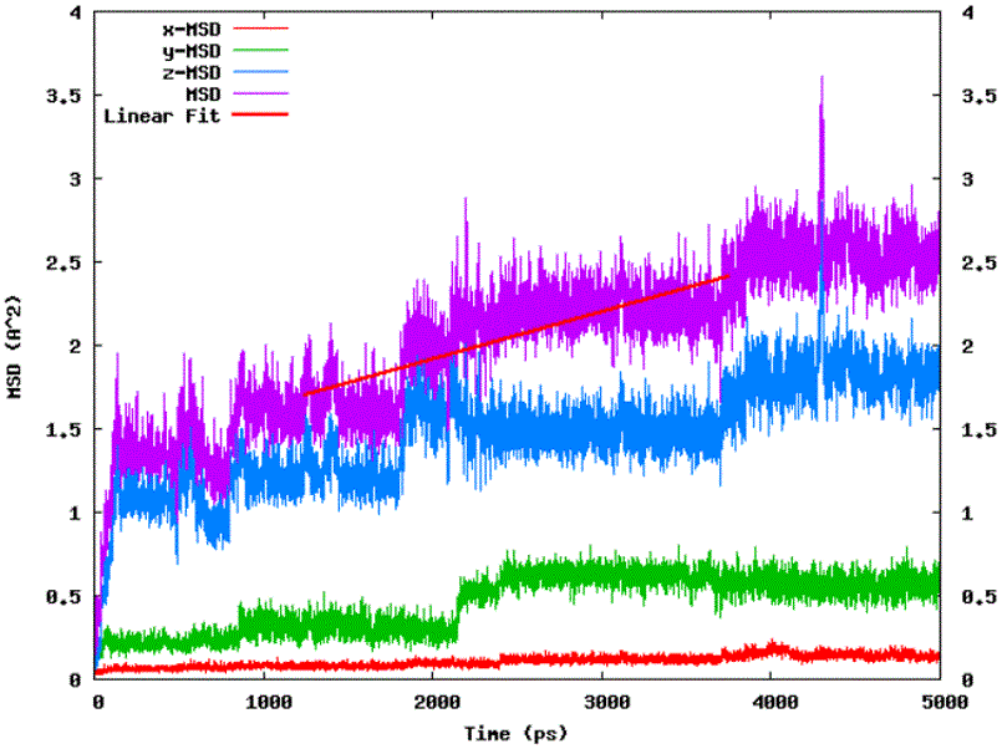

Figure 40: MSD vs time along the [010], [100], and [001] directions for 10 ns simulation for $Na_{0.75}MnPO_4$ at 300 K.

The gradients of the MSD for $Na_{0.25}MnPO_4$, $Na_{0.5}MnPO_4$, and $Na_{0.75}MnPO_4$ were determined to be $2.636x10^{-7}$, $2.812x10^{-7}$, and $2.487x10^{-7}$, respectively. In Figure 38 of $Na_{0.25}MnPO_4$, the MSD of the Na^+-ions exhibits a comparable pattern to that of $Na_{0.5}MnPO_4$ at 100 K. Specifically, a sluggish diffusion is observed below 2 ns, followed by a sudden escalation leading to a consistent trend. This observation provides evidence that the rate of ion diffusion decreases at lower time intervals in these compositions. The Na^+ ions in $Na_{0.25}MnPO_4$ have a similar behaviour to those of $Na_{0.5}MnPO_4$, indicating that the composition of the material plays a significant role in the diffusion rate of ions. Sluggish diffusion below 2 ns may be attributed to the presence of barriers or obstacles that hinder the movement of ions. However, as time progresses, these barriers seem to diminish, allowing for more consistent and efficient ion diffusion. Overall, these findings highlight the importance of composition in determining the diffusion characteristics of ions in materials, for instance $Na_{0.25}MnPO_4$ characteristics.

Based on our computed results at a temperature of 300 K, it was observed that the MSD of all structures exhibits diffusion along distinct directions. Specifically,

$Na_{0.25}MnPO_4$ demonstrates diffusion along the [010] direction, $Na_{0.5}MnPO_4$ along the [001] direction, and $Na_{0.75}MnPO_4$ along the [100] direction, as depicted in Figure 38 to 40. Both $Na_{0.5}MnPO_4$ and $Na_{0.75}MnPO_4$ exhibit a linear relationship. This linear relationship serves as an indicator of the diffusion coefficient. It should be noted that the slope of the MSD curve along the crystallographic direction [001] is significantly reduced in $Na_{0.75}MnPO_4$ compared to other structural configurations. It is proposed that elevated temperature facilitates the movement of particles down narrower pathways that are orientated perpendicular to the primary axis of diffusion. This phenomenon can be attributed to the unique crystal structure of $Na_{0.75}MnPO_4$, where diffusion pathways are more constrained in the [001] direction. The reduced slope of the MSD curve suggests that diffusion in $Na_{0.75}MnPO_4$ is hindered along this direction, indicating a lower diffusion coefficient. This finding highlights the importance of considering crystallographic orientations when studying diffusion behaviour in materials, as it can greatly influence the transport properties.

7.4. Mean Square Displacements at 500 K

Figures 41 to 43 illustrate the MSD following a 5 ns time at a temperature of 500 K for $Na_{0.25}MnPO_4$, $Na_{0.5}MnPO_4$, and $Na_{0.75}MnPO_4$, respectively. Based on the calculations, it was observed that the MSD values for the NVT dynamics of $Na_{0.75}MnPO_4$ were calculated for the initial 3800 ps rather than the intended duration of 5 ns, as shown in Figure 43. The MSD data exhibited distinct increasing trends in each system, suggesting variations in the motion states of the Na^+ ions within the different models. The results showed that the calculated MSD gradients for $Na_{0.25}MnPO_4$, $Na_{0.5}MnPO_4$, and $Na_{0.75}MnPO_4$ are $1.064x10^{-6}$, $3.38x10^{-8}$, and $2.419x10^{-7}$, respectively. Moreover, the findings revealed that two of the structures exhibited diffusion in the same directions, that is, $Na_{0.25}MnPO_4$ and $Na_{0.75}MnPO_4$ in the [010] direction while $Na_{0.5}MnPO_4$ exhibited diffusion in the [001] direction as depicted in Figure 42. Additionally, above 4200 ps, $Na_{0.25}MnPO_4$ exhibited diffusion in the [010] direction. The $Na_{0.75}MnPO_4$ structure in the [001] direction showed a consistently linear relationship, which can be used as an indicator of the diffusion coefficient. It is worth noting that the slope of the MSD curve in the [001] direction exhibits a significant decrease in $Na_{0.25}MnPO_4$ compared to other structures.

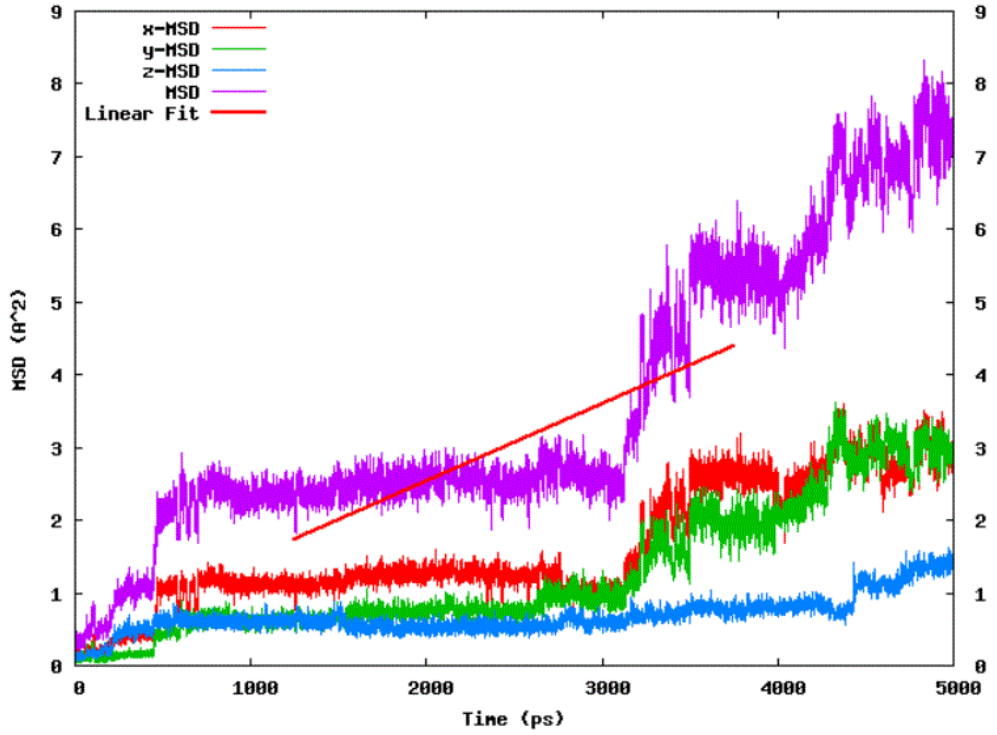

Figure 41: MSD vs. time for $Na_{0.25}MnPO_4$ at 500 K in the [100], [010], and [001] directions for a simulation of 5 ns.

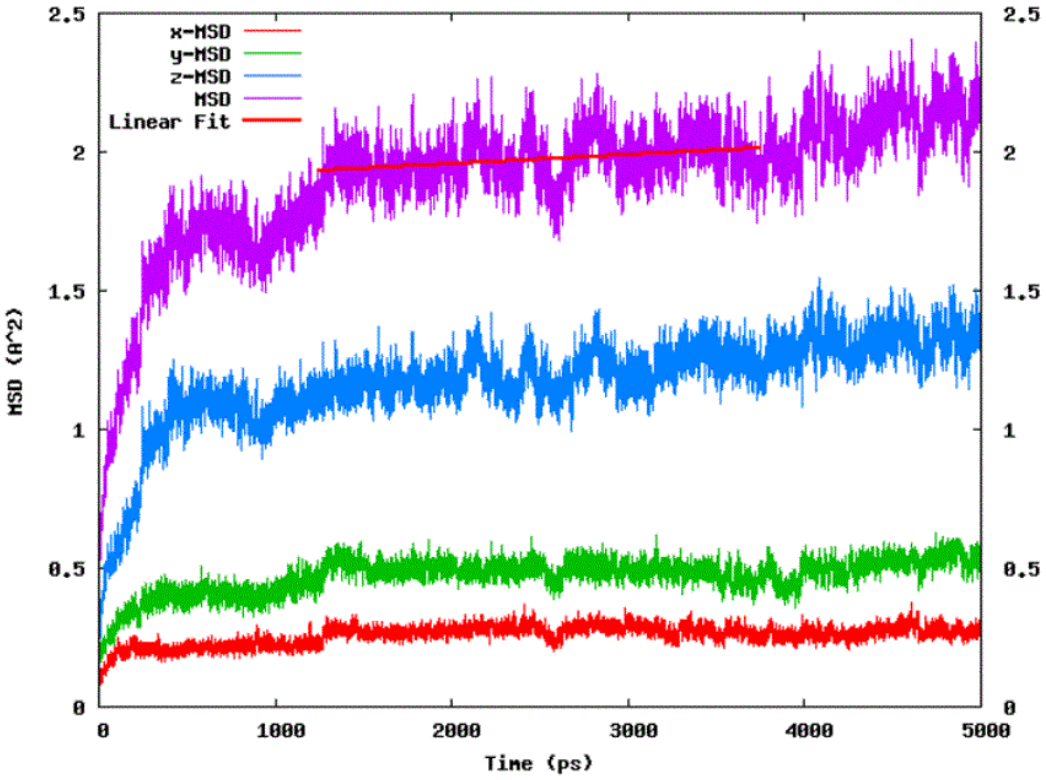

Figure 42: Mean square displacement versus time for $Na_{0.5}MnPO_4$ at 500 K in the [100], [010], and [001] directions for a simulation of 5 ns.

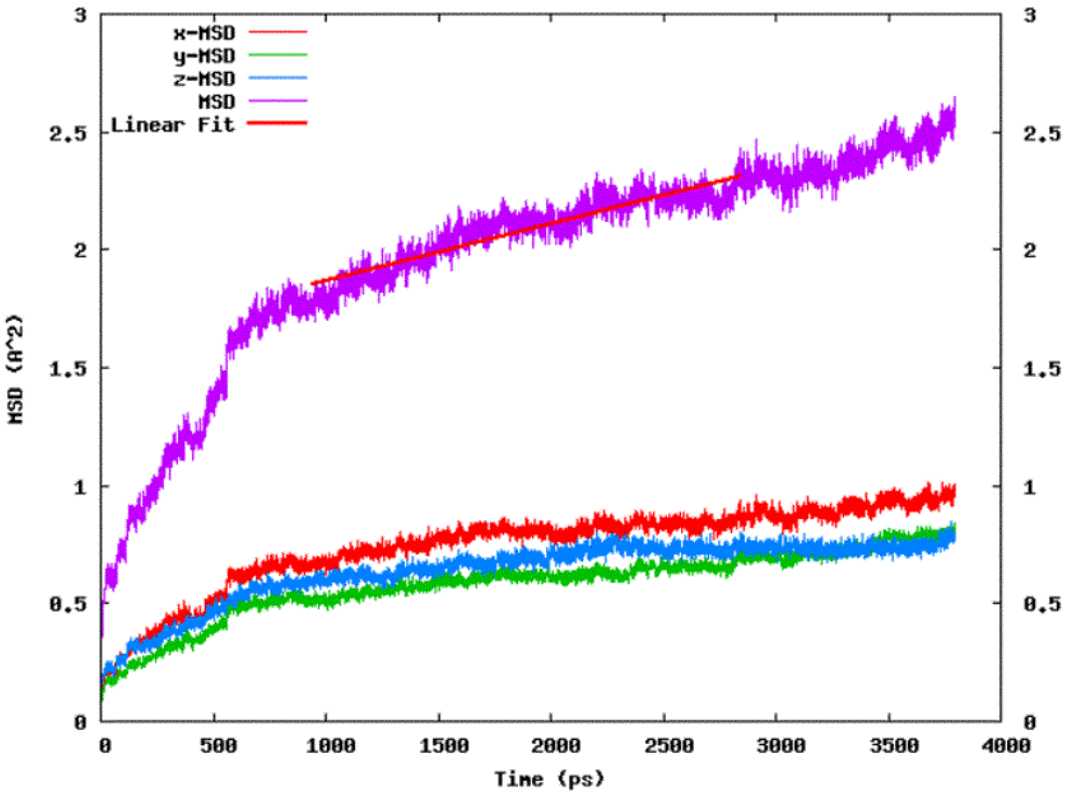

Figure 43: MSD against time for $Na_{0.75}MnPO_4$ at 500 K in the [100], [010], and [001] directions for a simulation of 5 ns.

7.5. Na-ion Diffusion Coefficients

MD simulations were conducted to investigate the long-range transport of Na ions by examining timeframes of 5 ns. On the basis of the investigation of MSD, it was revealed that diffusion occurs with unequal probability in all three spatial directions. The diffusion coefficients of Na^+ ions in olivine Na_xMnPO_4 were determined at temperature ranging from 100 K to 500 K and are listed in Table 15.

Table 15**:** The calculated Na^+ ion diffusion coefficients for Na_xMnPO_4 (x=0.25,0.5 and 0.75) for 5 ns at 100 K, 300 K, and 500 K.

Structures	Diffusion coefficients		
	100K	300K	500K
$Na_{0.75}MnPO_4$	$1.193x10^{-9}$	$4.146x10^{-9}$	$4.032x10^{-9}$
$Na_{0.5}MnPO_4$	$3.479x10^{-9}$	$4.686x10^{-9}$	$5.625x10^{-10}$
$Na_{0.25}MnPO_4$	$8.087x10^{-11}$	$1.507x10^{-9}$	$1.774x10^{-8}$

The diffusion coefficients of the Na_xMnPO_4 materials range from 8.087×10^{-11} to 3.479×10^{-9} cm^2s^{-1} at a temperature of 100 K. The observed diffusion coefficients suggest that the $Na_{0.25}MnPO_4$ structure exhibit comparatively slow diffusion dynamics. This observation implies that the rate of ion mobility inside the material at this specific temperature is relatively slow, potentially leading to significant implications for its overall efficacy. The range of observed values, within the temperature of 300 K, was found to be between 1.507×10^{-9} and 4.686×10^{-9} cm^2s^{-1}. At a temperature of 500 K, the measured values were found to be within the interval of 1.5.625x10−10 cm^2s^{-1} and 1.774x10−8 cm^2s^{-1}. The substantial difference in ion mobility between temperatures of 100 and 500 K suggests that the temperature may have a significant impact on the material's effectiveness. At 300 K, the slower diffusion dynamics may hinder the material's performance, while at 500 K, the higher ion mobility may lead to improved efficacy. These findings highlight the importance of temperature control and optimisation to effectively use this material. There are no literature results on Na_xMnPO_4 to compare with these calculated diffusion coefficients. However, for comparison, experimentally derived apparent Na^+ ion diffusion coefficients in $Na_{0.44}MnO_2$ were determined to vary between 1.08×10^{-13} to $9.15x10^{-12}$ cm^2s^{-1} and $5.75x10^{-16}$ to 14×10^{-14} cm^2 s^{-1} [142]. The discrepancy between the higher calculated values and the experimental values can be attributed to the exclusion of several experimental constraints in the calculations, as well as to a slightly higher estimated volume compared to the experimental data obtained at ambient temperature. It is important to note that, while the exact magnitudes of the absolute values may differ, the observed patterns are deemed to be reliable.

$Na_{0.25}MnPO_4$ materials have relatively high diffusion coefficients compared to other materials at elevated temperatures. Nevertheless, it is important to acknowledge that the diffusion rates exhibit a greater range of values at higher temperatures in comparison to those reported at 100 K. This observation indicates that there is an increase in the rate of ion transport within the material with an elevation in temperature. The significance of these discoveries lies in their contribution to understanding the behaviour exhibited by Na_xMnPO_4 materials and its potential applications. The diffusion rates identified in this study have the potential to impact several processes, including the rates at which batteries are charged and discharged, as well as the transportation of ions in solid-state electrolytes. This observation also indicates that

temperature significantly influences the diffusion behaviour of Na_xMnPO_4 materials. At reduced temperatures, the diffusion rates exhibit deceleration, suggesting a more regulated and effective charge-discharge mechanism within batteries. On the contrary, elevated temperatures facilitate heightened diffusion rates, thus potentially accelerating the transportation of ions in solid-state electrolytes. The results presented in this study provide a foundation to enhance the efficiency of Na_xMnPO_4 materials in various applications by manipulating temperature and a comprehensive understanding of its impact on diffusion coefficients.

7.6. Summary

In this chapter, the effect of temperature on diffusion properties for CE predicted structures were simulated using molecular dynamics method. The findings revealed that Na+ ion migration in $Na_{0.25}MnPO_4$, $Na_{0.5}MnPO_4$, and $Na_{0.75}MnPO_4$ at different temperatures have different diffusion behaviour influenced by the composition and crystal structure of the materials. At a temperature of 100 K, the MSD plots showed that Na+ ions exhibit ballistic motion over short durations but become increasingly diffusive over longer periods of time. The diffusion coefficient was found to be lower in $Na_{0.75}MnPO_4$ compared to the other two compositions, possibly due to structural constraints. At a temperature of 300 K, the diffusion behaviour of the ions was observed to be more pronounced, with a higher number of particles engaged in hopping. The MSD plots showed a direct correlation between the MSD of Na+ ions and time, indicating diffusion behaviour. The diffusion coefficients were found to be similar in $Na_{0.25}MnPO_4$ and $Na_{0.5}MnPO_4$, suggesting that composition plays an important role in ion diffusion. At 500 K, the MSD plots showed variations in the motion states of Na^+ ions within the different structures. The diffusion coefficients were found to be different in each structure, with $Na_{0.25}MnPO_4$ exhibiting the highest diffusion coefficient in the [010] direction and $Na_{0.75}MnPO_4$ exhibiting the lowest diffusion coefficient in the [001] direction. Empirical data obtained within the temperature range of 100 to 500 K indicate that variations in temperature can exert a substantial influence on the efficacy of the material. These findings highlight the importance of considering composition and crystallographic orientations when studying diffusion behaviour in materials.

Chapter 8. Monte Carlo Simulations of Predicted Structures

8.1. Introduction

Predicting the stable phases of multicomponent systems is an essential process in comprehending the thermodynamics of compounds. The growing accessibility of DFT-based techniques, along with systematic methodologies for phase prediction such as the cluster-expansion method, have been important in modelling systems with a small number of components. Nevertheless, acquiring phase diagrams for material compositions has proven to be a difficult and frequently impractical task due to the complexity of the problem. Furthermore, an additional difficulty is precisely predicting the coexistence of different phases and determining their percentages. This holds especially true when managing systems that consist of several components and involve complex relationships among them.

Advanced computational techniques and algorithms have been developed to tackle these challenges by precisely predicting phase diagrams and the coexistence of multiple phases in complex systems. One such approach is the use of MC simulations, which are based on statistical sampling methods. MC simulations involve generating many random configurations of the system and calculating their energies. By iteratively sampling and updating these configurations, the MC algorithm can approximate the most probable states and predict phase behaviour. This method is a valuable tool for understanding and modelling complex systems because it allows the exploration of large configuration spaces and yields accurate phase diagrams.

Xingyu *et al*. [143]. performed Canonical Monte Carlo simulations to investigate the phase diagrams of the rock salt Li_3V2O_5 anode material by adjusting the temperature to a point where the system experiences an order-disorder transition. The MC simulations were conducted with the cluster expansion models that had been fitted. The authors observed that the expected critical temperature (T_c) for the order-disorder phase transition is approximately 1000 K, which is slightly lower than the experimentally reported value of 1775 K for $LiVO_2$. At temperatures below Tc, it was shown that both E_f and C_v exhibit minimal variation with temperature, indicating the presence of a well-organised crystal structure. The authors concluded that Li_3V2O_5

remains in an ordered state at low temperatures. However, as the temperature increases beyond T_c, the E_f and C_v values start to show significant changes, suggesting a disordering of the crystal structure. In this study, the incorporation of configurational entropies is achieved by using Monte Carlo simulations that rely on cluster expansion components. The MC is a probabilistic technique frequently employed in the field of statistical thermodynamics. The primary utilisation of this method is in the estimation of integrals, the computation of average values, and the exploration of global minima inside the phase space. The current study used the MC approach, excluding lattice vibrations.

8.2. Computational Details

The Monte Carlo simulation was performed in UNCLE code within MedeA, and this was done through a flowchart based on the effective cluster interactions from cluster expansion. The same structures used for cluster expansion were made to be active to conduct these calculations. The simulation cell was configured to a 10 x 10 x 10 supercell of the initial unit cell. Concentrations were set such that 0.25 0.75, 0.5 0.5, 0.75 0.25.

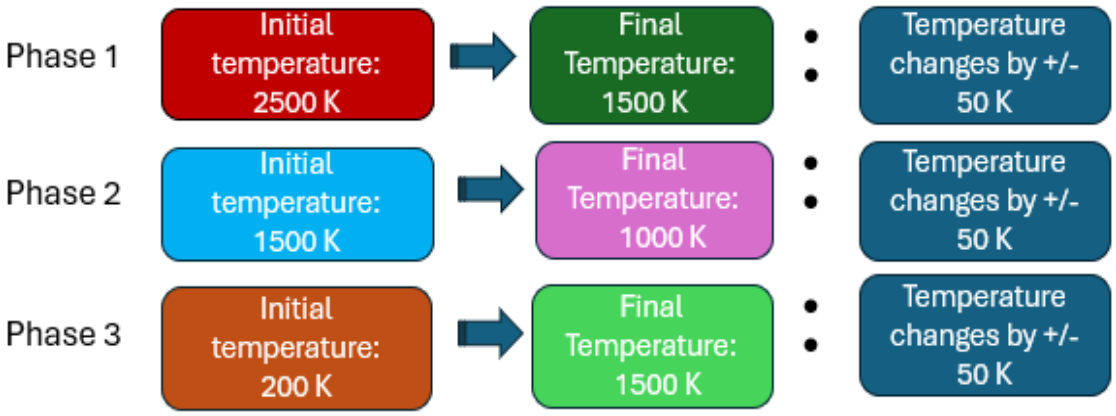

Figure 44: The temperature schedule schematic.

The current MC stage has been configured with three phase temperature schedules. The canonical ensemble was utilised to conduct a simulation that aimed to enhance understanding of the phase separation phenomenon in relation to temperature. The averages were evaluated over 500000 steps and the convergence criterion the accuracy of the energy was set to be less than 0.0001 eV.

8.3. Phase Stability

The effective cluster interactions obtained from the optimised cluster expansion were utilised in extensive MC simulations to stochastically investigate the system's states, ensuring that the probabilities align with the expected physical outcomes. The MC method is employed in the determination of thermodynamic averages, the derivation of thermodynamic potentials based on these averages, and the investigation of phase transition phenomena as a function of temperature. Monte Carlo simulation was conducted based on convergent CE to assess the phase stability of Na_xMnPO_4 structures.

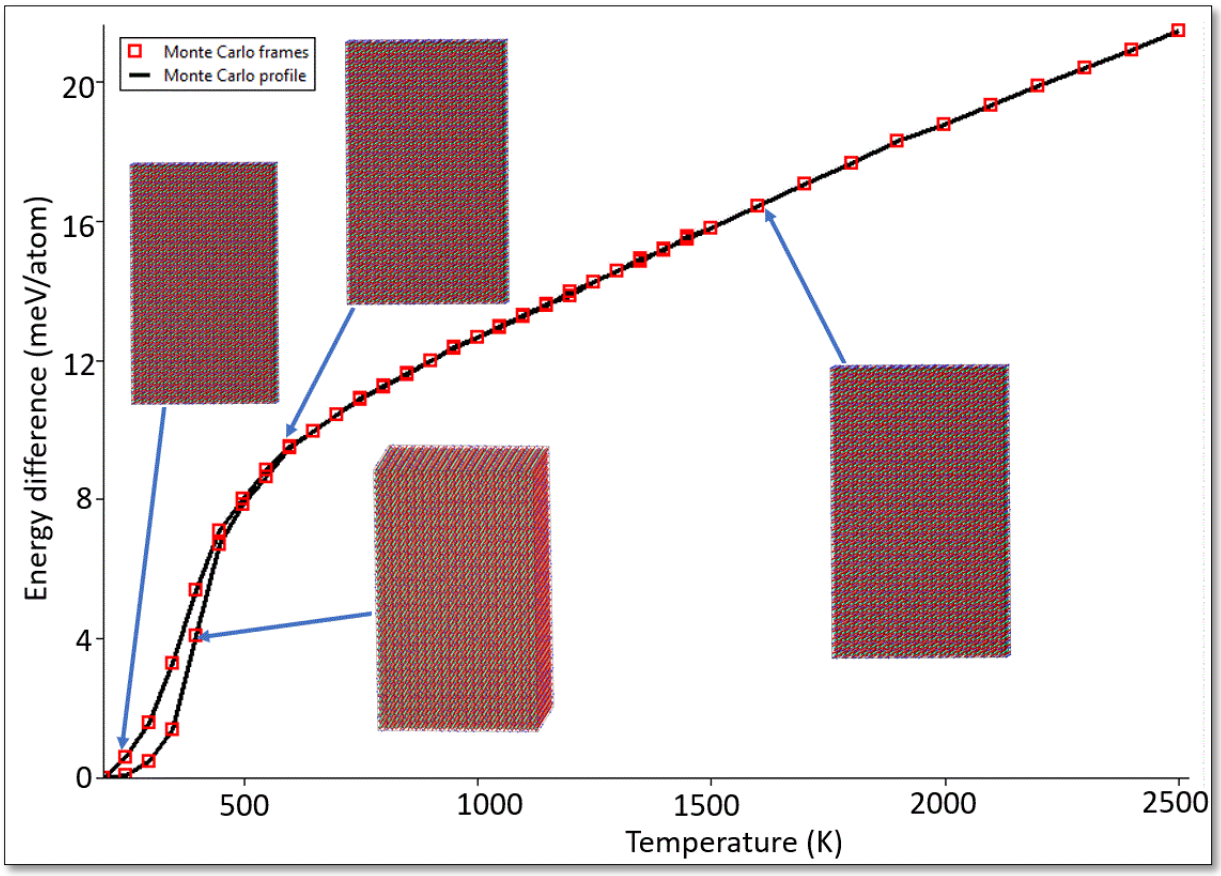

Figure 45: The temperature profiles of the 10×10×10 Monte Carlo simulation cells of $Na_{0.25}MnPO_4$.

Figures 45 to 47 depict the temperature profile of the MC system at three different concentrations of de-intercalation, namely 25%, 50%, and 75%, with respect to both Na and vacancies. It is noted that the pictures exhibited no phase separation or mixing throughout for all the three structures with different concentrations. Thus, phase

separation was observed to not occur in any of the de-intercalated structures at both low and high temperatures. The CE results validate the anticipated miscibility observed during the ground-state investigation, albeit with a marginal disparity in energy levels. It is worth mentioning that the hysteresis loop depicted in Figures 45 and 47 for $Na_{0.25}MnPO_4$ and $Na_{0.75}MnPO_4$, respectively, have shorter lengths compared to the hysteresis loop in Figure 46, indicating a higher critical temperature value for $Na_{0.5}MnPO_4$.

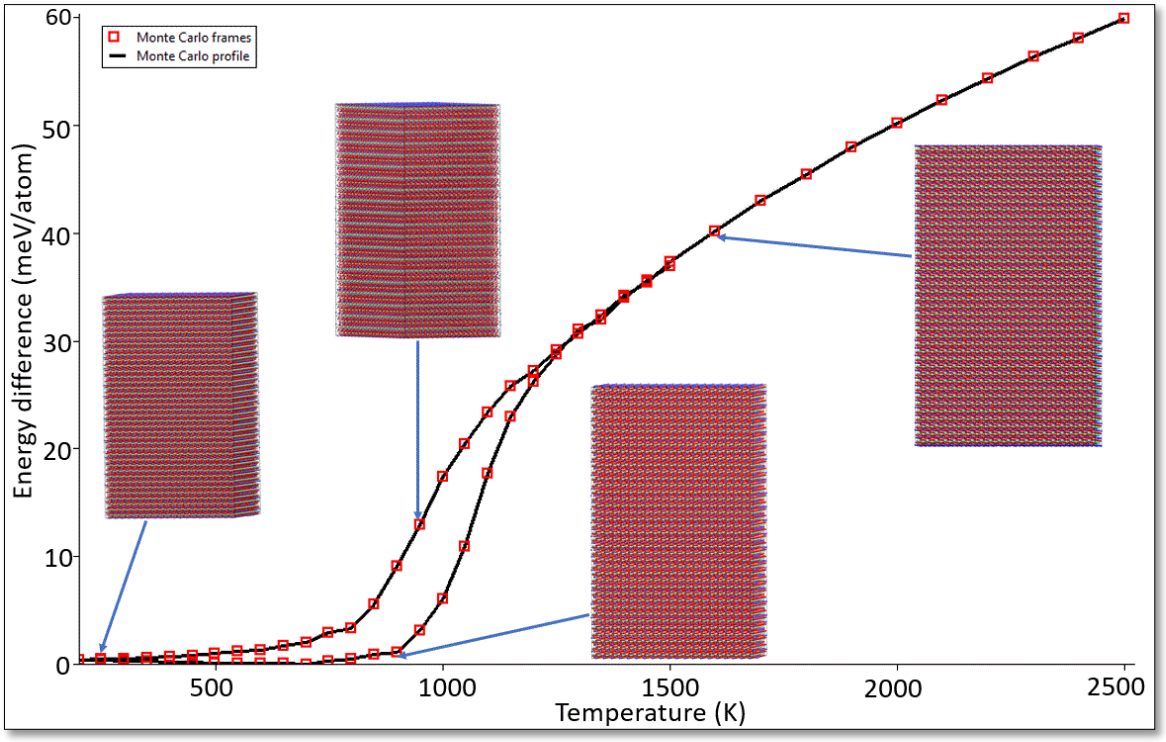

Figure 46: The temperature profiles of 10×10×10 Monte Carlo simulation cells of $Na_{0.5}MnPO_4$.

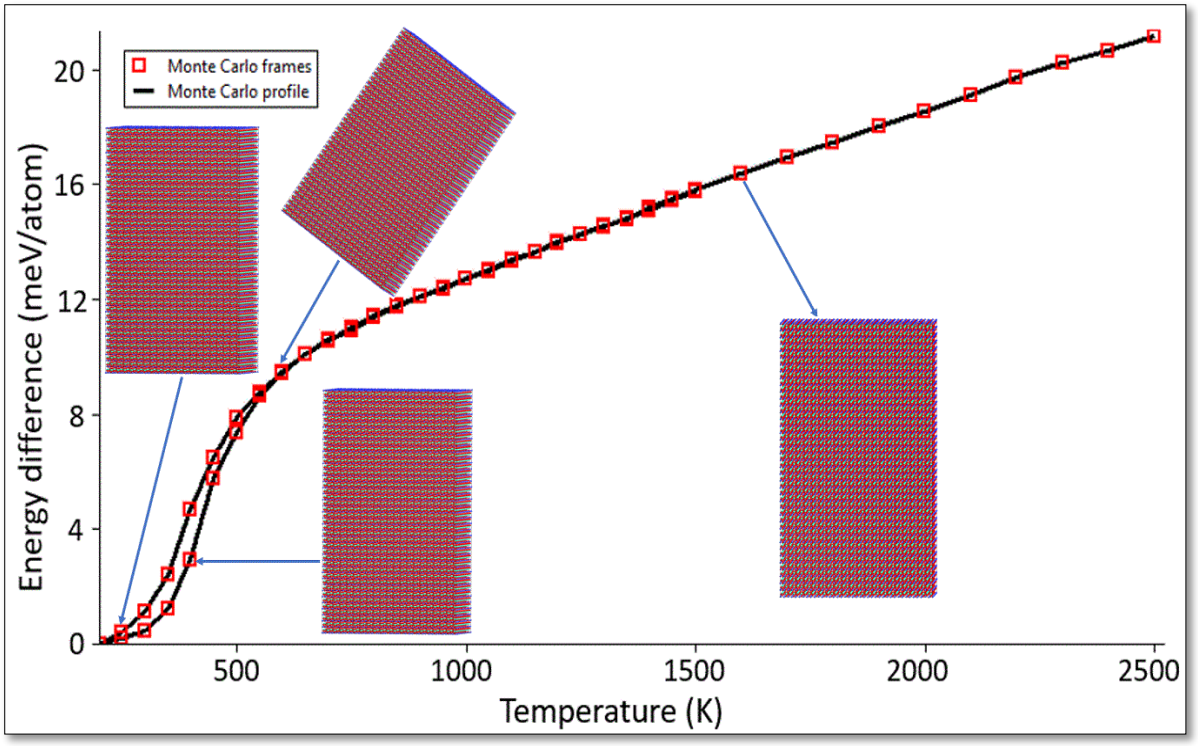

Figure 47: Temperature profiles of the 10×10×10 Monte Carlo simulation cells of $Na_{0.75}MnPO_4$.

8.4. Summary

In this chapter, the MC method was used to investigate the phase stability of Na_xMnPO_4 compounds. The simulated results did not show any phase separation or mixing for all the three structures with different concentrations, validating the anticipated miscibility observed during the ground-state investigation. The hysteresis loop for $Na_{0.25}MnPO_4$ and $Na_{0.75}MnPO_4$ had a shorter length, indicating a higher critical temperature value. The CE results validated the miscibility observed during the ground-state investigation, albeit with a marginal disparity in energy levels.

Chapter 9. Conclusion and Future Prospects

In conclusion, the use of MSM in the investigation of $NaMnPO_4$ cathode material has demonstrated its efficacy and provided significant information. A thorough knowledge of the complex electrochemical processes and structural changes that take place in $NaMnPO_4$ during intercalation and de-intercalation has been executed by the integration of different modelling approaches at multiple lengths and time scales, as offered by MSM. This study successfully used MSM methods to investigate properties of de-intercalated and intercalated Na_xMnPO_4. examine the fitting and testing of interatomic potentials by combining first-principle simulations with classical molecular dynamics. This method was used to accurately determine and validate the Buckingham interatomic potentials for $NaMnPO_4$. The utilisation of MSM was also used to assess phase stability, diffusion coefficient, and MSD. This research included a variety of computational tools in its methodology. First, local cluster expansion calculations were performed to examine the binary diagram and get insight into the somewhat disordered states inside the Na-vacancy arrangement. Additionally, molecular dynamics simulations were used to determine diffusion coefficients by statistical modelling of ion migration within a $NaMnPO_4$ system. Finally, Monte Carlo simulations were used to examine the phase stability of Na_xMnPO_4 compounds by implementing stochastic simulations. Details of each method's complete implementation and conclusions are provided in the following section.

9.1. Conclusions

Firstly, we used the first-principles approach to investigate the structural and electrochemical characteristics of the Na_xMnPO_4 (x = 0.25, 0.5, 0.75 and 1) structures, which were created using random substitution technique. The use of the PBE+U exchange correlation functional was implemented to conduct a more comprehensive analysis of the electrochemical characteristics exhibited by the de-intercalated systems. This choice was made because of its ability to faithfully replicate the structural parameters and energy band gap values, as evidenced by a comprehensive comparison with the PBE and PBEsol PBE+U functionals. First-principle simulations have been used to investigate the consequences of Na^+ ion de-intercalation on the structural, electronic, mechanical and thermodynamic characteristics of both maricite and olivine $NaMnPO_4$. The investigation elucidates that the structural characteristics

of maricite Na_xMnPO_4 persist unaltered throughout the discharge process, encompassing a voltage range of 5.132 V to 4.655 V. The phenomenon of metallicity in maricite $NaMnPO_4$ exhibits an increase as a consequence of the extraction of Na^+. The formation energy values of all $NaMnPO_4$ systems are observed to be negative, which signifies the presence of solid solution for de-intercalation states. The presence of mechanical instability is indicated in the case of $NaMnPO_4$, where the structures Na_1MnPO_4, $Na_{0.75}MnPO_4$, and $Na_{0.25}MnPO_4$ exhibit ductile behaviour, while $MnPO_4$ shows brittleness. In contrast, the investigation explored the lattice parameters and volume of olivine Na_xMnPO_4, uncovering a deviation of no more than 6% throughout the Na de-intercalation phases. The material exhibited a discernible transition toward a more metallic nature from the initial stages to the third stage, while the fourth stage demonstrated the presence of a band gap characteristic of a semiconductor. Negative values of the formation energy signify the material's propensity for the formation of a solid state. All systems that underwent de-intercalation satisfied the stability criteria, and their structures exhibited both ductile and brittle behaviour, as determined by the Pugh criterion. The de-intercalation process of $NaMnPO_4$ results in a decrease in sound velocities and $\boldsymbol{\theta_D}$ values, indicating a decrease in covalent strength. Surprisingly, the thermal conductivity of the material is not affected by the removal of Na, as there is a slight decrease in $\boldsymbol{\theta_D}$. However, in the fourth step of de-intercalation, there is an increase in volumetric density, sound velocities, and Debye temperature. Thermodynamics calculations show a significant increase in C_v for all de-intercalation phases at low temperatures, reaching a classical asymptotic limit at high temperatures. The fluctuation of free energy and C_v suggests a rise in free energy at lower temperatures.

Secondly, the study successfully fitted the interatomic potentials for $NaMnPO_4$ using empirical methods and validated them through an accurate estimation of structural properties that are consistent with experimental and other theoretical results. The radial distribution functions, diffusion coefficients and mean square displacement were calculated at different temperatures, revealing that higher temperatures promote faster ion diffusion. The Na-Mn interaction exhibited the most significant separation distance, and the diffusion of Na^+ ions in $NaMnPO_4$ was influenced by Na concentration, with lower concentrations resulting in faster and more efficient ion diffusion. The Na-ion diffusion coefficients were found to be relatively low at 100 K but increased at 300 K,

indicating a faster movement of ions within the material. These findings are important for understanding the behaviour and potential applications of Na_xMnPO_4 materials, as diffusion rates can impact processes such as charge/discharge rates in batteries and ion transport in solid-state electrolytes.

Thirdly, we investigated the utilisation of cluster expansion as a method for studying phase stabilities in relation to vacancies. The proposed methodology successfully determines stable crystal structures and evaluates metastable structures using first-principles density functional approaches. The phase diagram exhibits 62 various configurations with different concentrations and symmetries, out of which 7 were found to be thermodynamically stable. These 7 stable phases were further investigated by calculating their electronic, mechanical and thermodynamic properties, which were compared with those obtained using random substitution technique. The cluster expansion used in this study is of good quality, as indicated by a low cross-validation score of 1.1 meV. Electronic structure analysis reveals semiconducting behaviour in the parent structures $NaMnPO_4$ and $MnPO_4$ whereas the semi-metallic characteristics were observed in the case of de-intercalation Na_xMnPO_4 structures. The mechanical stability of Na_xMnPO_4 (x = 1, 0.825, 0.75, 0.625, 0.5, 0.25) structures was confirmed through elastic constant calculations, except for the parent structure, $MnPO_4$. The structures with Na^+ ions exhibit ductile characteristics, with higher Na concentrations leading to increased ductility. In general, the addition of Na^+ ions were found to improve the ductility of the $Na_{1-x}MnPO_4$ structures. The findings from the investigation of thermodynamic parameters using DFT suggest that temperature has a significant impact on specific heat at constant volume (Cv), free energy, and entropy for all intercalation phases. At low temperatures, the rate of increase of Cv is rapid for all intercalation stages. However, during high temperature intercalation, the value of Cv approaches the classical asymptotic limit, known as the Dulong-Petit limit, for all stages of intercalation. Additionally, at low temperatures, there is a significant increase in free energy for all intercalation stages, as observed from the fluctuation of free energy versus temperature.

Fourthly, MD simulations were performed on CE predicted structures to evaluate the influence of temperature on transport properties. The findings demonstrated that the diffusion behaviour of Na+ ions in Na_xMnPO_4 materials is influenced by composition, crystal structure, and temperature. The diffusion coefficients vary depending on the

composition and crystallographic orientations, with $Na_{0.75}MnPO_4$ exhibiting lower diffusion coefficients compared to $Na_{0.25}MnPO_4$ and $Na_{0.5}MnPO_4$. The diffusion rates are relatively slow at lower temperatures and increase with higher temperatures. These findings highlight the importance of considering composition, crystallographic orientations, and temperature in studying diffusion behaviour in materials. The results have implications for various applications, such as battery charging and discharging rates and ion transit in solid-state electrolytes. Regulation and optimisation of temperature are crucial to the efficient use of Na_xMnPO_4 materials.

Finally, the application of the MC approach, utilising the convergent CE, shown that Na_xMnPO_4 compounds do not undergo any phase separation or mixing at any concentration. This finding confirms the anticipated miscibility observed during the analysis of the ground state. Investigation of the hysteresis loop revealed that $Na_{0.25}MnPO_4$ and $Na_{0.75}MnPO_4$ have higher critical temperature values. The study of the canonical ensemble greatly enhanced the comprehension of the phenomenon of phase separation in relation to temperature. Nevertheless, there was a slight discrepancy in energy levels. The marginal discrepancy in energy levels indicates the possibility of minor deviations from optimal behaviour in the Na_xMnPO_4 complexes. The use of the canonical ensemble further deepened our understanding of phase separation in relation to temperature, although there were slight discrepancies in energy levels. These minor deviations suggest that there may still be room for optimizing the behaviour of $NaxMnPO_4$ complexes.

9.2. Multiscale Modelling Framework

The adoption of MSM has become a powerful tool for investigating the complexity involved with $NaMnPO_4$ cathode materials. Research findings have significant effects not only in advancing the fundamental understanding of these materials but also in driving the progress of next-generation energy storage technologies. As we continuously improve our understanding of materials across various scales, the integration of mesoscopic and macroscopic phenomena into battery investigation shall definitely play an essential role in our search for enhanced and environmentally viable energy accumulation alternatives. MSM models were developed using both DFT and CE. Thus, DFT calculations provided the necessary input for constructing a cluster expansion calculation, where the energies of different atomic configurations obtained

from DFT were used to fit parameters in the CE model, allowing the prediction of energies for a wide range of predicted configurations. In cluster expansion + Monte Carlo simulations, the developed cluster expansion models were incorporated into Monte Carlo simulations. Monte Carlo simulations then explore the configurational space of the selected stable predicted structures, sampling different arrangements of atoms based on the cluster expansion parameters. This enabled the investigation of finite-temperature properties. The used multiscale modelling framework flow chart of the computational approach is presented in Figure 46 below.

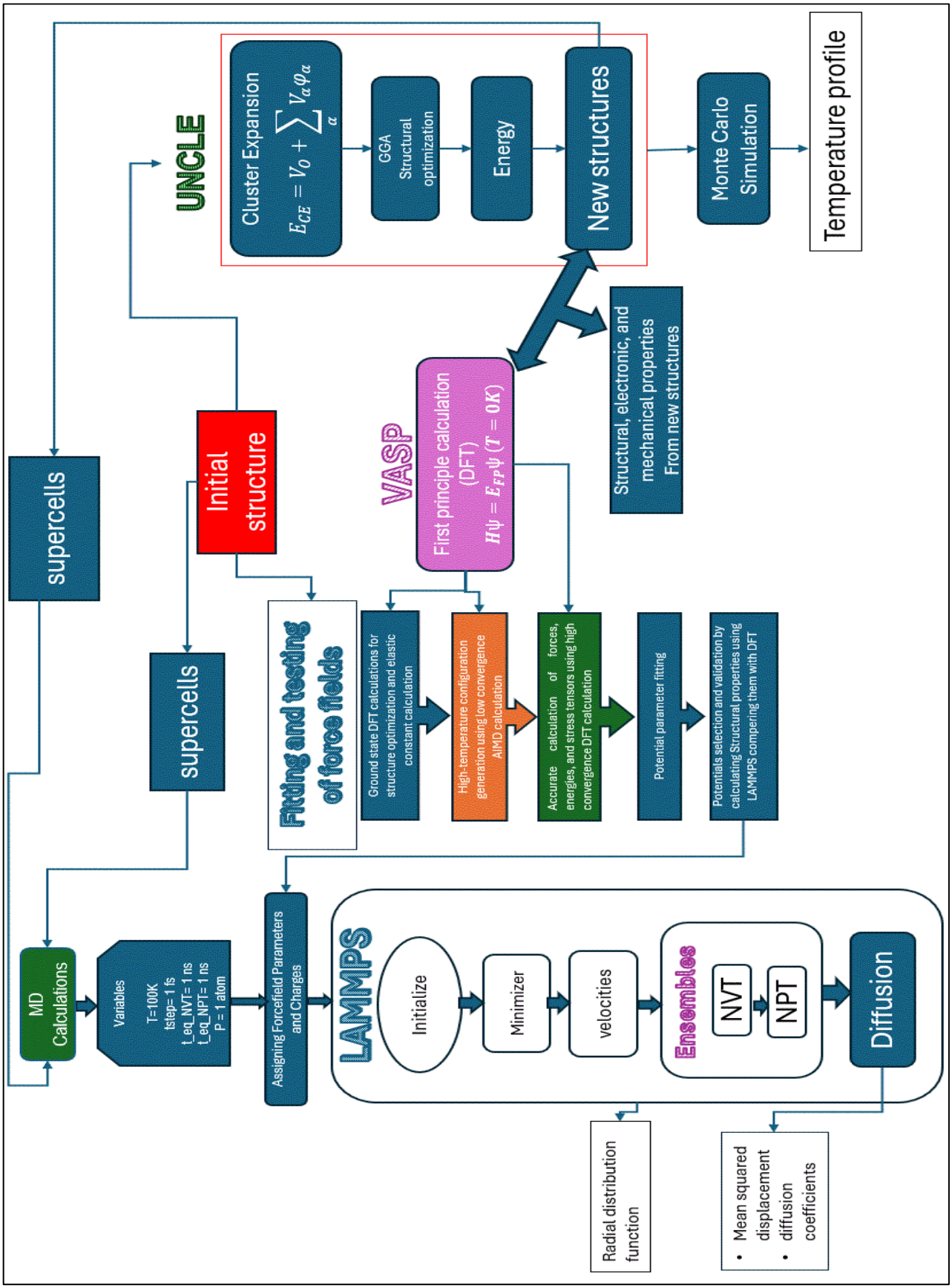

Figure 46: Multiscale modelling framework for computational approaches developed in the study.

9.3. Future Prospects

Based on the findings presented in this thesis, a few suggestions for further research have been provided as follows.

- Further molecular dynamics simulations to investigate the processes of de-intercalated and intercalated of transition-metal-doped $NaMnPO_4$ structures, utilising interatomic potential models that have been accurately fitted as a base model for developing new potentials.

- A comparison study between ab initio MD methods and classical MD methods to evaluate the accuracy of properties calculated using the fitted interatomic potentials.

- Subsequent investigation of the diffusivity phenomenon utilising the MedeA-UNCLE computational tool at high temperatures.

- A combination of the quantum mechanical method and continuum method simulations to assess the phase transformation and fracture phenomena that occur within individual Na_xMnPO_4 materials.

- Phase-field approach to comprehensively investigate the complex processes of Na-ion intercalation, de-intercalation, and fracture.

Reference

1. Eisenberg, R.; Nocera, D. G. Preface: Overview of the forum on solar and renewable energy. *Inorganic Chemistry* **2005***, 44*, 6799-6801.

2. Trollip, H.; Butler, A.; Burton, J.; Caetano, T.; Godinho, C. Energy Security in South Africa. **2014**, 17, 1.

3. Ni, Q.; Bai, Y.; Wu, F.; Wu, C. Polyanion-type electrode materials for sodium-ion batteries. *Advanced Science* **2017***, 4*, 1600275.

4. X. Zhu; Lin, T.; Manning, E.; Zhang, Y.; Yu, M.; Zuo, B.; Wang, L. Recent advances on Fe- and Mn-based cathode materials for lithium and sodium ion batteries. *Journal of Nanoparticle Research*, **2018**, 20, 1-40.

5. Thackeray, M. M.; Wolverton, C.; Isaacs, E. D. Electrical energy storage for transportation-approaching the limits of, and going beyond, lithium-ion batteries. *Energy & Environmental Science* **2012***, 5*, 7854-7863.

6. Pan, H.; Hu, Y.; Chen, L. Room-temperature stationary sodium-ion batteries for large-scale electric energy storage. *Energy & Environmental Science* **2013***, 6*, 2338.

7. N. Yabuuchi; Kubota, K.; Dahbi, M.; Komaba, S. Research development on sodium-ion batteries. *Chemical Reviews* **2014**, 114, 11636.

8. Kim, S.; Seo, D.; Ma, X.; Ceder, G.; Kang, K. electrode materials for rechargeable sodium-ion batteries: potential alternatives to current lithium-ion batteries. *Advanced Energy Materials* **2012***, 2*, 710-721.

9. Pan, H.; Hu, Y.; Chen, L. Room-temperature stationary sodium-ion batteries for large-scale electric energy storage. *Energy & Environmental Science* **2013***, 6*, 2338.

10. Slater, M. D.; Kim, D.; Lee, E.; Johnson, C. S. Sodium-ion batteries. *Advanced Functional Materials* **2013***, 23*, 947-958.

11. Ceder, G.; Kang, B. Battery materials for ultrafast charging and discharging. *Nature* **2009***, 458*, 190-193.

12. Kim, J.; Seo, D.; Kim, H.; Park, I.; Yoo, J.; Jung, S.; Park, Y.; Goddard III, W. A.; Kang, K. Unexpected discovery of low-cost maricite $NaFePO_4$ as a high-performance electrode for Na-ion batteries. *Energy & Environmental Science* **2015**, *8*, 540-545.

13. Kumar; N. &.; Yang, L.; Brehm, W.; Adelhelm, P. Batteries from lithium-ion to sodium-ion batteries: advantages, challenges and surprises. *Advanced Energy Materials* **2018**, 57.

14. Eisenberg, R.; Nocera, D. G. Preface: Overview of the forum on solar and renewable energy. *Inorganic Chemistry* **2005**, *44*, 6799-6801.

15. Franco, A. A. Rechargeable lithium batteries*: From Fundamentals to Applications;* Elsevier: **2015**.

16. Franco, A. A. A multiscale physical model of electrochemical energy storage devices. *ECS Transactions* **2013**, *45*, 11-19.

17. Franco, A. A. Multiscale modelling and numerical simulation of rechargeable lithium-ion batteries: concepts, methods and challenges. *RSC Advances* **2013**, *3*, 13027-13058.

18. Delmas, C.; Fouassier, C.; Hagenmuller, P. Structural classification and properties of the layered oxides. *Physica B+C* **1980**, *99*, 81-85.

19. Yabuuchi, N.; Kubota, K.; Dahbi, M.; Komaba, S. Research development on sodium-ion batteries. *Chemical Reviews* **2014**, *114*, 11636-11682.

20. Qi, X.; Liu, L.; Song, N.; Gao, F.; Yang, K.; Lu, Y.; Yang, H.; Hu, Y.; Cheng, Z.; Chen, L. Design and comparative study of O3/P2 hybrid structures for room temperature sodium-ion batteries. *ACS Applied Materials & Interfaces* **2017**, *9*, 40215-40223.

21. Billaud, J.; Singh, G.; Armstrong, A. R.; Gonzalo, E.; Roddatis, V.; Armand, M.; Rojo, T.; Bruce, P. G. $Na_{0.67}Mn_{1-x}Mg_xO_2$ ($0 \leq x \leq 0.2$): a high-capacity cathode for sodium-ion batteries. *Energy & Environmental Science* **2014**, *7*, 1387-1391.

22. Konarov, A.; Jo, J. H.; Choi, J. U.; Bakenov, Z.; Yashiro, H.; Kim, J.; Myung, S. Exceptionally highly stable cycling performance and facile oxygen-redox of

manganese-based cathode materials for rechargeable sodium batteries. *Nano Energy* **2019**, *59*, 197-206.

23. Yabuuchi, N.; Kajiyama, M.; Iwatate, J.; Nishikawa, H.; Hitomi, S.; Okuyama, R.; Usui, R.; Yamada, Y.; Komaba, S. P2-type $Na_x[Fe1/2Mn_{1/2}]O_2$ made from earth-abundant elements for rechargeable Na batteries. *Nature Materials* **2012**, *11*, 512-517.

24. Bucher, N.; Hartung, S.; Gocheva, I.; Cheah, Y. L.; Srinivasan, M.; Hoster, H. E. Combustion-synthesized sodium manganese (cobalt) oxides as cathodes for sodium ion batteries. *Journal of Solid-State Electrochemistry* **2013**, *17*, 1923-1929.

25. Lu, Z.; Dahn, J. R. In situ X-ray diffraction study of P 2 $Na_{2/3}[Ni1/3Mn_{2/3}]O_2$. *Journal of the Electrochemical Society* **2001**, *148*, A1225.

26. Kang, W.; Zhang, Z.; Lee, P.; Ng, T.; Li, W.; Tang, Y.; Zhang, W.; Lee, C.; Yu, D. Y. W. Copper substituted P2-type $Na_{0.67}CuxMn_{1-x}O_2$: a stable high-power sodium-ion battery cathode. *Journal of Materials Chemistry A* **2015**, *3*, 22846-22852.

27. Kubota, K.; Dahbi, M.; Hosaka, T.; Kumakura, S.; Komaba, S. Towards K-ion and Na-ion batteries as “beyond Li-ion”. *The Chemical Record* **2018**, *18*, 459-479.

28. Zhang, R.; Lu, Z.; Yang, Y.; Shi, W. First-principles investigation of the monoclinic $NaMnO_2$ cathode material for rechargeable Na-ion batteries. *Current Applied Physics* **2018**, *18*, 1431-1435.

29. Jo, I.; Ryu, H.; Gu, D.; Park, J.; Ahn, I.; Ahn, H.; Nam, T.; Kim, K. The effect of electrolyte on the electrochemical properties of Na/α-$NaMnO_2$ batteries. *Materials Research Bulletin* **2014**, *58*, 74-77.

30. Gong, Z.; Yang, Y. Recent advances in the research of polyanion-type cathode materials for Li-ion batteries. *Energy & Environmental Science* **2011**, *4*, 3223-3242.

31. Padhi, A. K.; Nanjundaswamy, K. S.; Goodenough, J. B. Phospho-olivines as positive-electrode materials for rechargeable lithium batteries. *Journal of the Electrochemical Society* **1997**, *144*, 1188.

32. Masquelier, C.; Croguennec, L. Polyanionic (phosphates, silicates, sulfates) frameworks as electrode materials for rechargeable Li (or Na) batteries. *Chemical Reviews* **2013**, *113*, 6552-6591.

33. Guo, S.; Li, J.; Xu, Q.; Ma, Z.; Xue, H. Recent achievements on polyanion-type compounds for sodium-ion batteries: syntheses, crystal chemistry and electrochemical performance. *Journal of Power Sources* **2017**, *361*, 285-299.

34. Oh, S.; Myung, S.; Hassoun, J.; Scrosati, B.; Sun, Y. Reversible $NaFePO_4$ electrode for sodium secondary batteries. *Electrochemistry Communications* **2012**, *22*, 149-152.

35. Casas-Cabanas, M.; Roddatis, V. V.; Saurel, D.; Kubiak, P.; Carretero-González, J.; Palomares, V.; Serras, P.; Rojo, T. Crystal chemistry of Na insertion/deinsertion in $FePO_4$ $NaFePO_4$. *Journal of Materials Chemistry* **2012**, *22*, 17421-17423.

36. Saracibar, A.; Carrasco, J.; Saurel, D.; Galceran, M.; Acebedo, B.; Anne, H.; Lepoitevin, M.; Rojo, T.; Cabanas, M. C. Investigation of sodium insertion–extraction in olivine Na_xFePO_4 ($0 \leq x \leq 1$) using first-principles calculations. *Physical Chemistry Chemical Physics* **2016**, *18*, 13045-13051.

37. Koleva, V.; Boyadzhieva, T.; Zhecheva, E.; Nihtianova, D.; Simova, S.; Tyuliev, G.; Stoyanova, R. Precursor-based methods for low-temperature synthesis of defectless $NaMnPO_4$ with an olivine- and maricite-type structure. *CrystEngComm* **2013**, *15*, 98-989.

38. Boyadzhieva, T.; Koleva, V.; Zhecheva, E.; Nihtianova, D.; Mihaylov, L.; Stoyanova, R. Competitive lithium and sodium intercalation into sodium manganese phospho-olivine $NaMnPO_4$ covered with carbon black. *RSC Advances* **2015**, *5*, 87694-8775.

39. Venkatachalam, P.; Ganesan, S.; Rengapillai, S.; Marimuthu, S. Gradual development of maricite $NaMnPO_4$ with the influence of diol chain length on the polyol process of surpassed sodium intercalation. *Industrial & Engineering Chemistry Research* **2021**, *60*, 5861-5868.

40. Chowdary, B. B. V.; Chandana, S.; Chaitanya, B. K. First-principles study of olivine-type $NaMnPO_4$ AS positive electrode materials for rechargeable sodium ion batteries. *International Journal of Advanced Research* **2017**, *5*, 1298-1303.

41. Bonilla, M. R.; Lozano, A.; Escribano, B.; Carrasco, J.; Akhmatskaya, E. Revealing the mechanism of sodium diffusion in Na_xFePO_4 using an improved force field. *The Journal of Physical Chemistry C* **2018**, *122*, 8065-8075.

42. Mattsson, A. E. In Designing meaningful density functional theory calculations in materials science*; In APS Shock Compression of Condensed Matter* **2005**, 5, 1.

43. Mattsson, A. E.; Schultz, P. A.; Desjarlais, M. P.; Mattsson, T. R.; Leung, K. Designing meaningful density functional theory calculations in materials science—a primer. *Modelling and Simulation in Materials Science and Engineering* **2004**, *13*, 1.

44. Kohn, W.; Sham, L. J. Self-consistent equations including exchange and correlation effects. *Physical Review* **1965**, *140*, 1133.

45. Hohenberg, P.; Kohn, W. Inhomogeneous electron gas. *Physical Review* **1964**, *136*, 864.

46. Slater, J. C. Quantum theory of molecular and solids. *The self-Consistent Field for Molecular and Solids* **1974**, *4*.

47. Jeanmairet, G.; Levy, N.; Levesque, M.; Borgis, D. Introduction to classical density functional theory by a computational experiment. *Journal of Chemical Education* **2014**, *91*, 2112-2115.

48. Gunnarsson, O.; Lundqvist, B. I. Exchange and correlation in atoms, molecules, and solids by the spin-density-functional formalism. *Physical Review B* **1976**, *13*, 4274.

49. Langreth, D. C.; Perdew, J. P. Exchange-correlation energy of a metallic surface: Wave-vector analysis. *Physical Review B* **1977**, *15*, 2884.

50. Dodson, B. W. Development of a many-body Tersoff-type potential for silicon. *Physical Review B* **1987**, *35*, 2795.

51. Ho, K.; Bohnen, K. P. Stability of the missing-row reconstruction on fcc (110) transition-metal surfaces. *Physical Review Letters* **1987**, *59*, 1833.

52. Perdew, J. P.; Yue, W. Accurate and simple density functional for the electronic exchange energy: Generalized gradient approximation. *Physical Review B* **1986**, *33*, 8800.

53. Perdew, J. P.; Ernzerhof, M.; Burke, K. Rationale for mixing exact exchange with density functional approximations. *Journal of Chemical Physics.* **1996**, *105*, 9982-9985.

54. Anisimov, V. I.; Gunnarsson, O. Density-functional calculation of effective Coulomb interactions in metals. *Physical Review B* **1991**, *43*, 7570.

55. Cohen, M. L.; Heine, V. In The fitting of pseudopotentials to experimental data and their subsequent application. *Solid State Physics* **1970**, 24, 37-248.

56. Heine, V.; Weaire, D. In Pseudopotential theory of cohesion and structure. *Solid State Physics* **1970**, 24, 249-463.

57. Lehtola, S. A review on non-relativistic, fully numerical electronic structure calculations on atoms and diatomic molecules. *International Journal of Quantum Chemistry* **2019**, *119*, 25968.

58. Phillips, J. C. Energy-band interpolation scheme based on a pseudopotential. *Physical Review* **1958**, *112*, 685.

59. Hellmann, H. A new approximation method in the problem of many electrons. *Journal of Chemical Physics* **1935**, *3*, 61.

60. Vanderbilt, D. Soft self-consistent pseudopotentials in a generalized eigenvalue formalism. *Physical Review B* **1990**, *41*, 7892.

61. Shiozaki, T. BAGEL: brilliantly advanced general electronic-structure library. *Wiley Interdisciplinary Reviews: Computational Molecular Science* **2018**, *8*, 1331.

62. Kohn, W.; Sham, L. J. Self-consistent equations including exchange and correlation effects. *Physical Review* **1965**, *140*, A1133.

63. Ernzerhof, M.; Scuseria, G. E. Perspective on “Inhomogeneous electron gas” Hohenberg P, Kohn W (1964) Phys Rev 136: B864. *Theoretical Chemistry Accounts* **2000**, *103*, 259-262.

64. Milman, V.; Akhmatskaya, E. V.; Nobes, R. H.; Winkler, B.; Pickard, C. J.; White, J. A. Systematic ab initio study of the compressibility of silicate garnets. *Acta Crystallographica Section B: Structural Science* **2001**, *57*, 163-177.

65. Matsuda, A.; Sugita, S.; Fujii, T.; Watanabe, T. Study of pseudogap phenomena by STM and other probes. *Journal of Physics and Chemistry of Solids* **2001**, *62*, 65-68.

66. Basov, D. N.; Pierce, F. S.; Volkov, P.; Poon, S. J.; Timusk, T. Optical conductivity of insulating Al-based alloys: Comparison of quasiperiodic and periodic systems. *Physical Review Letters* **1994**, *73*, 1865.

67. Beckstein, O.; Klepeis, J. E.; Hart, G. L. W.; Pankratov, O. First-principles elastic constants and electronic structure ofα−$Pt_2Si$and PtSi. *Physical Review. B, Condensed Matter* **2001**, *63*.

68. Zhou, Z.; Joós, B. Stability criteria for homogeneously stressed materials and the calculation of elastic constants. *Physical Review. B, Condensed Matter* **1996**, *54*, 3841-3850.

69. Born, M.; Huang, K. *Dynamical Theory of Crystal Lattices 1st ed;* **1982**, 210.

70. Fast, L.; Wills, J.; Johansson, B.; Eriksson, O. Elastic constants of hexagonal transition metals: Theory. *Physical Review. B, Condensed Matter* **1995**, *51*, 17431-17438.

71. Patil, S. K. R.; Khare, S. V.; Tuttle, B. R.; Bording, J. K.; Kodambaka, S. Mechanical stability of possible structures of PtN investigated using first-principles calculations. *Physical Review. B, Condensed Matter and Materials Physics* **2006**, *73*.

72. Ravindran, P.; Fast, L.; Korzhavyl, P. A.; Johansson, B.; Wills, J.; Eriksson, O. Density functional theory for calculation of elastic properties of orthorhombic crystals: Application to $TiSi_2$. *Journal of Applied Physics* **1998**, *84*, 4891-4904.

73. Zhang, H.; Banfield, J. F. Aggregation, coarsening, and phase transformation in ZnS nanoparticles studied by molecular dynamics simulations. *Nano Letters* **2004**, *4*, 713-718.

74. Frenkel, D.; Smit, B. Understanding molecular simulation: from algorithms to applications; Elsevier **2023**.

75. Verlet, L. Computer" experiments" on classical fluids. I. Thermodynamical properties of Lennard-Jones molecules. *Physical Review* **1967**, *159*, 98.

76. Komanduri, R.; Chandrasekaran, N.; Raff, L. M. Molecular dynamics (MD) simulation of uniaxial tension of some single-crystal cubic metals at nanolevel. *International Journal of Mechanical Sciences* **2001**, *43*, 2237-2260.

77. Komanduri, R.; Chandrasekaran, N.; Raff, L. M. Molecular dynamic simulations of uniaxial tension at nanoscale of semiconductor materials for micro-electro-mechanical systems (MEMS) applications. *Materials Science and Engineering: A* **2003**, *340*, 58-67.

78. Sachdeva, P. Lattice vibration study of silica nanoparticle in suspension **2006**.

79. Singh, S. K.; Kunche, L.; Natarajan, U. Detailed Molecular Structure of Glassy Poly (phenylene oxide)(PPO) Studied by Molecular Dynamics Simulations. *Journal of Macromolecular Science, Part B* **2020**, *59*, 796-820.

80. Onsager, L. Crystal statistics. I. A two-dimensional model with an order-disorder transition. *Physical Review* **1944**, *65*, 117.

81. Catlow, C.; Gale, J. D.; Grimes, R. W. Recent computational studies in solid state chemistry. *Journal of Solid State Chemistry* **1993**, *106*, 13-26.

82. Born, M. K. Huang Dynamical theory of crystal lattices. *Oxford University Press* **1954**.

83. Gibbs, J. W. The Collected Papers, *Thermodynamics*. **1928,** 1.

84. Ewald, P. P. Die Berechnung optischer und elektrostatischer Gitterpotentiale. *Annalen der physik* **1921**, *369*, 253-287.

85. Lewis, G. V.; Catlow, C. Potential models for ionic oxides. *Journal of Physics C: Solid State Physics* **1985**, *18*, 1149.

86. Yarnell, J. L.; Katz, M. J.; Wenzel, R. G.; Koenig, S. H. Structure factor and radial distribution function for liquid argon at 85 K. *Physical Review A* **1973**, *7*, 2130.

87. Chandler, D. Introduction to modern statistical. *Mechanics.Oxford University Press, Oxford, UK* **1987**, *5*, 449.

88. Frenkel, D.; Smit, B. Understanding molecular simulation: from algorithms to applications; Elsevier: **2001**, 1.

89. Frenkel, D.; Smit, B.; Ratner, M. A. Understanding molecular simulation: from algorithms to applications; Academic Press San Diego: **1996**, 2.

90. Lerch, D.; Wieckhorst, O.; Hart, G. L.; Forcade, R. W.; Müller, S. UNCLE: a code for constructing cluster expansions for arbitrary lattices with minimal user-input. *Modelling and Simulation in Materials Science and Engineering* **2009**, *17*, 055003.

91. Sanchez, J. M.; Ducastelle, F.; Gratias, D. Generalized cluster description of multicomponent systems. *Physica A: Statistical Mechanics and its Applications* **1984**, *128*, 334-350.

92. Van Baal, C. M. Order-disorder transformations in a generalized Ising alloy. *Physica* **1973**, *64*, 571-586.

93. Teeriniemi, J.; Melander, M.; Lipasti, S.; Hatz, R.; Laasonen, K. Fe–Ni nanoparticles: A multiscale first-principles study to predict geometry, structure, and catalytic activity. *The Journal of Physical Chemistry C* **2017**, *121*, 1667-1674.

94. Cao, L.; Mueller, T. Rational design of Pt_3Ni surface structures for the oxygen reduction reaction. *The Journal of Physical Chemistry C* **2015**, *119*, 17735-17747.

95. Schmidt, D. J.; Chen, W.; Wolverton, C.; Schneider, W. F. Performance of cluster expansions of coverage-dependent adsorption of atomic oxygen on Pt (111). *Journal of Chemical Theory and Computation* **2012**, *8*, 264-273.

96. Müller, S. Bulk and surface ordering phenomena in binary metal alloys. *Journal of Physics: Condensed Matter* **2003**, *15*, R1429.

97. Mayer, J. E.; Montroll, E. Molecular distribution. *Journal of Chemical Physics* **1941**, *9*, 2-16.

98. Sanchez, J. M.; Ducastelle, F.; Gratias, D. Generalized cluster description of multicomponent systems. *Physica A: Statistical Mechanics and its Applications* **1984**, *128*, 334-350.

99. Hart, G. L.; Blum, V.; Walorski, M. J.; Zunger, A. Evolutionary approach for determining first-principles hamiltonians. *Nature Materials* **2005**, *4*, 391-394.

100. Ungerer, P.; Tavitian, B.; Boutin, A. Applications of molecular simulation in the oil and gas industry: Monte Carlo methods; Editions Technip: **2005**.

101. Bortz, A. B.; Kalos, M. H.; Lebowitz, J. L. A new algorithm for Monte Carlo simulation of Ising spin systems. *Journal of Computational Physics* **1975**, *17*, 10-18.

102. Gómez-Jeria, J. S. A new set of local reactivity indices within the Hartree-Fock-Roothaan and density functional theory frameworks. *Canadian Chemical Transactions* **2013**, *1*, 25-55.

103. Plimpton, S. Fast parallel algorithms for short-range molecular dynamics. *Journal of Computational Physics* **1995**, *117*, 1-19.

104. Tarascon, J.; Armand, M. Issues and challenges facing rechargeable lithium batteries. *Nature* **2001**, *414*, 359-367.

105. Delmas, C. Sodium and sodium-ion batteries: 50 years of research. *Advanced Energy Materials* **2018**, *8*, 1703137.

106. J. Moring; Kostiner, E. The crystal structure of $NaMnPO_4$. J*ournal of Solid-State Chemistry* **1986**, 61, 379.

107. Palomares, V.; Serras, P.; Villaluenga, I.; Hueso, K. B.; Carretero-Gonzlez, J.; Rojo, T. Na-ion batteries, recent advances and present challenges to become low cost energy storage systems. *Energy & Environmental Science* **2012**, *5*, 5884-591.

108. Zheng, L.; Wang, H.; Luo, M.; Wang, G.; Wang, Z.; Ouyang, C. Na_2MnO_3 as cathode materials for Na ion batteries: From first-principles investigations. *Solid State Ionics* **2018**, *320*, 210-214.

109. Zhu, L.; Li, L.; Wen, J.; Zeng, Y. Structural stability and ionic transport property of $NaMPO_4$ (M = V, Cr, Mn, Fe, Co, Ni) as cathode material for Na-ion batteries. *Journal of Power Sources* **2019**, *438*, 227016.

110. Aydinol, M. K.; Kohan, A. F.; Ceder, G.; Cho, K.; Joannopoulos, J. Ab initio study of lithium intercalation in metal oxides and metal dichalcogenides. *Physical Review B* **1997**, *56*, 1354.

111. Berthelot, R.; Carlier, D.; Delmas, C. Electrochemical investigation of the P2–Na_xCoO_2 phase diagram. *Nature Materials* **2011**, *10*, 74-80.

112. Wang, Y.; Yu, X.; Xu, S.; Bai, J.; Xiao, R.; Hu, Y.; Li, H.; Yang, X.; Chen, L.; Huang, X. A zero-strain layered metal oxide as the negative electrode for long-life sodium-ion batteries. *Nature Communications* **2013**, *4*, 2365.

113. Komaba, S.; Takei, C.; Nakayama, T.; Ogata, A.; Yabuuchi, N. Electrochemical intercalation activity of layered $NaCrO_2$ vs. $LiCrO_2$. *Electrochemistry Communications* **2010**, *12*, 355-358.

114. Kim, H.; Shakoor, R. A.; Park, C.; Lim, S. Y.; Kim, J.; Jo, Y. N.; Cho, W.; Miyasaka, K.; Kahraman, R.; Jung, Y.; Choi, J. W. $Na_2FeP_2O_7$as a Promising Iron-Based Pyrophosphate Cathode for Sodium Rechargeable Batteries: A Combined Experimental and Theoretical Study. *Advanced Functional Materials* **2013**, *23*, 1147-1155.

115. Kresse, G.; Furthmüller, J. Efficient iterative schemes for ab initio total-energy calculations using a plane-wave basis set. *Physical Review. B, Condensed Matter* **1996**, *54*, 11169-11186.

116. Kresse, G.; Joubert, D. From ultrasoft pseudopotentials to the projector augmented-wave method. *Physical Review B* **1999**, *59*, 1758.

117. Kresse, G.; Hafner, J. Ab initio molecular-dynamics simulation of the liquid-metal–amorphous-semiconductor transition in germanium. *Physical Review B* **1994**, *49*, 14251.

118. Kresse, G.; Hafner, J. Ab initio molecular dynamics for open-shell transition metals. *Physical Review B* **1993**, *48*, 13115.

119. Koyama, Y.; Tanaka, I.; Nagao, M.; Kanno, R. First-principles study on lithium removal from Li_2MnO_3. *Journal of Power Sources* **2009**, *189*, 798-801.

120. Losey, A.; Rakovan, J.; Hughes, J. M.; Francis, C. A.; Dyar, M. D. Structural variation in the lithiophilite-triphylite series and other olivine-group structures. *Canadian Mineralogist* **2004**, *42*, 1105-1115.

121. Avdeev, M.; Mohamed, Z.; Ling, C. D.; Lu, J.; Tamaru, M.; Yamada, A.; Barpanda, P. Magnetic structures of $NaFePO_4$ maricite and triphylite polymorphs for sodium-ion batteries. *Inorganic Chemistry* **2013**, *52*, 8685-8693.

122. Priyanka, V.; Savithiri, G.; Subadevi, R.; Sivakumar, M. An emerging electrochemically active maricite $NaMnPO_4$ as cathode material at elevated temperature for sodium-ion batteries. *Applied Nanoscience* **2020**, *10*, 3945-3951.

123. Anubhav, J.; Shyue, P. O.; Geoffroy, H.; Wei, C.; William, D. R.; Stephen, D.; Shreyas, C.; Dan, G.; Gerbrand, C.; Kristin A., P. Commentary: The Materials Project: A materials genome approach to accelerating materials innovation. *APL Materials* **2013**, *1*, 011002.

124. H. Huang; Yin, S.; Nazar, L. F. Approaching Theoretical Capacity of $LiFePO_4$ at Room Temperature at High Rates. *Electrochemical and Solid-State Letters* **2001**, 4, 170.

125. A. Yamada; Chung, S. C.; Hinokuma, K. Optimized $LiFePO_4$ for lithium battery cathodes. *Journal of the Electrochemical Society*, **2001**, 148, 224.

126. Andersson, A. S. Thermal stability of $LiFePO_4$ based cathodes. *Electrochemical and Solid-State Letters* **1999**, *3*, 66.

127. Fang, Y.; Liu, Q.; Xiao, L.; Ai, X.; Yang, H.; Cao, Y. High-Performance Olivine NaFePO4 Microsphere Cathode Synthesized by Aqueous Electrochemical Displacement Method for Sodium Ion Batteries. *ACS Applied Materials & Interfaces* **1900**, *7*, 17977-17984.

128. Man Huon Han; Gonzalo, E.; Casas-Cabanas, M.; Rojo, T. Structural evolution and electrochemistry of monoclinic $NaNiO_2$ upon the first cycling process. *Journal of Power Sources* **2014**, *258*, 266-271.

129. Zelang Jian; Liang Zhao; Huilin Pan; Hu, Y.; Hong Li; Wen Chen; Liquan Chen Carbon coated $Na_3V_2(PO_4)_3$ as novel electrode material for sodium ion batteries. *Electrochemistry Communications* **2012**, *14*, 86-89.

130. Moring, J.; Kostiner, E. The crystal structure of $NaMnPO_4$. *Journal of Solid-State Chemistry* **1986**, *61*, 379-383.

131. Moreau, P.; Guyomard, D.; Gaubicher, J.; Boucher, F. Structure and Stability of Sodium Intercalated Phases in Olivine $FePO_4$. *Chemistry of Materials* **2010**, *22*, 4126-4128.

132. Lee, K. T.; Ramesh, T. N.; Nan, F.; Botton, G.; Nazar, L. F. Topochemical synthesis of sodium metal phosphate olivine's for sodium-ion batteries. *Chemistry of Materials* **2011**, *23*, 3593-3600.

133. S. Chakrabarti; Thakur, A. K.; Biswas, K. DFT Analysis of Lithium De-Intercalation in Li_2FeVO_4. *Ionics* **2013**, 19, 1515.

134. Brissonnet, Y.; Compain, G.; Renoux, B.; Daligault, F.; Deniaud, D.; Papot, S.; Gouin, S. G. Design of multivalent glucuronides with self-immolative linkers and their hydrolysis rate by β-glucuronidase. *RSC advances* **2019**.

135. Lethole, N. L.; Ngoepe, P. E.; Chauke, H. R. First-principles study: Effect of lithium and sodium intercalation in transition metal phosphates, MPO_4 (M: Mn, Fe, Co). *Computational Condensed Matter* **2020**, *22*, 00437.

136. Chung, D. H.; Buessem, W. R. The elastic anisotropy of crystals. *Journal of Applied Physics* **1967**, *38*, 2010-2012.

137. D. Morgan; Van Der Ven, A.; Ceder, G. Li conductivity in $LixMPO_4$ (m= mn, fe, co, ni) olivine materials. *Electrochemical and Solid-State Letters* **2003**, 7, 2, 30.

138. Mendelev, M. I.; Ackland, G. J. Development of an interatomic potential for the simulation of phase transformations in zirconium. *Philosophical Magazine Letters* **2007**, *87*, 349-359.

139. Chiba, H.; Nishidate, K.; Baba, M.; Kumagai, N.; Sato, T.; Nishikawa, K. Molecular dynamics study of a V_2O_5 crystal. *Solid State Communications* **1999**, *110*, 497-502.

140. Tealdi, C.; Spreafico, C.; Mustarelli, P. Lithium diffusion in $Li_{1-x}FePO_4$: the effect of cationic disorder. *Journal of Materials Chemistry* **2012**, *22*, 24870-24876.

141. Van Baal, C. M. Order-disorder transformations in a generalized Ising alloy. *Physica* **1973**, *64*, 571-586.

142. Kim, D. J.; Ponraj, R.; Kannan, A. G.; Lee, H.; Fathi, R.; Ruffo, R.; Mari, C. M.; Kim, D. K. Diffusion behavior of sodium ions in $Na_{0.44}MnO_2$ in aqueous and non-aqueous electrolytes. *Journal of Power Sources* **2013**, *244*, 758-763.

143. Guo X, Chen C, Ong SP. Intercalation chemistry of the disordered rocksalt $Li_3V_2O_5$ anode from cluster expansions and machine learning interatomic potentials. *Chemistry of Materials* **2023** 35, 1537.

Appendix A

Papers Presented at Local and International Conferences

1. SAIP2021, 22-30 July 2021 North-West University, Victual conference. First principles calculations study of O3 and P2 $NaMn_{1/2}Fe_{1/2}O_2$ as potential cathode for sodium ion battery application.
2. CCP2023 - 34th IUPAP Conference on Computational Physics, august 4 (Fri) - 8 (Tue), 2023, Kobe International Conference Center, Kobe Port Island, Kobe, Japan.
3. SAIP 2024 - 68th annual conference of the South African Institute of Physics (SAIP2024) - to be held 1st-5th July 2024 at Rhodes University.
4. CCP-2024 — 35th IUPAP Conference on Computational Physics to be held from 07 July 2024 to 12 July 2024 in Thessaloniki, Greece.

Publications Papers

1. RS Dima, PM Maleka, EN Maluta, RR Maphanga. First principles study on sodium de-intercalation from NaMnPO4. Materials Today: Proceedings, 62, 1, 2022, S7-S11
2. RS Dima, PM Maleka, NE Maluta, RR Maphanga. Structural, electronic, mechanical, and thermodynamic properties of Na deintercalation from olivine NaMnPO4: First-principles study. Materials 15 (15), 5280